New Approaches for the Study of the Kinetics

of Reactions at Immiscible Liquid/Liquid and

Air/Liquid Interfaces

by

Christopher John Slevin

A thesis submitted for the degree of Doctor of Philosophy at

the University of Warwick

Faculty of Science

Department of Chemistry

University of Warwick

Coventry

CV4 7AL

March 1999

For my parents, without whose support this would not

have been possible

Acknowledgements

First and foremost, I would like to thank Professor Patrick Unwin for his infectious enthusiasm and constant support at all times during the research and writing up stages of this work.

I would particularly like to thank Julie Macpherson, not only for her invaluable help in completing this thesis, but also for being a great work colleague and friend. Thanks are due to the other members of the group, both past (Rachel and Mark) and present (Nick, Claire, Anna, Samina, Phil, Bex, Lou, Nicky, Sofia and Jie), for all of their contributions which have helped me complete this PhD and for making the lab an enjoyable place to work.

I would also like to acknowledge Ken Westwood, Lee Butcher and Norman Horner in the mechanical workshop, Philip Roskelly and Kirk Harris in the electronics workshop, and Alex Stuart and Peter Brindley in the glassblowing workshop, for all their efforts and consummate skills which went into producing exactly what was required to get the job done whenever asked.

I must finally thank those who funded this work, namely the EPSRC and Zeneca, and my supervisors at Zeneca Huddersfield Works, John Atherton and John Umbers, for their contributions over the last three years.

Declaration

I hereby declare that all of the work contained within this thesis is my own apart from where otherwise stated.

Experiments described in Chapter 4 were carried out in collaboration with Professor D. J. Walton and Dr S. Ryley at the Centre for Molecular and Biomolecular Electronics, School of Natural and Environmental Sciences, Coventry University, Priory Street, Coventry, United Kingdom CV1 5FB.

MEMED measurements using nanode probes were made with Mr M. A. Webb, as part of an MSc project.

The following is a list of all the work arising from this thesis that has been published in refereed journals:

A. L. Barker, M. Gonsalves, J. V. Macpherson, C. J. Slevin and P. R. Unwin, Scanning Electrochemical Microscopy: Beyond the Solid/Liquid Interfaces, *Anal. Chim. Acta*, in press.

C. J. Slevin, S. Ryley, D. J. Walton and P. R. Unwin, A New Approach for

Measuring the Effect of a Monolayer on Molecular Transfer Across an Air/Water Interface Using Scanning Electrochemical Microscopy, *Langmuir*, **1998**, *14*, 5331 - 5334.

A. L. Barker, J. V. Macpherson, C. J. Slevin and P. R. Unwin, Scanning Electrochemical Microscopy (SECM) as a Probe of Transfer Processes in Two-Phase Systems: Theory and Experimental Applications of SECM-Induced Transfer with Arbitrary Partition Coefficients, Diffusion Coefficients and Interfacial Kinetics, *J. Phys. Chem. B*, **1998**, *102*, 1586 - 1598.

C. J. Slevin, J. V. Macpherson and P. R. Unwin, Measurement of Local Reactivity at Liquid/Solid, Liquid/Liquid and Liquid/Gas Interfaces with the Scanning Electrochemical Microscope: Principles, Theory and Applications of the Double Potential Step Chronoamperometric Mode, *J. Phys. Chem. B*, **1997**, *101*, 10851 - 10859.

C. J. Slevin and P. R. Unwin, Measurement of Liquid/Liquid Interfacial Kinetics by Directly Probing the Concentration Profiles at Expanding Droplets, *Langmuir*, **1997**, *13*, 4799 - 4803.

C. J. Slevin, J. A. Umbers, J. H. Atherton and P. R. Unwin, A New Approach to the Measurement of Transfer Rates Across Immiscible Liquid/Liquid Interfaces, *J. Chem. Soc., Faraday Trans.*, **1996**, *96*, 5177 - 5180.

Abstract

This thesis describes the development of new techniques and new approaches for studying the kinetics and mechanisms of reactions which occur at the interface between two immiscible liquids. New approaches for studying the kinetics of transfer processes at the air/water interface are also described.

Scanning electrochemical microscopy (SECM) is employed in the equilibrium perturbation (EP) mode for studying reversible transfer processes at liquid/liquid and air/water interfaces. In this application, an ultramicroelectrode (UME) located in an aqueous phase, at micrometre distances from the interface of interest, is employed to drive a transfer process, initially at equilibrium, in the direction of the aqueous phase by depleting the local aqueous concentration of a target species by electrolysis. The UME current flow depends on the transfer kinetics at the interface. The development of a submarine UME allows SECM to be conducted at the air/water interface, or at a liquid/liquid interface with the electrode in the more dense phase. The kinetics of the extraction/stripping reactions of aqueous copper (II) with an oxime ligand (Acorga P50) in 1,2-dichloroethane (DCE) and heptane are first investigated. Subsequently, measurements of the kinetics of oxygen transfer across a condensed monolayer of 1-octadecanol, as a function of surface area, demonstrate that the accessible free area of the interface primarily governs the rate of oxygen transfer.

SECM double potential step chronoamperometry is developed to study irreversible transfer processes at interfaces. Theoretical modelling is applied and tested through experimental measurements on model interfaces. Subsequently, the rate of transfer of bromine from aqueous solutions to DCE and to air is shown to be above the upper limit measurable by the technique, however, a lower limit on the first order transfer rate constant of 0.5 cm s^{-1} is assigned.

A new technique, termed microelectrochemical measurements at expanding droplets (MEMED) is developed for studying spontaneous reactions at liquid/liquid interfaces. In MEMED, the two liquids are contacted by flowing one (feeder) through a capillary submerged in the second (receptor), resulting in the growth of drops at the capillary tip. The interfacial reaction generates a product or reactant concentration profile, which extends into the receptor phase. This is probed directly using a UME positioned opposite the capillary in the solution, operated in either a potentiometric or an amperometric mode, as a local concentration probe. A numerical model for mass transport in this configuration is developed, and the technique and model are assessed by measuring both bromine transfer from aqueous sulfuric acid solutions to drops of DCE, and bimolecular electron transfer between iridium (IV) chloride in the aqueous solution and ferrocene in the organic phase, which exhibit transport-controlled transfer rates under the conditions employed. The MEMED technique is applied to measure the kinetics of the hydrolysis of triphenylmethyl chloride (TPMCl), at the DCE/water interface, through potentiometric measurement of the chloride ion concentration profile. The reaction is shown to be first-order in TPMCl, occurring interfacially, with a rate constant of 6.5×10^{-5} cm s^{-1}. Subsequently, the oxidation of methylanisole (MA) (feeder) by aqueous solutions of cerium (IV) (Ce(IV)) (receptor), is probed. Under the conditions of this study, the reaction at the interface dominates, with a negligible contribution from the aqueous phase reaction between dissolved MA and Ce(IV).

TABLE OF CONTENTS

STEP CHRONOAMPEROMETRIC MODE: PRINCIPLES, THEORY AND APPLICATIONS

CHAPTER 1

INTRODUCTION

This chapter provides an overview of the significance of reactions which occur at the interface between two immiscible liquid phases, and reviews some of the approaches employed for investigating the kinetics and mechanisms of this class of reaction. The review of techniques is divided into two main sections, consisting of general techniques and electrochemical techniques, and focuses specifically on more recent and novel approaches that have not yet been widely reviewed in the literature. The application of scanning electrochemical microscopy (SECM) is considered in detail, since it is employed extensively in the studies described in this thesis. The aims of this study are outlined at the close of this chapter.

1.1 Kinetics of Reactions at Liquid/Liquid Interfaces

Reactions that occur at the interface between two immiscible solutions are very common in a wide range of areas. Industrially important processes such as the solvent extraction of metals ions[1,2] and phase transfer catalysis,[3] rely on controlling reactions at liquid/liquid interfaces. In addition, immiscible liquid/liquid interfaces can be considered as useful analogues of biomembranes[4,5,6] for the experimental investigation of cell membrane transfer processes including drug delivery systems.[7] On a more general level, interest in the study of charge transfer processes at immiscible liquid/liquid interfaces has been rapidly increasing recently.[8,9] This research has led to developments in areas such as analysis with amperometric ion selective electrodes,[10] as well as in

1

understanding the fundamentals of charge transfer mechanisms at liquid/liquid interfaces.[8,11]

An improved understanding of the kinetics and mechanisms of these interfacial processes is of crucial importance in establishing the fundamentals of the key processes, and in development of procedures and techniques for industrial processes. An important part of this development is the introduction of new techniques which advance research in this area.

The investigation of the kinetics of reactions which occur at the interface between two immiscible liquids requires the consideration of a number of factors. As with all studies of reaction kinetics, all possible rate-limiting steps must be considered. For interfacial processes at solid/liquid or liquid/liquid interfaces, the overall rate may be limited by the transport of the reactants, intermediates and products to and from the interface, true interfacial processes, or by a combination of the two, as illustrated in Figure 1.1. For the simplest situation where transport is important in one phase only, the rate of conversion of R to P may be expressed as:

$$\frac{1}{j_r} = \frac{1}{j_t} + \frac{1}{j_i} \quad (1.1)$$

In equation 1.1, j_r is the overall reaction rate (mol cm^{-2} s^{-1}), j_t is the rate of the reaction under mass transport control, which varies with the mass transport rate, and j_i is the rate of the interfacial reaction. In order to measure interfacial reaction rates it is therefore necessary to either work under conditions where the overall rate is limited only by the rate of the interfacial reaction, i.e., the transport step is fast, or to make the transport step well-defined and calculable, so that its

2
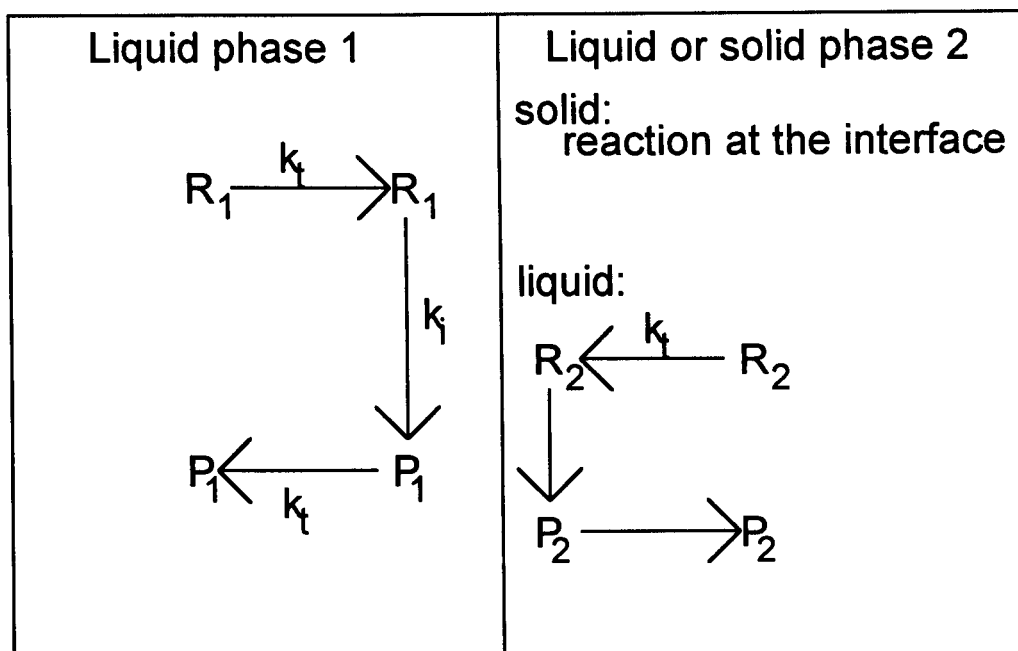
Figure 1.1   Schematic illustrating the steps involved in an interfacial reaction at a liquid/solid or liquid/liquid interface. R_i and P_i represent reactants and products in phase i (1 or 2), respectively, and the rate constants for the mass transport and interfacial reaction steps are indicated by k_t and k_i respectiveley.

effect can be accounted for when interpreting rate data.

Attaining controlled, variable (over a wide range) and calculable mass transport is the ideal situation for investigating the mechanisms and kinetics of interfacial reactions, so that a more complete picture of the reaction can be established. For the study of reactions at immiscible liquid/liquid interfaces, achieving a well-defined contact, with known interfacial area, under conditions where variable and high rates of mass transport are possible, is not trivial. The major additional complications introduced when two liquid phases, rather than a solid/liquid interface, are studied are that the transport on both sides of the interface, in each of the phases, must be considered, and achieving a stable interface of known area is much more difficult.

1.2 Methods for Studying Liquid/Liquid Interfacial Reaction Kinetics

The aim of this section is to review some of the more widely used and successful techniques that have been proposed for measuring the kinetics of reactions that occur at the interface between two immiscible liquids.

1.2.1 The Lewis Cell

Early attempts to address, experimentally, some of the difficulties associated with making kinetic measurements at immiscible liquid/liquid interfaces were made by Lewis[12,13] using the stirred cell design illustrated in Figure 1.2. The Lewis cell employs direct contact between the two immiscible liquids, and reaction rates are evaluated by measuring concentration changes in the bulk of one of the two phases, usually by a batch extraction technique. The rate of change of concentration is related to the interfacial reaction flux, j_i, by:

$$\frac{dc}{dt} = \frac{j_i A_{int}}{V} \quad (1.2)$$

where A_{int} is the interfacial area and V is the volume of the phase in which the concentration change is monitored. Stirrers are employed in each phase to generate convective transport to the interface on both sides. This reduces the contribution of diffusion to the overall kinetics, and it is generally assumed that the reaction rate can be evaluated by neglecting diffusion. The basic cell employed stirrers rotating at the same speed to minimise surface break-up, thereby achieving a relatively flat interface of determinable area.

Although the rate of mass transport to the interface can be increased by increasing the rate of stirring, the hydrodynamics are relatively ill-defined and

4
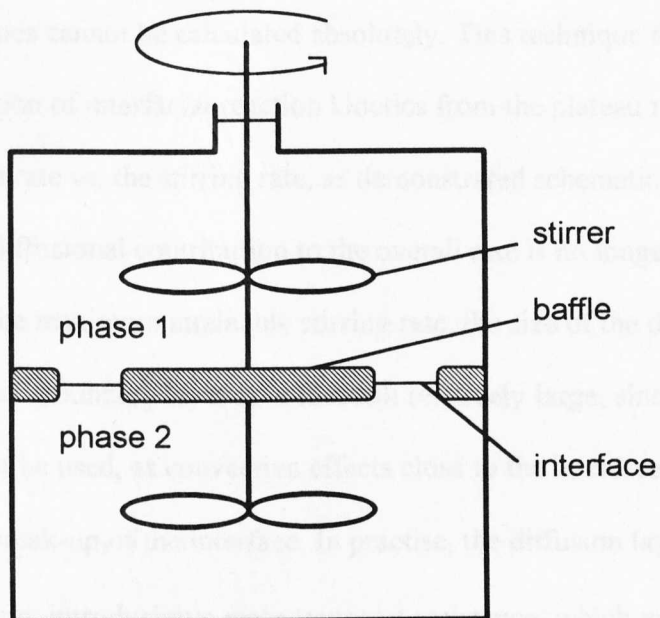
Figure 1.2   Schematic diagram showing the basic Lewis cell design.
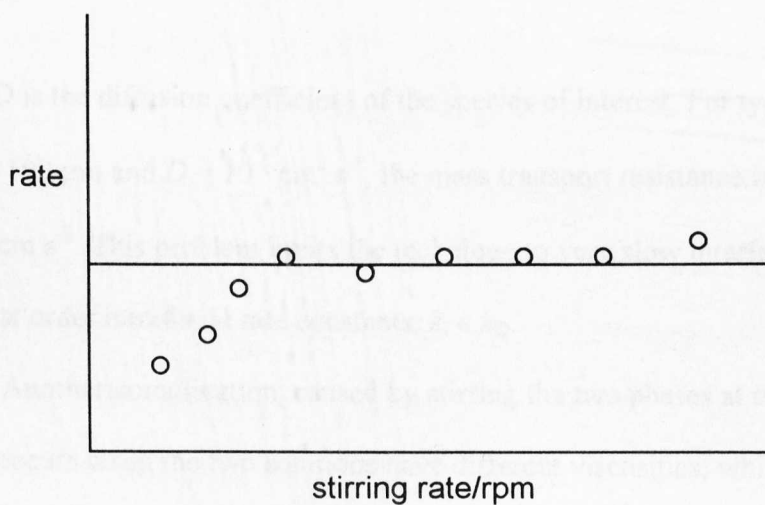
Figure 1.3   Schematic illustration of a typical plot constructed for the analysis of Lewis cell data.

5

transport rates cannot be calculated absolutely. This technique therefore relies on the calculation of interfacial reaction kinetics from the plateau region of a plot of the reaction rate vs. the stirring rate, as demonstrated schematically in Figure 1.3, where the diffusional contribution to the overall rate is no longer a limiting factor. At the maximum attainable stirring rate, the size of the diffusion concentration boundary layer is in fact still relatively large, since high stirring rates cannot be used, as convective effects close to the interface would cause excessive break-up of the interface. In practise, the diffusion layer thickness, δ_D, is *ca.* 100 µm, introducing a mass transport resistance, which may be evaluated using equation 1.3.

$$k_D = \frac{D}{\delta_D} \qquad (1.3)$$

where D is the diffusion coefficient of the species of interest. For typical values of $\delta_D = 100$ µm and $D = 10^{-5}$ cm^2 s^{-1}, the mass transport resistance is of the order of 10^{-3} cm s^{-1}. This problem limits the technique to very slow interfacial kinetics, with first order interfacial rate constants, $k_i \ll k_D$.

Another complication, caused by stirring the two phases at the same speed, occurs when the two solutions have different viscosities, which is common for immiscible liquids. The key fluid flow parameter is the Reynolds number, Re, which is expressed as the ratio of inertial to viscous forces in the solution as indicated in equation 1.4.

$$Re = vl \, / \, v \qquad (1.4)$$

In this equation, v is the fluid velocity, l is a characteristic length, and v is the kinematic viscosity of the fluid. When the viscosities of the two phases are different, the Reynolds numbers on each side of the interface will be unequal, resulting in differences in the flow characteristics and the diffusional properties between the two solutions. This makes the quantitative analysis of results obtained with this technique more difficult.

Developments in the design of the Lewis cell were made to overcome some of the problems associated with the initial design. The introduction of screens close to the interface, on either side, by Nitsch,[14] allowed stirring to be carried out at different speeds in each phase, thus making it possible to achieve the same Reynolds number on both sides of the interface. This modification to the cell also allowed more vigorous stirring and more efficient mixing in the bulk region without disturbances to the interface, thereby reducing the size of the diffusion layer and increasing the kinetic range of the technique.

A useful development in the design was the introduction of a flow loop to the system by Danesi,[15] eliminating the need for large volumes of solution, and the batch type sampling procedures that were previously required. Further developments included the use of a porous gauze[16] to support the interface with stirring close to the gauze employed to enhance mass transport. However, even with these advances, the main problems associated with using the Lewis design of contact cell remain, in that the mass transport characteristics are very poorly characterised. The technique is essentially limited to measuring first-order interfacial rate constants, $k_i < 10^{-5}$ cm s^{-1}.[3]

1.2.2 The Rotating Diffusion Cell

1.2.2.1 Description of the Technique

The rotating diffusion cell (RDC)[17] enables the study of liquid/liquid reaction kinetics under conditions where interfacial hydrodynamics are well defined and calculable. The design of the RDC is based on the rotating disc electrode,[18] which has been widely used for kinetic measurements at solid/liquid interfaces. The rotating disc electrode, which consists of a disc shaped electrode sealed in an insulating cylinder and rotated in a solution, has well defined hydrodynamics which have been calculated to give a complete description of the flow field in the contacting solution.[18] The mass transfer coefficient for this device under transport-limited conditions has been shown to be given by:[18]

$$k_t = 1.554 D^{2/3} v^{-1/6} \omega^{1/2} \qquad (1.5)$$

where D is the diffusion coefficient of the reacting species in $cm^2 s^{-1}$, v is the kinematic viscosity of the solution in $cm^2 s^{-1}$, and ω is the rotation frequency of the disc in Hz. The assumptions behind the derivation of equation 1.5 are that flow is laminar and the Schmidt number, $Sc = v / D$, is in excess of 10^3. These assumptions generally hold for most practical conditions.[19] In practice, the rate of mass transport to the disc can be controlled readily through the rotation speed. For rotation speeds up to 100 Hz, which is experimentally accessible for a solid electrode, the corresponding mass transport parameter, for typical D and v values of 1×10^{-5} $cm^2 s^{-1}$ and 1×10^{-2} $cm^2 s^{-1}$, respectively, is variable up to $\approx 1.5 \times 10^{-2}$ cm s^{-1}. This corresponds to a diffusion layer thickness of $ca.$ 7 μm.

The RDC, depicted schematically in Figure 1.4, operates with the
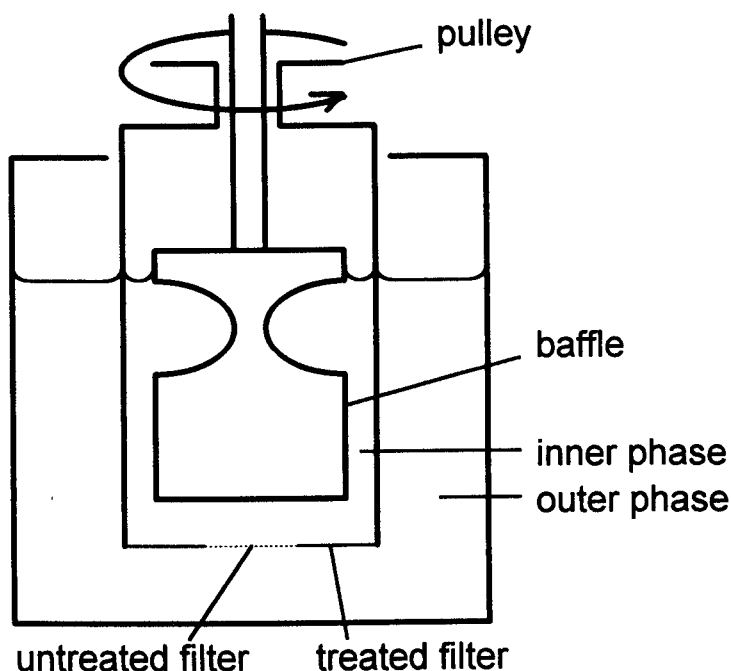
Figure 1.4   Schematic illustration of the rotating diffusion cell. The reaction is followed by sampling the bulk solution using a suitable technique.

interface supported at a thin porous membrane between the inner and outer compartments of the cell. A number of different arrangements are possible, the most common being to have aqueous solutions in both the inner and outer compartments, with the organic phase impregnated within the membrane. Abbreviated to w/o/w, this results in two aqueous/organic phase interfaces. Alternatively, w/o/o, w/w/o and o/o/o arrangements have also been used.[20] The membrane is rotated in the solution and the mass transfer profiles of the rotating disc are set up on both sides of the membrane. Liquid/liquid contact is achieved with a known area by treating the membrane with a solution which blocks the pores, except in a small circular area in the centre, which is untreated. Interfacial reactions are usually studied by measuring changes in the bulk concentrations of reacting species as described above for the Lewis cell, although interfacial fluxes can be measured directly by modifying the technique, as described later.

The kinetics of the reaction must be calculated from the combined kinetics of the system, which also includes transport to and from the disc shaped contacting area and transport through the membrane. The three resistances may be expressed according to the following equation, here considered for simple solute transfer in a water/oil (membrane)/water system, i.e. the two compartments contain aqueous phases with differing initial solute concentrations, separated by a membrane impregnated with the organic solvent:[20]

$$\frac{1}{P} = \frac{2\delta_D}{D_a} + \frac{K_P l_m}{\alpha_m D_o} + \frac{2}{\alpha_m k_{-1}} \quad (1.6)$$

In equation 1.6, P is the overall permeability constant, $2\delta_D / D_a$ describes the diffusion through the stagnant layers adjacent to the membrane in the aqueous phases on each side, D_a is the aqueous phase diffusion coefficient, and δ_D is the diffusion layer thickness, which for the hydrodynamic rotating disc arrangement, is given by:

$$\delta_D = 0.643 \nu^{1/6} D_a^{1/3} \omega^{-1/2} \quad (1.7)$$

$K_P l_m / \alpha_m D_o$ gives the resistance due to solute diffusion within a membrane of thickness l_m and porosity α_m. D_o is the organic phase diffusion coefficient, and K_P is the aqueous/organic partition coefficient. The term $2/\alpha_m k_{-1}$ represents the resistance at the interface, where k_{-1} is the heterogeneous rate constant for transfer of the solute from the aqueous to the organic phase.

Analysis of the data obtained from the RDC, involves plotting the

measured flux, usually as j_r^{-1}, against $\omega^{-1/2}$, and extrapolating to infinite rotation speed ($\omega^{-1/2} = 0$), such that the diffusion layer thickness is zero and diffusion is discounted. The y-axis intercept gives a measure of the flux, which is governed by the interfacial resistance term, and the resistance due to transport in the membrane, which must be subtracted in order to obtain the interfacial resistance. Figure 1.5 is a schematic of the form of an RDC data plot.
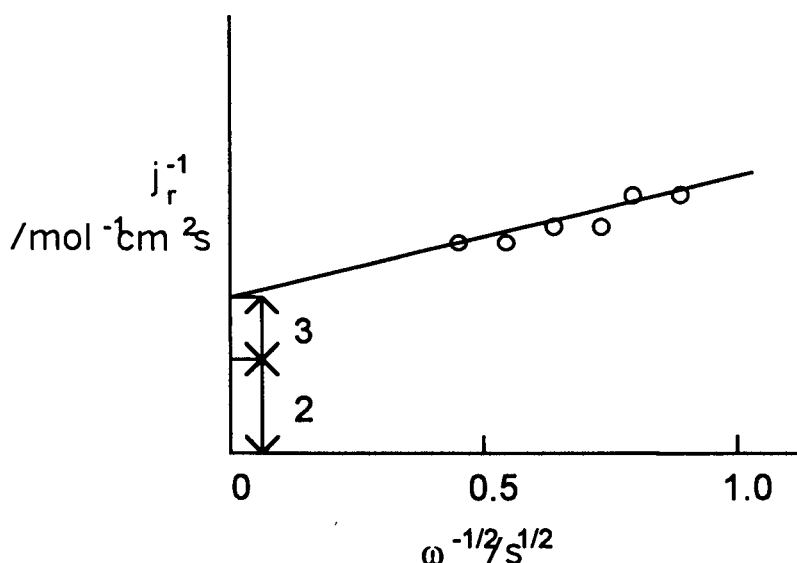
Figure 1.5   Schematic representation of a typical RDC plot, 2 and 3 indicate the contributions to the overall transport resistances due to the second and third terms on the right hand side of equation 1.6.

In contrast to the RDE, the range of rotation speeds used is limited in this experimental arrangement, the upper limit is around 6-8 Hz, while equation 1.7 breaks down below approximately 1-2 Hz, where the hydrodynamic boundary layer, δ_H, which may be evaluated by equation 1.8:

$$\delta_H = 3.6(\nu / \omega)^{1/2} \qquad (1.8)$$

becomes comparable with the rotating disc radius.[21] Consequently, the rate data
is obtained over a very narrow range of mass transport coefficients, the
maximum k_t available being only 4.4×10^{-3} cm s^{-1}. The significant extrapolation
of this data to $\omega^{-1/2} = 0$ has been suggested to be an unreliable way to calculate
the interfacial kinetics.[20]

A modification of the RDC design, based on the ring-disc arrangement of
the rotating disc electrode[22] incorporated an arc electrode[23,24] deposited on the
surface of the membrane around the untreated area. This facilitated the
electrochemical detection of the species reacting at the interface at short times
following the reaction. This method was used to study the solvent extraction of
copper, where cupric ions were reduced to copper metal at the arc electrode, and
the resulting current flow could be related to the interfacial flux at the membrane.

In addition to the problems of data analysis highlighted above, there are
several other drawbacks of the RDC that should be emphasised. First, the fact
that the interface must be supported adds a further, considerable, resistance to the
transport of species, which is in addition to the concentration boundary layers on
both sides of the membrane. This limits the range of kinetic systems that can be
studied. Second, blocking of the membrane can be problematic with some
reactions, and studies of the effects of surfactants on interfacial reactions are
difficult. Third, as mentioned above, the measurements are generally made in the
bulk of the solution and not at the interface.

1.2.2.2 Systems Studied With the RDC

The majority of RDC studies have concentrated on the measurement of
solute transfer resistances, in particular, focussing on their relevance as model

systems for drug transfer across the skin.[17,25,26,27] In these studies, isopropylmyristate is commonly used as solvent, as it has been proposed as a model compound for skin lipids. However, it has since been reported that the interfacial resistances measured in these studies are overestimates, and that the true interfacial resistances cannot be resolved with the RDC technique due to the severe mass transport limitations inherent in the technique.[20] The RDC technique has also been used to study more complicated interfacial processes such as microemulsion kinetics,[28] where one of the compartments contains an emulsion. A comprehensive study of the complex interfacial processes in the solvent extraction of copper by oxime ligands was also carried out with the RDC.[23,24]

1.2.3 The Liquid Jet Recycle Reactor (LJRR)

The LJRR[29,30] provides a method of measuring liquid/liquid reaction kinetics with direct contact, known interfacial area and reasonably defined hydrodynamics. This method operates by employing an aqueous liquid jet flowing in a cocurrent, coaxially flowing organic solution, shown schematically in Figure 1.6. The aqueous solution flows from the jet nozzle to a receiving
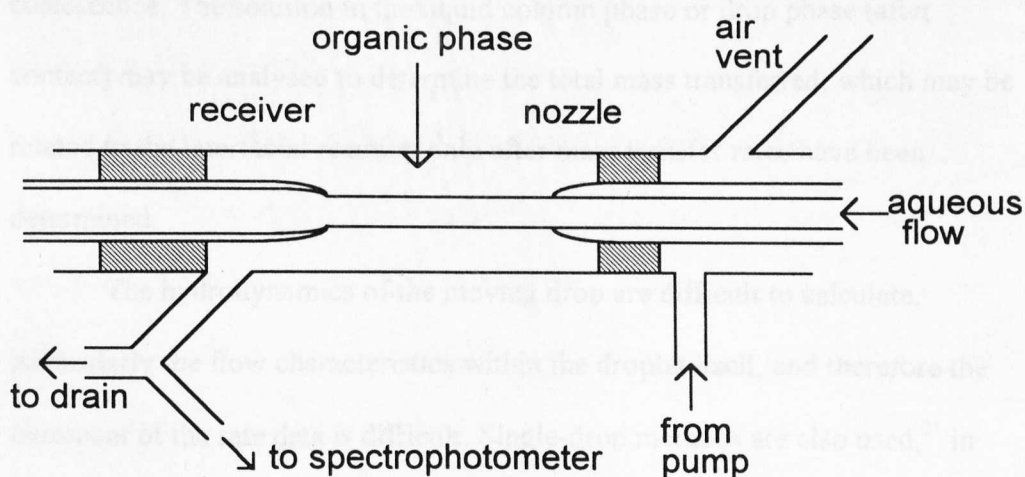
Figure 1.6   The liquid jet recycle reactor.

13

capillary with no overflow into the outer stream, resulting in short contact times of around 0.05 s. The analysis is carried out by flowing the outer organic phase continually through a closed loop and monitoring concentration changes spectrophotometrically. The apparatus used by Freeman and Tavlarides employed capillaries with internal diameters of 2 mm, and the jet length was 3.54 cm. The aqueous jet was arranged vertically, and a gravity fed flow system was used. This approach enabled measurements to be made on a clean interface with a known area (measurable by photography), however, the mass-transfer analysis is not trivial, and the convective-diffusion regime not as well-defined as in other approaches.

1.2.4 Moving Drops

The moving drop method[2] employs a column of one liquid phase through which drops of a second liquid can rise or fall. The drops are produced at a nozzle situated at one end of the column and collected at the other end. The contact time and size of the drop are measurable. Three regimes of mass transport are observed, namely drop formation, free rise (or fall) and drop coalescence. The solution in the liquid column phase or drop phase (after contact) may be analysed to determine the total mass transferred, which may be related to the interfacial reaction only after mass transfer rates have been determined.

The hydrodynamics of the moving drop are difficult to calculate, particularly the flow characteristics within the droplet itself, and therefore the treatment of the rate data is difficult. Single-drop methods are also used,[31] in which an individual drop of a liquid is grown and then withdrawn from a

capillary tip submerged in a second phase. Analysis of the concentration changes in the drop forming liquid following contact with the second liquid gives the experimental mass transfer data. A growing drop method has been reported[32] for measuring interfacial liquid/liquid reactions, in which mass transport to the growing drop was considered to be well-defined and calculable. This approach was applied to study the kinetics of the solvent extraction of copper by complexing ligands.

1.2.5 Other Approaches

Control of the interfacial transport and contact between two liquid phases has been attempted by several other techniques, some of which will be mentioned briefly here.

A constant interfacial area cell was developed, whereby laminar flow of the two phases parallel to the interface was produced through the addition of flow deflectors.[33] By forcing flow parallel to, rather than towards, the interface, it was proposed that the interface was less likely to be disrupted. Equations were derived to describe the flow velocities in the two-phases such that mass transport at the interface was calculable. Reactions were followed by sampling changes in the bulk solution concentrations.

Controlled contact of the two immiscible liquids has been achieved by flowing one liquid along a solid support submerged in the second phase.[34,35] Several different arrangements have been used, although all are based on the same principles. For example, a wetted wall column which offered liquid/liquid contact times of 0.5 – 10 s was used to measure solute transfer rates.[35] These techniques offer a known interfacial area under convective flow conditions,

thereby enhancing mass-transport rates. However, as with most other approaches, interfacial reaction rates must be determined from bulk solution measurements.

A pre-filled capillary was employed in one study[36] to establish contact between the two phases. The transport of a radiolabelled solute from the single end of the capillary exposed to a second stirred phase was measured by the concentration change in the receptor phase. The loss of solute across the well-defined interface at the end of the capillary was calculated by solving Fick's second law of diffusion, with appropriate boundary conditions for the system of interest.

The use of stirred suspensions of droplets for studying liquid/liquid reactions lacks the necessary control over the interfacial area and the transport step for determination of the fundamental interfacial processes.[3] These measurements are thus only of use in limited cases. However, they are of some value as they reproduce conditions in industrial processes.

1.2.6 Summary

The techniques described, thus far, show the range of different approaches used to achieve control in measurements of reaction kinetics at liquid/liquid interfaces. However, all of the techniques described have significant drawbacks, and no one technique fulfils all the requirements sufficiently for the unambiguous study of interfacial processes. The Lewis cell employs direct contact of the two liquids, but does not have well-defined hydrodynamics. The RDC introduces the added transport resistance of a supported interface in an effort to obtain well-defined hydrodynamics. The LJRR does have both direct contact and reasonably defined hydrodynamics. However, mathematical

modelling of the flowing solutions is complex, and the method is difficult to use experimentally.

With all of these methods, the measurements of concentration changes occurs in the bulk of solution and not at the interface where the reaction occurs. This therefore introduces a time lag, limiting the resolution of the measurement in determining interfacial kinetics.

1.3 Electrochemical Methods

Controlling interfacial mass transport at electrode/electrolyte interfaces is an important consideration in electrochemistry. As with all interfacial techniques, an accurate determination of the role of transport is crucial in measuring charge transfer kinetics. The polarised liquid/liquid interface, often termed the interface between two immiscible electrolyte solutions (ITIES), has many similar properties to the polarised metal electrode/electrolyte interface,[6] and has recently been a subject of major interest to researchers. Several detailed reviews on this topic have been published recently.[8,9] The aim of this section is to highlight some of the more recent, novel applications which have served to advance this area of research, and to provide details on those areas which are not currently covered by reviews. In particular, the techniques of greatest interest here are those which achieve controlled, variable and rapid mass-transport in order to resolve the fastest interfacial charge transfer processes.

1.3.1 Quiescent Polarised Interfaces

The first systematic studies of charge transfer processes at liquid/liquid interfaces involved measurements of ion transfer at polarised quiescent

17

liquid/liquid interfaces. Experimental techniques were limited until the

introduction of a four-electrode potentiostat in 1977,[37,38] illustrated schematically

in Figure 1.7, which made it possible to apply a range of conventional

electrochemical techniques, such as cyclic voltammetry,[37,38] polarography,[39]

potential step chronoamperometry,[40] and *ac* impedance methods[41] to the study of

liquid/liquid interfaces.
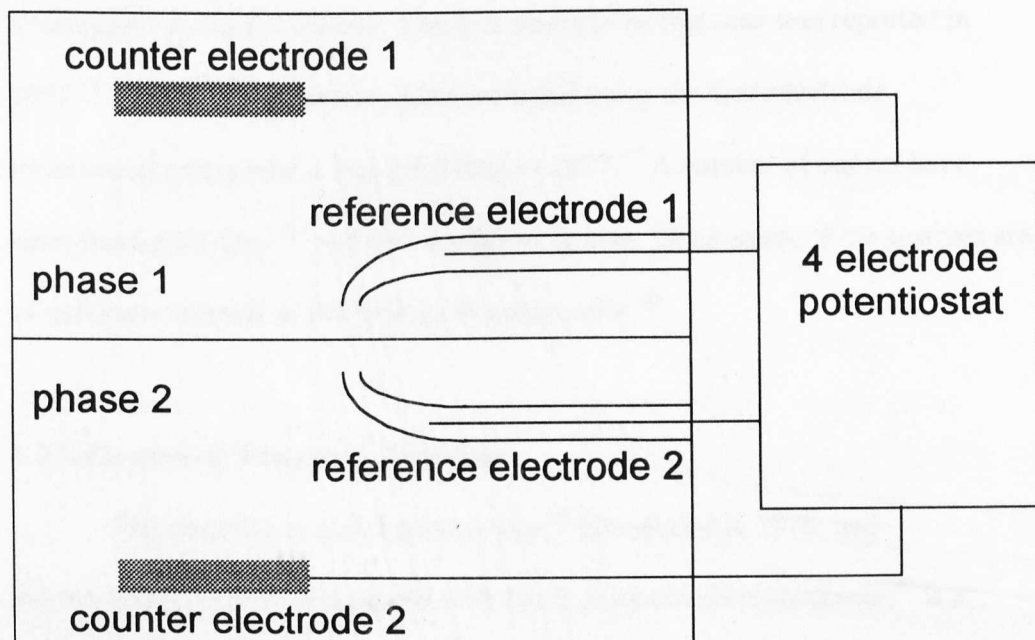
Figure 1.7   Schematic diagram of the experimental arrangement for
voltammetric measurements at the interface between two
immiscible electrolyte solutions using four electrodes.

Studies of ion and electron transfer processes have concentrated mainly

on kinetics and mechanisms, with a view to understanding the effect of

interfacial structure and developing theoretical models which describe charge

transfer.[8,11,42] Ion transfer studies are also particularly important in

electroanalysis for the detection and measurement of ionic species.[10] In this area,

the application of dynamic electrochemical methods (potential and current scan

techniques) offer greater control for the measurement of species, than the traditional use of potentiometry with ion sensitive electrodes.[10] Additionally, through the use of novel ligands, the electrochemical measurement of species not previously accessible by electrolysis at solid electrodes becomes possible.[43] Polarised interfaces, in particular, are of interest as models for ion and drug transfer across biomembranes.[44,45]

Electron transfer at immiscible liquid/liquid interfaces has only been investigated in depth recently. The first example of this case was reported in 1975,[46] and the first voltammogram recorded using the four-electrode potentiostat arrangement was published in 1977.[47] A number of papers have since been published,[8,9] and this is a growing area. Once again, these systems are of particular interest to the biological community.[48]

1.3.2 Electrolyte Dropping Electrode

The electrolyte dropping electrode,[39] introduced in 1976, and subsequently used in conjunction with the four-electrode potentiostat,[49] is a hydrodynamic technique, offering controlled convective transport. In essence, this approach is identical to the dropping mercury electrode,[50] however, in this case the drop consists of a flowing electrolyte liquid phase which, with the continuous phase form a polarised ITIES. In this approach, the interface is continually refreshed, minimising the possible problems of interfacial blocking (by reactants, intermediates and products). Due to the renewable interface, ion transfer at the polarised ITIES is particularly important in analysis. It has been used for the amperometric detection of a range of species, where the response may be characterised by evaluating the limiting current:

$$i = \kappa n_e F D^{1/2} q^{2/3} t^{1/6} c \qquad (1.9)$$

where κ is the Ilkovich constant, n_e is the number of electrons transferred for each redox event, F is Faraday's constant, c is the concentration of the species of interest, q is the volume flow rate and t is the drop time. Many species which are not accessible by conventional electrolysis, may be measured through the application of this technique with complexing ligands, as described above. A review focussing on the analytical applications of the technique has appeared.[51]

A comprehensive and systematic investigation of the fundamental factors in ion transfer measurements in the electrolyte dropping electrode arrangement has been carried out.[52] A hanging electrolyte drop has also been applied for the determination of ionic species in solution using differential pulse stripping voltammetry procedures.[53] Particular emphasis was given to assessing the selectivity and sensitivity of the method. The technique of current-scan polarography has also been applied in the study of electron transfer[54] reactions at the ITIES in this configuration.

1.3.3 Microhole Interface

The introduction of micrometre-sized liquid/liquid interfaces supported at capillary tips represented a significant advance in the study of interfacial ion and electron transfer kinetics.[55,56] This approach offers similar advantages to the use of ultramicroelectrodes (UMEs) (discussed below in section 1.4.1) in conventional (electrolytic) electrochemistry, in that an efficient hemispherical diffusion field is established at one side of the interface, thereby increasing the

mass transfer rate in that phase and enabling more rapid interfacial kinetics to be measured.[57] Additionally, the problems of iR_s drop which occur with interfaces of conventional size is reduced. Moreover, problems of ion pairing which could occur at the high supporting electrolyte concentrations normally required to reduce resistances in the organic phase with conventional-sized interfaces, are removed due to the possibility of using lower concentrations.

An interesting consequence of supporting an interface at a capillary tip is that there are quite different diffusional profiles for transfer in opposite directions. For ion transfer from the internal to the external solution (egress), linear diffusion in the confines of the capillary is observed, however, for transfer in the opposite direction, hemispherical diffusion occurs, as shown in Figure 1.8. The resulting differences in the voltammetric responses were exploited to obtain mechanistic information on the nature of assisted ion transfer reactions.[58]
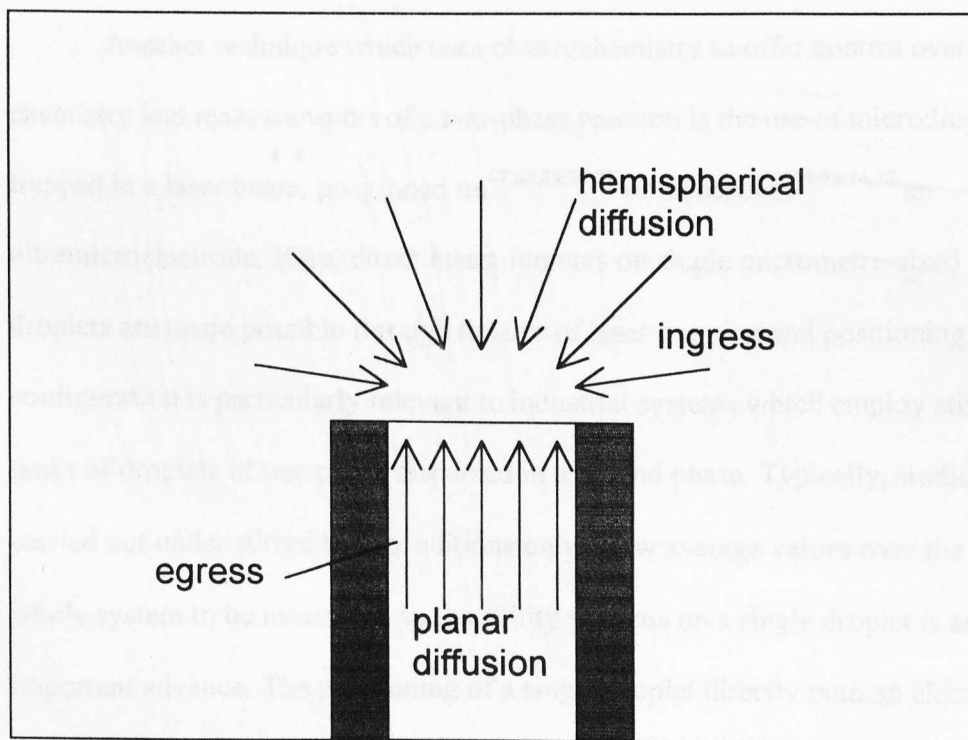
Figure 1.8   Schematic diagram illustrating the contrasting diffusion profiles for ingress and egress transport at a microcapillary tip supported liquid/liquid interface.

A number of systems have been investigated using various approaches, including voltammetry of assisted ion transfer at micrometre,[59,60] and nanometre[57] sized interfaces, as well as *ac* impedance studies.[61,62] Liquid/liquid interfaces supported at micromachined holes[63] have also been employed. The removal of the resistances caused by the long shank of the capillary enables measurements to now be made with little or no supporting electrolyte in either of the two phases. A recently described novel approach to forming liquid/liquid microelectrodes employed a recessed metal microelectrode to provide a micro-sized cavity which contained the organic or aqueous liquid. This liquid electrode was then simply placed in the second liquid.[64] The use of arrays of microinterfaces has also recently been investigated.[65,66]

1.3.4 Laser Trapped Drops

Another technique which uses electrochemistry to offer control over the chemistry and mass transport of a two-phase reaction is the use of microdroplets trapped in a laser beam, positioned on[67,68,69,70,71] or adjacent to[72,73,74,75] an ultramicroelectrode. Here, direct measurements on single micrometre-sized droplets are made possible through the use of laser trapping and positioning. This configuration is particularly relevant to industrial systems which employ stirred tanks of droplets of one phase dispersed in a second phase. Typically, studies carried out under stirred tank conditions only allow average values over the whole system to be measured, so the ability to focus on a single droplet is an important advance. The positioning of a single droplet directly onto an electrode enables electrochemistry to be carried out inside that droplet. This has enabled the study of mass transfer of ions across the single nitrobenzene droplet/water

phase interface,[67] the reaction being driven by the depletion of the target species in the drop. Alternatively, by positioning the droplet close to the electrode, but not in direct contact, a reaction at the organic microdroplet/water interface can be induced through generation of a reactant at the electrode surface from a precursor species in solution. This approach has been used in the study of a two-phase dye formation reaction,[72] as well as in the investigation of electron transfer rates across the interface of single droplets.[75] It should be noted, however, that the response times using this approach are, hitherto, relatively slow, and diffusion profiles are not particularly well-defined.

1.3.5 Spectroscopic Techniques

Total internal reflectance spectroscopy and fluorometry have been combined with electrochemical measurements to directly probe the interfacial region. The detection of fluorescence on applying a potential to drive ion transfer across the interface in voltage scan fluorometry and potential step chronofluorometry modes has been conjectured as a more sensitive technique than conventional electrochemical approaches.[76,77,78] Total internal reflection laser induced fluorescence offers a way of monitoring the interface directly, and has been employed alongside voltage scan[79] and ac impedance[80] techniques to study ion transfer.

Second-harmonic and sum-frequency spectroscopic techniques are particularly suited to studying interfaces, as these spectroscopic approaches are not influenced by the bulk material response; only the asymmetric environment at the interface gives a signal. The use of this approach to study interfaces has been reviewed,[81] with particular emphasis on the application to electrochemical

systems.[82]

1.3.6 Theoretical Approaches

Simulations of the liquid/liquid interface structure and of chemical reactions occurring at these interfaces have been carried out using a number of approaches. Molecular dynamics simulations of the water/1,2-dichloroethane (DCE)[83] and the water/nitrobenzene[84] interfaces have revealed detail of the microscopic, molecular level, structure of these interfaces. In particular, interesting solvent interactions at the interface have been identified. These systems were chosen because of their widespread use in electrochemical studies of polarised interfaces. Chemical reaction at the interface has also been investigated by various different simulation techniques. For example, molecular dynamics simulations[85,86,87,88] and other approaches[89,90,91] have been employed to investigate ion and solute transfer. A review which focuses on theoretical approaches for investigating various properties of liquid/liquid interfaces and their reactions has recently been provided by Benjamin.[92]

1.4 Scanning Electrochemical Microscopy

The scanning electrochemical microscope (SECM) was first introduced in 1989 by Bard and co-workers[93] and is one of a family of scanned probe microscopes. The SECM employs a UME[94,95,96] probe which is operated in close proximity to a target interface submerged in a solution such that the electrochemical response of the UME is governed by mass transport between the interface and UME, as well as by chemical reactions at the interface. In this way, the SECM reveals both topographical and interfacial reactivity information as a

function of a surface position. The spatial resolution is comparable with the dimensions of the UME tip, typically of the order of 1 - 25 μm.

The SECM has been widely used to investigate reactions that occur at solid/liquid interfaces, showing particular excellence in determining the kinetics of rapid interfacial processes. A number of reviews have recently been published covering the range of SECM measurements.[97,98,99,100,101,102] SECM has more recently been applied to studies of liquid/liquid interfaces, with the first report in 1995.[103] These experiments have concentrated mainly on kinetic studies of ion and electron transfer reactions at immiscible liquid/liquid interfaces.

1.4.1 Basics of Operation

The tip used in SECM is usually a disc-shaped UME which consists of a small wire, typically 1-25 μm in diameter, sealed in a glass capillary which is then polished back to expose the wire, resulting in an electrode of micrometre dimensions (Figure 1.9). The electrochemical cell commonly contains an
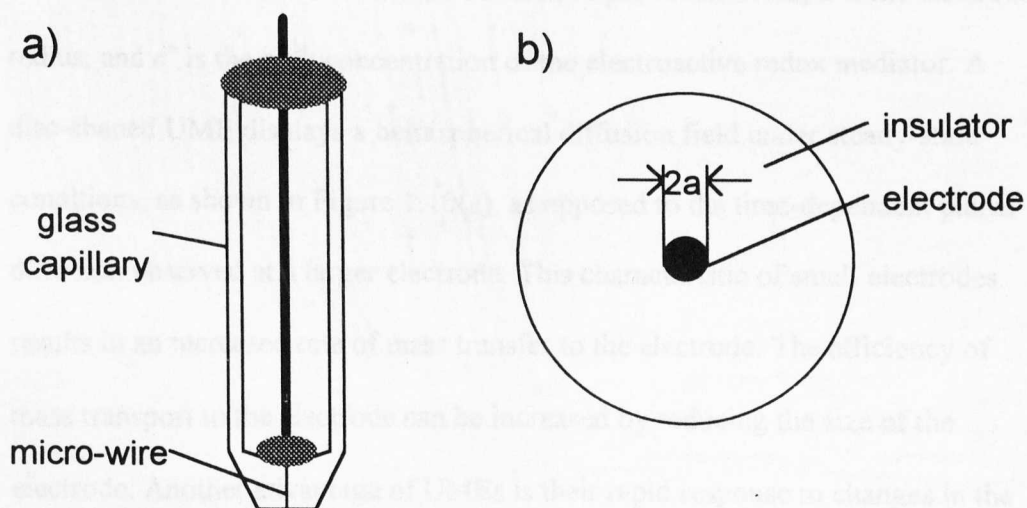
Figure 1.9   Schematic diagram of a glass-coated UME: a) side view, b) end view.

25

electroactive mediator which may be oxidised or reduced at the UME, as well as a supporting electrolyte. The SECM is usually operated in an amperometric mode, and a two-electrode set-up usually suffices, with the UME as working electrode, together with a quasi-reference electrode. This is possible because the low currents associated with UMEs, due to their small size, result in negligible iR_s drop and polarisation of the reference electrode.[94] In fact, UMEs can be used in media with low dielectric constants, [94] a particular advantage in studies of liquid/liquid interfaces, where operation of the UME in electrically resistive organic media may be required.

The steady-state diffusion-limited current observed at a UME in bulk solution, $i(\infty)$, without any influence of a substrate interface, is given by equation 1.10 for a simple electron transfer process.[104]

$$i(\infty) = 4n_e FDac^* \qquad (1.10)$$

where n_e is the number of electrons transferred per redox event, a is the electrode radius, and c^* is the bulk concentration of the electroactive redox mediator. A disc-shaped UME displays a hemispherical diffusion field under steady-state conditions, as shown in Figure 1.10(a), as opposed to the time-dependent planar diffusion observed at a larger electrode. This characteristic of small electrodes results in an increased rate of mass transfer to the electrode. The efficiency of mass transport to the electrode can be increased by reducing the size of the electrode. Another advantage of UMEs is their rapid response to changes in the applied potential. The effects of double layer charging are reduced to short timescales due to the small physical size of the electrode, making measurements

26
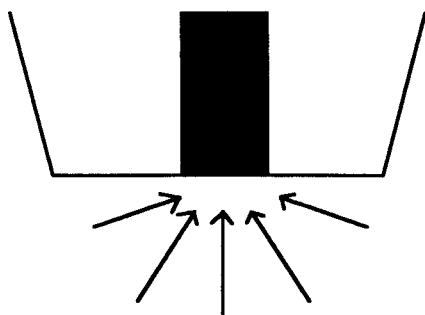
Figure 1.10a Steady-state hemispherical diffusion to a UME in bulk solution.

Insulating surface
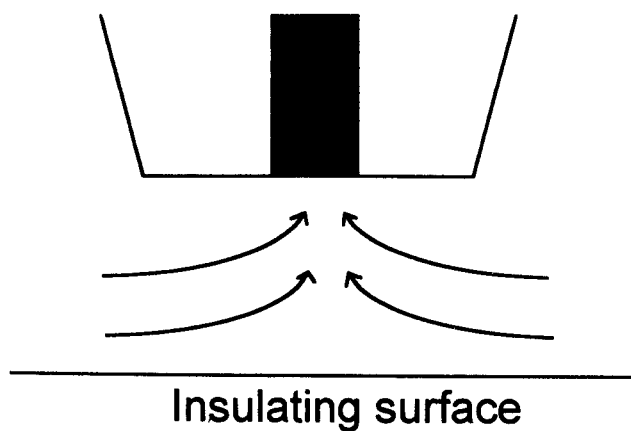
Figure 1.10b Hindered diffusion to a UME positioned close to an inert surface.

Conducting surface
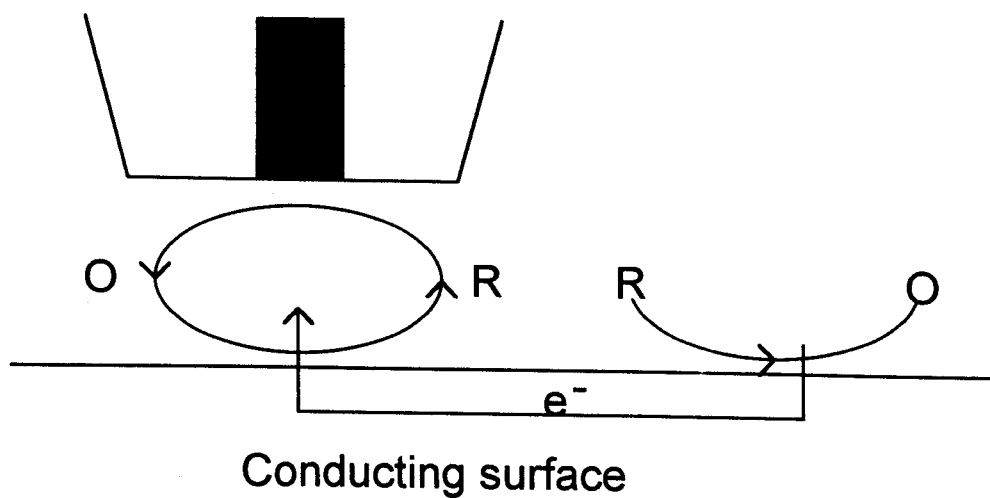
Figure 1.10c Feedback response at an unbiased conductor.

possible on the microsecond to nanosecond timescale. [94]

A typical SECM set-up is shown in Figure 1.11. The UME is positioned in three axes using piezoelectric elements, which expand or contract on the application of a voltage, allowing positioning with sub-micron level resolution. Electrochemical measurements may then be made in close proximity to a target interface, typically as a function of the tip-interface separation or as a function of the lateral position over the surface of interest.
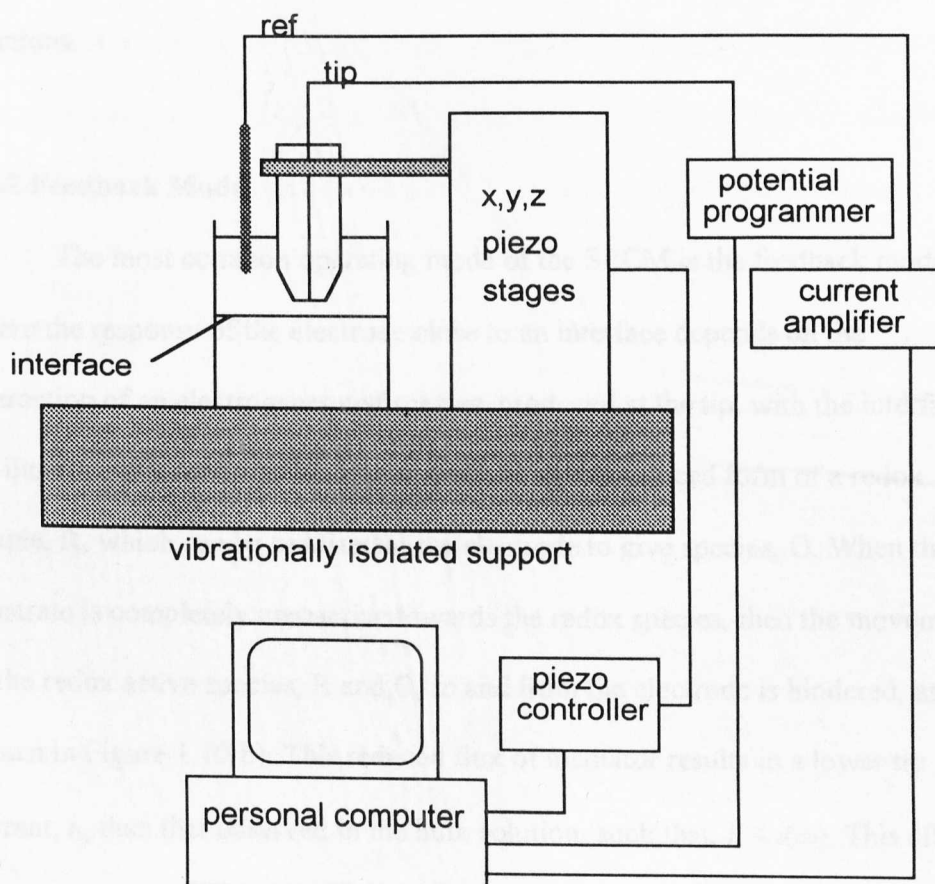
Figure 1.11 Schematic diagram showing a typical SECM set-up.

28

With the electrode positioned close to the target interface, within about one electrode radius, the flux of material to the electrode is perturbed compared to the diffusional profile in Figure 1.10(a). The effect on the current depends on the nature of the interface (i.e. its reactivity) and the distance of the electrode from the surface. The current measured depends on the flux of the mediator to the electrode. In the SECM geometry, control of the electrode-substrate separation allows the rate of mass transport between the electrode and the surface to be varied. High rates of mass transfer are achievable with rapid response times, which is clearly of vital importance in the measurement of fast interfacial reactions.

1.4.2 Feedback Mode

The most common operating mode of the SECM is the feedback mode, [105] where the response of the electrode close to an interface depends on the interaction of an electrogenerated species, produced at the tip, with the interface. To illustrate this, consider a solution containing the reduced form of a redox couple, R, which can be oxidised at the electrode to give species, O. When the substrate is completely unreactive towards the redox species, then the movement of the redox active species, R and O, to and from the electrode is hindered, as shown in Figure 1.10(b). This reduced flux of mediator results in a lower tip current, i_t, than that observed in the bulk solution, such that, $i_t < i(\infty)$. This effect is termed negative feedback. [105]

When the substrate potential is biased at a value sufficient to regenerate R from O, at a diffusion controlled rate, then the electrogenerated species, O, can diffuse to the substrate, be converted back to R, and diffuse back to the UME.

29

This redox cycle, shown in Figure 1.10(c), results in an enhanced flux of R to the electrode, compared with the bulk case, and the observed current is increased, such that $i_t > i(\infty)$. This effect is termed positive feedback. [105]

The size of the negative and positive feedback effects seen are dependent on the tip-substrate separation, and the positive feedback response also depends on the rate of the interfacial redox reaction.

The dependence of the current on distance can be used to record topographical data for a particular surface. In particular, at close distances the current changes significantly with only small changes in separation. Resolution of distances normal to the interface on the sub-micron level is possible even with a tip electrode tens of micrometres in diameter. In this application, the SECM is scanned across the surface of a substrate in a raster pattern while the current is monitored. Currents can be converted to a tip-interface distance, which in turn gives topographical information, if the surface reactivity is known. [106,107] Alternatively, an image of the reactivity of the substrate can be built up, where the topography is known. [108] A particular strength of SECM is the ability to use a solution which contains two separate mediators to record both topography and reactivity in subsequent raster scans.

For measuring the kinetics of reactions that occur at an interface, it is possible to construct approach curves, where the normalised current, $i_t/i(\infty)$ is plotted against the tip-substrate separation, d. The limiting cases described as negative and positive feedback are plotted in Figure 1.12; these correspond to surface reaction kinetics where the rate is zero, and where the rate of the redox reaction occurring at the substrate is controlled by mass transport, respectively. Kinetic cases for reaction rates between these two limits can be measured with

30
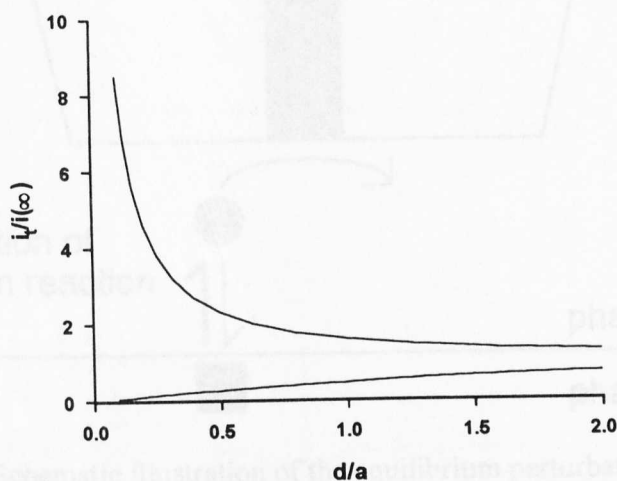
Figure 1.12 Plot of the feedback curves for positive (upper curve) and
negative (lower curve) feedback behaviour. Data from J. Kwak
and A. J. Bard, *Anal. Chem.*, **1992**, *61*, 1221.

this technique by fitting experimental data to simulated working curves.[109] Since

diffusion is fast for the SECM configuration, measurements of fast kinetics can

be made, in the cm s^{-1} domain.[110,111]

1.4.3 Other SECM Modes

1.4.3.1 Induced Reactions Using the Equilibrium Perturbation Mode

SECM has been used to induce and monitor reversible interfacial phase

transfer processes through the perturbation of an equilibrium. In general, the

UME is positioned in a liquid phase close to an interface at which the chemical

process is initially at equilibrium. Electrolysis is employed to remove a target

solution species adjacent to the interface, driving the interfacial process in the

direction of interest. The basic operation of this mode is shown schematically in

Figure 1.13.
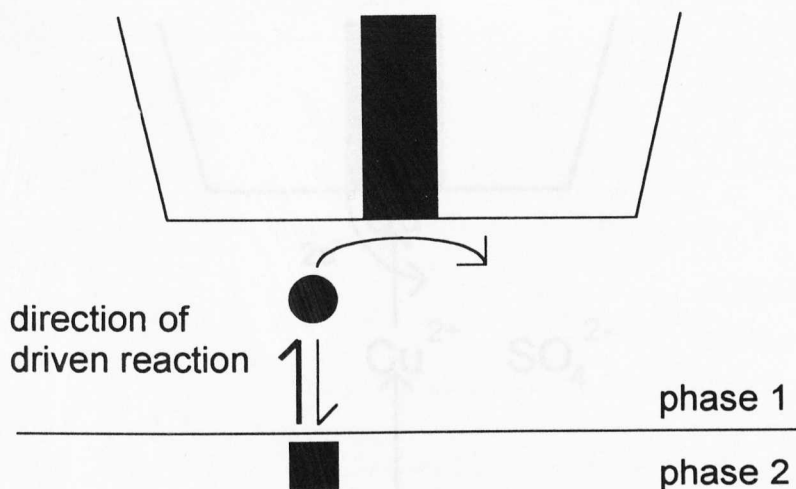
Figure 1.13 Schematic illustration of the equilibrium perturbation mode of the SECM.

This technique has been used to study both the desorption of protons from a titanium dioxide, rutile (100), surface,[112] and the dissolution of ionic single crystals.[113,114,115,116,117,118,119] The first example demonstrated the ability of SECM to resolve adsorption/desorption processes, solution diffusion and lateral surface diffusion of protons.[112] Dissolution from a copper sulfate single crystal was a further example of the use of the method of induced dissolution.[113] The crystal was secured in the base of a cell containing a saturated copper sulfate solution. Dissolution was induced by reducing copper (II) to copper (0) at an SECM tip electrode, positioned close to the surface of the single crystal. This created an undersaturated region in the tip-substrate gap, which drove the dissolution reaction. A schematic representation of this process is given in Figure 1.14. Current-time transients gave an indication of the rates and mechanisms of the dissolution reaction for various substrate conditions. With SECM, it was possible to compare reactions at different faces of a single crystal, as well as comparing areas on a surface with few dislocations to those that were highly dislocated.[114]
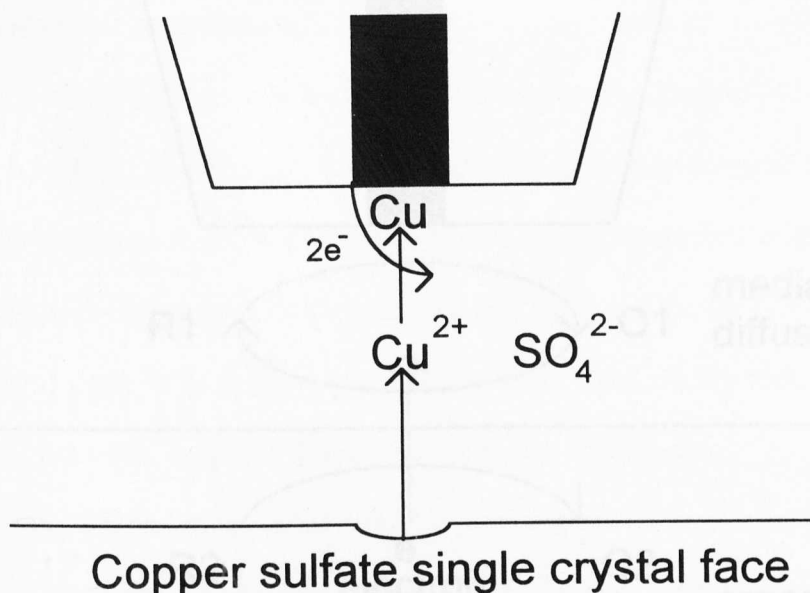
Figure 1.14   Diagram showing the induced dissolution approach to studying copper sulfate dissolution.

1.4.4 Investigation of Reactions at Liquid/Liquid Interfaces Using the

Feedback Mode of the SECM

The SECM technique, operating in the feedback mode, has been applied to study a number of processes at liquid/liquid interfaces. Because of the in-plane homogeneity of liquid/liquid interfaces, approach curve measurements have generally been used in these investigations. One study has employed one-directional imaging to examine heterogeneities in electron transfer rates across phospholipid monolayers at liquid/liquid interfaces. This said, liquid/liquid interfacial studies generally require only a one directional high resolution scanning apparatus, and so a much simpler SECM instrument can be used.

Initial studies were made on charge transfer across the interface, involving electron transfer between species confined in the two different phases, and associated ion transfer for maintaining electroneutrality.[103] A generalised
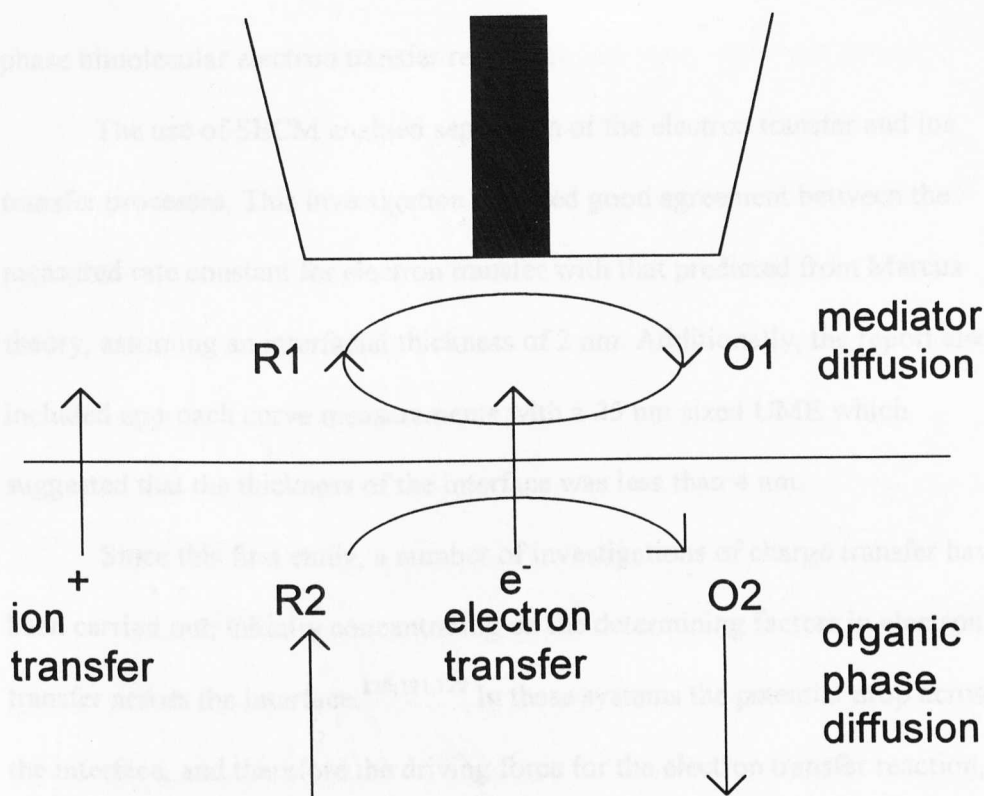
Figure 1.15 Schematic diagram showing the processes occurring during SECM feedback experiments at a liquid/liquid interface.

schematic representation of the processes occurring is shown in Figure 1.15.

Four stages were identified as having an effect on the observed current, namely;

mediator diffusion in the phase containing the UME, the interfacial electron

transfer reaction, diffusion of the redox species in the organic phase, and charge

compensation by ion transfer.[103] The interfacial electron transfer system studied

involved the following redox reaction:

$$Ru(bpy)_{3\,(aq)}^{3+} + Fc_{(org)} \xrightarrow{k_{12}} Ru(bpy)_{3\,(aq)}^{2+} + Fc_{(org)}^{+} \quad (1.11)$$
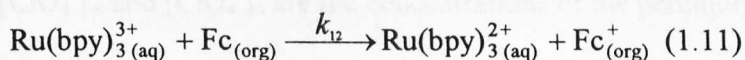
where $Ru(bpy)_3^{3+}$ is the tris (bipyridyl) ruthenium (III) ion, and Fc/Fc^+ represents

the ferrocene/ferrocinium ion redox couple, k_{12} is the rate constant for the two-

phase bimolecular electron transfer reaction.

The use of SECM enabled separation of the electron transfer and ion transfer processes. This investigation revealed good agreement between the measured rate constant for electron transfer with that predicted from Marcus theory, assuming an interfacial thickness of 2 nm. Additionally, the report also included approach curve measurements with a 25 nm sized UME which suggested that the thickness of the interface was less than 4 nm.

Since this first study, a number of investigations of charge transfer have been carried out, initially concentrating on the determining factors in electron transfer across the interface.[120,121,122] In these systems the potential drop across the interface, and therefore the driving force for the electron transfer reaction, was controlled by varying the concentrations of potential determining ions in the two phases. For example with the perchlorate ion, the potential drop across the liquid/liquid interface is given by:[121]

$$\Delta_w^o \varphi = \Delta_w^o \varphi^0 ClO_4^- - 0.059 \log \frac{[ClO_4^-]_w}{[ClO_4^-]_o} \qquad (1.12)$$

In equation 1.12, $\Delta_w^o \varphi$ is the potential drop across the interface, $\Delta_w^o \varphi^0 ClO_4^-$ is the standard potential for transfer of the perchlorate ion from the oil to the water phase, and $[ClO_4^-]_w$ and $[ClO_4^-]_o$ are the concentrations of the perchlorate ion in the water and oil phases respectively. Strictly, activities should be employed here, but a reasonable approximation is achieved by employing concentrations.[18] By careful choice of the potential determining ion, and concentration ratio, a wide range of potentials is achievable.

By measuring the rate constant for the reduction of the cationic zinc porphyrin complex (ZnPor$^+$) generated at the UME in benzene, by the hexacyanoruthenium (II) ion the aqueous phase, as a function of $\Delta_w^o \varphi$, it was possible to determine a value of approximately 0.5 for the transfer coefficient, α.[121] This suggested that electron transfer theories for metal electrode/electrolyte interfaces were also applicable to immiscible liquid/liquid systems. This result also indicated that the potential drop occurred over a small distance, i.e. there were no thick mixed ion layers adjacent to the interface.

By controlling the interfacial potential using the tetraphenyl arsonium cation, TPAs$^+$, as the potential determining ion, it also proved possible to drive uphill electron transfer across the interface from a redox couple with a higher standard reduction potential to a redox couple with a lower standard reduction potential in a second phase.[120] For these studies, the species were, respectively, ferrocyanide (in water) and 7,7,8,8-tetracyanoquinodimethane (TCNQ) (in DCE).

The effect of an adsorbed lipid monolayer on the electron transfer rates across a liquid/liquid interface has also been studied. Initial work measured the rate of electron transfer as a function of the distance between the redox centres, controlled by the lipid hydrocarbon chain length.[123] These studies revealed a decrease in the transfer rate as the number of methylene groups in the hydrocarbon chain was increased. Subsequently, the use of conjugated rather than saturated hydrocarbon chains revealed an increased electron transfer rate,[124] attributed to electron transfer along 'conductive wires' embedded in the insulating matrix. Moreover, through the use of lateral scanning across a mixed monolayer of saturated and conjugated lipid molecules, domains of relatively high and low electron transfer rates, with dimensions in the region of tens of

microns, were identified.[124]

Other chemical systems have also been studied using SECM techniques. For example, the SECM approach was considered as a model for studying the kinetics of the complex electrochemical catalytic reaction of vitamin B-12 in microemulsions,[125] which is difficult to study directly.

More recently, the equilibrium perturbation mode of SECM was used to investigate the transfer kinetics of ferrocenylmethanol and tris-phenanthroline cobalt (II) ($Co(phen)_3^{2+}$) across the nitrobenzene/water interface,[126] from solutes initially partitioned between the two phases at equilibrium. In the former case, diffusion was limiting and a lower limit on the rate constant of 0.1 cm s^{-1} was assigned, whereas the transfer rate constant for $Co(phen)_3^{2+}$ was determined to be 0.05 cm s^{-1}.

A novel operating mode for SECM uses a liquid/liquid interface supported at a micrometre-sized capillary as the tip, rather than a metal UME. By immersing a micropipette, filled with a concentrated aqueous electrolyte solution (ferro/ferricyanide), in a solution of TCNQ in DCE, it was possible to effect the transfer of electrons across the interface at the tip by the application of an external bias. This mimics a conventional SECM experiment with TCNQ as the mediator species controlling the tip current. Using this arrangement, SECM imaging of a solid substrate was effected using the feedback mode,[127] achieving equivalent spatial resolution to that obtained with a metal UME of similar dimensions. Ion transfer at this type of liquid interface electrode has also been investigated as a further SECM imaging mode.[128] In this case the substrate being imaged, a Pt disc electrode was biased to generate I$^-$ from a solution of I$_2$ by electrochemical reduction, I$^-$ could subsequently be detected at the probe tip

37

through measuring the current due to transfer of the I^- ion across the interface. This approach has been further developed through the use of a facilitated ion transfer reaction at the capillary tip, namely facilitated potassium ion transfer to obtain positive feedback currents due to potassium ion transfer at a substrate interface.[129] This opens up the possibilities for amperometric study of interfacial reactions involving important species which are of physiological significance.

1.5 Aim of This Work: New Techniques for Studying Liquid/Liquid Interfaces and Interfacial Processes

The aim of this work was to develop new techniques for investigating a range of chemical reactions at liquid/liquid (or, more generally, fluid/fluid) interfaces. The studies reported include the advancement of SECM morphology for investigating reactions that can be induced and monitored amperometrically, and the introduction of wholly new methods for investigating reactions that occur when two immiscible solutions come into contact.

Chapter 3 describes the use of the SECM equilibrium perturbation mode for probing the kinetics of the extraction and stripping reactions in the solvent extraction of copper (II) ions by oxime ligands. This is the first application of this powerful SECM mode for studying liquid/liquid interfacial reactions.

In Chapter 4, the SECM equilibrium perturbation technique is then applied to study the transfer of oxygen at the air/water interface. These studies incorporate a Langmuir trough into the experimental arrangement to enable the investigation of the effect of a monolayer at variable compressions on the oxygen transfer rate. These studies are the first of their type.

Subsequently, Chapter 5 outlines the development of a new SECM mode,

double potential step chronoamperometry, which enables rapid irreversible reactions at the liquid/liquid interface to be measured. The experimental procedure and modelling are described in detail, and exemplified with measurements on the transfer of electrogenerated bromine across the aqueous/DCE interface. The application of this SECM mode, for the first time, at the air/water interface is then described with experiments on bromine transfer from an aqueous solution to an air phase.

Chapter 6 describes the development of a new technique based on microelectrochemical measurements at expanding droplets (MEMED) for measuring liquid/liquid interfacial reactions. This approach overcomes many of the problems, outlined in section 1.1, associated with existing (conventional) methods for studying spontaneous reactions. This chapter outlines the operation of the technique, with both amperometric and potentiometric detector electrodes, along with the development of a theoretical model. The new approach is characterised using model interfacial reactions, and the range of interfacial reaction kinetics accessible is identified. Extension of the method to probe reactions at the boundary of a free jet and a second phase is considered briefly.

In Chapter 7, the application of the MEMED technique to two different two-phase reactions is described. The hydrolysis of triphenylmethyl chloride at the organic drop/aqueous solution interface, and the oxidation of methylanisole, which forms the drop, by aqueous solutions of cerium (IV) are the two reactions which are probed in detail. The determination of the kinetics and mechanism of the reaction is the focus, with emphasis on determining the location of the reaction. This is an important question, which has proved difficult to answer, but to which this technique is particularly well suited.

CHAPTER 2

EXPERIMENTAL

This chapter describes the experimental aspects of the studies herein. Details are given of the various methods used to manufacture electrodes, the apparatus and procedures for general electrochemical, SECM, Langmuir trough, MEMED and UV/visible spectrophotometric measurements, and the grades and suppliers of all chemicals used. Due to the variety of techniques and conditions used, some specific detail may also be found separately in each chapter.

2.1 Electrodes

2.1.1 Glass Coated Microdisc Electrodes

2.1.1.1 10 – 50 μm Diameter UMEs

Glass coated microdisc electrodes of diameter 10 – 50 μm were prepared by the following procedure. Firstly a borosilicate glass capillary (2 mm outer diameter, 1.16 mm inner diameter, Clark Electromedical Instruments, Reading) was drawn to a fine tip using a gravity-operated, vertically-mounted pipette puller (Narishige, Japan). The capillary tip was then cut to the desired length and sealed in the flame of a Bunsen burner until closed. A 10 mm length of platinum or silver wire of the appropriate diameter (Goodfellow, Cambridge) was then placed in the tip end of the capillary and the air was pumped out using a vacuum pump for at least 15 minutes.

Under reduced pressure a resistively heated (20 V *ac* applied) nichrome wire coil (Annealed Ni80Cr20, 0.75 mm diameter, Goodfellow) was used to evenly heat the tip of the capillary. The result of this was to seal the wire in the

40

glass with the exclusion of air bubbles, which may compromise the electrode response.

Connection to the wire was made through a tinned solid core copper wire (RS Components, Corby) inserted into the capillary. A slug of solder (60:40 tin:lead alloy, RS Components) was first inserted, and the connection was completed by heating the solder using a soldering iron (440 °C) applied to the outside of the glass capillary. The connecting wire was secured using Araldite Rapid (Ciba-Geigy, Cambridge). Figure 2.1 shows a schematic diagram of the completed electrode.
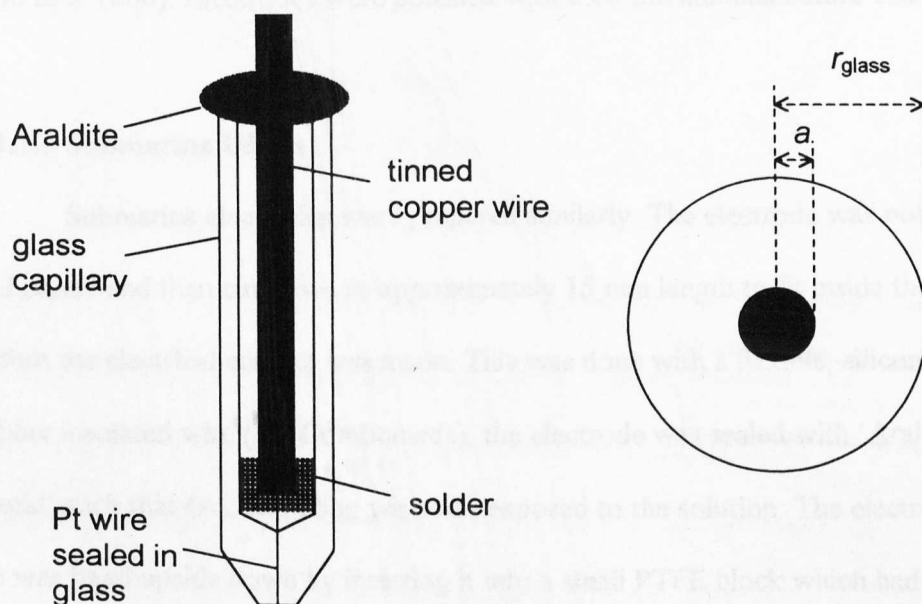
Figure 2.1   Schematic diagram of a glass sealed microdisc electrode.

The electrode was polished flat using a 600 grit polishing pad (Buehler, Coventry) until the wire became exposed. The required tip geometry was achieved by polishing the tip into a cone shape using the 600 grit polishing pad. The apex of electrodes were characterised by a particular *RG* value, where:

41

$$RG = \frac{r_{glass}}{a} \qquad (2.1)$$

In equation 2.1, r_{glass} is the overall radius of the tip of the electrode including the

insulating glass sheath, as illustrated in Figure 2.1. Final polishing of the electrode

using 0.05 μm alumina (Buehler) on a wet polishing cloth (Kemet, Maidstone)

yielded smooth electrode surfaces. The RG value and smoothness were

determined by optical microscopy using an Olympus BH2 light microscope,

equipped with Nomarski differential contrast objectives (overall magnification

× 50 to × 1000). Electrodes were polished with 0.05 μm alumina before each use.

2.1.1.2 Submarine UMEs

Submarine electrodes were prepared similarly. The electrode was polished

and coned and then cut down to approximately 15 mm length to fit inside the cell

before the electrical contact was made. This was done with a flexible, silicone

rubber insulated wire (RS Components), the electrode was sealed with 'Araldite

Rapid' such that no connecting wire was exposed to the solution. The electrode

tip was fixed upside down by inserting it into a small PTFE block which had two

parallel holes drilled through it, and inserting a second borosilicate glass capillary

into the other hole to attach the assembly to the electrode holder. In order to

ensure a tight fit in the PTFE holder, PTFE tape was wound around both the

electrode and the glass capillary before assembling the electrode. After use, the

electrode assembly could be taken apart, to allow the tip to be polished. A

diagram of the submarine UME is given in Figure 2.2.
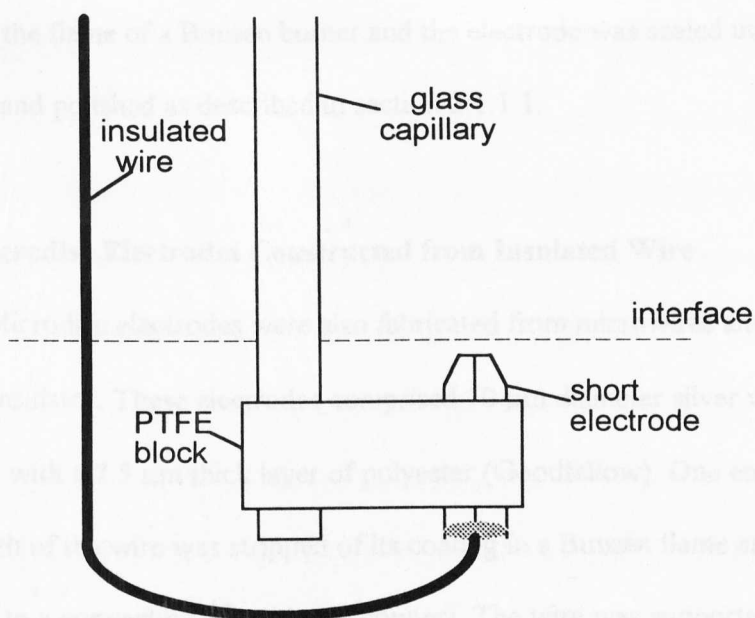
Figure 2.2 Schematic diagram showing the submarine electrode construction.

2.1.1.3 1 and 2 μm Diameter Pt UMEs

Microdisc electrodes of 1 and 2 μm diameter were constructed in a similar manner to that described above, however Wollaston wire was used (Goodfellow) in which the fine Pt wire was supplied with a Ag coating, approximately 50 μm in diameter, in order to make handling easier and to protect the fragile wire. The Wollaston wire was placed in the tip of a capillary that had been pulled but left open-ended. The wire was bent such that it would not fall out of the end. The Ag coating was removed from the tip end of the wire, inside the capillary, by repeatedly dipping the tip of the capillary, in turn, in concentrated nitric acid solution (S.G. = 1.42, Laboratory Reagent, Fisons, Loughborough) and in water. Touching the tip of the capillary against a tissue allowed the liquid to be removed between successive immersions. Once the Ag coating had been removed from a 3 – 5 mm length section at the end of the wire, it was washed in water and acetone and then dried in an oven (200 °C, 10 minutes). The end of the capillary was then

43

sealed in the flame of a Bunsen burner and the electrode was sealed under reduced pressure and polished as described in section 2.1.1.1.

2.1.2 Microdisc Electrodes Constructed from Insulated Wire

Microdisc electrodes were also fabricated from microwires already coated with an insulator. These electrodes comprised 50 μm diameter silver wire insulated with a 7.5 μm thick layer of polyester (Goodfellow). One end of a 15 mm length of the wire was stripped of its coating in a Bunsen flame and then soldered to a connecting wire (tinned copper). The wire was supported in the end of a pulled glass capillary, and the connecting parts were insulated from the solution by sealing with 'Araldite Rapid'. The end of the wire was cut using a scalpel to expose a disc-shaped electrode. For chloride ion detection, the tip was coated with a silver chloride film by anodic deposition vs. a Ag wire counter electrode (30 nA maintained for 15 minutes) in a 0.1 mol dm^{-3} HCl (Analytical Reagent, Sigma-Aldrich, Gillingham) solution.

2.1.3 Nanodes

Nanodes were constructed by first attaching a 25 or 50 μm diameter platinum wire, by soldering, to a solid core tinned copper connecting wire. This assembly was then inserted into a pulled glass capillary, such that approximately 3 – 5 mm of the microwire protruded from the tip of the capillary. The tip of the capillary was then heated in a heating coil to seal the glass around the wire leaving only the tip of the wire exposed to the solution. The tip of this wire was then etched to a sharp point using a procedure previously described by Lee et al.[130] The end 2 mm of the wire was submerged in an electrochemical etching solution

comprising saturated sodium nitrite (97 %, super free flowing grade, Sigma-Aldrich) and an *ac* voltage of 1.2 V was applied between the microwire and a platinum coil counter electrode. The wire to be etched was dipped in the solution in the centre of the coil to ensure symmetrical etching of the tip. The etching procedure was complete when no current flowed, i.e. the wire was etched until it was no longer in contact with the solution. The etched tip was simply cleaned by rinsing in deionised water, and stored before coating.

In order to achieve a tiny exposed electrode area, the tip was coated with an insulating material, which left only the very end of the tip uncoated. The coatings used were deposited on the platinum surface electrochemically. Two types of electrodepositing paint were used; one which coated anodically (Glassophor ZQ 84-3225, BASF, Münster, Germany) and one which was deposited cathodically (PPG powercron 641 lead free paint, paste P982201:resin T3992C8480 ratio 1:5, with 1 % butyl glycol, 0.4 % phenoxy propanol, kindly supplied by ANCA Electrocoat, Warwick). The anodic paint was deposited from a 20 times diluted solution by applying 1.2 V vs. Pt wire for 3 s, the coating was then completed by curing in an oven at 200 °C for 180 s, one or two repeat coatings were applied to achieve the desired electrode dimensions. The cathodic paint was deposited at −5 V for 150 s and cured as with the anodic paint. With this paint, only one coat was required.

The anodically deposited paint consists of a polyacrylic carboxylic acid solvated by partial neutralisation due to addition of base. The mechanism of deposition[131,132] combines migration of the negatively charged ions to the anode with protonation at the anode due to the local generation of protons arising from the oxidation of water. The protonated form is insoluble and deposits at the

anode. Curing in an oven results in an insulating coating which, during curing, contracts to leave the tip exposed. The cathodically deposited paint is deposited by a similar mechanism,[133,134] however, the active constituent of the paint in this case has a positive charge and as a result migrates to the cathode during the application of a voltage. In the alkaline boundary layer around the cathode, resulting from the evolution of hydrogen gas and hydroxyl ions due to the reduction of water, the paint is neutralised and deposits at the cathode. Once again, curing in an oven results in an insulating coating with a tiny exposed tip region.

2.2   Electrochemical Measurements

UME voltammetry and amperometry measurements were generally made in a two-electrode set-up, with silver wire (Goodfellow) operating as a pseudo-reference electrode (AgQRE). The potential was controlled using a purpose-built triangular wave/pulse generator (Cólburn Instruments) and the current was measured using a home-built current follower (gains 10^{-5} to 10^{-9} A/V). The current-potential behaviour (voltammogram) was recorded through a data acquisition card (NI-DAQ Lab PC card, National Instruments, Austin, TX) in a pentium personal computer using home-written software (written in Quick Basic, Microsoft). The software included data averaging routines. Chronoamperometric behaviour was similarly recorded using the PC and home-written software. The programs employed, cv.bas and trans.bas respectively, are included in Appendix 1.

Linear sweep voltammetry, where the current was recorded as a function of potential, was carried out at a range of scan rates between 5 and 1000 mV/s.

The chronoamperometric response (transient) was recorded by stepping from a potential where no redox process occurred, to one where the electrolysis at the electrode occurred at a diffusion-controlled rate. The potentials employed for potential step experiments were obtained by first measuring the steady-state voltammogram. Chronoamperometry, itself, involved recording the current response with time. The steady-state diffusion-controlled electrolysis current could be obtained from the transient data at long times, where the current has reached a constant value.

Potentiometric measurements were typically recorded against a saturated calomel electrode (SCE) (Radiometer Analytical S.A., Lyon, France) as a stable reference electrode. A home-built voltage follower offering high impedance was used to sample the voltage measurements which were recorded with the PC.

2.3 SECM Set-up

The SECM set-up used is shown schematically in Figure 2.3. The SECM rig comprised x, y and z direction translators (Newport Corp., Fountain Valley, Ca., $2 \times$ M-421-M, $1 \times$ M-431-M and an M-360-90 L-piece mount were combined), the z axis actuator was an SM50, while SM25 actuators were used for the x and y axes. Movement in the z-direction with a range of 40 μm and control of around 0.1 μm resolution was achieved using a piezoelectric system, incorporating a strain gauge sensor (Physik Instrumente, Germany; translator model P173, controller model P273). The apparatus was fixed to a marble block with sealed tapped holes (Physik Instrumente), and mounted on a home-built marble table incorporating vibrational isolators. The rig was shielded from external electrical interferences by enclosing the apparatus in a Faraday cage.

ref

tip

optical
window

piezo

manual
x,y,z
stages

potential
programmer

video
microscope

current
amplifier

interface

vibrationally isolated support

piezo
controller

video recorder

personal
computer
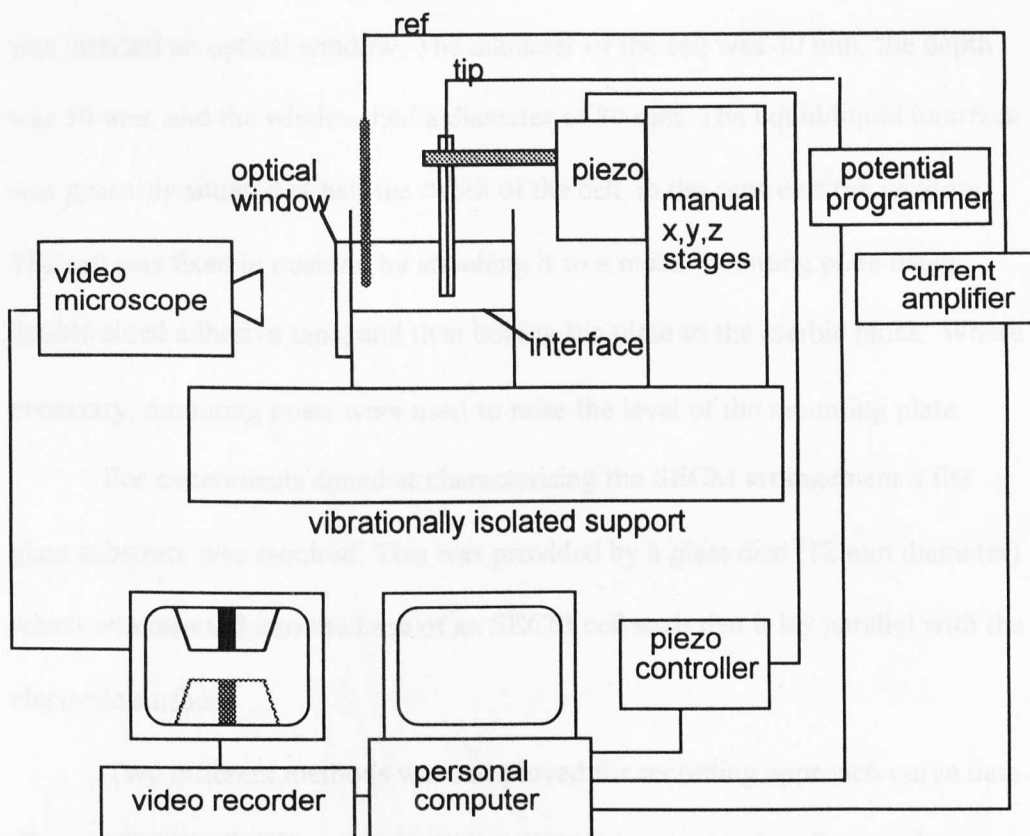
Figure 2.3 Schematic diagram showing the SECM set-up used to study liquid/liquid interfacial reactions.

To enable accurate positioning, aided by microscopy during experiments, a horizontally-mounted stereo zoom optical microscope (model 700-Z, Motic) with attached CCD colour video camera (model TK-C601, JVC) and monitor (model TM-14EK(B), JVC) was used. This offered magnification on screen of approximately $\times 40$ to $\times 200$. The video camera output was also connected to a video recorder (HS-541V, Mitsubishi) to allow recording and subsequent playback of data, and to a video capture card (Win/TV-Celebrity, Hauppauge Computer Works, Inc., New York) in the PC to enable images to be stored and processed.

Cells required optically flat windows to facilitate microscopy. For the SECM experiments, a single piece cylindrical cell was used, into the side of which

48

was inserted an optical window. The diameter of the cell was 40 mm, the depth was 50 mm, and the window had a diameter of 30 mm. The liquid/liquid interface was generally situated at half the depth of the cell, in the centre of the window. The cell was fixed in position by attaching it to a metal mounting plate using double-sided adhesive tape, and then bolting the plate to the marble block. Where necessary, mounting posts were used to raise the level of the mounting plate.

For experiments aimed at characterising the SECM arrangement a flat glass substrate was required. This was provided by a glass disc (12 mm diameter) which was inserted into the base of an SECM cell such that it lay parallel with the electrode surface.

Two different methods were employed for recording approach curve data. The steady-state limiting current response could be recorded at discrete distances through voltammetric or potential step measurements, or alternatively it was possible to bias the electrode at the potential for steady-state electrolysis of the target species, and scan the electrode towards the interface at a constant rate while recording the current and distance responses simultaneously. A home-written program (scan.bas, Appendix 1) controlled the expansion of the piezoelectric element, whilst the current data was acquired.

2.4 Combined Langmuir Trough-SECM Arrangement

2.4.1 Langmuir Trough Details

Langmuir trough experiments were carried out in the Centre for Molecular and Biomolecular Electronics (School of Natural and Environmental Sciences, Coventry University). The Langmuir trough (Nima Technology, Coventry, U.K. Model no. 2011.) was housed in a clean room (US Federal Standard 209B, class

10000) to prevent contamination of the liquid surface by airborne particles. The trough was cleaned carefully before use with a solution of potassium octanoate, a short chain soap which could be completely removed by rinsing several times with water. The absence of surface active contaminants was confirmed by recording a pressure-area (π-A_s) isotherm on the clean surface and ensuring that no increase in the pressure above 0.1 mN m^{-1} was observed.

Monolayers were formed by spreading 100 µl of a solution of the surfactant in chloroform (99.9+ %, Sigma-Aldrich) dropwise on the surface of the aqueous subphase. The solvent was allowed to evaporate for 10 minutes before proceeding with experiments. The π-A_s isotherms were recorded at a fixed compression rate of 50 - 100 cm^2 min^{-1}, from an initial area of 950 cm^2.

During experiments where fixed pressure measurements were made, the system was allowed to settle for 2 minutes, following any pressure adjustments, before recording data. During acquisition of the electrochemical response, π-time and A-time data were recorded simultaneously to ensure that the monolayer was stable during local electrochemical measurements.

2.4.2 SECM Arrangement for Langmuir Film Measurements

The submarine electrode was employed for studies of monolayers at air/water interfaces. This was attached to the piezo-element as described for the SECM set-up. The piezoelectric element was attached to a single translation stage (Newport Corp., Model M-431-M, SM50 micrometer) in order to adjust the position of the electrode normal to the interface. A home-built mounting platform

was used to position the electrode in the well section of the Langmuir trough, whilst ensuring the electrode remained vertical at all times.

All measurements were made in a two-electrode arrangement with an AgQRE. Both the UME and AgQRE were positioned in the well section of the Langmuir trough.

2.5 Experimental Arrangement for MEMED studies

The set-up for MEMED experiments is illustrated schematically in Figure 2.4. The design is based on the SECM rig with identical positioning stages, marble table, Faraday cage and microscope arrangement. The electrochemical apparatus used was generally identical to the SECM arrangement, however, for certain experiments where electrical noise was a problem due to the low currents measured, an alternative potentiostat (Cypress Systems, Lawrence, Kansas, model EI-400 bipotentiostat, gains down to 10^{-10} A V^{-1}) with a built-in 2-pole low pass filter (frequencies 2 - 150 Hz) was employed for current measurements.

Capillaries were of pulled borosilicate glass construction, they were identical to those used in UME construction, and pulled in the same way. In order to achieve a flat end, the pulled capillaries were initially cut by hand using a hand-held blade. This resulted in capillaries of approximately the correct diameter, typically 100 µm. Final polishing was carried out using a home-built polishing wheel. A computer hard-drive unit was employed, providing a flat rotating surface to which diamond impregnated polishing pads (0.1 to 30 µm grade, Buehler) could be attached. The capillary was positioned normal to the polishing surface using x, y, z positioning stages (Newport Corp., model no. M-461-xyz-M, with AJS screws on the x and y axes, and a DM13 differential micrometer controlling

51
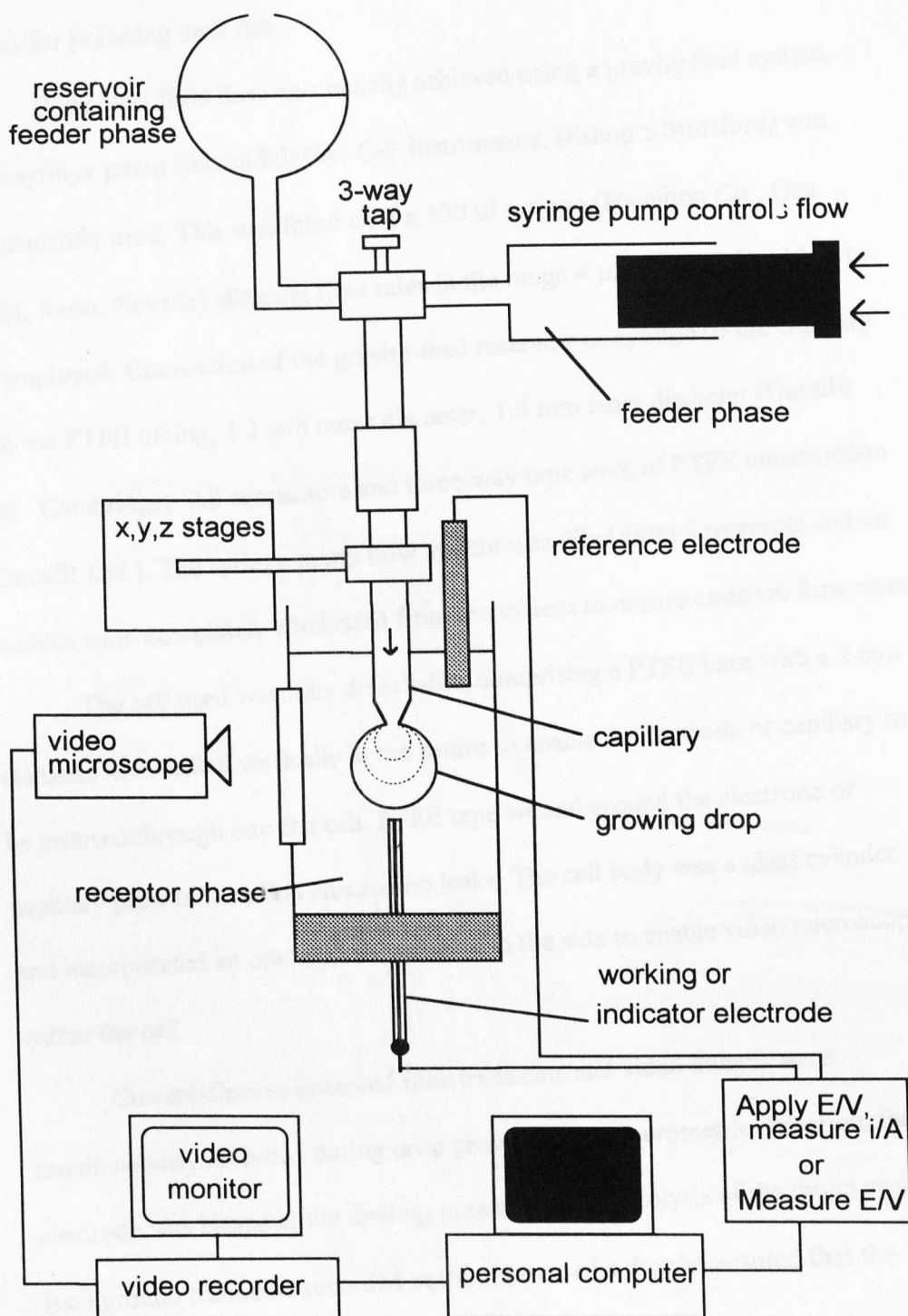
Figure 2.4 Schematic diagram of the set-up for microelectrochemical measurements at expanding droplets (not to scale). For amperometric detection a two-electrode system was used, with the potential (E) of the working electrode held at an appropriate value to cause the transport-limited electrolysis of the target species. For potentiometric detection the potential was measured between a suitable indicator electrode and the reference electrode.

the *z* axis). With this apparatus, the capillary could be lowered carefully onto the surface for polishing until flat.

Controlled fluid flow was initially achieved using a gravity feed system, but a syringe pump (model KD100, C-P Instruments, Bishop's Stortford) was subsequently used. This was fitted with a 500 μl syringe (Hamilton Co., Gas Tight, Reno, Nevada) allowing flow rates in the range 4 μl hr^{-1} to 6359 μl hr^{-1} to be employed. Connection of the gravity-feed reservoir or syringe to the capillary was via PTFE tubing, 3.2 mm outer diameter, 1.5 mm inner diameter (Omnifit Ltd., Cambridge). All connectors and three-way taps were of PTFE construction (Omnifit Ltd.). The syringe pump flow system was filled from a reservoir and air bubbles were completely eliminated from the system to ensure constant flow rates.

The cell used was fully detachable, comprising a PTFE base with a 2 mm diameter hole drilled vertically in the centre to enable an electrode or capillary to be inserted through into the cell. PTFE tape wound around the electrode or capillary prior to insertion ensured no leaks. The cell body was a glass cylinder and incorporated an optically flat window in the side to enable video microscopy within the cell.

Current-time or potential-time transients and video images were simultaneously recorded during drop growth. For amperometric detection, the electrode was biased at the limiting potential for electrolysis of the target species. Background transients recorded in the absence of a droplet ensured that the measurement was stable and provided a normalisation current. The background potentiometric response was also measured.

2.6 UV/Visible Spectroscopy

2.6.1 Recording UV/Visible Spectra

UV/visible spectra were recorded by scanning between 400 nm and 900 nm using a uv/visible spectrometer (8700 series, Unicam). Calibration solutions were made up for each solution to check for Beer-Lambert characteristics and to determine molar absorptivities.

2.6.2 Absorption Transients

Homogeneous kinetic measurements were made in a 1 cm path length, 4 ml volume quartz cuvette, with solutions mixed in the cuvette. Initial concentrations were varied by adjusting either the concentrations or the relative volumes of the two solutions to be mixed. Absorbances were recorded at a fixed wavelength, as a function of time using an ATI Unicam, model 8625, spectrometer interfaced to a PC.

2.7 General Solutions

All aqueous solutions (other than those in Langmuir trough experiments) were prepared using Milli-Q-reagent water (Millipore Corp., resistivity ≥ 18 MΩ cm). Aqueous solutions in Langmuir trough experiments used distilled water pumped through an Elgastat Spectrum A deioniser (resistivity ≥ 18 M Ω cm, The Elga Group, High Wycombe, U.K.). Organic solutions employed either 1,2-dichloroethane (99.8%, HPLC grade, Sigma-Aldrich, Gillingham) or heptane (99+%, HPLC grade, Sigma-Aldrich) as solvent.

The grades and suppliers of all other chemicals employed are identified in Table 2.1. The compositions of the solutions used will be outlined in the text.

54

Solutions were generally prepared freshly each time immediately prior to use, particular care was taken with solutions containing ferrocyanide, as the ferrocyanide ion can be oxidised, albeit very slowly, in the presence of atmospheric oxygen. All experiments were conducted at 298 ($\pm$ 2) K.

Solution pH was measured using a pH meter (Radiometer, model PHM-201, with pH electrode PHC-3005-8), calibrated with appropriate buffers (pH 4 citrate buffer, pH 7 phosphate buffer and pH 10 carbonate buffer, Radiometer Analytical S.A.).

Table 2.1 Chemical grades and suppliers, A.R. is analytical reagent grade.

Chemical	Grade	Supplier
Acorga P50	94.78 % w/w	Zeneca
Bromine	99.99 %	Sigma-Aldrich
Cerium (IV) sulfate	99 %	Sigma-Aldrich
Cerium (III) sulfate octahydrate	99.999 %	Sigma-Aldrich
Chloroform	99.9+ %	Sigma-Aldrich
Copper sulfate pentahydrate	A.R.	Fisons
Ferrocene	98 %	Sigma-Aldrich
Hydrochloric acid	A.R. 0.5 N Volumetric standard	Sigma-Aldrich
4-Methylanisole	99 %	Sigma-Aldrich
1-Octadecanol	99 %	Sigma-Aldrich
Potassium chloride	A.R.	Fisher
Potassium bromide	A.R.	Fisher
Potassium dihydrogen orthophosphate	A.R	BDH
Potassium ferrocyanide trihydrate	A.R.	Fisher
Potassium hexachloroiridate (III)	99 %	Sigma-Aldrich
Potassium nitrate	A.R.	Fisons
Potassium sulfate	A.R.	Fisons
Sodium hexachloroiridate (IV) hexahydrate	99 %	Strem
Sodium hydroxide	> 98 %	Fluka
Sodium nitrite	97 %, super free flowing	Sigma-Aldrich
Sodium perchlorate hydrate	99.99 %	Sigma-Aldrich
Stearic acid	99+ %	Sigma-Aldrich
Sulfuric acid	A.R., specific gravity 1.84	Sigma-Aldrich
Tetra-n-hexylammonium perchlorate	97+ %	Alfa
Triphenylmethyl chloride	98 %	Sigma-Aldrich

CHAPTER 3

DEVELOPMENT OF THE SECM EQUILIBRIUM PERTURBATION
MODE AT LIQUID/LIQUID INTERFACES AND APPLICATION TO
THE STUDY OF THE EXTRACTION/STRIPPING REACTION OF
AQUEOUS COPPER (II) WITH AN EXTRACTANT OXIME LIGAND

This chapter describes a new application of the SECM equilibrium perturbation

mode, here used for inducing and quantitatively measuring the transport of

chemical species across immiscible liquid/liquid interfaces. In this application, a

disc-shaped UME located in the aqueous phase, at micrometre distances from the

interface of interest, is employed to drive the transfer process, initially at

equilibrium, in the direction of the aqueous phase. This is achieved by applying a

potential to the UME, sufficient to electrolyse the target species at a diffusion-

controlled rate. The resulting depletion in the local aqueous concentration

provides the thermodynamic force for the transfer process and species crossing

the interface contribute to the UME current flow, the magnitude of which

depends on the transfer kinetics. The technique is illustrated with measurements

on the extraction/stripping reaction of aqueous Cu^{2+} with extractant oxime ligand

in an organic phase (either heptane or DCE). The rate constants for the

extraction and stripping processes are evaluated through the application of a

numerical model.

3.1 Introduction

The SECM equilibrium perturbation (EP) mode has been employed

successfully to study transfer processes at solid/liquid interfaces, such as

dissolution/growth[113,114,115,116,117,118] and adsorption/desorption[112] but not,

hitherto, at liquid/liquid interfaces. Microband electrodes have, however, recently

been used in conjunction with laser trapping methods, in an approach related to

the EP mode, to study electrochemically-induced transfer kinetics at individual

organic droplets in aqueous solution.[67,68,69,70,71,72,73,74,75] In these studies, which

have provided valuable *in-situ* information on reaction rates on a timescale of

several seconds, the interfacial transfer reaction of interest was induced and

studied through local concentration perturbations, generated by electrodes. The

studies described here are the first application of the SECM EP mode for

studying liquid/liquid interfacial reaction kinetics and demonstrate that a

considerably faster kinetic regime is accessible with this SECM technique, under

greatly simplified experimental conditions where mass transport is better defined.

To illustrate the applicability of the SECM EP mode, the

extraction/stripping of Cu^{2+} from aqueous solutions by the oxime ligand Acorga

P50 (HL) in immiscible organic solvents is considered:

$$Cu_{(aq)}^{2+} + 2HL_{(org)} \underset{\text{stripping}}{\overset{\text{extraction}}{\rightleftarrows}} CuL_{2(org)} + 2H_{(aq)}^{+} \qquad (3.1)$$
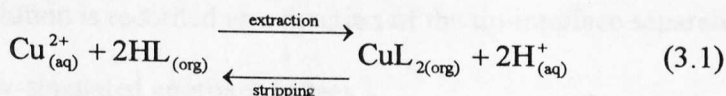
where HL has the following structure:

57
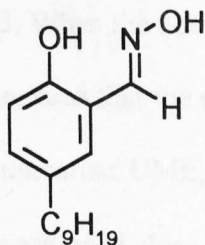
Although this system has been the subject of previous detailed kinetic studies with the RDC,[22,23] further complementary studies are valuable, not least because some workers have questioned the validity of the RDC in certain applications.[20] The experimental studies are supported with theoretical simulations to enable the interfacial kinetics to be determined quantitatively.

3.2 The SECM EP Approach

The concept of the SECM EP mode in this application is to allow equation 3.1 to come to an initial equilibrium and then employ an amperometric UME located in the aqueous phase, at micrometre distances from the interface, to drive the process to the left by depleting the local concentration of $Cu_{(aq)}^{2+}$ through reduction to Cu at the UME. As will be demonstrated below, the current flowing is strongly dependent on the flux of Cu^{2+} across the interface and the kinetics and mechanism of the transfer process may be determined directly from the current response. Kinetic measurements are made by comparing experimental approach curves, in which the steady-state current for the reduction of Cu^{2+} in aqueous solution is recorded as a function of the tip-interface separation, d, with theoretically-simulated approach curves.

A schematic of the experimental apparatus for studies where the immiscible organic solution had a density greater than that of the aqueous solution, was given in Figure 2.3. When the density of the organic phase was less than that of the aqueous solution, such that the organic solution was uppermost in the SECM cell, an inverted 'submarine' UME, as shown schematically in Figure 2.2 was used. The tip was first positioned close to the interface (within the 40 μm range of the piezoelectric positioner) using the manual x, y, z stages, while the tip

position was observed on a video monitor. An image of a typical probe in an aqueous solution close to an aqueous/DCE interface is shown in Figure 3.1. Although the interface cannot be seen directly, its location is readily inferred from the reflection of the tip. The UME probe was then translated towards the interface in discrete micrometre-sized steps using the piezoelectric device to achieve accurate positioning.
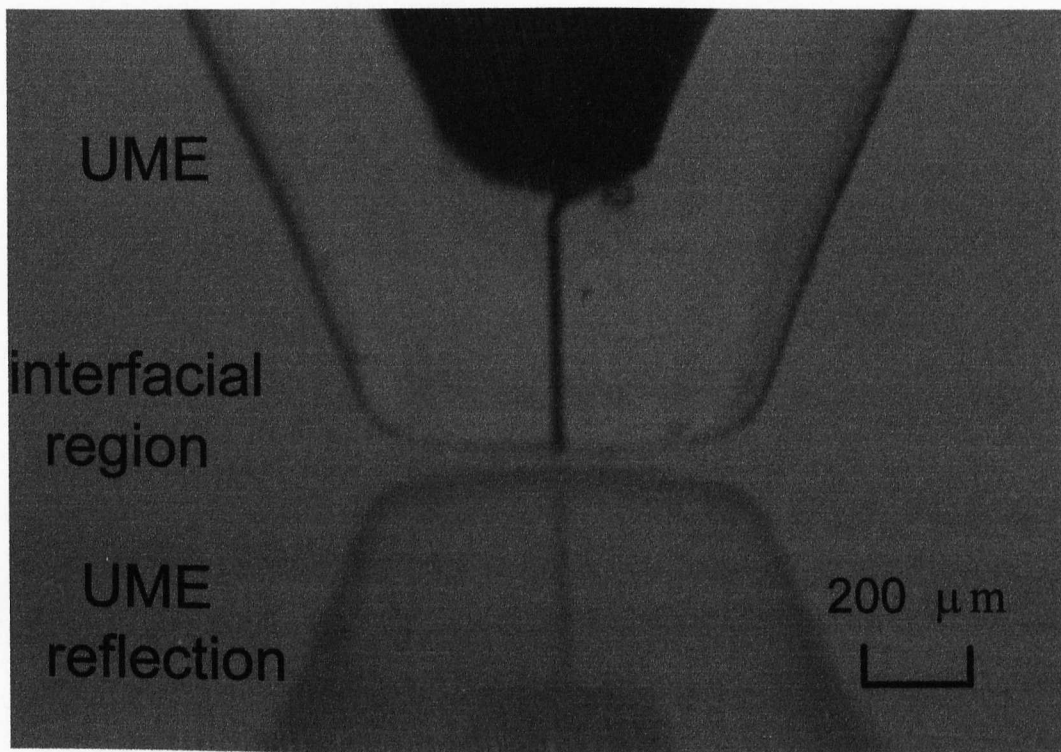
Figure 3.1   Typical image of a conventional UME located in an aqueous solution, close to an aqueous/DCE interface. The 25 μm diameter wire used to construct the disc UME can clearly be seen.

Steady-state currents at each distance were determined by two methods, either from voltammetric measurements or by measuring the current at several seconds following a potential step once a steady-state current was attained, the two approaches giving identical results. For the stepped potential approach, the initial potential was 0.00 V where no electrolysis occurred and the stepping

potential was -0.70 V vs. AgQRE where Cu^{2+} was reduced at a diffusion-controlled rate, the potentials being identified by voltammetry as demonstrated below. For each experimental data set, the steady-state current was normalised with respect to $i(\infty)$, the steady-state diffusion-limited current which flowed when Cu^{2+} reduction was effected at a tip located at an effectively infinite ($\approx$ 1 cm) distance from the interface compared to the electrode radius, a.

3.3 Results and Discussion

3.3.1 Determination of Solution Composition and Physical Constants

The compositions of the solutions of interest employed to study Cu^{2+} extraction and stripping kinetics are shown in Table 3.1. The equilibrium, equation 3.1, was established by shaking a 50 cm^3 volume of an organic Acorga P50 solution with an equivalent volume of an aqueous copper sulfate solution, over a period of *ca.* 15 minutes. The initial concentrations of Cu^{2+} were 8.00 × 10^{-2} mol dm^{-3} and 0.120 mol dm^{-3} for experiments with DCE and heptane solutions, respectively, while the ligand concentration was 0.3 mol dm^{-3}. Sulfuric acid was added in some cases as extraction suppressor. The validity of this procedure, which has been shown to be sufficient for the attainment of equilibrium in similar chemical systems,[22,23,135] was confirmed from the fact that

Table 3.1   Equilibrium composition of the two-phase systems.

	aqueous/DCE	aqueous/heptane
$[Cu^{2+}]_{(aq)}$	6.0×10^{-3} mol dm^{-3}	5.0×10^{-3} mol dm^{-3}
$[CuL_2]_{(org)}$	7.4×10^{-2} mol dm^{-3}	0.115 mol dm^{-3}
[free HL]$_{(org)}$	0.152 mol dm^{-3}	7.0×10^{-2} mol dm^{-3}
pH	1.04	0.91

the compositions of the two solutions were found to be unchanged following longer mixing periods (> 12 hours). The defined conditions were selected so that upon perturbing the initial equilibrium, the corresponding mass transport problem was reduced to the consideration of the diffusion of Cu^{2+} in the aqueous phase alone, as discussed below.

The concentration of Cu^{2+} in the aqueous phase and CuL_2 in the organic phases were determined spectrophotometrically, the bulk concentration of Cu^{2+} in aqueous solution, $c_{Cu^{2+}}^{*}$, was also determined from the steady-state diffusion-limited current for Cu^{2+} reduction at a Pt disc UME, via equation 1.10.

3.3.1.1 UV/visible Spectroscopic Determination

Calibration plots of absorbance vs. concentration were constructed by making up a series of solutions at different copper sulfate concentrations (with the appropriate sulfuric acid concentration) and measuring their UV/visible spectra. From these calibration plots, the molar absorptivities could be determined using the Beer-Lambert law, equation 3.2.

$$A = \varepsilon c l \qquad (3.2)$$

where A is the absorbance, ε is the molar absorptivity, c is the concentration and l is the path length. For the aqueous phase this simply involved making up copper sulfate solutions around 1×10^{-2} mol dm^{-3} (the concentration employed in the experiments), and recording the spectra. For the complexed copper in the organic phase, it was necessary to make up aqueous solutions containing a known concentration of copper sulfate, and then use an excess of concentrated organic

61
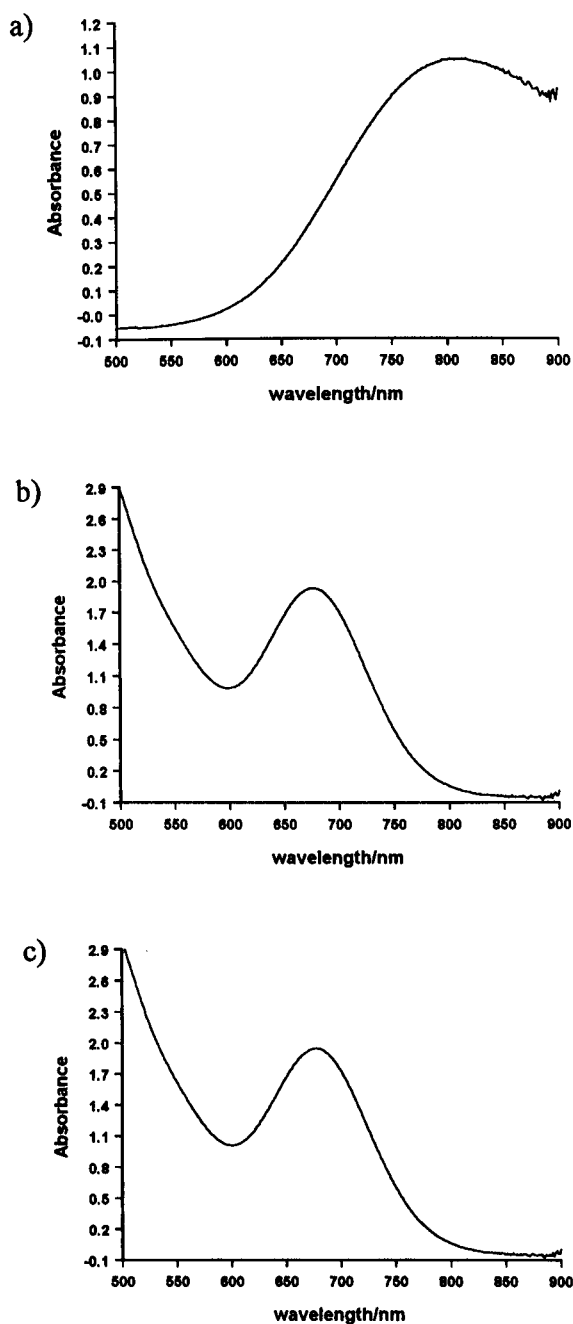
Figure 3.2 UV/visible absorption spectra for solutions containing a) 0.1 mol dm^{-3} CuSO$_4$ in aqueous solution, b) 2 × 10^{-2} mol dm^{-3} CuL$_2$ in heptane and c) 2 × 10^{-2} mol dm^{-3} CuL$_2$ in DCE. The organic solutions also contained some remaining free ligand.
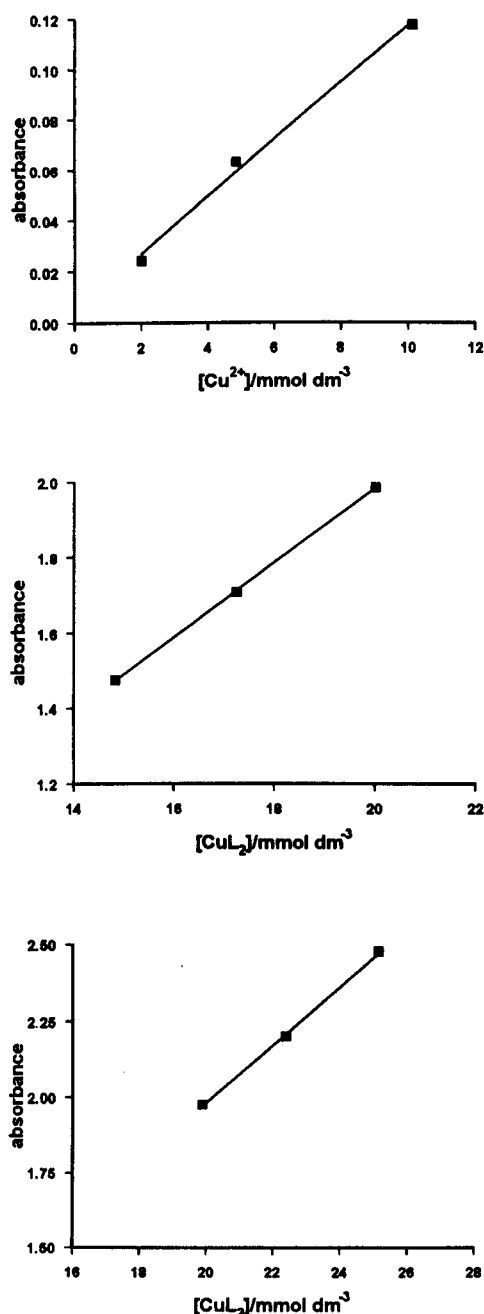
Figure 3.3   UV/visible spectroscopy calibration plots for a) aqueous Cu^{2+}, b) the CuL_2 complex in DCE and c) the CuL_2 complex in heptane. The data for a) were obtained from the absorption maximum at 805 nm, while for b) and c) the maximum was at 680 nm. The solid lines correspond to linear regression fits, enabling the molar absorptivities ε, a) 11.6×10^3 cm^2 mol^{-1}, b) 97.6×10^3 cm^2 mol^{-1}, and c) 95.1×10^3 cm^2 mol^{-1} to be determined.

ligand solution to extract all of the copper into the organic phase. Uncomplexed HL did not absorb at the wavelength of maximum absorption of CuL_2. Complete extraction was confirmed by recording the spectrum of the remaining aqueous phase to check for aqueous Cu^{2+}. Typical spectra corresponding to aqueous Cu^{2+} and the complex CuL_2 in heptane and in DCE are in Figure 3.2. Measurements were taken at the peak values of approximately 680 nm for CuL_2 in the organic phase, and at 805 nm for Cu^{2+} in the aqueous phase. Typical calibration plots, along with the calculated molar absorptivities are given in Figure 3.3.

Once the molar absorptivities had been determined on solutions of known concentration, absorption measurements were used to determine Cu^{2+} and CuL_2 concentrations in extracted solutions using equation 3.2.

3.3.1.2 Electrochemical Measurements

The concentration of Cu^{2+} in the aqueous phase following extraction was confirmed by measuring the steady-state diffusion-controlled current for the reduction of Cu^{2+} to Cu at a 25 μm diameter Pt UME. A typical reduction wave for Cu^{2+}, recorded at a scan rate of 50 mV s^{-1}, is shown in Figure 3.4. The steady-state current was taken from the voltammogram, and the Cu^{2+} concentration was calculated using equation 1.10, where D is the diffusion coefficient of Cu^{2+} and $n_e = 2$ is the number of electrons transferred per redox event. In order to do this it was first necessary to measure the diffusion coefficient for Cu^{2+}. This was achieved by measuring the current observed at the microdisc electrode in a solution of known concentration. A value of $D = 6.3 \times 10^{-6}$ cm^2 s^{-1} was determined through the voltammetric reduction of Cu^{2+} from a 5 $\times 10^{-3}$ mol dm^{-3} solution, under similar conditions of background electrolyte and
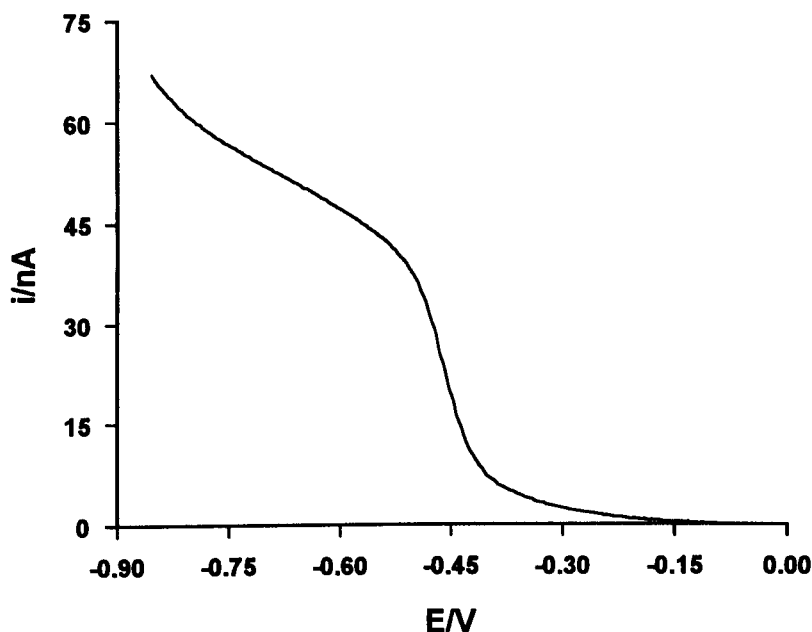
Figure 3.4 Typical voltammogram recorded for the reduction of Cu^{2+} in an aqueous solution at partial extraction. The solution initially contained 4×10^{-2} mol dm^{-3} copper sulfate and was extracted with an equal volume of 0.12 mol dm^{-3} P50 in DCE.

sulfuric acid concentration. This is in agreement with diffusion coefficients quoted by others.[136] The pH (and corresponding anion concentration) in the equilibrated aqueous solutions (Table 3.1) ensured that there was a considerable excess of supporting electrolyte, compared to the concentration of the electroactive species, such that the use of equation 1.10 was appropriate. The diffusion coefficient determined here was subsequently used in modelling the data.

The diffusion coefficient for CuL_2 in DCE was determined by an alternative method, since the use of equation 1.10 requires that c and n_e are known, and n_e was

unknown here. The diffusion coefficient was determined from the shape of the current vs. time response,[137,138,139] measured as the potential was stepped from a potential at which no electrolysis process occurs at the electrode to a potential where the electrolysis of the target species occurs at a diffusion-controlled rate. The measured current (normalised with respect to the steady-state current) was plotted vs. $(t/s)^{-1/2}$ and compared with the predicted theoretical response, for a diffusion-controlled electrolysis process at a disc UME, using an analytical method described by equation 3.3.[140]

$$\frac{i}{i(\infty)} = 0.7854 + 0.4431 \left(\frac{tD}{a^2}\right)^{-1/2} + 0.2146 \exp\left(-0.3911\left(\frac{tD}{a^2}\right)^{-1/2}\right) \quad (3.3)$$

For measurement of the diffusion coefficient of CuL_2 in DCE by direct electrochemistry, a solution containing 5.33×10^{-4} mol dm^{-3} CuL_2, with 5.0×10^{-2} mol dm^{-3} tetra-n-hexylammonium perchlorate as background electrolyte, was employed. This solution was prepared by extracting Cu^{2+} from a 1.0 mol dm^{-3} aqueous copper sulfate solution into a DCE solution containing 1.07×10^{-3} mol dm^{-3} Acorga P50 and 0.05 mol dm^{-3} tetra-n-hexylammonium perchlorate by shaking together as described above. The CuL_2 concentration quoted above was determined by UV/visible spectrophotometry, and is half the initial ligand concentration, indicating that no free ligand remains in the solution. Both phases were degassed with argon for 15 minutes prior to recording data. For CuL_2 measurement, the potential was stepped from 0 V to -1.4 V vs. AgQRE, where reduction at the electrode was diffusion-controlled, as identified by a plateau in the voltammetric response (Figure 3.5(b)). An excellent fit to equation 3.3 was achieved with $D = 5 \times 10^{-6}$ cm^2 s^{-1}, at times greater than 2.5 ms, as shown in Figure 3.5(a). This is the first direct electrochemical measurement of this
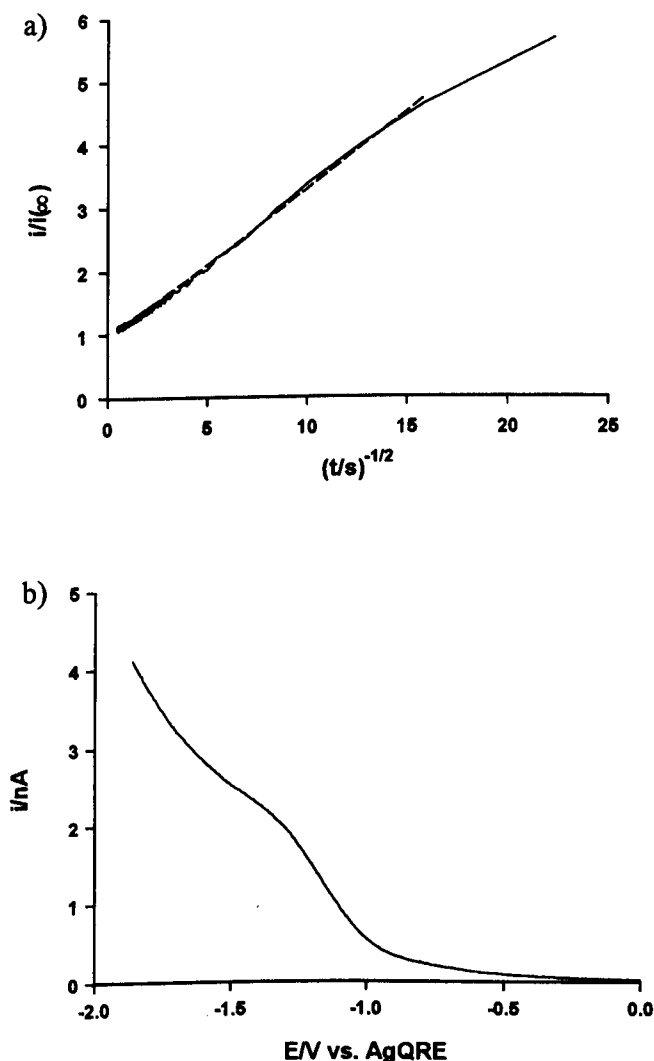
Figure 3.5 Electrochemical response, presented as a) potential step transient and b) voltammetric response, for the reduction of a solution of 5.33×10^{-4} mol dm^{-3} CuL$_2$ in DCE with 5.0×10^{-2} mol dm^{-3} tetra-n-hexylammonium perchlorate as supporting electrolyte. The data in a) (solid line) was recorded by stepping the potential from 0.0 V to -1.4 V vs. AgQRE, and was normalised by the limiting current, $i(\infty) = 2.53$ nA. The dashed line represents the theoretical response based on $D = 5.0 \times 10^{-6}$ cm^2 s^{-1}.

organic phase diffusion coefficient. In conjunction with the voltammetric measurement, taking $i(\infty) = 2.53$ nA, then the number of electrons transferred during this electrochemical reduction, calculated from equation 1.10, is 1.97. This result confirms the accuracy of these measurements, since it is likely under these conditions that a two-electron reduction of CuL_2 would occur.

3.3.1.3 Other Species

The concentration of free HL remaining in the organic phase (after the equilibrium defined by equation 3.1 was established) was simply calculated from the other measured concentrations by assuming the formation of a 1:2 complex between Cu^{2+} and L^-, which is a valid assumption.[23,24,135,141]

3.3.1.4 Solution Composition Results

Given the equilibrium constant for the extraction process:

$$K_{ex} = \frac{[CuL_2][H^+]^2}{[Cu^{2+}][HL]^2} \qquad (3.4)$$

it is clear from Table 3.1 that extraction is least effective in DCE, with values of K_{ex} of 4.4 (DCE) and 71.0 (heptane). This deduction is consistent with previous studies which have found that an increase in the dielectric constant of the organic solvent reduces the extent of metal ion extraction by oxime ligands.[141]

3.3.2 Characterisation of the UME Response Close to Liquid/Liquid Interfaces

It was first necessary to verify the limiting current-distance characteristics of the technique under the well-defined conditions presented by an inert interface. Figure 3.6 shows typical approach curves of the diffusion-limited current for the reduction of Cu^{2+} in aqueous solution as UME probes of conventional and submarine design approached aqueous/DCE and aqueous/heptane interfaces, respectively. The aqueous solution contained 7×10^{-3} mol dm^{-3} CuSO$_4$ and 0.5

Figure 3.6   Typical approach curves of the normalised steady-state diffusion-limited current for Cu^{2+} reduction as UME probes, of conventional and submarine design, approach aqueous/DCE (O) and aqueous/heptane (□) interfaces, respectively. The solid line is the theoretical response expected for hindered diffusion with an inert interface.[105]

mol dm^{-3} K$_2$SO$_4$, while the organic phases contained no added species. As the probe approaches the interface, diffusion of Cu^{2+} to the UME becomes hindered, resulting in a decrease in the flux of Cu^{2+} at the electrode, and hence a reduced current.

In both cases, data are in quantitative agreement with the theory for diffusion-controlled hindered diffusion with an inert interface as described in section 1.4.2.[105] This indicates that the geometries of the liquid/liquid interface and probes of interest are well-described in terms of a planar stable interface lying perpendicular to the axis of the UME. Although this type of behaviour has been observed recently for other immiscible liquid/liquid interface systems studied with SECM UME probes of conventional design,[103,120,121,122,123,124,125,126,129] the satisfactory characteristics obtained with the submarine UME are particularly noteworthy. In particular, these model studies confirm that the small diameter of the mounting capillary, 2 mm, compared to that of the cell, 40 mm, ensured that there were negligible changes in the level of the interface in the cell compared to the distance over which the tip was displaced when the connecting capillary was translated normal to the interface.

Taken together, the results in Figure 3.6 demonstrate, for the first time, that processes at liquid/liquid interfaces could be studied through dynamic electrochemical probes located in phases which have either lesser or greater densities compared to the second liquid phase. The results also indicate that for the Cu^{2+} concentrations and electrolysis periods of interest, Cu deposition on the electrode surface was not sufficiently extensive to significantly alter the planar disc geometry, or separation between the UME and interface during the course of each measurement. In fact, when the potential was returned to 0.00 V, between

successive measurements, electrodeposited Cu was anodically stripped from the probe electrode, ensuring it did not build up on the tip during the course of a series of measurements.

3.3.3 Approach Measurements Under Induced Transfer Conditions

Typical steady-state approach curves for the reduction of Cu^{2+} at a probe UME, in the aqueous phase side of the separated extraction solutions, as the UME approached the aqueous/DCE and aqueous/heptane interfaces, are shown in Figure 3.7. The solution compositions were those defined in Table 3.1. The
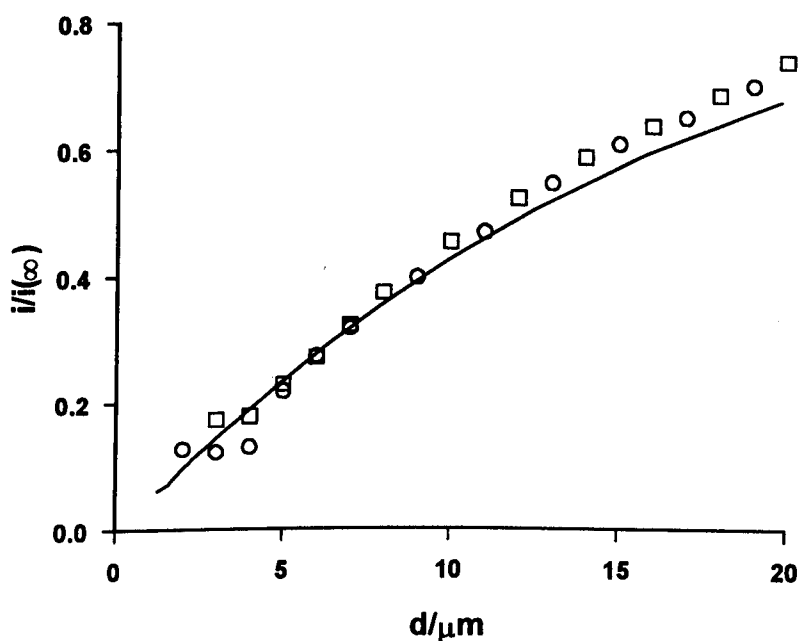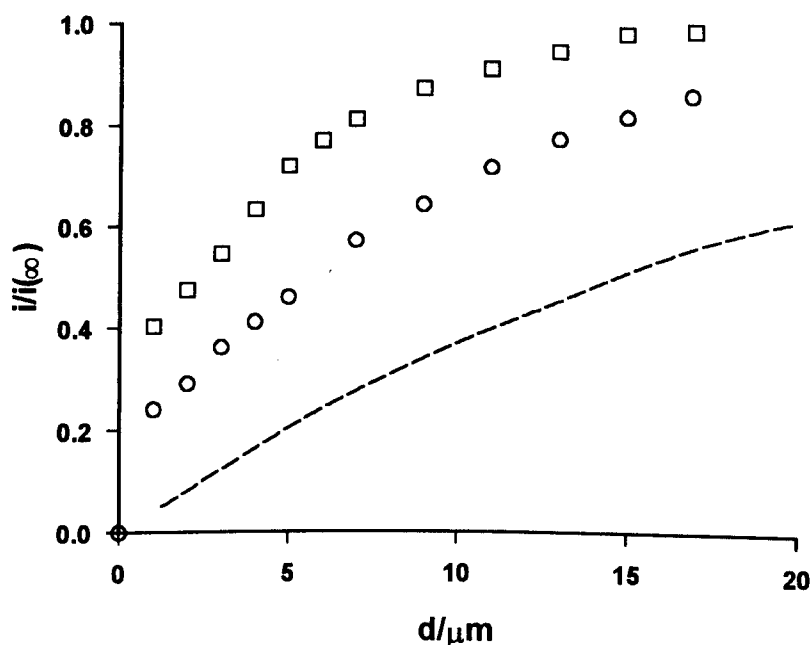

Figure 3.7 Typical approach curves of the normalised steady-state diffusion-limited current for Cu^{2+} reduction as UME probes, of conventional and submarine design, approach aqueous/DCE (O) and aqueous/heptane (□) interfaces, respectively, with the chemical composition as outlined in Table 3.1. The dashed line shows the theoretical response expected for hindered diffusion with an inert liquid/liquid interface.[105]

position at which the tip contacted the interface (i.e., $d = 0$ μm) was readily established both visually from video microscopy and from the observation that no current flowed, over the potential range of interest, with the tip in this location. Qualitatively it is observed that the approach curves lie at higher normalised current values than those predicted for the case where no interfacial reaction occurs, indicating an enhanced flux of Cu^{2+} at the electrode due to transfer across the interface. The electrolysis process depletes the concentration of Cu^{2+} locally and, at close probe/interface separations, this serves to drive the equilibrium, equation 3.1, to the left. The resulting transfer of Cu^{2+} from the organic to the aqueous phase provides additional material for electrolysis, resulting in a higher current flow compared to the situation where there is no interfacial transfer.

3.4 Analysis

3.4.1 Simulation

The strength of this technique is that the geometry of the SECM arrangement is very well defined, and diffusion in the tip-interface gap can readily be modelled with a variety of boundary conditions. Initial work by Kwak and Bard led to the development of a finite-element model for the steady-state feedback response of the UME tip for both conductive and inert surfaces,[105] the results of which have been widely used.[97,98,99,100,101,102] The steady-state model was subsequently developed to include the chronoamperometric positive and negative feedback responses, simulated using both a Krylov integrator[142] and the alternating direction implicit finite difference method (ADIFDM).[143] The latter method was used to investigate the effect of unequal diffusion coefficients of the redox mediator couple on the chronoamperometric positive feedback response.[144]

The effects of finite heterogeneous kinetics and arbitrary substrate size on the feedback responses were also considered.[145] Models for the chronoamperometric feedback and generation/collection modes for complex electrode reactions involving coupled homogeneous kinetics have also been introduced.[146,147,148]

The response of the electrode is governed by diffusion of the species of interest in the tip-interface gap and any reactions at the interface. The tip and interface form an axisymmetric cylindrical geometry, the result of which is that the diffusion problem may be reduced to two dimensions to make the solution much simpler. Diffusion within the axisymmetric cylindrical geometry of the SECM may be written in dimensionless terms as follows:

$$\frac{\partial C}{\partial \tau} = \frac{\partial^2 C}{\partial R^2} + \frac{1}{R}\frac{\partial C}{\partial R} + \frac{\partial^2 C}{\partial Z^2} \qquad (3.5)$$

where C is the concentration of the species of interest, in this case aqueous Cu^{2+}, normalised with respect to the concentration in bulk solution, $c_{Cu^{2+}}^{*}$ (also described as the equilibrium distribution concentration or the initial concentration in the EP mode). In equation 3.5, τ is the normalised time, and R and Z are the co-ordinates which describe the cylindrical geometry in, respectively, the radial and normal directions with respect to the electrode surface, which have their origin at the centre of the disc electrode.

The terms in equation 3.5 were normalised using the following expressions:

$$R = r/a \qquad (3.6)$$

$$Z = z/a \qquad (3.7)$$

$$\tau = tD/a^2 \qquad (3.8)$$

Figure 3.8 illustrates the SECM cylindrical geometry schematically, and outlines some of the boundaries that will be discussed below.
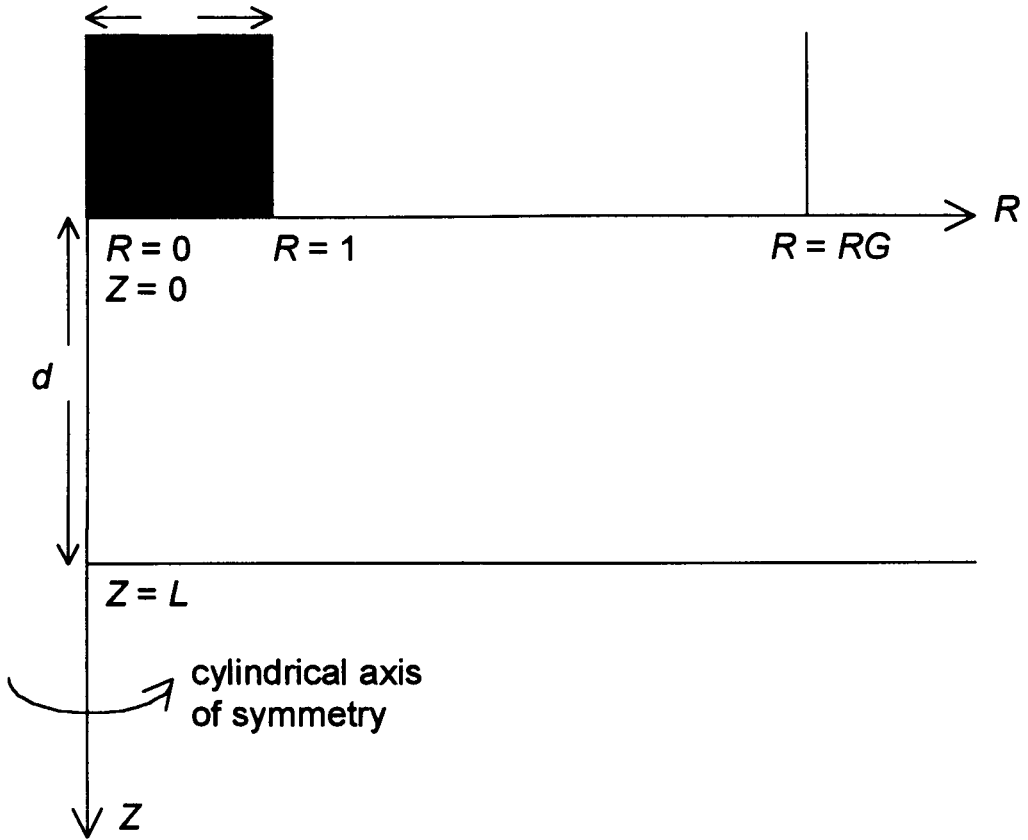
Figure 3.8   Illustration of the SECM geometry including the locations of the boundaries used in the simulation.

The following initial condition identifies the concentrations of the solution species prior to electrolysis:

$$\tau = 0, \text{ all } R, \text{ all } Z: \qquad C = 1 \qquad (3.9)$$

74

The simulation determines the complete transient behaviour following a potential step at the electrode for each distance, however, here we are only interested in the steady-state behaviour. Following the potential step, Cu^{2+} is reduced at a diffusion-controlled rate at the electrode surface, thus, all Cu^{2+} reaching the electrode surface is electrolysed. This is reflected in the following boundary condition at the electrode surface:

$$Z = 0, \ 0 \le R \le 1: \qquad C = 0 \qquad (3.10)$$

Additional boundary conditions account for the fact that Cu^{2+} is inert on the glass sheath surrounding the electrode and maintains the bulk value at radial distances from the active region of the order of the distance to the outer edge of the glass sheath of the electrode. This is a reasonable assumption for the probes used practically in most SECM studies.[97,98,99,100,101,102,105]

$$Z = 0, \ 1 < R \le RG: \qquad \partial C/\partial Z = 0 \qquad (3.11)$$

$$R > RG, \ 0 < Z < L: \qquad C = 1 \qquad (3.12)$$

In equation 3.12,

$$L = d / a \qquad (3.13)$$

Additionally, due to the axisymmetric geometry of the SECM arrangement:

$$R = 0, \ 0 < Z < L: \qquad \partial C/\partial R = 0 \qquad (3.14)$$

The interface of interest forms the remaining boundary, and the boundary condition applied corresponds to the interfacial reaction. Under the conditions defined in Table 3.1, it is reasonable to assume that [CuL$_2$], [HL] and [H$^+$] remain constant during the electrochemically induced transfer process, such that the process defined in equation 3.1 can be represented by:

$$Cu^{2+}{}_{(aq)} \xrightleftharpoons[k_s]{k_e} \text{organic phase} \qquad (3.15)$$
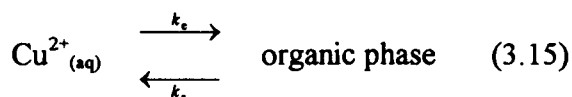
where k_e is the extraction rate constant and k_s is the stripping rate constant. The extraction process may be assumed to be first order in Cu^{2+}, while the stripping reaction is represented as a zero order process, given the high concentration of CuL$_2$ in each of the experiments.[23,24] The flux of Cu^{2+} across a liquid/liquid interface, $j_{Cu^{2+}}$ (mol cm^{-2} s^{-1}), is then given by:

$$j_{Cu^{2+}} = k_s - k_e c_{z=d} \qquad (3.16)$$

where $c_{z=d}$ is the Cu$^{2+}{}_{(aq)}$ concentration adjacent to the liquid/liquid interface. By noting that at equilibrium:

$$k_s = k_e c_{Cu^{2+}}{}^* \qquad (3.17)$$

equation 3.16 may be written in terms of the stripping rate constant alone:

$$j_{Cu^{2+}} = k_s(1 - C_{z=d}) \quad (3.18)$$

where $C_{z=d}$ is the normalised interfacial concentration, $c_{z=d}/c_{Cu^{2+}}^*$. By introducing the normalised rate constant,

$$K = k_s a/D \, c_{Cu^{2+}}^* \quad (3.19)$$

the boundary condition at the interface, defined in equation 3.18, may be written as:

$$Z = L, \, 0 < R \le RG: \quad \partial C/\partial Z = K(1 - C_{z=d}) \quad (3.20)$$

Equation 3.18 has an identical form to the rate equation which applies to the dissolution of a symmetrical electrolyte in a solution containing no supporting electrolyte, under linear interfacial undersaturation control.[118] This problem has recently been treated numerically under SECM induced dissolution conditions, and the model outlined elsewhere[118] may be applied directly to the present situation. The ADIFDM solution, which has been used to solve many SECM problems, was employed. The problem was solved using a previously-written FORTRAN program, and the steady-state response was extracted from the time-dependent solution when steady-state within the simulation was achieved.

The current response of the electrode, which is the experimentally measured parameter, may be calculated from the total flux of Cu^{2+} at the

electrode surface, determined from the simulation, using the following expression:

$$\frac{i}{i(\infty)} = \frac{\pi}{2}\int_0^1 (\partial C / \partial Z)_{z=0} RdR \quad (3.21)$$

3.4.2 Data Analysis

Figures 3.9 and 3.10 show the data for the aqueous/DCE and the aqueous/heptane systems, respectively, along with approach curves simulated theoretically using the rate constants indicated. The theoretical model is seen to provide a good description of the current-distance characteristics for measurements on both of the systems of interest. The best fits to the data were obtained with the following kinetic parameters under the experimental conditions of interest: $k_s = 6.3 \times 10^{-9}$ mol cm^{-2} s^{-1} (heptane/aqueous) and 2.4×10^{-9} mol cm^{-2} s^{-1} (DCE/aqueous). The former value is in close agreement with the fluxes measured by the RDC far from equilibrium under stripping conditions with similar pH and concentrations of CuL_2.[23,24] Although HL was present in the organic phase in the SECM EP studies, in contrast to most of the RDC measurements, it is anticipated to have a negligible influence on the stripping kinetics under the defined conditions.

The kinetics of the extraction/stripping process in DCE have not previously been measured. Since previous studies have found a first-order dependence of the extraction rate on [H$^+$] and a zero order dependence on [CuL_2] in the concentration range of interest,[23,24] part of the difference in the k_s values may be due to a difference in the pH of the two aqueous solutions (and to

78
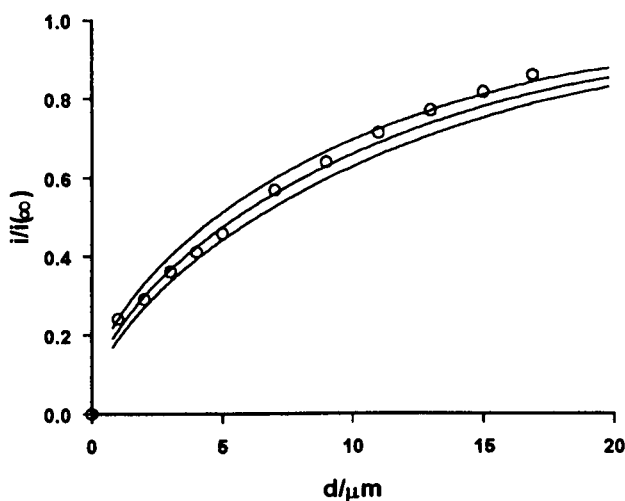
Figure 3.9 Typical approach curve of the normalised steady-state diffusion-limited current for Cu^{2+} reduction as a UME probe, of conventional design, approaches the aqueous/DCE (O) interface, with the chemical composition as outlined in Table 3.1. The solid lines through the data points are the best fits using equation 3.18 with, from top to bottom, $k_s = 3.8 \times 10^{-9}$, 2.4×10^{-9} and 1.9×10^{-9} mol cm^{-2} s^{-1}.
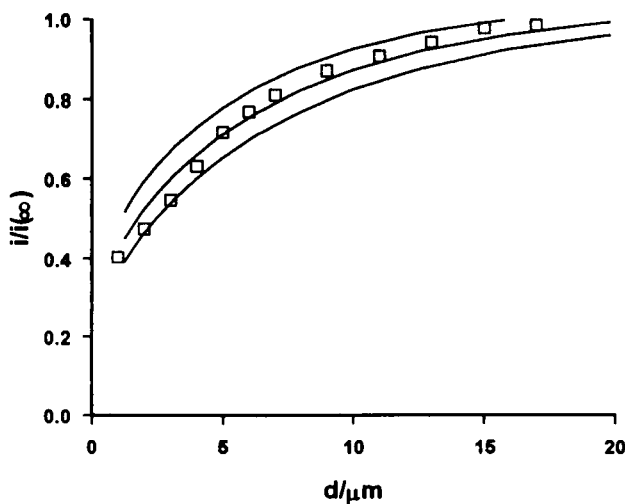
Figure 3.10 Typical approach curve of the normalised steady-state diffusion-limited current for Cu^{2+} reduction as a UME probe of submarine design, approaches the aqueous/heptane ($\square$) interface, with the chemical composition as outlined in Table 3.1. The solid lines through the data points are the best fits using equation 3.18 with, from top to bottom, $k_s = 8.0 \times 10^{-9}$, 6.3×10^{-9} and 5.0×10^{-9} mol cm^{-2} s^{-1}.

a lesser extent the different HL concentrations in the two organic phases).

Further studies of the DCE/water system, under conditions where the aqueous

phase was acidified with 0.05 mol dm^{-3} sulfuric acid - such that at equilibrium the

following speciation prevailed: pH = 0.91, $[Cu^{2+}]$ = 1.2 × 10^{-2} mol dm^{-3}, $[CuL_2]$ =

6.8 × 10^{-2} mol dm^{-3} and [HL] = 0.164 mol dm^{-3} - yielded k_a = 4.8 × 10^{-9} mol cm^{-2}

s^{-1}.

The apparent extraction rate constant, equation 3.17, under conditions of

similar pH, is much lower for DCE than for heptane. This is expected given that

the k_a values for the two systems are close at the same pH, but extraction is less

extensive in DCE. The value of k_e = 1.3 × 10^{-3} cm s^{-1} found for heptane is also

lower than (but of the same order as) that measured by the RDC.[23,24] The

conditions of the latter studies were, however, predominantly far from

equilibrium, where product (CuL_2) build up was negligible, while the UME

studies are for conditions closer to equilibrium. Given that $[CuL_2]$/[HL] > 1 in the

organic phase in the UME studies, CuL_2 may compete effectively for the

interface with HL, thereby diminishing the extraction rate constant compared to

the situation where CuL_2 is absent.

3.5 Conclusions

The above results demonstrate, for the first time, that the SECM EP

mode is a powerful probe of transfer processes at liquid/liquid interfaces. To a

certain extent, the technique complements the RDC by providing information on

the kinetics of transfer processes close to equilibrium. However, the SECM EP

technique also overcomes several intrinsic limitations of the RDC. In the latter

technique, the need for a filter to separate the two liquids of interest adds an

additional resistance to mass transfer, which may be difficult to quantify in some applications and limits the technique to moderate kinetics. Furthermore, for certain classes of reactions the membrane can become blocked, thereby changing the contact area between the liquids and ultimately making the cell unusable. In contrast, the SECM EP mode allows the study of transport across unsupported interfaces, of defined area, under conditions of well-defined and high mass transport rates. These properties will enable the study of much faster processes than accessible with the RDC. It should be noted that the rate constants measured herein are at the lower end of the range accessible to UME methods,[109,110,111] but approach the fastest values that may be determined with the RDC.

The SECM EP mode should be applicable to a wide range of species (both charged and neutral). Widespread application in the metal extraction area is envisaged, particularly through the use of mercury film UMEs, which facilitate the amperometric determination of heavy metal ions. The development of an SECM mass transport model that includes consideration of diffusion in both phases, eliminating the need to operate with constant composition conditions in the second phase, as has recently been described,[149] will diversify the range of conditions accessible to study with this method. Chapters 6 and 7 describe the development of a complementary UME based technique, which will enable transfer processes to be studied immediately following contact of the two-phases, under conditions far from equilibrium.

CHAPTER 4

APPLICATION OF THE SECM EQUILIBRIUM PERTURBATION

MODE FOR MEASURING THE EFFECT OF A MONOLAYER ON

MOLECULAR TRANSFER ACROSS AN AIR/WATER INTERFACE

The application of the SECM EP mode for the quantitative study of the effect of a monolayer on solute transfer rates across an air/water interface is described in this chapter. The technique is illustrated through measurements of oxygen transfer across two different monolayers, namely 1-octadecanol and stearic acid, as a function of compression. The experimental approach uses an inverted submarine UME, positioned in the water phase in a Langmuir trough, close to the air/water interface, to induce the transfer of oxygen from air to water via the reduction (and depletion) of oxygen. The steady-state current response, measured as a function of UME-interface separation at various monolayer compressions, demonstrates that the accessible free area of the interface primarily governs the rate of oxygen transfer in the case of 1-octadecanol.

4.1 Introduction

As outlined in Chapter 1, the transfer of molecules and ions between immiscible phases is a fundamental and general phenomenon involved in a range of chemical and biological processes. Understanding the effects of monolayers on the mechanisms and rates of interfacial transfer is of particular importance, with practical implications ranging from membrane transport in biological systems[150,151,4] to the exchange of chemical species across phase boundaries in natural environments.[152,153]

For monolayers at air/water interfaces, the effects of amphiphile, chain length and packing on water evaporation have been studied widely[154,155,156,157] following the first demonstration by Rideal[158] that monolayers were effective in reducing evaporation rates. However, much less work has considered the permeability of monolayers at air/water interfaces to solute molecules. Of those studies that have been carried out in the latter area, several report that thin organic films have little effect on solute transfer across air/water interfaces,[152,153,159] but this may be attributed to the intrinsically low liquid phase mass transfer rates utilised. A gas absorption method introduced to overcome this problem[160,161] showed that various long chain alcohol monolayers reduced the initial uptake rates of several gases, including oxygen and carbon dioxide, by water. This approach and other methodologies[162] have, however, only been used to examine the effect of fully condensed monolayers on solute transfer kinetics.

Davies and Rideal[163] advocated that more precise studies of the effects of the density of packing of monolayers on gas transfer would be of great interest, however, such studies have not been carried out. The lack of quantitative information on diffusion across monolayers at air/water interfaces contrasts markedly with the level of knowledge on lateral transport processes in these 2-D systems, which have been studied comprehensively, as a function of compression, with electrochemical[164,165] and fluorescence[166,167] techniques.

This chapter describes the application of the SECM EP approach, described in the previous chapter, for studying quantitatively the effect of monolayer compression on solute transfer across air/water interfaces. The solute chosen for study is oxygen, due to the general importance of oxygen interfacial transfer in biological systems[150,151] and in the environment.[152,153] Transfer rates

83

across monolayers of 1-octadecanol and stearic acid were investigated as a function of compression, since these particular systems are widely used as model Langmuir monolayers.[168,169] As discussed above, the system is not without practical environmental relevance for water conservation, since monolayers of 1-octadecanol have been used to retard evaporation.[154,155,156,157,168]

The SECM EP approach was demonstrated at the liquid/liquid interface in the previous chapter. These new investigations greatly extend the methodology to the gas/liquid interface, and complement recent SECM kinetic studies of the effect of monolayers on electron transfer at liquid/liquid interfaces.[123]

4.2 The Technique

The proposed approach (Figure 4.1) uses a submarine UME, stationed in the water phase at micrometre distances from the air/water interface, to perturb the equilibrium distribution of oxygen between the two phases. The interface was established in a Langmuir trough, allowing the controlled compression of the monolayer of interest. The reduction of oxygen at the UME creates a depleted region adjacent to the interface, which provides the thermodynamic force for the transfer of oxygen from the air to the water phase. The steady-state current response is measured as a function of UME-interface separation, and is sensitive to the transfer kinetics, which can be characterised over a wide range, due to the variable and high mass transfer rates associated with UMEs in the SECM configuration, as described in Chapter 3.

All approach curves were measured by translating the UME towards the interface at a constant rate (0.32 μm s^{-1}). The UME was biased at the limiting potential for electrolysis of the target species, and current vs. distance data was
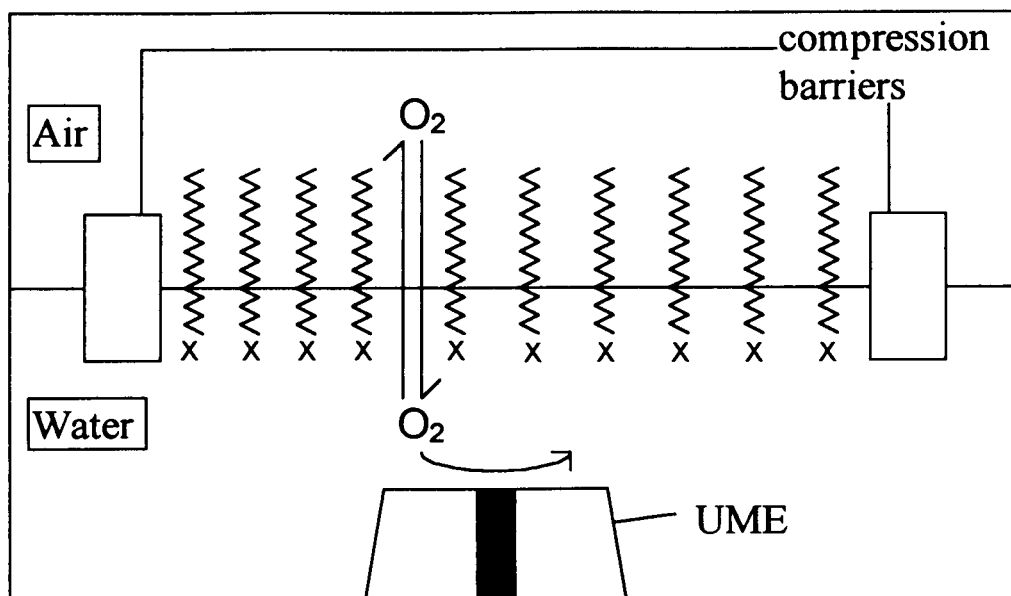
Figure 4.1 Schematic illustration of the equilibrium perturbation method for measuring oxygen transfer across a monolayer at the air water interface using an inverted (working) UME, where X represents the monolayer headgroup. Amperometry is effected using a two-electrode arrangement; the second (reference) electrode is not shown.

recorded. Due to the absence of a video microscope for these experiments, the electrode was initially brought close to the interface, within the range of the piezoelectric positioner, by observing the steady-state current while manually moving the electrode towards the interface. A detectable current change was observed at close ($< 2a$) distances due to the interception of the diffusion field at the electrode by the interface. An inflexion in the shape of the approach curve indicated when the electrode had attained a distance of closest approach from the interface (as discussed below).

4.3 Theoretical Treatment

To model the data, approach curves were simulated by solving the diffusion equation for oxygen within the SECM geometry as outlined in Chapter 3. Since the technique is identical, some of the boundary conditions already

described in the previous chapter, equations 3.10 to 3.14, apply here also. The format of the interfacial boundary condition must, however, be considered. The transfer of oxygen may be represented by:

$$O_2(aq) \xrightarrow[k_{aw}]{k_{wa}} O_2(air) \qquad (4.1)$$
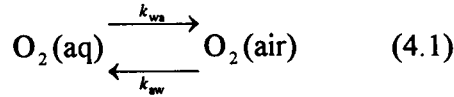
where k_{wa} and k_{aw} are first-order interfacial rate constants for water-air and air-water transfer. The oxygen flux from the gas phase, j_{O_2} / mol cm^{-2} s^{-1}, is given by:

$$j_{O_2} = k_{aw}c_{air} - k_{wa}c_{w,i} \qquad (4.2)$$

where $c_{w,i}$ is the interfacial concentration of oxygen in the water phase, and c_{air} is the concentration of oxygen in air, which is constant throughout the air phase so that:

$$j_{O_2} = k' - k_{wa}c_{w,i} \qquad (4.3)$$

where k' represents the pseudo-zero-order transfer rate constant for transfer from air to water. This equation is similar in form to equation 3.16, which described the copper extraction/stripping equilibrium, and a similar treatment may be applied. Considering that at equilibrium:

$$k' = k_{wa}c_{w,i} \qquad (4.4)$$

then equation 4.3 may be written as:

$$j_{O_2} = k'\left(1 - C_{w,i}\right) \qquad (4.5)$$

where $C_{w,i}$ is the concentration of oxygen in water at the air/water interface

normalised with respect to that in bulk solution, c_w. This expression forms the

kinetically-controlled boundary condition at the interface, and is identical to

equation 3.18 which formed the interfacial boundary condition for the Cu^{2+}

transfer problem outlined in the previous chapter. The model employed for the

copper system may be used here for simulation of the approach curves, the only

modification required being the different values for the diffusion coefficient and

rate constant.

4.4 Experimental Results

4.4.1 Oxygen Measurement

The technique requires that oxygen can be detected and measured

quantitatively by voltammetry at a UME in the SECM geometry. Voltammograms

for oxygen reduction at 25 μm diameter Pt and Ag electrodes recorded at 20 mV

s^{-1} in 0.1 mol dm^{-3} KNO_3 are shown in Figure 4.2. The Pt electrode was

pretreated by oxidising at 1.2 V for 3 s before recording the voltammogram.

Oxygen may be reduced by two separate two-electron transfer steps,

illustrated in equations 4.6 and 4.7 or by a single four-electron process, according

to equation 4.8.[170]
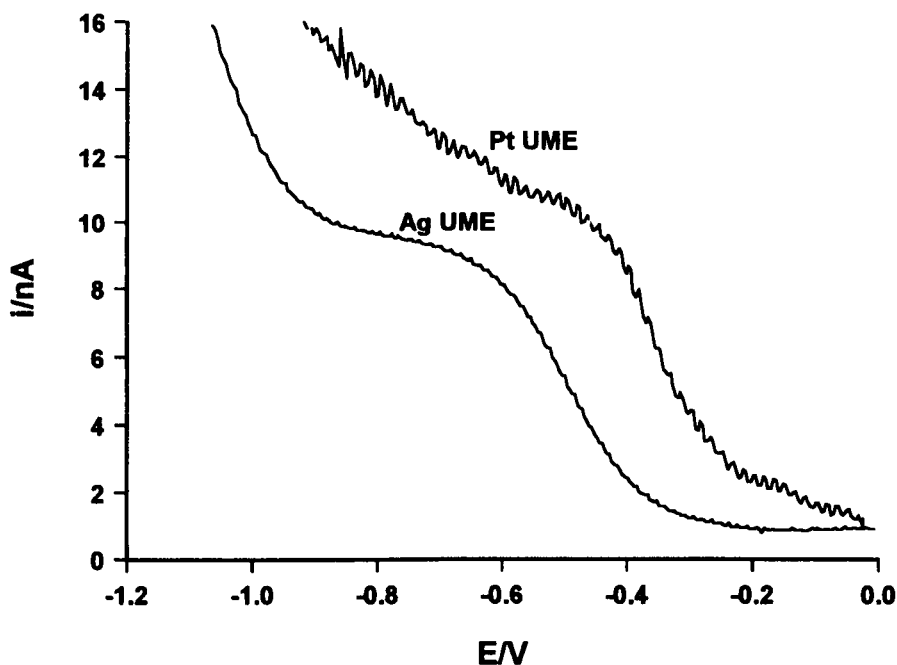
Figure 4.2   Voltammograms recorded, in a Langmuir trough, for the reduction of oxygen at 25 μm diameter Pt and Ag submarine UMEs in an air saturated 0.1 mol dm^{-3} KNO$_3$ solution. The scan speed was 20 mV s^{-1}.

$$O_2 + H_2O + 2e^- \rightarrow HOO^- + OH^- \qquad (4.6)$$

$$HOO^- + H_2O + 2e^- \rightarrow 3OH^- \qquad (4.7)$$

$$O_2 + 2H_2O + 4e^- \rightarrow 4OH^- \qquad (4.8)$$
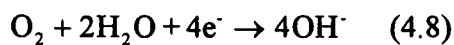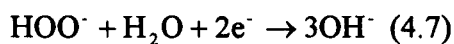
The observed response depends on the electrode material, for example, on Au surfaces, equations 4.6 and 4.7 are separated since these processes occur at quite different potentials,[170] whereas for Ag and Pt surfaces, the two processes occur at similar potentials. The response is also dependent on the mass transfer rate at the

electrode, with relatively high and low mass transfer rates favouring two and four-electron processes, respectively.[170,171] The steady-state voltammetric response of the Ag electrode in bulk solution showed a single cathodic wave of limiting current, $i(\infty) = 10.1$ ($\pm$ 0.2) nA for the reduction of oxygen according to equation 4.8. By applying equation 1.10, in which $n_e = 4$ is the number of electrons transferred, D is the diffusion coefficient of oxygen and $c_w = 2.5 \times 10^{-4}$ mol dm^{-3} is the bulk concentration of oxygen in an aerated salt solution with an ionic strength of 0.1 mol dm^{-3},[171,172] the calculated value, $D = 2.1 \times 10^{-5}$ cm^2 s^{-1} was as expected.[170] The voltammetry of O_2 at Pt is less well defined due to surface processes such as platinum oxide reduction, however, if the potential is held at $-$0.7 V for several seconds then the current attains a steady value of $ca.$ 10.0 ($\pm$ 0.2) nA.

Approach curves recorded using a Ag UME employed a bias of $-$0.88 V vs. AgQRE corresponding to the limiting current for oxygen reduction at this electrode. For Pt UMEs it was necessary to pretreat the UME before recording the approach curves as follows. The Pt UME was first oxidised at 1.2 V for 3 s to achieve a reproducible surface for each run, then held at $-$0.7 V for 1 minute to stabilise before recording the data at -0.7 V. Stable responses of both electrodes were confirmed by background scans in bulk solution, these measurements were made before each experiment to obtain the normalisation current, $i(\infty)$. Identical results were obtained with the two types of electrodes.

4.4.2 Characterising Approach Curves at Air/Water Interfaces

In order to characterise the stability of the air/water interface to SECM approach curve measurements, the ferrocyanide/ferricyanide couple was employed as a model system. Approach curves were recorded for the oxidation of ferrocyanide in a 5×10^{-3} mol dm^{-3} aqueous solution, with 0.1 mol dm^{-3} KNO_3 as supporting electrolyte, at a 25 diameter μm Pt UME biased at 0.8 V vs. AgQRE, the potential for diffusion-limited oxidation of ferrocyanide. Figure 4.3 shows that the response follows the theory for hindered diffusion.[105] The ferrocyanide and electrochemically-generated ferricyanide ions would not be expected to display
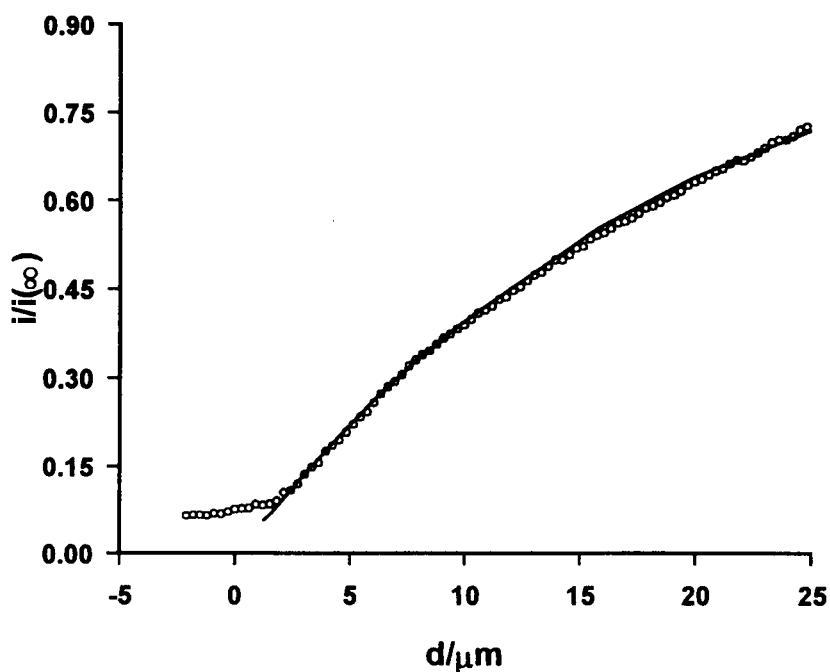

Figure 4.3 Normalised steady-state diffusion-limited current vs. UME-interface separation for the oxidation of ferrocyanide at a UME approaching a clean air/water interface (O). The solid line represents the predicted theoretical response for hindered diffusion.[105]

any chemical interaction with the interface. The excellent agreement observed

between theoretical and experimental responses illustrates that the interface is

stable on the scale of the SECM measurements. The deviation at close distances,

i.e., the flattening of the curve to a constant value, is indicative of a layer of water,

1.5 - 2.0 μm thick, being trapped by surface tension as the UME pushes against

the interface.[25] This phenomenon has previously been observed in SECM studies

of liquid/liquid interfaces.[103,110] The distance at which this deviation occurs

represents the minimum separation that is achievable between the UME and the

interface.

4.4.3 Oxygen Transfer Across a Clean Air/Water Interface

The rate of oxygen transfer was first measured across a clean air/water

interface. Figure 4.4 shows how the normalised steady-state current ($i/i(\infty)$) for

the reduction of oxygen at a 25 μm diameter Ag UME varies with the distance (d)

between the electrode and the air/water interface. The experimental results were

in good agreement with a theoretical approach curve based on rapid (diffusion-

controlled) transfer of oxygen from air to the water phase. This extreme

theoretical case is identical to the positive feedback model[105] already described.

The deviation at close distances is observed once again, indicating a layer of

trapped water of approximately 1.5 μm thickness. This was used as the distance

of closest approach for subsequent approach curve measurements.
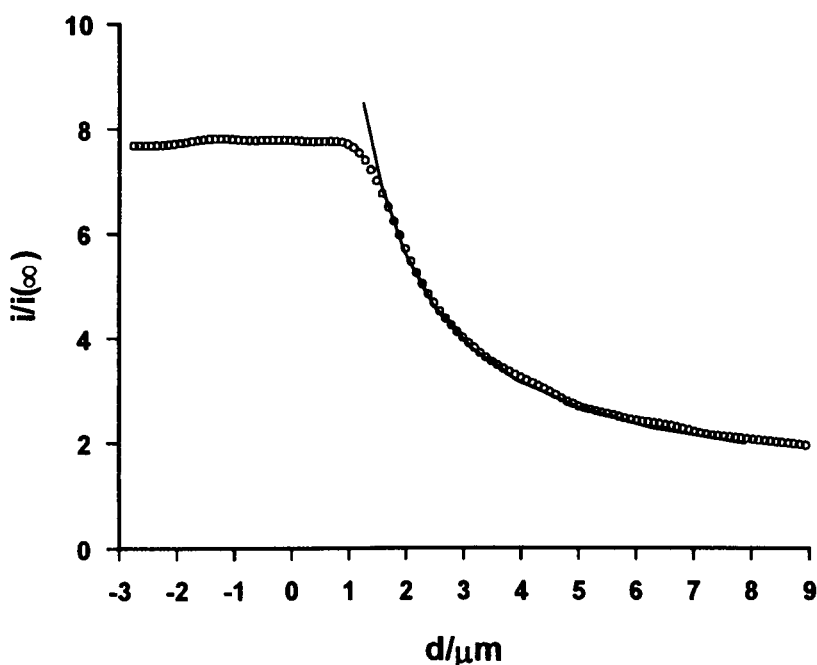
Figure 4.4 Normalised steady-state diffusion-limited current vs. UME-interface separation for the reduction of oxygen at a UME approaching a clean air/water interface (O). The solid line represents the predicted theoretical response for the transfer of oxygen from the air phase with diffusional-resistance from the aqueous phase alone (without interfacial kinetic limitations).

4.4.4 Effect of 1-Octadecanol on Oxygen Transfer

4.4.4.1 Isotherm Characteristics

Monolayer compression characteristics are illustrated through surface pressure (π)-area isotherm measurements. The film pressure, given by the difference between the surface tension of the pure fluid and that of the film covered surface,[168] is measured using a film balance and gives an indication of the state or arrangement of the monolayer molecules. Given that both the available surface area of the Langmuir trough (in cm^2) and the number of molecules on the
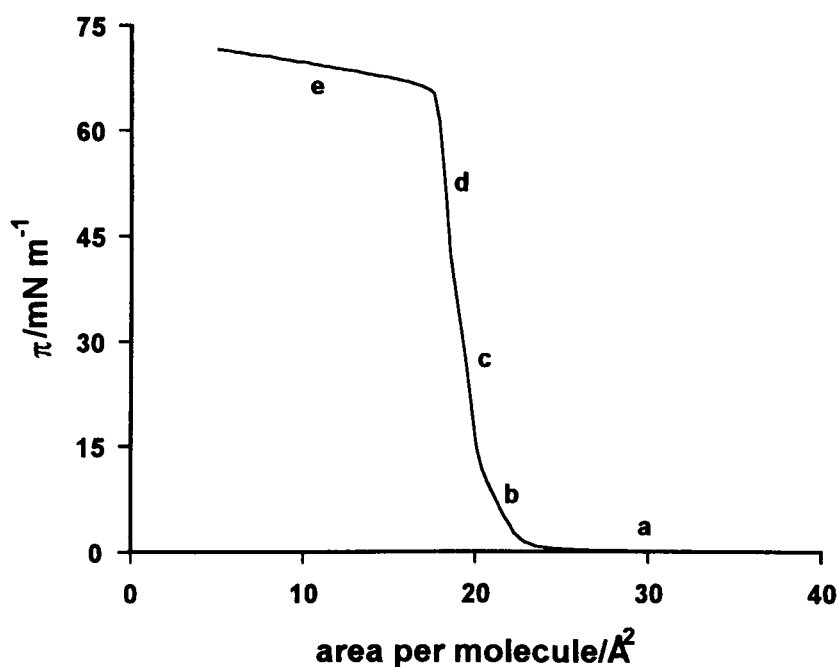
Figure 4.5 π-A_s isotherm for a 1-octadecanol monolayer on 0.1 mol dm^{-3} KNO$_3$.

surface are known, the available surface area for each molecule may be calculated, and is given in units of Å^2 molecule^{-1}.

The relationship between π and area per molecule of the surface, A_s, of 1-octadecanol on a sub-phase of 0.1 mol dm^{-3} KNO$_3$ is given in Figure 4.5, and is as expected.[173] The regions indicated correspond to well defined 2-D states observed for monolayer molecules; a) the gaseous state, b) the liquid expanded state, c) a liquid condensed state, d) a solid 2-D crystalline state and e) a 3-D collapsed multilayer film.[168] The π -A_s isotherm was recorded at a compression rate of 100 cm^2 min^{-1}, from an initial area of 950 cm^2. Identical results were obtained with compression at half this speed. Effectively identical isotherms were obtained with

93

and without the probe UME, indicating that the presence of the latter was non-perturbing. The isotherm enables the molecular area at collapse, A_0, to be determined, yielding a value of 17.9 $Å^2$ for this monolayer. This corresponds well with the alkyl chain cross-sectional area of 18.2 − 19.6 $Å^2$ in a three dimensional crystal.[174]

4.4.4.2 Approach Curve Measurements

A family of experimental approach curves at various surface pressures is shown in Figure 4.6. No contamination of the electrode surface was observed
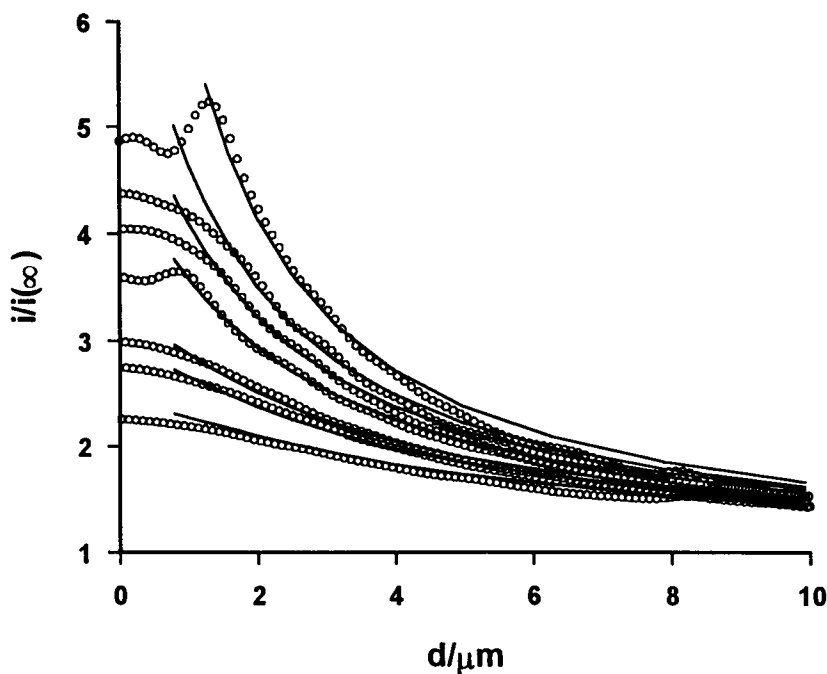
Figure 4.6 Normalised steady-state diffusion-limited current vs. UME-interface separation for the reduction of oxygen at a UME approaching an air/water interface with 1-octadecanol monolayer coverage (O). From top to bottom, the curves correspond to surface pressures of uncompressed, 5, 10, 20, 30, 40, and 50 mN m^{-1}. The solid lines represent the theoretical behavior for ($k'/10^{-8}$ mol cm^{-2} s^{-1}) = 6.7, 3.7, 3.3, 2.5, 1.8, 1.7, and 1.3.

between successive approach curve measurements as evidenced by consistent $i(\infty)$ values recorded between measurements. The distance of closest approach, identified earlier as 1.5 μm, was used here to correctly position the data on the distance axis, in each case this point was identified by an inflexion in the curve. As the monolayer is compressed, the normalised currents decrease, indicating that an increasing interfacial resistance is introduced into the transfer process. The solid lines indicate the best fit of the model for the rate constants indicated. It can be seen from these data that, quantitatively, the zero-order rate constant for the transfer of oxygen across the interface, k', falls from 3.7×10^{-8} mol cm^{-2} s^{-1} to 1.3 $\times 10^{-8}$ mol cm^{-2} s^{-1} as the surface pressure increases from 5 mN m^{-1} to 50 mN m^{-1}, and that an uncompressed, 1-octadecanol monolayer (in a 2-D gaseous state) offers some resistance to oxygen transfer.

4.4.4.3 Interpreting the Transfer Data

A number of models have been used to interpret evaporation rates through monolayers.[154,155,156,157,160,161,175] The simplest, and one of the most successful, is the accessible area model,[154] in which the flux is governed by the fraction of the interface, θ, that is free from surfactant. Equation 4.9 relates the transfer rate to the accessible area.

$$k' = k'_{\theta=1}\, \theta = k'_{\theta=1}\left(1 - \frac{A_{\theta=0}}{A_s}\right) \quad (4.9)$$

The same model appears to describe the transfer of oxygen through a monolayer of 1-octadecanol, as illustrated in Figure 4.7, which shows that there is a linear

dependence of k_{wa} and k_{aw} on A_s^{-1}. This plot yields $k_{\theta=1} = 0.68 \pm 0.04$ cm s^{-1} and

$A_{\theta=0} = 17.0 \pm 1.4$ Å^2. The former value is consistent with the measurements on the

clean interface which indicated that oxygen transfer was diffusion-controlled. The

maximum mass transfer coefficient in those measurements (Figure 4.4), $k_t \approx D/d =$

0.14 cm s^{-1}, which arises from thin layer cell theories,[176] is much lower than the

apparent interfacial resistance of the clean interface, deduced from Figure 4.7. The

observation that A_0 (measured in Figure 4.5) falls within the range of values of

$A_{\theta=0}$ (deduced from Figure 4.7), indicates that at the area of collapse, the

monolayer is close to a state where oxygen transfer is effectively completely

inhibited.
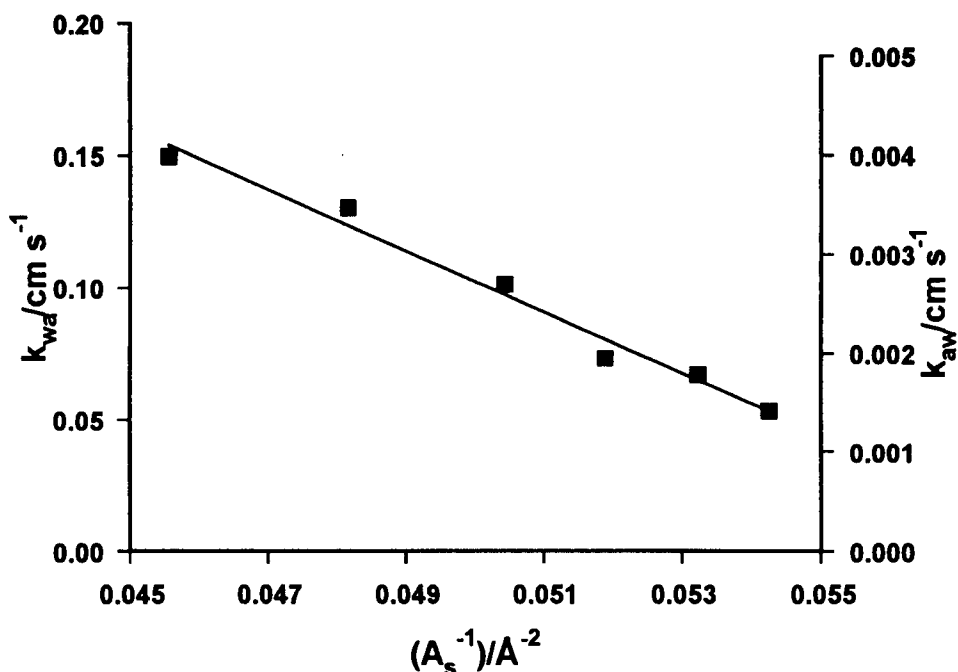
Figure 4.7   Oxygen transfer rate constants as a function of the reciprocal of the interfacial area per molecule.

4.4.5 Effect of Stearic Acid on Oxygen Transfer

4.4.5.1 Isotherm Characteristics

The effect of changing the amphiphile to stearic acid, which contains a carboxylic acid functionalised head-group was investigated. This monolayer displays a different packing density on the surface, indicated by the π - A_s isotherm obtained for this species on subphases of 0.1 mol dm^{-3} KNO$_3$ and 0.1 mol dm^{-3} KNO$_3$ with pH 6 buffer (5 × 10^{-2} mol dm^{-3} potassium dihydrogen phophate and 5.6 × 10^{-3} mol dm^{-3} sodium hydroxide) present, displayed in Figure 4.8. For this amphiphile, an important consideration was the pH of the sub-phase solution. The pKa of the amphiphilic head group was approximately 4.7. This
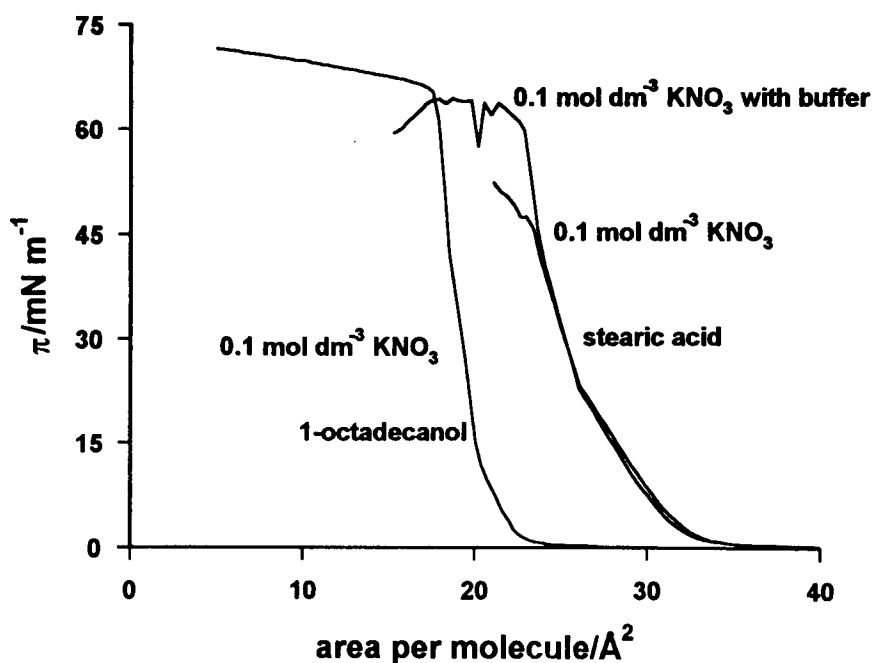
Figure 4.8 π-A_s isotherm for a stearic acid monolayer on subphases of 0.1 mol dm^{-3} KNO$_3$ with and without buffer. The 1-octadecanol isotherm is included for comparison.

monolayer displays lower surface densities than the 1-octadecanol monolayer over the same range of surface pressures used, and so its effect on the transport of oxygen is expected to be different.

4.4.5.2 Approach Curves

Approach curves recorded for oxygen reduction at a 25 μm diameter Pt UME, at the pressures indicated, with a 0.1 mol dm^3 KNO$_3$ subphase are shown in Figure 4.9. The data recorded at a pressure of 50 mN m^{-1} were recorded at a monolayer which was beginning to collapse, evidenced by the need for the area to be constantly reduced to maintain the pressure, however this data is still of value for qualitative analysis. The observation that transfer appears to be unaffected by the compressed monolayer may be due to the break-up of the monolayer. This may be expected when the electron transfer reaction at the UME, equation 4.8, is considered. The product of the oxygen reduction is hydroxide ions, which – under the SECM geometry – would be generated in high concentration in the gap between the probe UME and the interface. This increase in the local pH would be sufficient to cause significant deprotonation of the headgroup, pKa 4.7, the result being a charged head group which would be expected to repel like-charged amphiphile molecules nearby,[168] causing a local opening of the monolayer, allowing oxygen to transfer easily.

Addition of buffer at pH 6 to the sub-phase, to achieve a stable pH, resulted in the approach curves in Figure 4.10. The results indicate that the O$_2$ transfer may be somewhat retarded, but not to the same degree as in the case of 1-octadecanol. The shapes of the approach curves do not agree particularly well with the general shape of the simulated curves over the full range of distances.
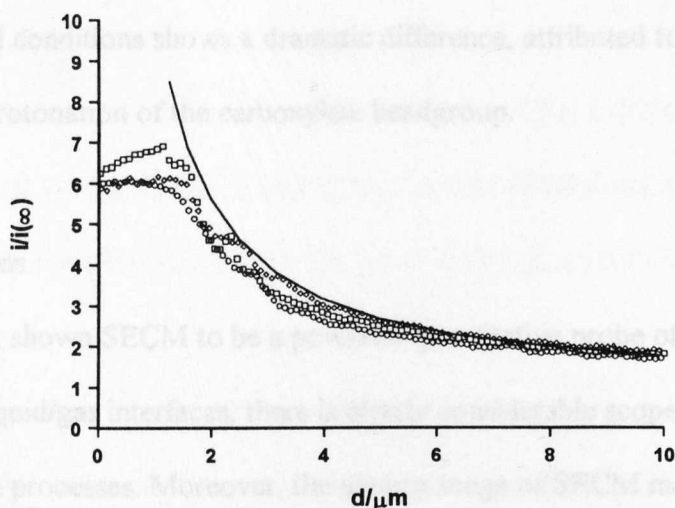
Figure 4.9 Normalised steady-state diffusion-limited current vs. UME-interface separation for the reduction of oxygen at a UME approaching an air/aqueous interface with stearic acid monolayer coverage. The subphase comprised 0.1 mol dm^{-3} KNO$_3$. The curves correspond to surface pressures of (O) 30, (□) 40, and (◊) 50 mN m^{-1}. The solid line represents the theoretical behaviour for transfer without interfacial kinetic limitations.
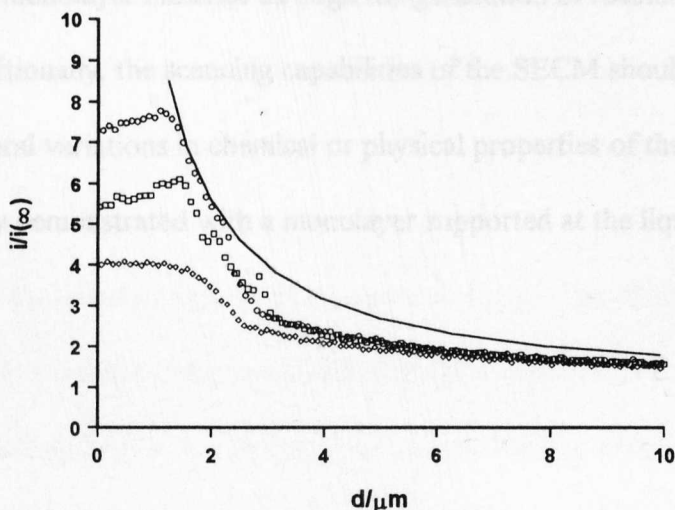
Figure 4.10 Normalised steady-state diffusion-limited current vs. UME-interface separation for the reduction of oxygen at a UME approaching an air/water interface with stearic acid monolayer coverage. The subphase comprised 0.1 mol dm^{-3} KNO$_3$ with pH 6 buffer. The curves correspond to surface pressures of (O) 30, (□) 40, and (◊) 50 mN m^{-1}. The solid line represents the theoretical behaviour for transfer without interfacial kinetic limitations.

However, at a qualitative level, comparison of the results obtained under buffered and unbuffered conditions shows a dramatic difference, attributed to the effect of pH on the deprotonation of the carboxylate headgroup.

4.5 Conclusions

Having shown SECM to be a powerful quantitative probe of transfer processes at liquid/gas interfaces, there is clearly considerable scope for further studies of such processes. Moreover, the diverse range of SECM modes available should enable non-invasive, local studies of other types of physicochemical processes in ultrathin films at liquid/gas interfaces such as adsorption/desorption, lateral charge transfer and diffusion. Following the studies of electrogenerated OH$^-$ on stearic acid monolayers, it is also expected that SECM may be used to locally modify monolayer moieties through the generation of reactants at the UME tip. Additionally, the scanning capabilities of the SECM should enable imaging of lateral variations in chemical or physical properties of the monolayer, as was recently demonstrated with a monolayer supported at the liquid/liquid interface.[123]

CHAPTER 5

MEASUREMENT OF LOCAL REACTIVITY AT LIQUID/SOLID, LIQUID/LIQUID AND LIQUID/GAS INTERFACES USING SECM IN THE DOUBLE POTENTIAL STEP CHRONOAMPEROMETRIC MODE: PRINCIPLES, THEORY AND APPLICATIONS

This chapter describes the development of the experimental and theoretical aspects of the SECM double potential step chronoamperometry (DPSC) mode. The concept of this new mode of SECM is to generate a reactant in an initial potential step at a tip UME positioned in close proximity to a target interface. The electrogenerated species diffuses from the tip to the interface, where it may be involved in a chemical process. The reactant is subsequently collected by electrolysis in a second potential step, and the form of the corresponding current-time curve provides information on the nature of the interaction between the initial tip-generated species and the interface. If the species is consumed in an irreversible interfacial process, the current flow during the second potential step is less than when the interface is inert with respect to the species of interest. The theoretical predictions are firstly examined with DPSC studies on the electrogeneration and collection of ferricyanide ions from aqueous ferrocyanide solutions, at a tip positioned close to aqueous/glass, aqueous/DCE and aqueous/air interfaces, as model examples of inert liquid/solid, liquid/liquid and liquid/gas interfaces. The case of an active interfacial process is illustrated through studies of the electrogeneration and collection of bromine, Br_2, from aqueous sulfuric acid solutions of potassium bromide, at a tip positioned close to aqueous/DCE and aqueous/air interfaces. The transfer of Br_2 across these

interfaces is found to be irreversible and effectively diffusion-controlled on the SECM timescale, putting a lower limit on the interfacial transfer rate constant of 0.5 cm s^{-1}.

5.1 Introduction

Section 1.4.4 described several applications of SECM in the feedback mode for studying charge transfer reactions at liquid/liquid interfaces, while in Chapter 3 the application of SECM induced transfer in the EP mode was described for studying more general reversible reactions at liquid/liquid interfaces. In order to diversify the range of processes that can be studied with SECM methods, SECM double potential step chronoamperometry (DPSC) is considered here as a new methodology for initiating and monitoring heterogeneous reactions at the local level. Specifically, SECM DPSC is developed as a new mode for accurately measuring rapid irreversible reactions at interfaces.

When used in conjunction with UMEs, in particular, DPSC has proved a powerful approach for characterising the diffusion coefficients of electrogenerated species[177] and the lifetimes of transient species involved in solution processes.[178,179] However, DPSC has not previously been used to investigate the kinetics of processes confined to a target interface.

The single potential step chronoamperometric mode has proved a particularly powerful method for inducing and monitoring reversible transfer processes at liquid/solid interfaces.[112,113,114,115,116,117,118] This mode operates in a similar way to the steady-state EP mode described in Chapters 3 and 4 for the study of processes at immiscible liquid/liquid and air/liquid interfaces. Reversible reactions have been studied using this chronoamperometric SECM EP mode,

including dissolution[113,114,115,116,117,118] and adsorption/desorption.[112] The DPSC mode described in this chapter complements the transient EP mode as it provides information on irreversible reactions which cannot be probed by the earlier approach.

In this chapter, a numerical model for SECM DPSC is first developed and examined in detail, to determine the range of information that can be obtained and the most appropriate experimental operating parameters. The theoretical predictions are then examined with model DPSC studies on inert liquid/solid, liquid/liquid and liquid/gas interfaces, provided by the electrogeneration and collection of ferricyanide ions from aqueous ferrocyanide solutions, at a tip positioned close to aqueous/glass, aqueous/DCE and aqueous/air interfaces. The case of an active interfacial process is then illustrated through studies of the transfer of Br_2, firstly across the aqueous/DCE interface, driven by enhanced solubility, and subsequently, across the aqueous/air interface due to the volatility of Br_2. These measurements are made through the electrogeneration and collection of Br_2, from aqueous sulfuric acid solutions of potassium bromide, at a UME positioned close to the interface.

5.2 The Technique

The basic concept of SECM DPSC is to employ a UME probe, positioned close ($d < a$) to the interface of interest, to electrochemically generate a reactive species (B in Figure 5.1) in an initial (forward) potential step for a fixed period. The species could be generated through the electrolysis of an inert precursor in the solution (A in Figure 5.1) or via the anodic dissolution of a pure or amalgam metal electrode.

a(i)   b(i)

forward step

A   A   A   A

B   B   B   B

W

O   no transfer   O   transfer

B   B

a(ii)   b(ii)

reverse step

A   A   A   A

B   B   B   B

W

O   no transfer   O   transfer

B   B
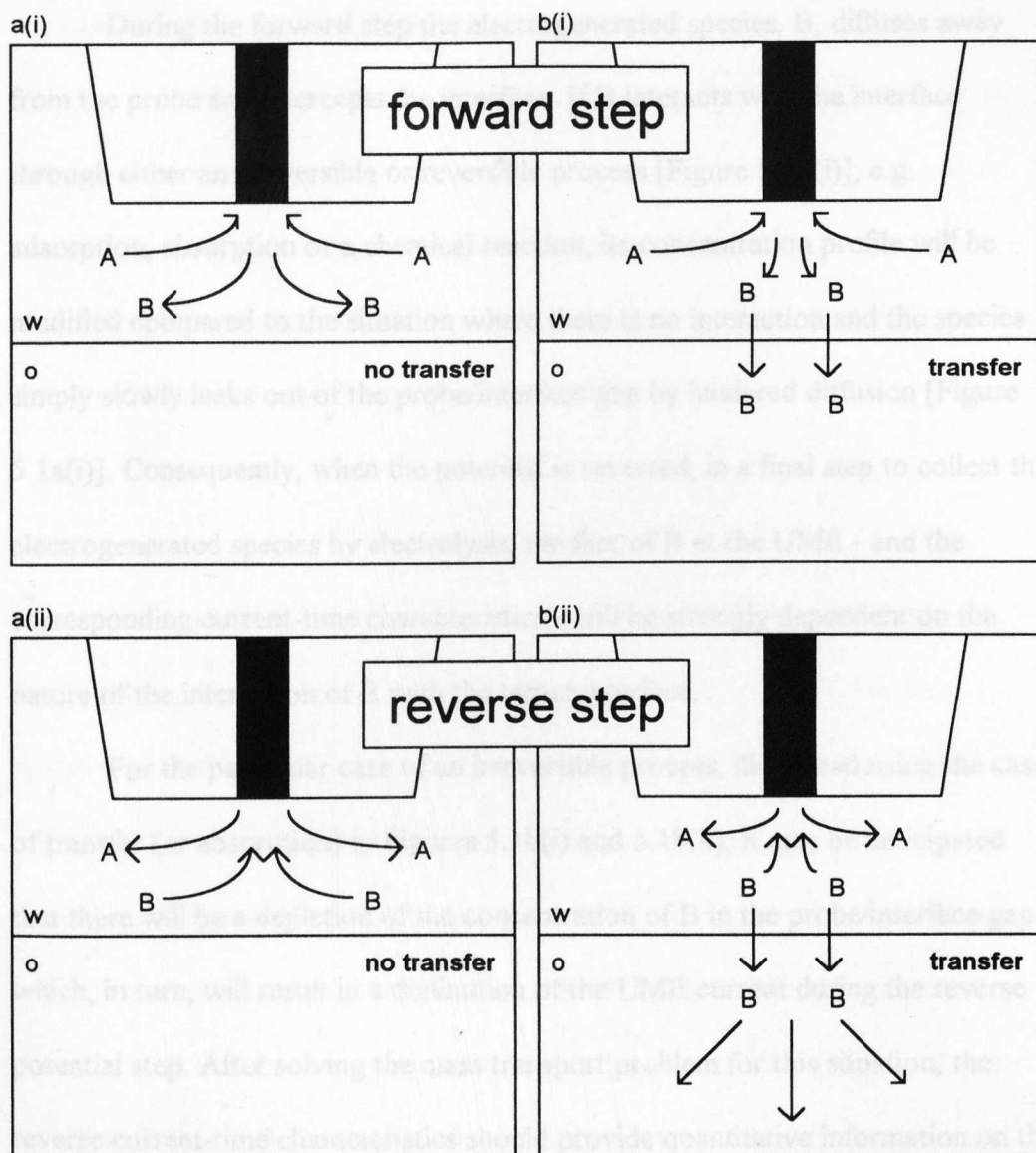
Figure 5.1   Schematic of the processes in the tip/interface gap for SECM DPSC, using the irreversible transfer of a solute across a water/organic (w/o) interface, as an example. During the forward step, species B is electrogenerated from A [a(i) and b(i)] in the local aqueous phase. If B is inert with respect to the target interface, it simply slowly leaks from the tip/interface gap by hindered diffusion [a(i)]. Consequently when the potential is stepped to reverse the electrode reaction, much of B is available for collection [a(ii)]. In contrast, if B is active with respect to the w/o interface, as in b(i) and (ii) where it partitions into the o-phase, there is a net depletion of B in the w-phase, resulting in a smaller collector flux [b(ii)] compared to the inert interface case [a(ii)].

During the forward step the electrogenerated species, B, diffuses away from the probe and intercepts the interface. If B interacts with the interface through either an irreversible or reversible process [Figure 5.1b(i)], e.g. adsorption, absorption or a chemical reaction, its concentration profile will be modified compared to the situation where there is no interaction and the species simply slowly leaks out of the probe/interface gap by hindered diffusion [Figure 5.1a(i)]. Consequently, when the potential is reversed, in a final step to collect the electrogenerated species by electrolysis, the flux of B at the UME - and the corresponding current-time characteristics - will be strongly dependent on the nature of the interaction of B with the target interface.

For the particular case of an irreversible process, illustrated using the case of transfer (or absorption) in Figures 5.1b(i) and 5.1b(ii), it may be anticipated that there will be a depletion of the concentration of B in the probe/interface gap which, in turn, will result in a diminution of the UME current during the reverse potential step. After solving the mass transport problem for this situation, the reverse current-time characteristics should provide quantitative information on the kinetics of the local interfacial process.

The experimental configuration was identical to that used in the EP mode studies. The electrode, of either conventional or submarine type, was positioned close to the interface using the x, y, z stages, aided by observation through a video microscope. Measurements were made at fixed distances, with the final accurate positioning of the UME being carried out with a piezoelectric positioner. The square wave potential was applied using a potential programmer unit. As previously demonstrated in Chapters 3 and 4, the quantitative application of SECM requires that the distance between the tip and target interface is known.

An attractive feature of the DPSC mode is that when the species of interest is electrogenerated via the diffusion-controlled electrolysis of a precursor in solution, which is inert with respect to the target interface, the forward current-time behaviour provides unambiguous independent information on the probe/interface separation,[143,180,181] enabling the quantitative interpretation of the reverse current-time characteristics.

5.3 Theory

In this chapter, a numerical model for SECM DPSC is developed using the ADIFDM, as described in section 3.4.1. In this case, the model is required to account for two species, the precursor and the reactant, and two separate time domains (the forward and reverse steps), and thus the simulation is more complicated. Specific consideration is given here to the case where the species of interest, electrogenerated at the UME probe through the diffusion-controlled electrolysis of a solution precursor, undergoes irreversible first-order loss at the interface. The model allows for arbitrary diffusion coefficients of the precursor and reactant species.

The general situation is considered, where the solution initially contains only a precursor species, A, which does not interact with the interface. At time, t = 0, the potential of the UME probe is stepped to a value to cause the following diffusion-controlled electrolysis:

$$A \pm n_e e^- \rightarrow xB \qquad (5.1)$$

resulting in the generation of the reactive species B. In equation 5.1, x denotes the number of moles of B generated during a single redox event, in which one mole of A is consumed.

The transport of species A and B in the axisymmetric cylindrical geometry of the SECM is governed by the following general dimensionless diffusion equation (where the subscript i denotes A or B):

$$\frac{\partial C_i}{\partial \tau} = \lambda_i \left[\frac{\partial^2 C_i}{\partial R^2} + \frac{1}{R} \frac{\partial C_i}{\partial R} + \frac{\partial^2 C_i}{\partial Z^2} \right] \quad (5.2)$$

The dimensionless terms, R, and Z in equation 5.2 are as defined in section 3.4.1. Dimensionless time is defined in this case by:

$$\tau = t D_A / a^2 \quad (5.3)$$

where D_A is the diffusion coefficient of A. The parameter

$$\lambda_i = D_i / D_A \quad (5.4)$$

where i = A or B, reflects the fact that A and B may have different diffusion coefficients. The concentrations of A and B have been normalised with respect to the bulk concentration of A, c_A^*, such that:

$$C_A = c_A / c_A^* \quad (5.5)$$

$$C_B = c_B/xc_A^{\bullet} \qquad (5.6)$$

The following boundary conditions are true following the initial potential step at τ = 0 and prior to the reverse step at $\tau = \tau_{switch}$:

$0 \leq \tau < \tau_{switch}$, $Z = 0$, $0 \leq R \leq 1$:

$$C_A = 0, \qquad -\lambda_B \left(\partial C_B / \partial Z \right) = \partial C_A / \partial Z \qquad (5.7)$$

$0 \leq \tau < \tau_{switch}$, $Z = 0$, $1 < R \leq RG$:

$$\partial C_A / \partial Z = 0, \qquad \partial C_B / \partial Z = 0 \qquad (5.8)$$

$0 \leq \tau < \tau_{switch}$, $R = 0$, $0 < Z < L$:

$$\partial C_A / \partial R = 0, \qquad \partial C_B / \partial R = 0 \qquad (5.9)$$

$0 \leq \tau < \tau_{switch}$, $R > RG$, $0 < Z < L$:

$$C_A = 1, \qquad C_B = 0 \qquad (5.10)$$

$0 \leq \tau < \tau_{switch}$, $Z = L$, $0 < R \leq RG$:

$$\partial C_A / \partial Z = 0, \qquad \partial C_B / \partial Z = KC_B \qquad (5.11)$$

Many of the above boundary conditions are similar to those outlined in section 3.4.1, however, their meanings will be discussed again here for clarity. Equations 5.7 and 5.8 denote that the electrolysis of A to B at the UME occurs at a diffusion-controlled rate, but both species are inert on the insulating sheath

108

surrounding the electrode. Equation 5.9 is a consequence of the axisymmetric cylindrical geometry, while equation 5.10 assumes that both species recover their bulk solution concentrations outside the thin layer zone formed by the probe and the target interface.

Equation 5.11 reflects the reactivity of A and B at the interface of interest. Species A is inert on this boundary, while B is lost in a first-order irreversible interfacial process, characterised by a normalised rate constant

$$K = k_1 a / D_B \qquad (5.12)$$

where k_1 (cm s^{-1}) is a first order heterogeneous rate constant.

For the period of the reverse step, in which B is electrolysed to A at the UME at a diffusion-controlled rate, it is only necessary to evaluate the concentration profile for B, by solving equation 5.2, with i = B, subject to the following boundary conditions:

$\tau_{switch} \leq \tau, Z = 0, 0 \leq R \leq 1$:

$$C_B = 0 \qquad (5.13)$$

$\tau_{switch} \leq \tau, Z = 0, 1 < R \leq RG$:

$$\partial C_B / \partial Z = 0 \qquad (5.14)$$

$\tau_{switch} \leq \tau, R = 0, 0 < Z < L$:

$$\partial C_B / \partial R = 0 \qquad (5.15)$$

$\tau_{switch} \leq \tau, R > RG, 0 < Z < L$:

$$C_B = 0 \qquad (5.16)$$

$\tau_{switch} \leq \tau, Z = L, 0 < R \leq RG$:

$$\partial C_B / \partial Z = KC_B \qquad (5.17)$$

The limiting case of an inert interface can be simulated with $K = 0$ in equations 5.11 and 5.17.

The aim of the model is to provide a solution for the current-time behaviour during the forward and reverse potential steps. For the forward step, the current, i, normalised with respect to $i(\infty)$ is given by:

$$i/i(\infty) = (\pi/2) \int_0^1 (\partial C_A / \partial Z)_{Z=0} R dR \qquad (5.18)$$

where

$$i(\infty) = 4n_e F D_A a c_A^* \qquad (5.19)$$

For the period of the reverse step, the normalised current ratio is given by:

$$i/i(\infty) = -\lambda_B (\pi/2) \int_0^1 (\partial C_B / \partial Z)_{Z=0} R dR \qquad (5.20)$$

The problem was once again solved numerically using a FORTRAN program, an example of which (secm-br.f) may be found in Appendix 2, based on the ADIFDM algorithm. The interface boundary conditions defined by equations 5.11 and 5.17 are readily incorporated into the general algorithm, with the consideration of a double potential step requiring only minor modifications to earlier single potential step programs.[112,113,114,115,116,117,118]

5.3.1 Theoretical Results and Discussion

The normalised DPSC response depends upon L, K, λ_B, τ_{switch} and, if long-time behaviour is considered, RG. The aim here is to consider the general DPSC characteristics, so the RG is set to 10 and $\lambda_B = 1$, and the effects of τ_{switch} and K on the current-time behaviour for typical probe to interface separations are evaluated.

5.3.1.1 Effect of τ_{switch}

The normalised current-time characteristics, with $K = 0$, for three different switching times, $\tau_{switch} = 0.01$, 0.1 and 1.0, are shown in Figure 5.2. For each switching time, three probe/interface separations, $\log(L) = -1.0$, -0.5 and 0.0, have been considered. The characteristics for both the forward and reverse steps are plotted together as $\left|i/i(\infty)\right|$ versus either $\tau^{-1/2}$ for the forward step or $(\tau - \tau_{switch})^{-1/2}$ for the reverse step, in order to emphasise the short-time characteristics for the forward and reverse steps, respectively.

The form of the forward transient, when the probe is close to an inert interface, has been discussed previously in connection with single potential step
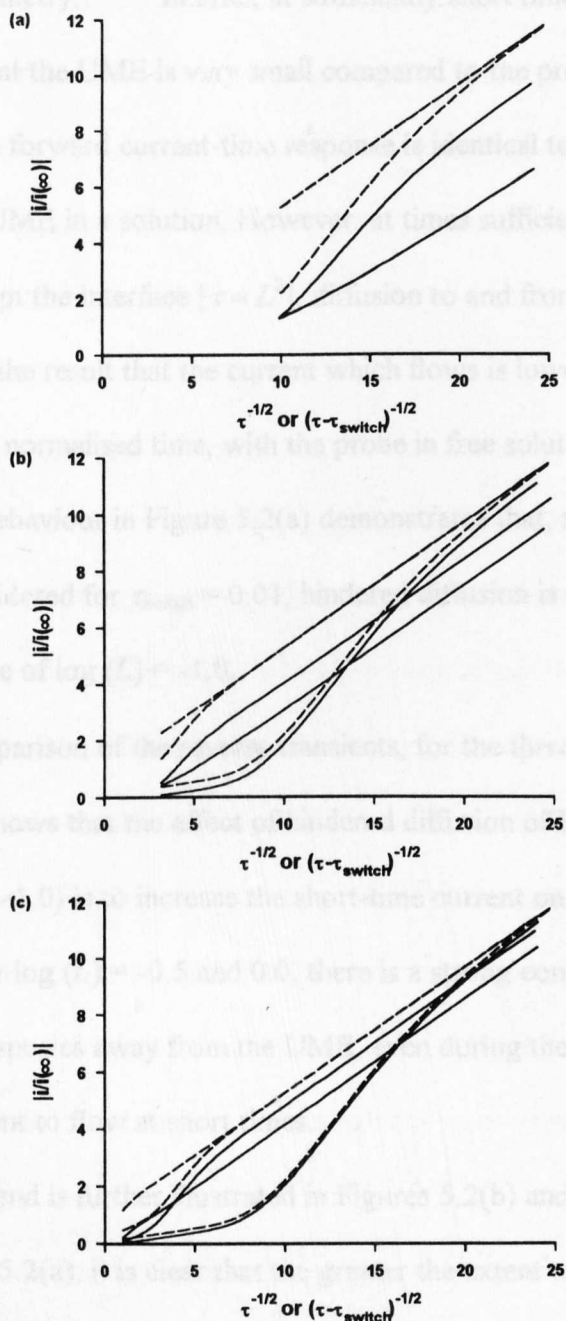
Figure 5.2 Forward (---) and reverse (——) current-time characteristics, plotted as $|i/i(\infty)|$ versus $\tau^{-1/2}$ (forward step) and $(\tau - \tau_{switch})^{-1/2}$ (reverse step) for $\tau_{switch} = 0.01$ (a), 0.1 (b) and 1.0 (c). For each switching time, data are shown for log (L) = -1.0 (lowest current at longest times on the forward step; highest current at shortest times on the reverse step) -0.5 and 0.0 (highest current at longest times on the forward step; lowest current at shortest times on the reverse step). In (a) only two pairs of transients appear, since the characteristics for log (L) = -0.5 and 0.0 are essentially identical on this switching timescale.

chronoamperometry. [137,180] In brief, at sufficiently short times such that the diffusion field at the UME is very small compared to the probe/interface separation, the forward current-time response is identical to that for a conventional UME in a solution. However, at times sufficient for the diffusion field to intercept the interface $[\tau \approx L^2]$, diffusion to and from the UME becomes hindered with the result that the current which flows is lower than that, at a corresponding normalised time, with the probe in free solution. The forward current-time behaviour in Figure 5.2(a) demonstrates that, at the probe/interface distances considered for $\tau_{switch} = 0.01$, hindered diffusion is only observed at the closest distance of log $(L) = -1.0$.

A comparison of the reverse transients, for the three distances with $\tau_{switch} =$ 0.01, clearly shows that the effect of hindered diffusion of B away from the UME (for log $(L) = -1.0$) is to increase the short-time current on the reverse transient. In contrast, for log $(L) = -0.5$ and 0.0, there is a strong concentration gradient of B driving this species away from the UME, even during the reverse step, causing a smaller current to flow at short times.

This trend is further illustrated in Figures 5.2(b) and (c). Together with the data in Figure 5.2(a), it is clear that the greater the extent to which diffusion is hindered during DPSC measurements, i.e. the closer the tip/interface separation and the longer the switching time, the closer are the forms of the forward and reverse current transients. Essentially, under conditions where diffusion in and out of the probe/interface gap is strongly impeded, there is a tendency for almost all of the material generated in the forward step to be collected in the reverse step.

The effect described above is evident in Figures 5.3(a) - (c), which show the concentration profiles for species B for the three distances of interest at three

times just after a reverse potential step at $\tau_{switch} = 0.1$. For $\log(L) = -1.0$, it can be seen that at the first time of interest [Figure 5.3a(i)], the gap between the probe and interface, directly under the active electrode, is filled with species B which may be rapidly recollected. Consequently, the reverse current is initially high [Figure 5.2(b)], but then rapidly decreases as B is consumed at the UME [Figure 5.3a(ii) and 5.3a(iii)].

For the larger probe/interface separations considered, there are concentration gradients both normal and radial to the UME that promote the diffusion of B away from the electrode during the initial collection process [Figures 5.3b(i) and 5.3c(i)]. The diffusion process away from the electrode is greatest, and thus the initial reverse diffusion-limited current lowest, at the largest probe/interface separation. However, at these larger probe/substrate separations, a greater fraction of B is able to survive to longer times, causing a higher current than at equivalent times for close tip/substrate separations. This can readily be seen by comparing, for example, Figures 5.3a(ii) and 5.3a(iii) with Figures 5.3b(ii) and 5.3b(iii), or by examining the long-time reverse currents in Figures 5.2(b) and 5.2(c).

In terms of the application of DPSC to the measurement of interfacial kinetics, the technique will be most sensitive to interfacial processes at the closest probe/interface separations, where the contribution to the current from solution diffusion is minimised, as found for other SECM modes.[97,98,99,100,101,102,105]

5.3.1.2 Effect of K

Having identified that SECM DPSC will be most sensitive to interfacial kinetics at the closest probe/substrate separations, the effect of interfacial kinetics
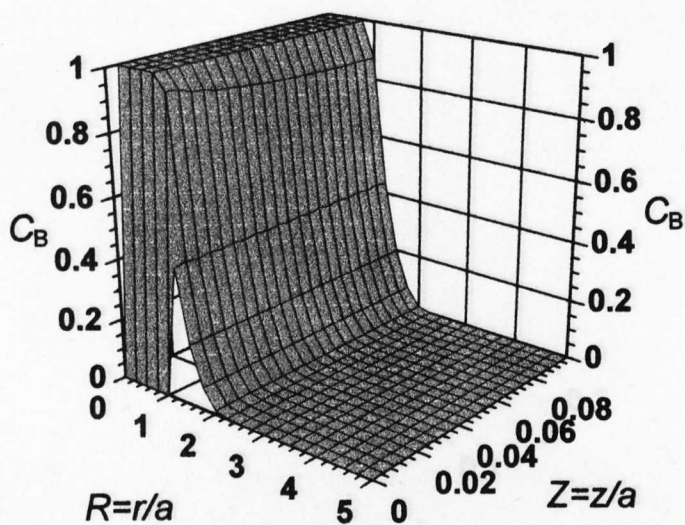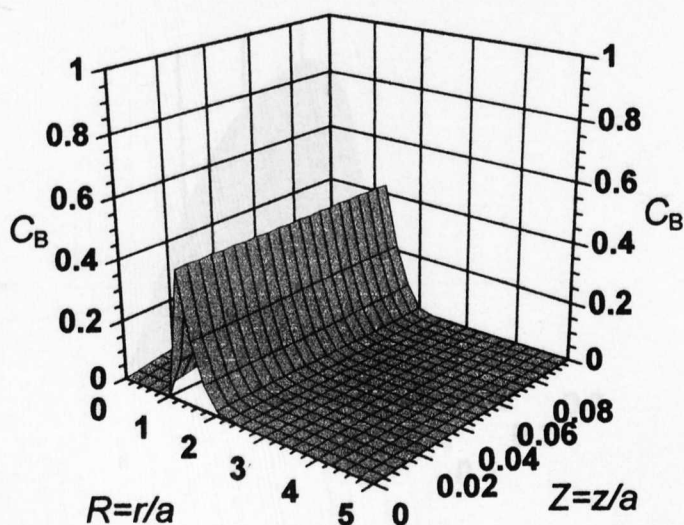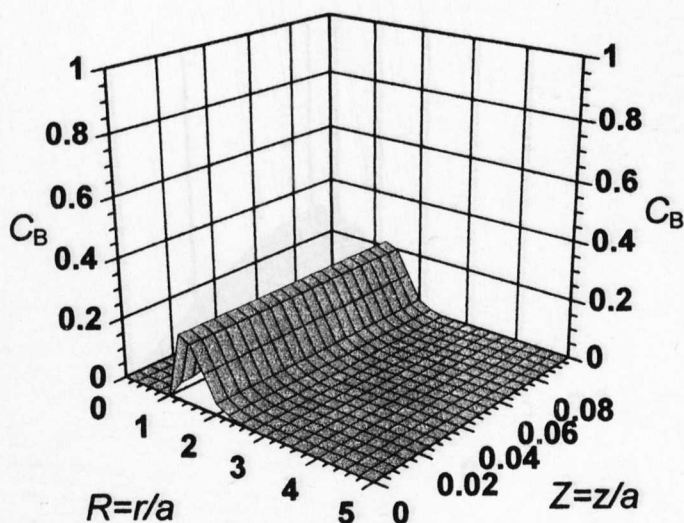
Figure 5.3(a) Distribution of species B in the tip/substrate gap during the reverse potential step, for $\tau_{switch} = 0.1$ with $K = 0$. Data are shown for $\log(L) = -1.0$ at $\tau = 0.10$ (i), 0.11 (ii) and 0.15 (iii).

Figure 5.3(b) Distribution of species B in the tip/substrate gap during the reverse potential step, for $\tau_{switch} = 0.1$ with $K = 0$. Data are shown for $\log (L) = -0.5$ at $\tau = 0.10$ (i), 0.11 (ii) and 0.15 (iii).
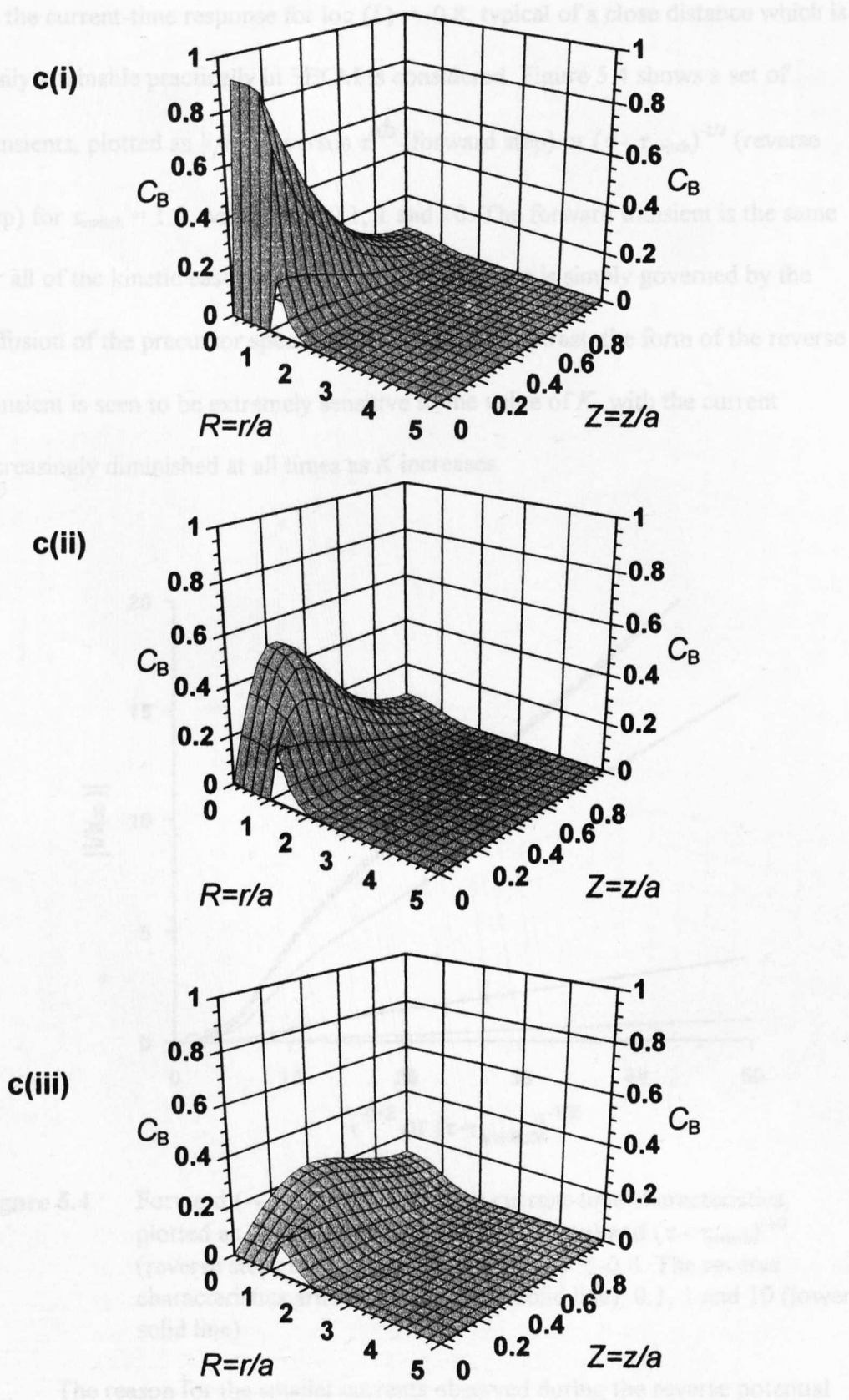
Figure 5.3(c) Distribution of species B in the tip/substrate gap during the reverse potential step, for $\tau_{switch} = 0.1$ with $K = 0$. Data are shown for log $(L) = 0.0$ at $\tau = 0.10$ (i), 0.11 (ii) and 0.15 (iii).
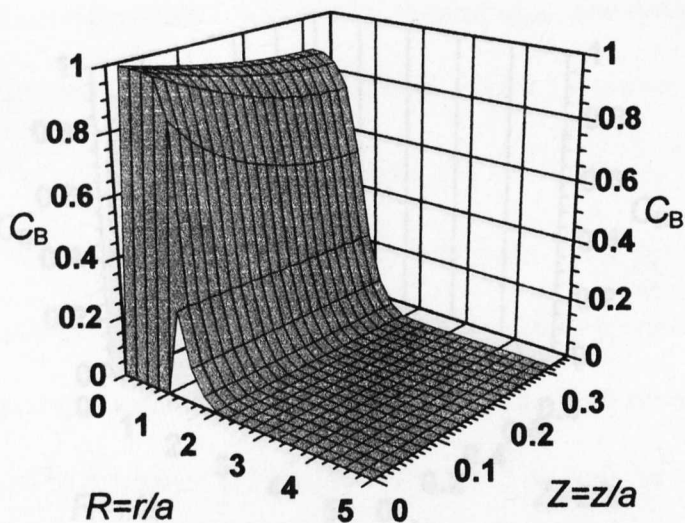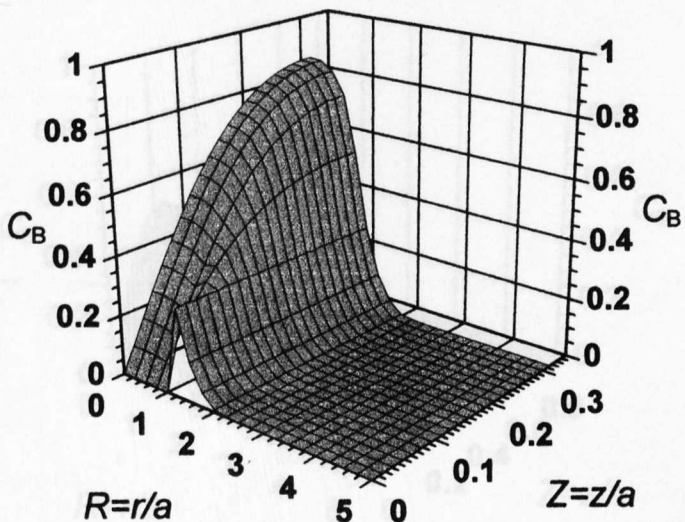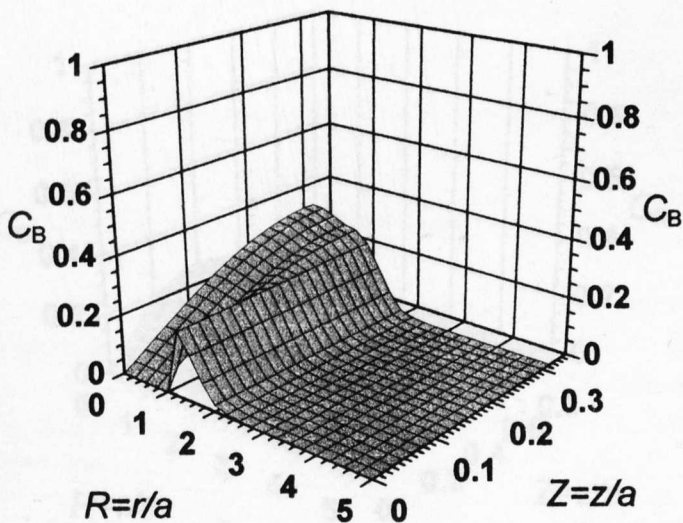
on the current-time response for log (L) = -0.8, typical of a close distance which is easily attainable practically in SECM is considered. Figure 5.4 shows a set of transients, plotted as $|i/i(\infty)|$ versus $\tau^{-1/2}$ (forward step) or $(\tau - \tau_{switch})^{-1/2}$ (reverse step) for τ_{switch} = 1.0, with K = 0, 0.1, 1 and 10. The forward transient is the same for all of the kinetic cases, since the current response is simply governed by the diffusion of the precursor species to the UME. In contrast, the form of the reverse transient is seen to be extremely sensitive to the value of K, with the current increasingly diminished at all times as K increases.

Figure 5.4   Forward (---) and reverse (———) current-time characteristics, plotted as $|i/i(\infty)|$ versus $\tau^{-1/2}$ (forward step) and $(\tau - \tau_{switch})^{-1/2}$ (reverse step) for τ_{switch} = 1.0 and log (L) = -0.8. The reverse characteristics are for K = 0 (upper solid line), 0.1, 1 and 10 (lower solid line).

The reason for the smaller currents observed during the reverse potential step with K > 0, is clear from Figure 5.5, which compares the evolving
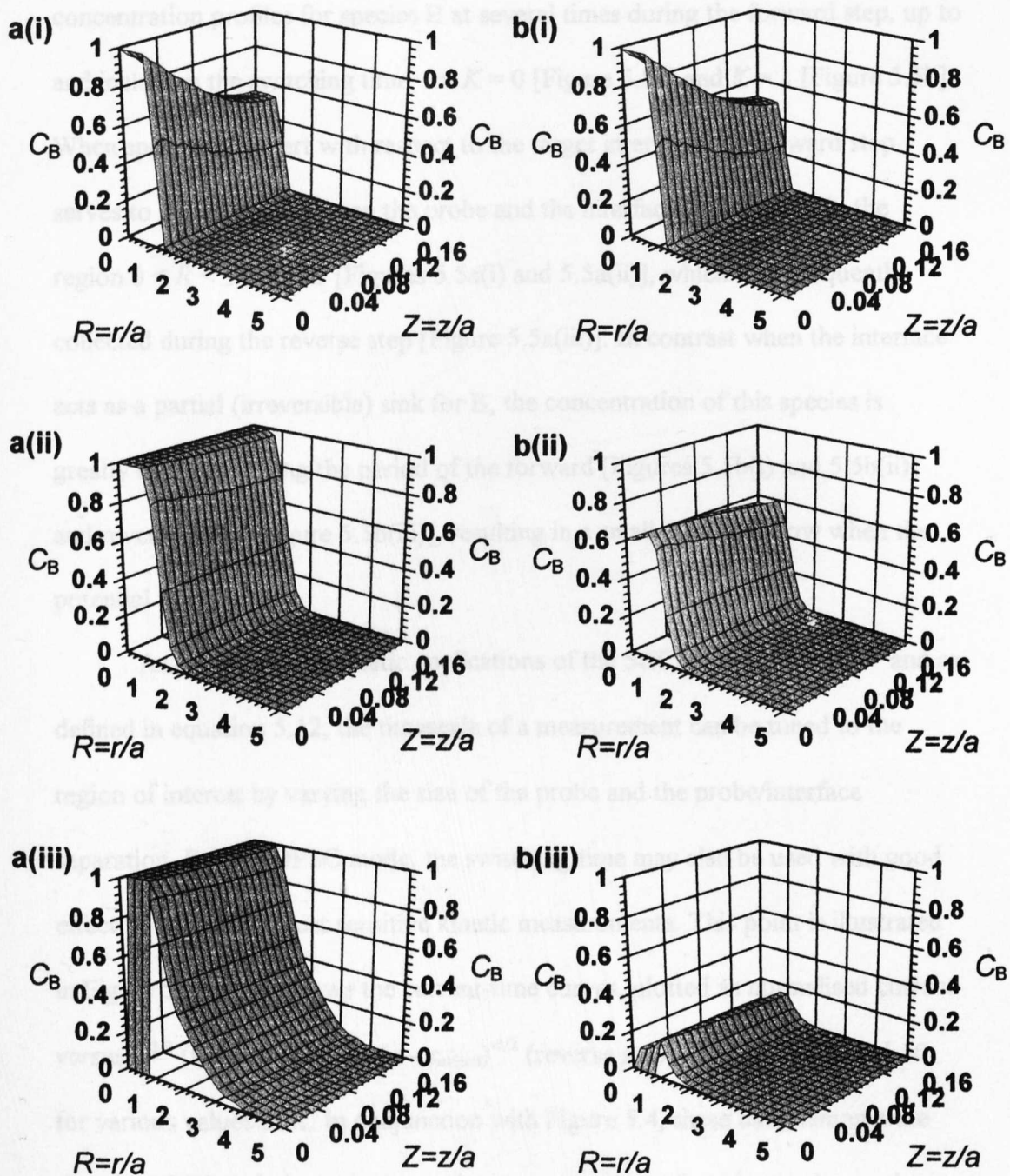
Figure 5.5   Evolution of the concentration distribution of species B in the tip/substrate gap (log (L) = -0.8) during the forward potential step, up to and including the reverse step (τ_{switch} = 1.0), for K = 0 (a) and 1 (b). In each case profiles are shown for τ = 0.01 (i), 0.1 (ii) and 1.0 (iii) (immediately after the potential was reversed).

concentration profiles for species B at several times during the forward step, up to and including the switching time, for $K = 0$ [Figure 5.5a] and $K = 1$ [Figure 5.5b]. When species B is inert with respect to the target interface, the forward step serves to fill the gap between the probe and the interface (particularly in the region $0 < R < 1$) with B [Figures 5.5a(i) and 5.5a(ii)], which is subsequently collected during the reverse step [Figure 5.5a(iii)]. In contrast when the interface acts as a partial (irreversible) sink for B, the concentration of this species is greatly depleted during the period of the forward [Figures 5.5b(i) and 5.5b(ii)] and reverse steps [Figure 5.5b(iii)], resulting in a smaller current flow when the potential is reversed.

As with previous kinetic applications of the SECM[109,110,111,116,117,118] and as defined in equation 5.12, the timescale of a measurement can be tuned to the region of interest by varying the size of the probe and the probe/interface separation. For the DPSC mode, the switching time may also be used with good effect to enable the most sensitive kinetic measurements. This point is illustrated in Figure 5.6, which shows the current-time curves, plotted as normalised current versus $\tau^{-1/2}$ (forward step) or $(\tau - \tau_{switch})^{-1/2}$ (reverse step) for $\tau_{switch} = 0.1$ and 10, for various values of K. In conjunction with Figure 5.4, these data demonstrate that the DPSC technique can be made most sensitive to fast kinetics by employing a short switching time, while slower interfacial reactions can be studied most effectively by employing a longer switching time.
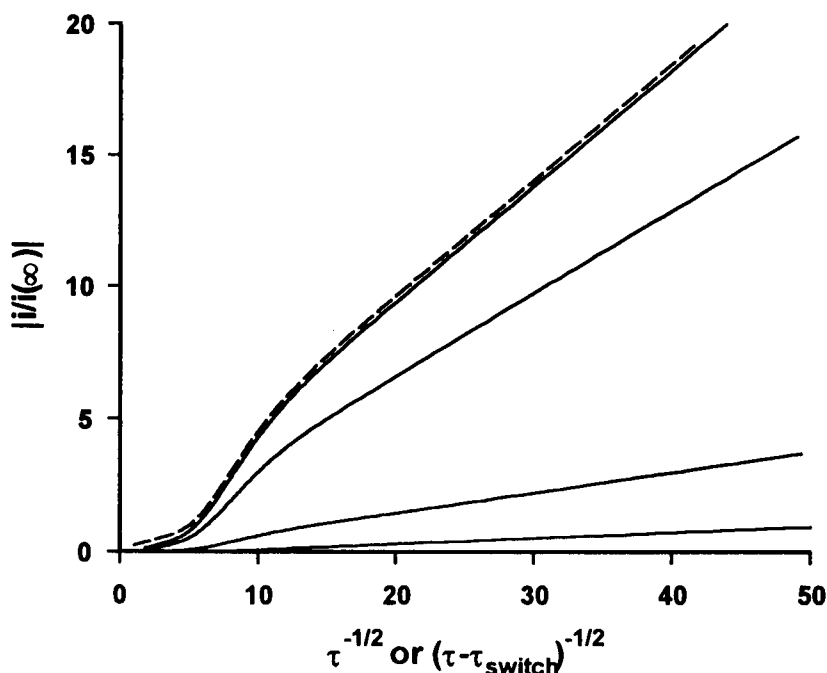
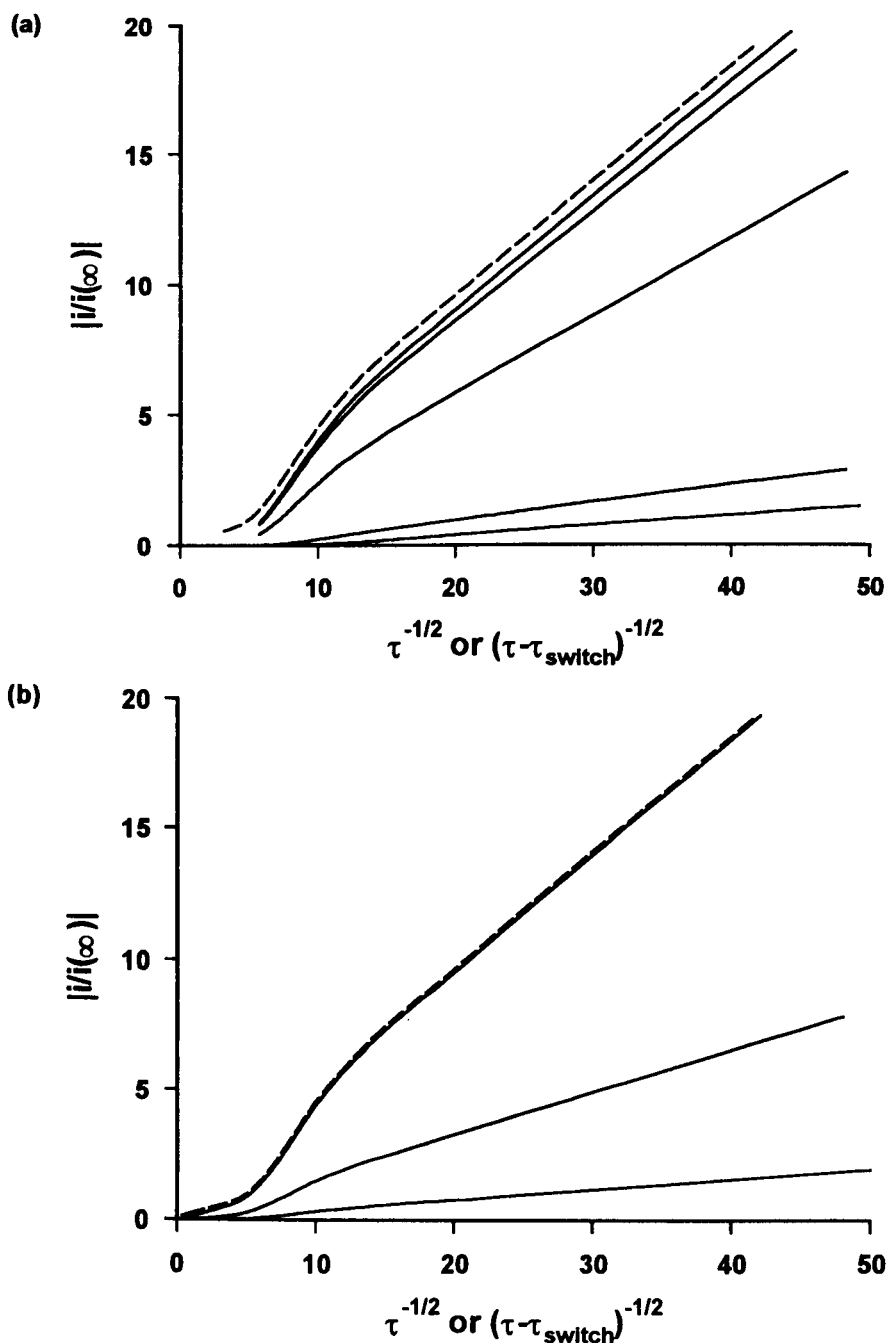**Figure 5.6**   Forward (---) and reverse (———) current - time characteristics, plotted as $|i/i(\infty)|$ versus $\tau^{-1/2}$ (forward step) and $(\tau - \tau_{switch})^{-1/2}$ (reverse step) for log (L) = -0.8 with: (a) τ_{switch} = 0.1 and K = 0 (upper solid curve), 0.1, 1, 10 and 100 (lower solid curve); (b) τ_{switch} = 10 and K = 0 (upper solid curve), 0.1 and 1 (lower solid curve).

5.4 Experimental Results and Discussion

5.4.1 DPSC Characteristics with Inert Mediators

In order to verify the theoretical predictions, initial experiments were carried out on the diffusion-controlled generation/collection of ferricyanide ions from 5.0×10^{-2} mol dm^{-3} potassium ferrocyanide solutions, containing 2.0 mol dm^{-3} KCl as supporting electrolyte, at a probe UME positioned close to (i) an aqueous/glass interface; (ii) an aqueous/DCE interface; and (iii) an aqueous/air interface. All of these are examples of interfaces which are chemically inert with respect to both the ferrocyanide and ferricyanide species.

5.4.1.1 Determination of Experimental Parameters

In order to model the DPSC transients it is essential to know precisely the diffusion coefficients of the two species in the solution of interest. As described in Chapter 3, the diffusion coefficient, D, may be calculated from the limiting current for the electrolysis of the target species at a UME of radius a, using equation 1.10, if c and n_e are known, or via the analytical method based on transient measurements described by equation 3.3. In addition, the i vs. $t^{1/2}$ transients measured for the forward and reverse steps may be compared with theoretically simulated transients using the model described in this chapter.

Ferrocyanide and ferricyanide diffusion coefficients were determined by voltammetry. The transient DPSC responses in bulk solution, modelled with the measured diffusion coefficients of 6.7×10^{-5} cm^2 s^{-1} and 7.6×10^{-5} cm^2 s^{-1}, respectively, are shown in Figure 5.7. For all ferrocyanide/ferricyanide DPSC measurements, the tip potential was stepped initially from 0.10 V, where no Faradaic processes occurred, to 0.70 V, where the oxidation of ferrocyanide was
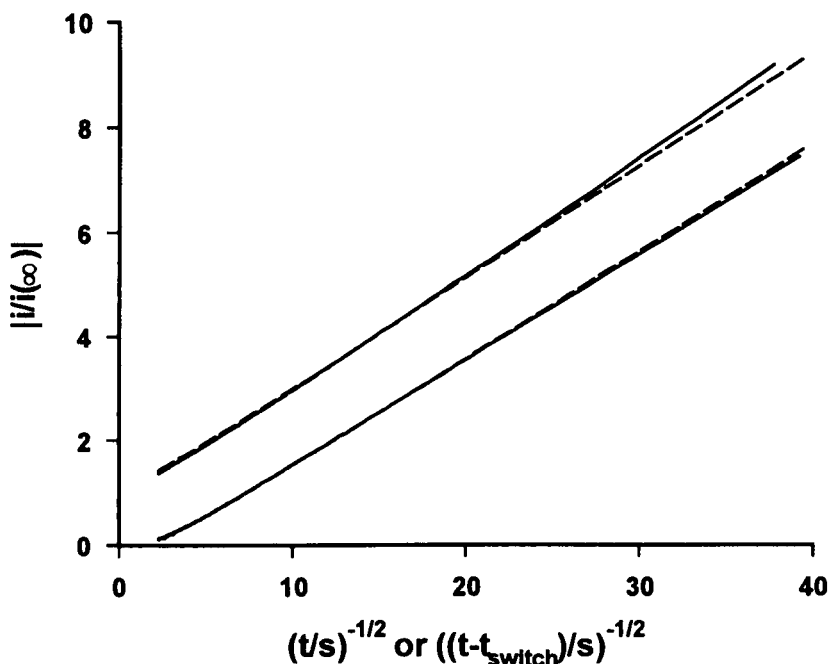
Figure 5.7   DSPC data (t_{switch} = 200 ms) for the oxidation of ferrocyanide (forward step; upper lines) and reduction of ferricyanide (reverse step; lower lines) at a tip in an aqueous solution containing 5×10^{-2} mol dm^{-3} ferrocyanide and 2 mol dm^{-3} KCl. The solid lines represent the experimental data, while the dashed lines correspond to the theoretical characteristics. Values of $D_{Fe(CN)_6^{4-}}$ = 6.7×10^{-6} cm^2 s^{-1} and $\lambda_{Fe(CN)_6^{3-}}$ = 1.13 were employed in the simulation.
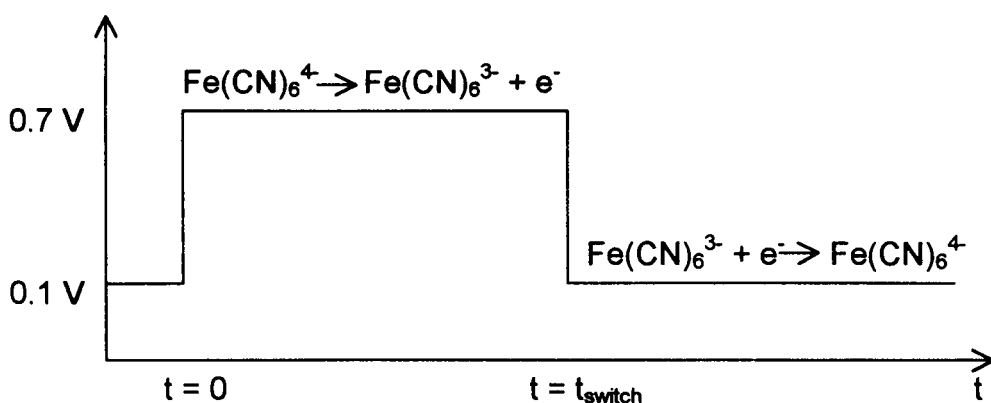
Figure 5.8   Illustration of the applied potential profile in the DPSC experiments with the ferro/ferricyanide couple.

123

diffusion-controlled, for a period, t_{switch}, typically of 200 ms. The potential was then stepped back to 0.10 V to collect ferricyanide by reduction to ferrocyanide. This process is illustrated schematically in Figure 5.8. These measurements confirm the calculated diffusion coefficients and demonstrate the excellent response of the redox couple in this particular situation.

5.4.1.2 Measurements at Model Interfaces

Figure 5.9 shows a series of typical generation/collection transients with the UME probe at various distances from an aqueous/glass interface. In the light of previous work, which has demonstrated that the chronoamperometric reduction of ferrocyanide under these conditions provides an excellent measure of the probe/interface separation,[116] the only variable involved in fitting the forward transient data was the probe/interface distance. A comparison between experiment and theory, for the forward step, shows an excellent agreement over the range of distances investigated.

With the tip/interface separation determined, and the diffusion coefficients measured, such that $\lambda_{Fe(CN)_6^{3-}} = 1.13$ is unambiguously calculated, there are no variables involved in the interpretation of the reverse transient behaviour for this system. The data in Figure 5.9 both verify the numerical model for SECM DPSC, as well as demonstrating that measurements can readily be made quantitatively on timescales less than 200 μs, with the experimental arrangement described.

Figure 5.9 DPSC data for the oxidation of ferrocyanide (forward step; upper curves) and reduction of ferricyanide (reverse step; lower curves) at a tip in aqueous solution, positioned at distances of 1.5 (a), 3.0 (b) and 4.5 (c) μm from a glass surface. In each case the switching time was 200 ms. The solid lines are experimental data, while the dashed lines are the theoretical characteristics. A value of $D_{Fe(CN)_6^{4-}} = 6.7 \times 10^{-6}$ cm^2 s^{-1} was employed to convert normalized time to real time, while $\lambda_{Fe(CN)_6^{3-}} = 1.13$ gave the best fit to the reverse current-time behaviour in each case.

5.4.1.3 Measurements at Target Interfaces

5.4.1.3.1 DPSC Characteristics at an Inert Liquid/DCE Interface

In order to demonstrate the application of the DPSC mode to probe chemical processes at immiscible liquid/liquid interfaces, the experimental characteristics for the generation/collection of ferricyanide at the aqueous/DCE interface were examined. Using the same aqueous solution conditions outlined above, similar timescales, and tip/substrate separations between 1.5 and 9.0 μm, excellent agreement was found between experiment and theory. Representative cases are illustrated in Figure 5.10, which shows the DPSC characteristics for a switching time of 200 ms, with the tip positioned at several distances from the aqueous/DCE interface.

5.4.1.3.2 DPSC Characteristics at an Inert Liquid/Air Interface

Using the probe design shown in Figure 2.3, DPSC experiments were carried out close to the aqueous/air interface, to determine whether SECM measurements at liquid/gas interfaces were viable. DPSC characteristics were obtained on similar timescales, and over the same range of tip/interface separations, to the experiments described above. Experimental data were found to be in good agreement with theory in all cases, demonstrating that SECM DPSC can, indeed, be used to probe liquid/gas interfaces. Typical results are shown in Figure 5.11 for various tip/interface separations. It can be seen that the experimental data are of a high quality and consistent with the theoretical predictions. Some oscillations in the transient response is observed at long times, which may result from oscillations at the air/water interface due to vibrational

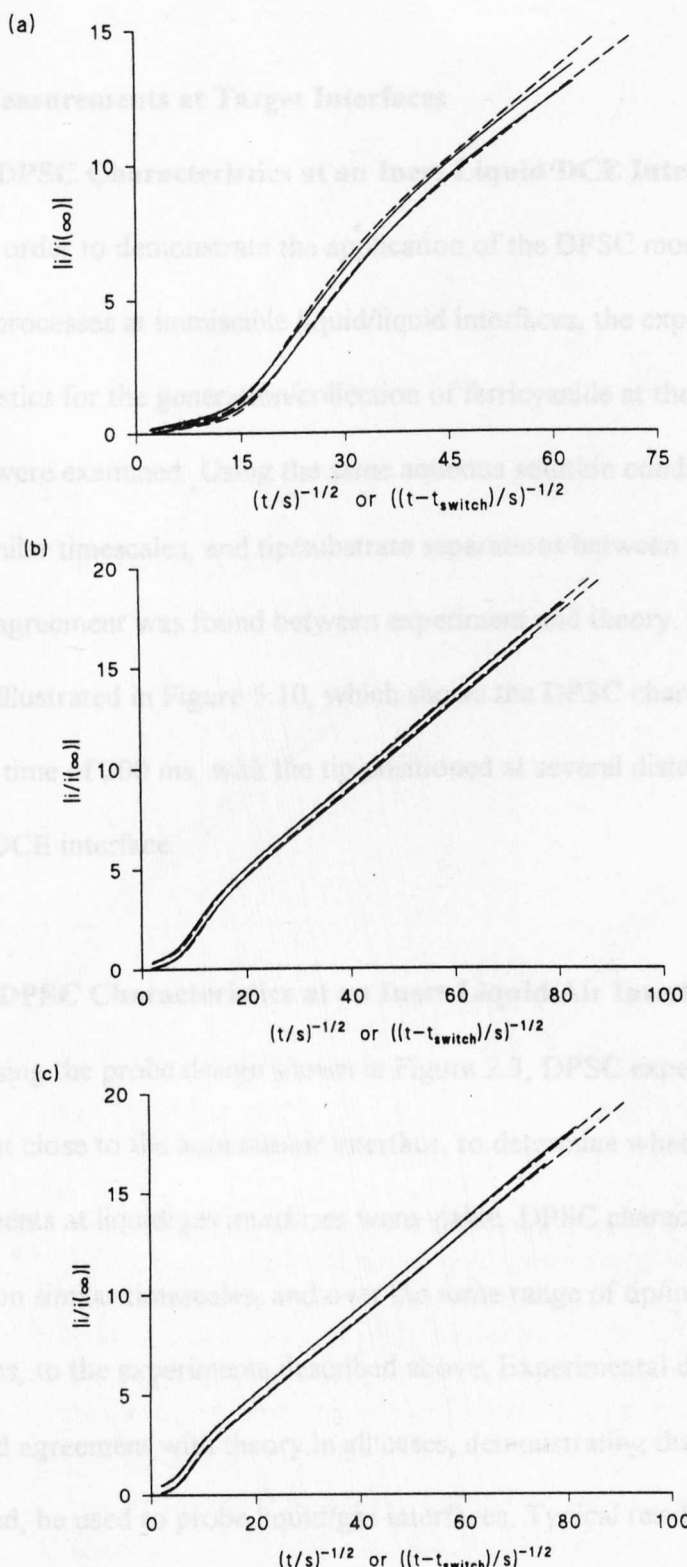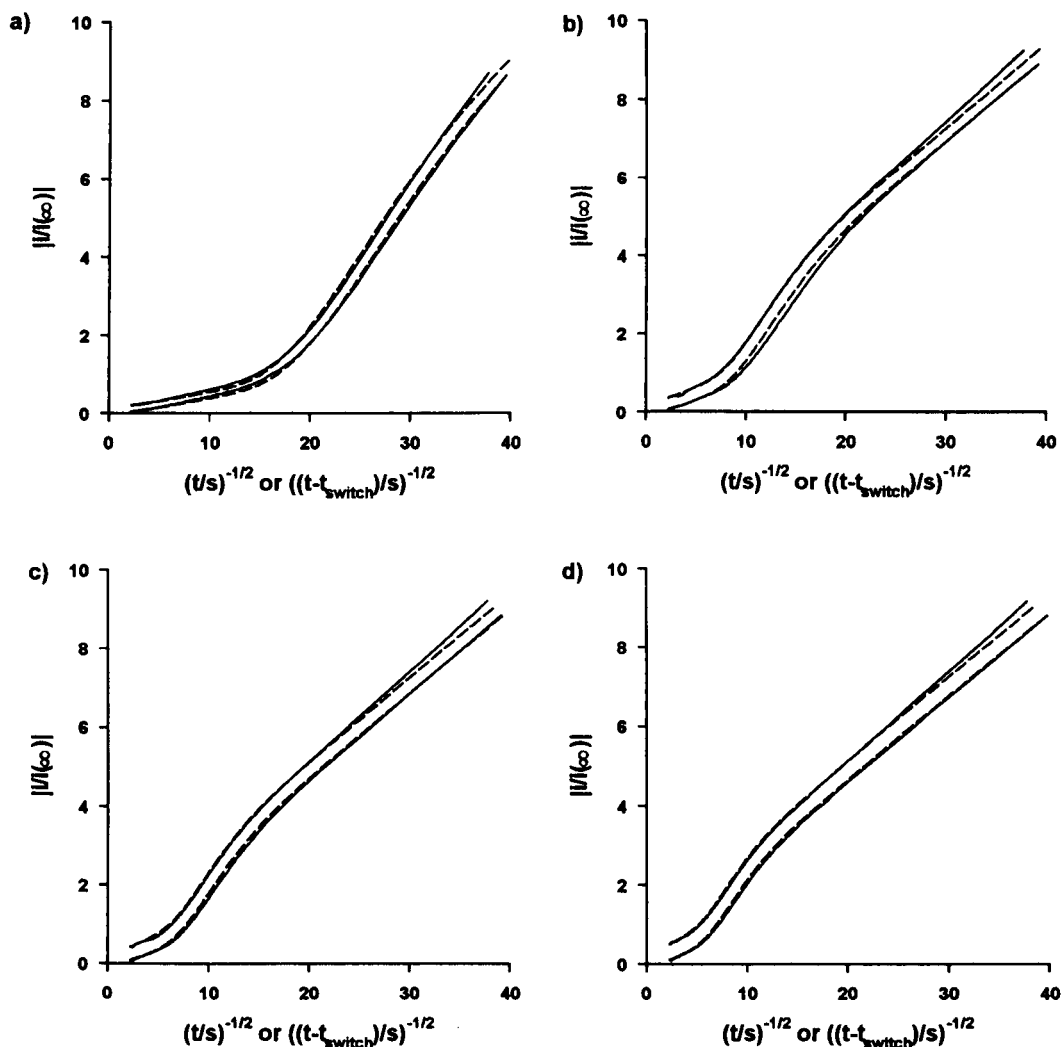**Figure 5.10** Typical DPSC data (t_{switch} = 200 ms) for the oxidation of ferrocyanide (forward step; upper curves) and reduction of ferricyanide (reverse step; lower curves) at a tip in aqueous solution, positioned at distances of a) 1.3, b) 2.8, c) 3.4 and d) 4.1 μm from an aqueous/DCE interface. The solid lines represent the experimental data, while the dashed lines correspond to the theoretical characteristics. A value of $D_{Fe(CN)_6^{4-}}$ = 6.7 × 10^{-6} cm^2 s^{-1} was employed to convert normalised time to real time, and $\lambda_{Fe(CN)_6^{3-}}$ = 1.13 was used for the simulation.
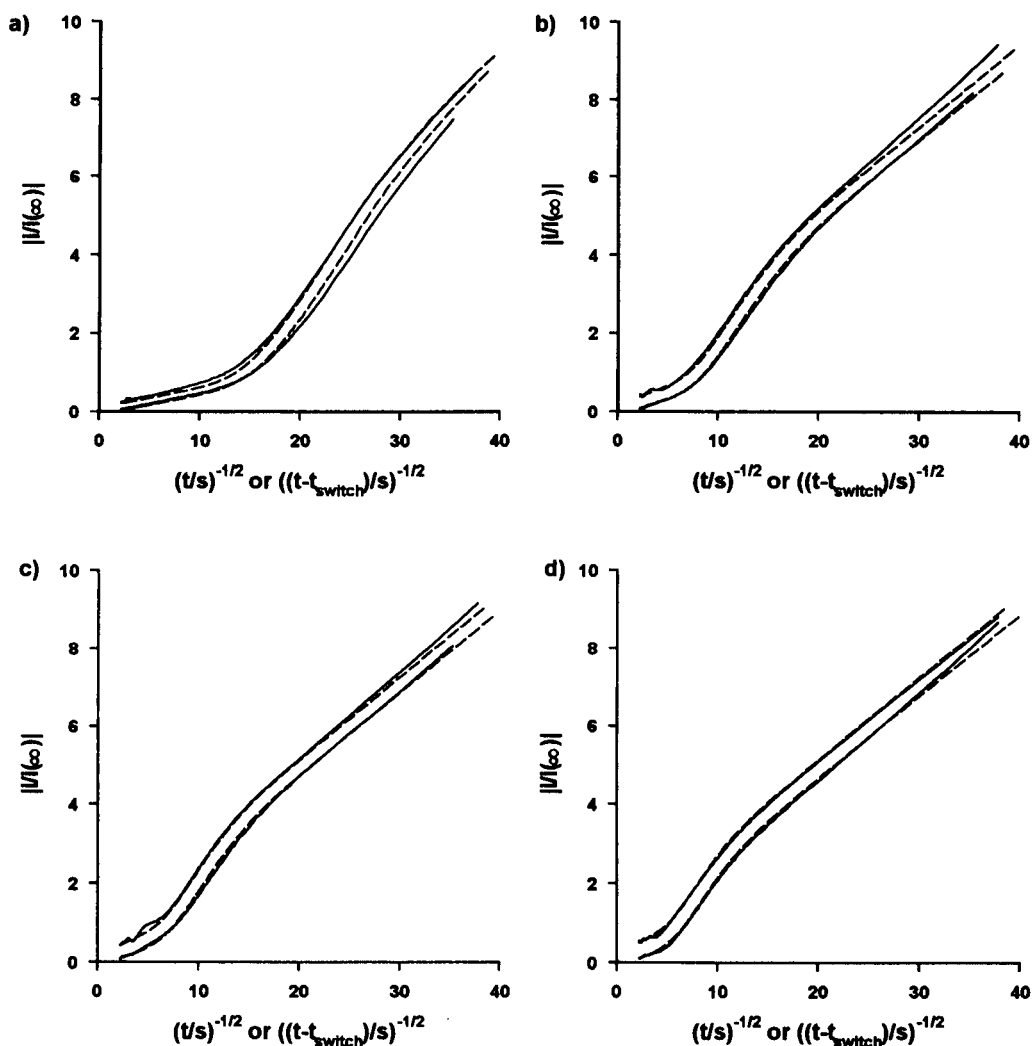
Figure 5.11 Typical DSPC data ($t_{switch} = 200$ ms) for the oxidation of
ferrocyanide (forward step; upper curves) and reduction of
ferricyanide (reverse step; lower curves) at a tip in aqueous
solution, positioned at distances of a) 1.5, b) 2.9, c) 3.4 and d) 4.1
μm from an aqueous/air interface. The solid lines represent the
experimental data, while the dashed lines correspond to the
theoretical characteristics. A value of $D_{Fe(CN)_6^{4-}} = 6.7 \times 10^{-6}$ cm^2 s^{-1} was employed to convert normalised time to real time, and
$\lambda_{Fe(CN)_6^{3-}} = 1.13$ was used for the simulation.
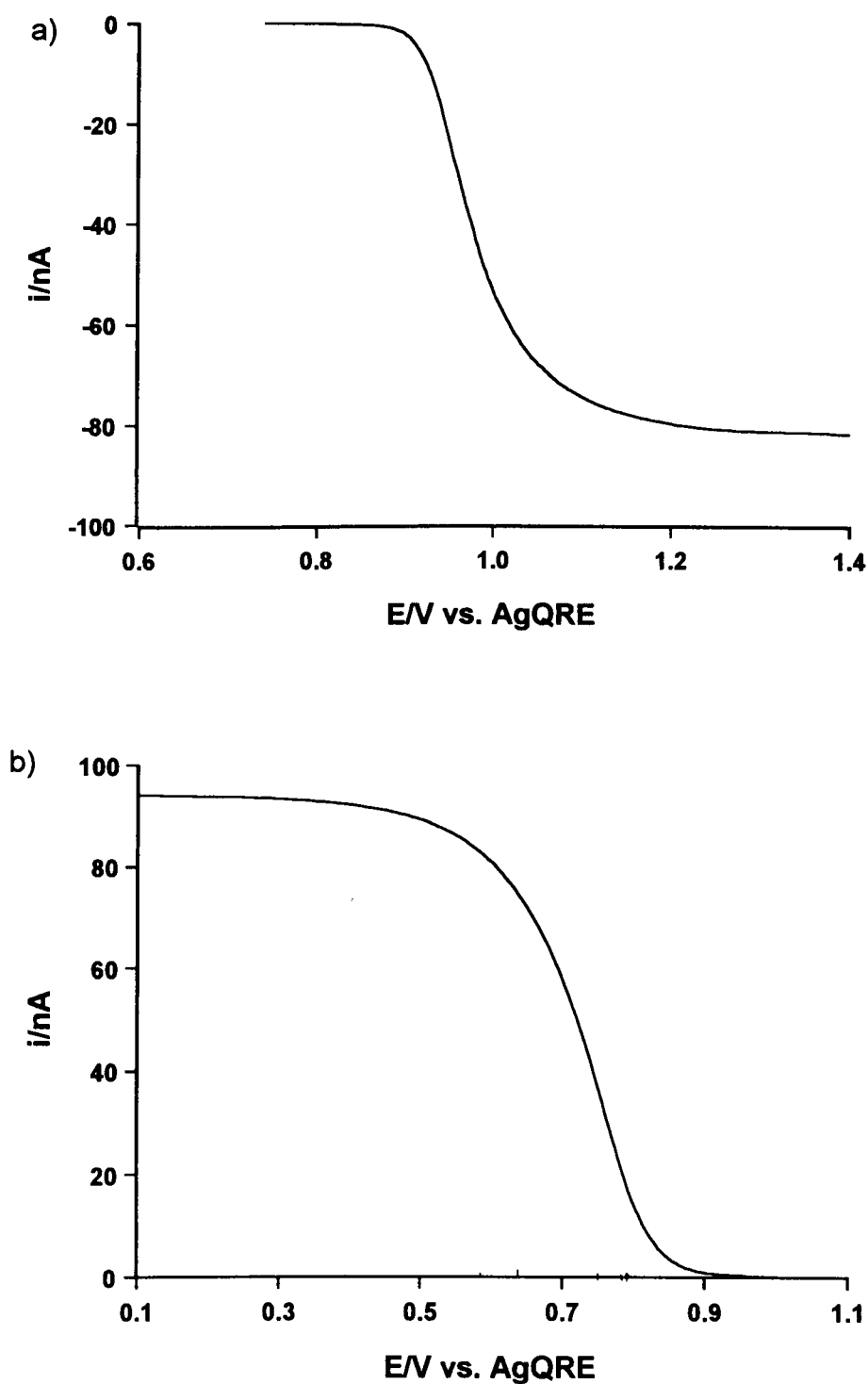
Figure 5.12 Voltammetric response for a) bromide oxidation in a solution of 1
× 10⁻² mol dm⁻³ KBr containing 0.5 mol dm⁻³ H₂SO₄, and b)
bromine reduction in a solution of 1 × 10⁻² mol dm⁻³ Br₂ with 0.5
mol dm⁻³ H₂SO₄. The scan rate used was 20 mV s⁻¹ in each case.

disturbances. It can be seen that despite these small oscillations it is still quite possible to accurately fit the data to the theoretical model.

5.4.2 DPSC Characteristics at Active Liquid/Liquid Interfaces

5.4.2.1 Determination of Experimental Parameters

Voltammograms recorded for the oxidation of bromide and the reduction of bromine are shown in Figure 5.12. Diffusion coefficients calculated from the limiting currents for bromide oxidation and bromine reduction, using equation 1.10, are 1.8×10^{-5} cm^2 s^{-1} and 9.4×10^{-6} cm^2 s^{-1} respectively. Figure 5.13 shows
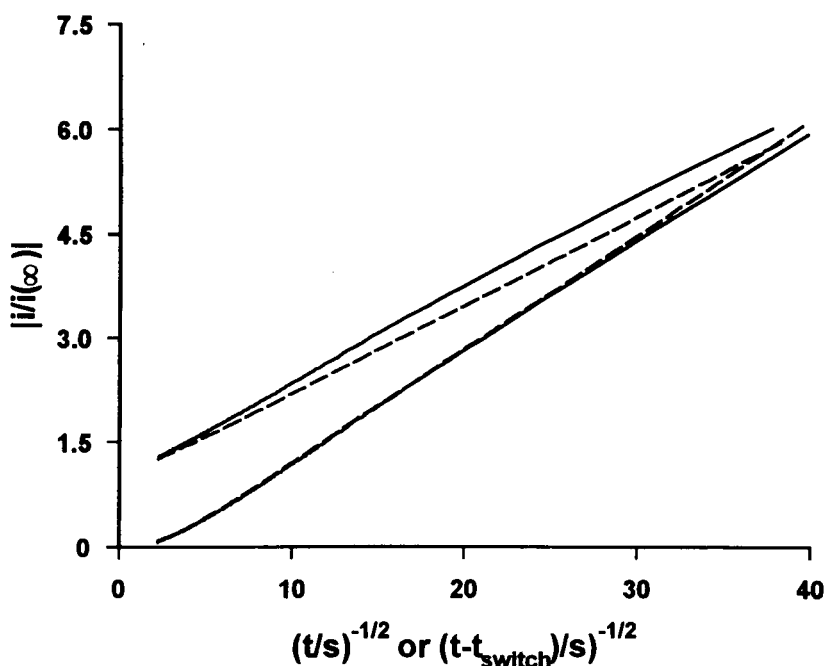
Figure 5.13   DSPC data (t_{switch} = 200 ms) for the oxidation of bromide (forward step; upper lines) and reduction of bromine (reverse step; lower lines) at a tip in an aqueous solution containing 1×10^{-2} mol dm^{-3} KBr and 0.5 mol dm^{-3} H$_2$SO$_4$. The solid lines represent the experimental data, while the dashed lines correspond to the theoretical characteristics. Values of D_{Br_2} = 1.8×10^{-5} cm^2 s^{-1} and D_{Br^-} = 9.4×10^{-5} cm^2 s^{-1} were employed in the simulation.

the bulk phase DPSC experimental and simulated transients based on the diffusion coefficients calculated above. In all experiments, Br⁻ was first oxidised to Br$_2$ in an initial potential step, from 0.70 V to 1.20 V, for a period in the range 10 - 200 ms, after which the potential was stepped to 0.70 V to effect the diffusion-controlled collection of Br$_2$ by reduction to Br⁻. This may be illustrated schematically according to Figure 5.14.
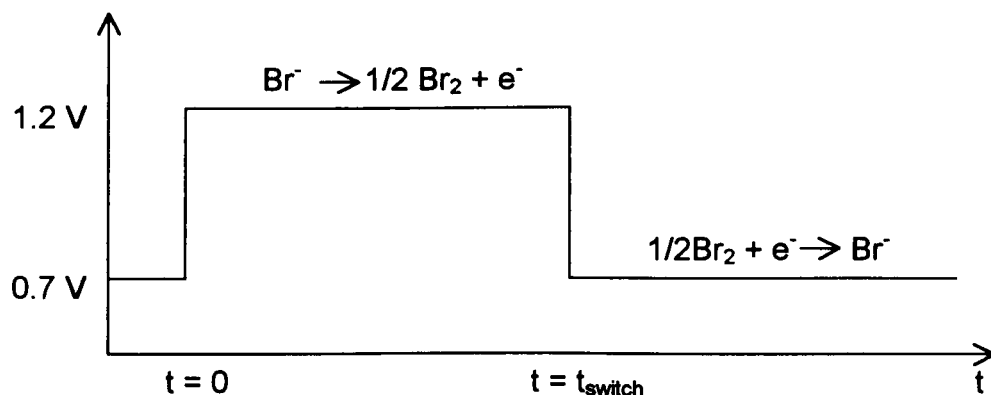
Figure 5.14   Illustration of the applied potential profile in the DPSC experiments with the bromide/bromine couple.

The forward step transient in Figure 5.13 shows slightly higher currents, particularly at short times which is probably due to the oxidation of the Pt electrode surface on this timescale. The reverse step transient fits very well with the predicted response. Both of the values of the diffusion coefficients are in good agreement with those reported earlier under similar solution conditions.[182] It should be noted that the formation of Br$_3^-$, through the equilibration of Br$_2$ and Br⁻,[182,183] can be neglected, so that the basic theoretical model described herein is valid. Moreover, under the experimental conditions for many of the systems below, the rapid transfer of Br$_2$ across the interface (and thus out of the

131

tip/interface gap) results in a dramatic depletion in the concentration of Br_2 in the aqueous phase in any case, so that the concentration of Br_3^- is negligible.

5.4.2.2 Measurements at a Model Liquid/Glass Interface

Before the interaction of bromine with organic liquid and air phases was investigated, it was first necessary to characterise the response with an inert interface. For this purpose, DPSC transients were recorded for bromine generation from bromide and subsequent collection at a UME positioned close to an aqueous/glass interface. Figure 5.15 shows a series of forward and reverse transients along with the simulated profiles at a range of UME-interface separations. The difference in the shapes of the forward and reverse transients compared with the ferrocyanide/ferricyanide case arises from the significant difference in the diffusion coefficients of the bromine and bromide species, $\lambda_{Br_2} = 0.52$.

5.4.2.3 Measurements at Active Interfaces

5.4.2.3.1 DPSC Characteristics at an Active Aqueous/DCE Interface

Br_2 shows enhanced solubility in many organic solvents compared to aqueous solutions.[184] The partition coefficient of Br_2 in the DCE/0.5 mol dm^{-3} sulfuric acid system was determined voltammetrically by first measuring the steady-state limiting current for the reduction of 1×10^{-2} mol dm^{-3} Br_2 in 0.5 mol dm^{-3} sulfuric acid solution at a 25 μm diameter Pt UME (i_{L1}), and the corresponding limiting current after shaking the solution with an equal volume of DCE (i_{L2}). Under these conditions, the coefficient defining the partitioning of Br_2 between DCE and aqueous solution is then given by:

132

Figure 5.15 Typical DSPC data (solid lines, t_{switch} = 200 ms) for the oxidation of bromide (forward step) and reduction of bromine (reverse step) at a UME in aqueous solution, positioned at distances of a) 2.2, b) 3.1, c) 4.2 and d) 10.2 μm from an aqueous/glass interface. The forward and reverse step dashed lines are the theoretical responses for the defined tip/interface separation, with D_{Br^-} = 1.8 × 10^{-5} cm^2 s^{-1} and D_{Br_2} = 9.4 × 10^{-6} cm^2 s^{-1}, respectively.

$$K_p = \frac{[Br_2]_{DCE}}{[Br_2]_{aq}} = \frac{i_{L1} - i_{L2}}{i_{L2}} \tag{5.21}$$

A value of K_P = 37 (± 1) was deduced. This implies that Br$_2$ electrogenerated

through the oxidation of Br$^-$ in the aqueous phase, close to an aqueous/DCE

interface, will undergo effectively irreversible transfer across the interface,

providing an ideal model system for examining the DPSC technique as a probe of irreversible interfacial kinetics.

Initial SECM DPSC measurements were made with a time step characterised by t_{switch} = 200 ms, as with the ferrocyanide/ferricyanide system described above. Results obtained at a range of UME-interface separations are shown in Figure 5.16. All experimental data, obtained at tip/interface separations from 2.5 to 9.1 μm, for the step time defined above, were found to be in good agreement with the theoretical predictions for the irreversible diffusion-controlled loss of Br_2 at the interface. The distances being accurately determined by fitting the forward experimental transients to the forward step theory. The results at this time step demonstrate that the bromine is transferred across the interface on a rapid timescale, and by applying the simulation with a range of rate constants the transfer rate constant may be identified as being faster than 0.05 cm s^{-1} (approaching the diffusion-controlled limit under these conditions). At this transient time it is not possible to further resolve the rate constant, so measurements at shorter time steps are required.

A typical result for the shortest time step examined (t_{switch} = 10 ms), at a tip/interface separation of 2.8 μm, is shown in Figure 5.17. Measurements must be made close to the interface when the time step is short in order to allow sufficient time for electrogenerated bromine to diffuse to the interface. The data have been plotted as $|i / i(\infty)|$ vs. $t^{1/2}$ (forward step) or $(t-t_{switch})^{-1/2}$ (reverse step). The reverse current-transient is in good agreement with theory for a diffusion-controlled process, particularly for $(t-t_{switch})^{-1/2}$ < 20 s$^{-1/2}$. At longer reverse times, the experimental currents are slightly higher than those predicted theoretically. This may be attributed to a small effect of electrochemically-induced back-transfer
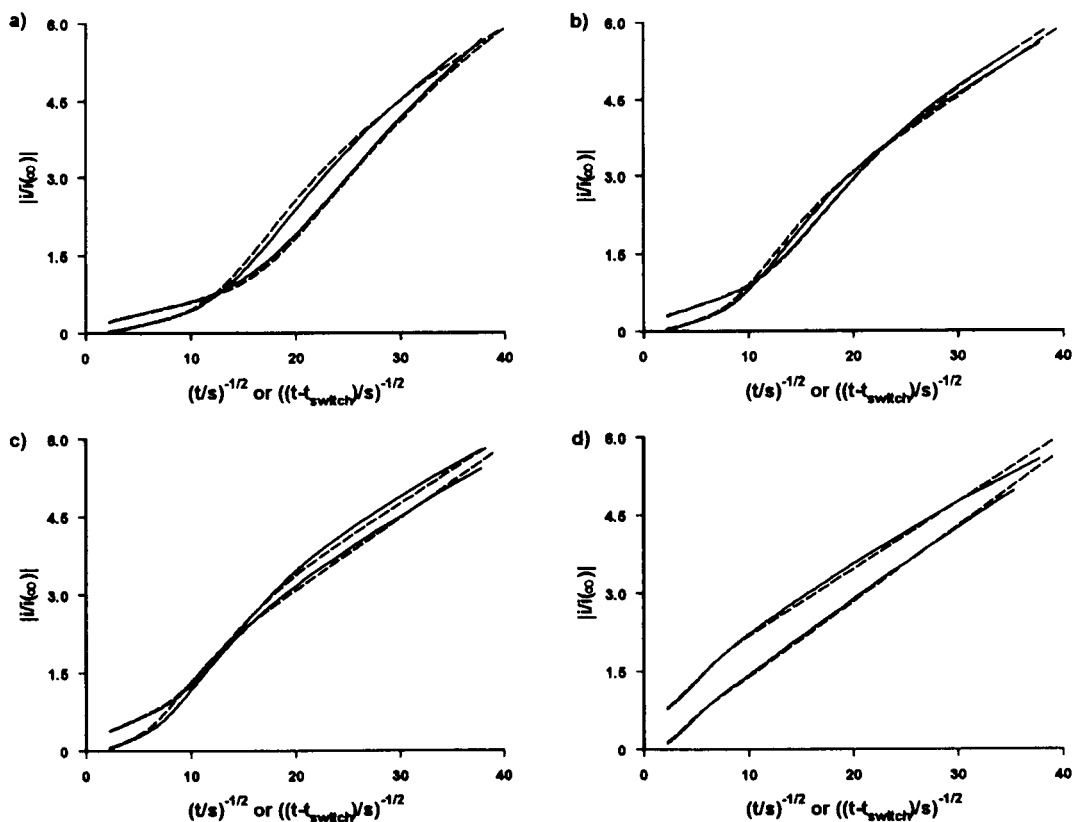
Figure 5.16 Typical DSPC data (solid lines, t_{switch} = 200 ms) for the oxidation of bromide (forward step) and reduction of bromine (reverse step) at a UME in aqueous solution, positioned at distances of a) 2.8, b) 4.2, c) 5.6 and d) 7.0 μm from an aqueous/DCE interface. The forward and reverse step dashed lines are the theoretical responses for the defined tip/interface separation, with D_{Br^-} = 1.8 × 10^{-5} cm^2 s^{-1} and D_{Br_2} = 9.4 × 10^{-6} cm^2 s^{-1}, respectively. The reverse transients are simulated for transfer rate constants, k_1, with the values marked on the plot.

Figure 5.17 Typical DPSC data (t_{switch} = 10 ms) for the oxidation of bromide (forward step; upper solid curve) and reduction of bromine (reverse step; lower solid curve) at a tip in aqueous solution, positioned at a distance of 2.8 μm from an aqueous/DCE interface. The upper dashed line is the theoretical response for the forward step at the defined tip/interface separation, with D_{Br^-} = 1.8 × 10^{-5} cm^2 s^{-1}. The remaining dashed lines are the reverse transients for various transfer rate constants, k_1, with the values marked on the plot. A value of D_{Br_2} = 9.4 × 10^{-6} cm^2 s^{-1} was used for the simulation.

of Br_2 from DCE to the aqueous phase due to the extensive depletion of Br_2 in the aqueous phase during the collection process. Nonetheless, the transfer of Br_2 from the aqueous phase to DCE, under the conditions of these experiments, tends towards irreversibility, and is effectively rate-limited by diffusion of Br_2 in the aqueous phase. Based on the data in Figure 5.17, the rate constant for the transfer of Br_2 from the aqueous to the DCE phase, under conditions where DCE acts as an empty sink, must be in excess of 0.5 cm s^{-1}, the upper limit of this technique.

5.4.2.3.2 DPSC Characteristics at an Active Aqueous/Air Interface

The volatility of Br_2 in aqueous solutions in contact with air, under open system conditions, makes the process described above - in which bromine is electrogenerated close to an interface - an ideal one to investigate the use of SECM DPSC as a probe of dynamic processes at liquid/gas interfaces. Experiments were carried out using an identical protocol to that described in the preceding section, with an inverted submarine UME positioned at distances of 2.5 to 9.1 μm from an aqueous/air interface. All experimental data for switching times of 10 ms and longer were found to agree well with the theoretical predictions for the irreversible diffusion-controlled loss of Br_2 at the aqueous/air interface, using the diffusion coefficients defined above.

Typical results for t_{switch} = 200 ms at a range of distances are shown in Figure 5.18 and are similar to the results obtained under conditions of transfer to DCE. A typical result for the shortest time step examined (t_{switch} = 10 ms), at a tip/interface separation of 2.5 μm, is shown in Figure 5.19. The data have been plotted as $|i \,/\, i(\infty)|$ vs. $t^{1/2}$ (forward step) or $(t-t_{switch})^{-1/2}$ (reverse step). The reverse transient in Figure 5.19 lies slightly above the theory for a diffusion-controlled
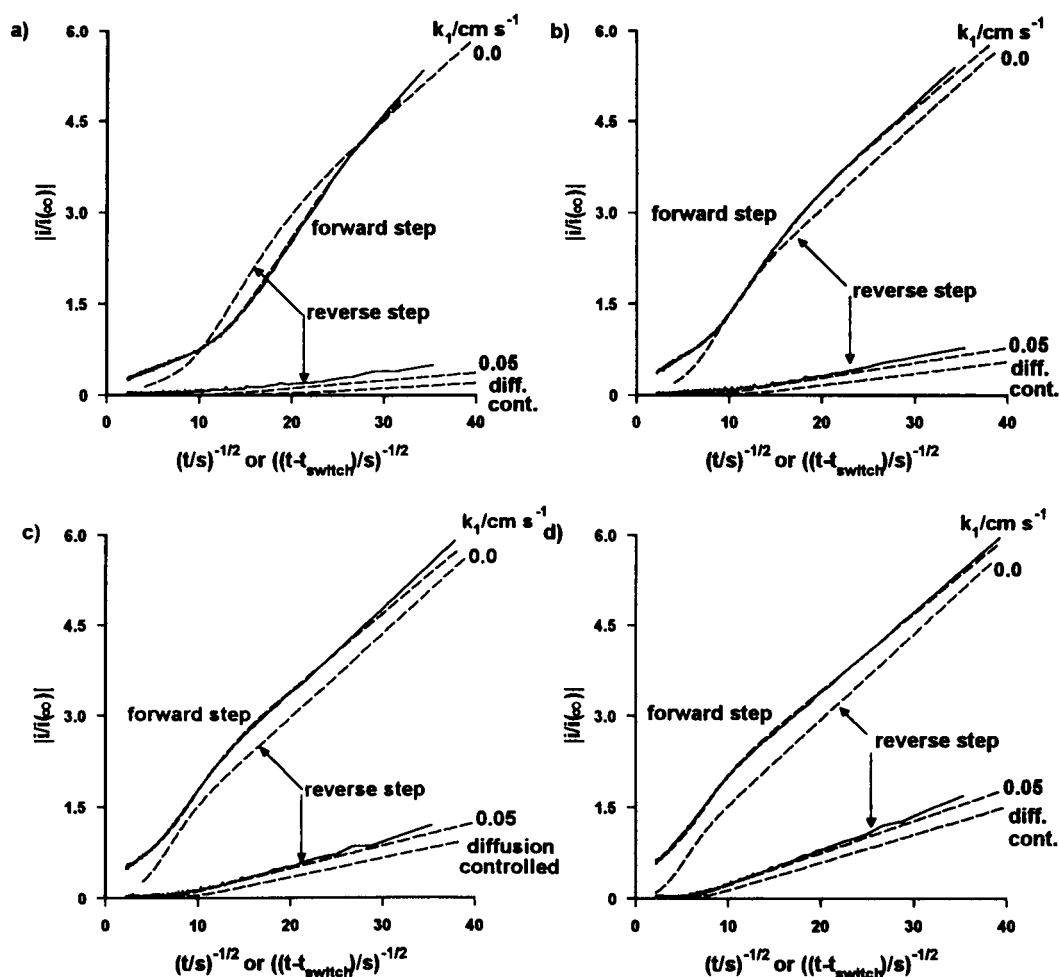
137
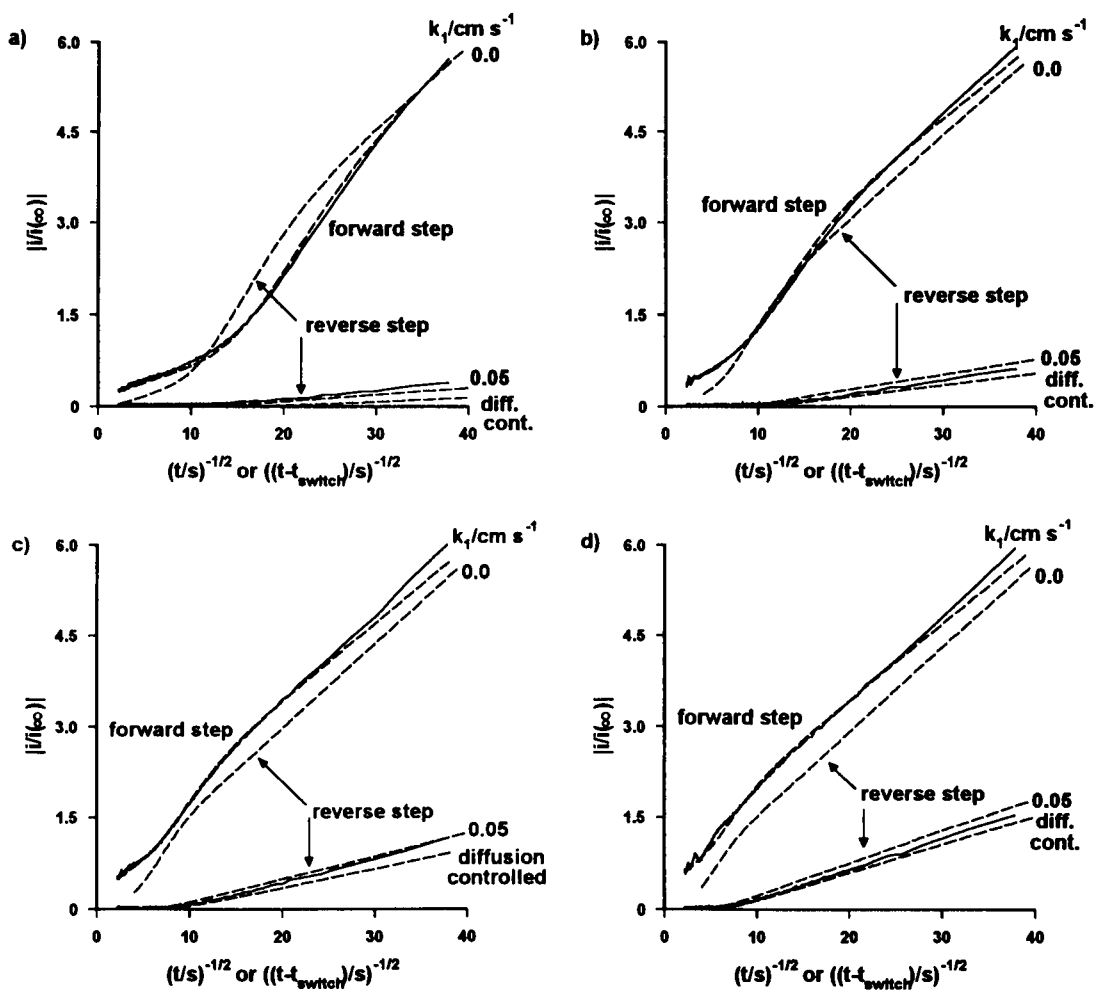
Figure 5.18 Typical DSPC data (solid lines, t_{switch} = 200 ms) for the oxidation of bromide (forward step) and reduction of bromine (reverse step) at a submarine UME in aqueous solution, positioned at distances of a) 2.5, b) 4.2, c) 5.6 and d) 7.0 μm from an aqueous/air interface. The forward and reverse step dashed lines are the theoretical responses for the defined tip/interface separation, with D_{Br^-} = 1.8 × 10^{-5} cm^2 s^{-1} and D_{Br_2} = 9.4 × 10^{-6} cm^2 s^{-1}, respectively. The reverse transients are simulated for transfer rate constants, k_1, with the values marked on the plot.
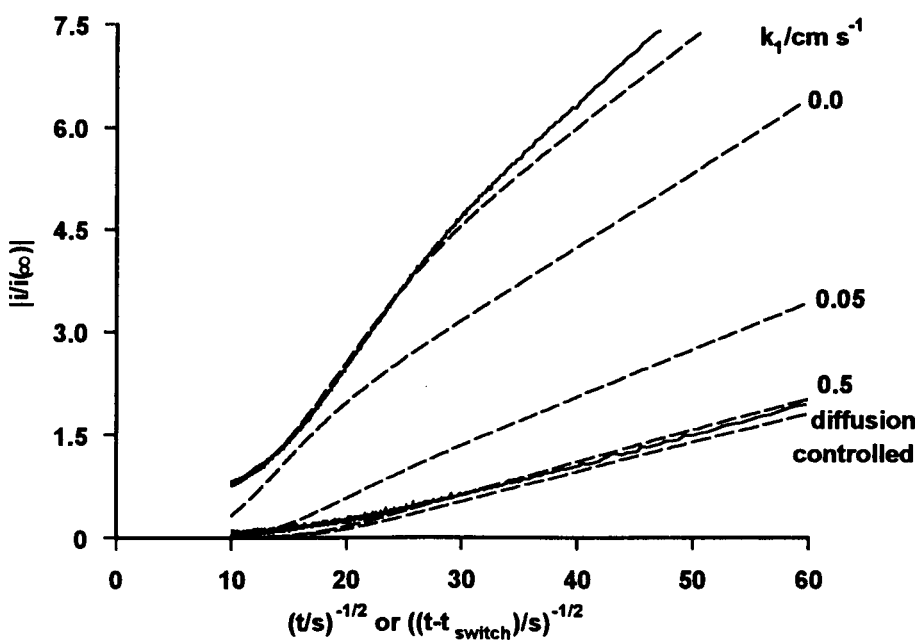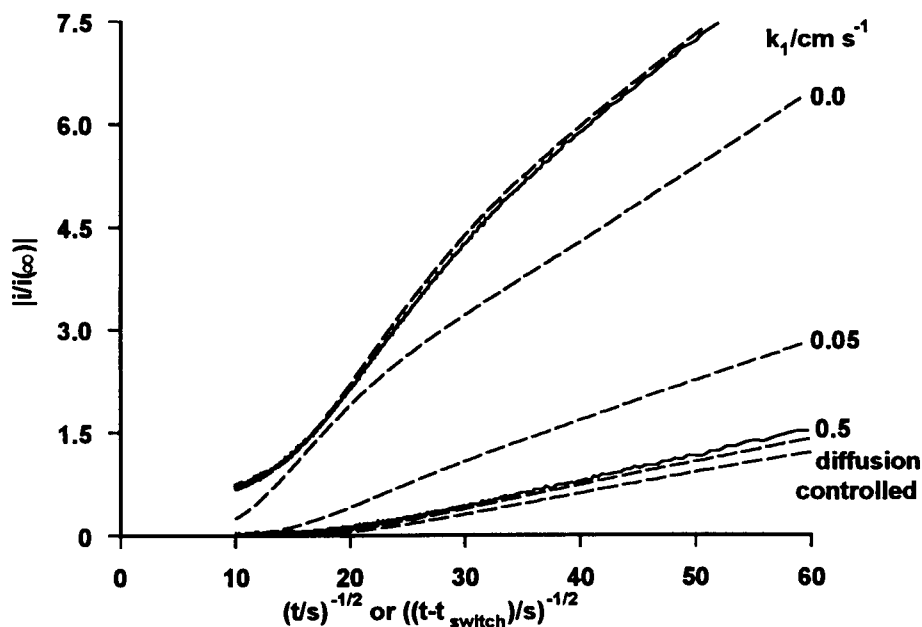
Figure 5.19 Typical DPSC data (t_{switch} = 10 ms) for the oxidation of bromide (forward step; upper solid curve) and reduction of bromine (reverse step; lower solid curve) at a submarine UME in aqueous solution, positioned at a distance of 2.5 μm from an aqueous/air interface. The upper dashed line is the theoretical response for the forward step at the defined tip/interface separation, with D_{Br^-} = 1.8×10^{-5} cm^2 s^{-1}. The remaining dashed lines are the reverse transients for various transfer rate constants, k_1, with the values marked on the plot. A value of D_{Br_2} = 9.4×10^{-6} cm^2 s^{-1} was used for the simulation.

process (particularly at short times), which might indicate very slight interfacial control of the transfer process. However, it was not possible to go to sufficiently shorter times or closer tip/interface separations to determine whether there was a measurable interfacial resistance to the transfer process. From the data in Figure 5.19, it may therefore be deduced that the transfer of Br_2 from aqueous solution to air is a rapid process, which approaches a limiting rate controlled by diffusion of Br_2 in solution. As in the DCE study (Section 5.4.2.3.1) a lower limit of 0.5 cm s^{-1} may be assigned to the rate constant defining the interfacial transfer process.

Notice that, in contrast to the reverse transient data for Br_2 transfer from aqueous solution to DCE (Figure 5.17), the reverse currents at longer times ($t^{1/2}$ < 20 $s^{-1/2}$) in Figure 5.19 are closer to the diffusion-controlled theoretical case for an irreversible transfer process. This suggests that electrochemically-induced back transfer of Br_2 from air to aqueous solution, during the collection process, is a negligible process. In part, this may be attributed to the much higher transport rate of Br_2 in air compared to DCE, i.e., once Br_2 crosses the interface it is rapidly transported away and is thus not available for back transfer during the collection step.

5.5 Conclusions

SECM DPSC has been shown to be a potentially powerful technique for investigating the chemical kinetics of reactions of tip-generated species at liquid/solid, liquid/liquid and liquid/air interfaces. The technique complements earlier equilibrium perturbation transient SECM methods, by allowing the study of irreversible interfacial chemical processes for the first time. The DPSC mode has been verified experimentally with the model ferrocyanide/ferricyanide system, and

used to show that the absorption of Br_2 by both air and DCE from aqueous solutions is controlled by diffusion of Br_2 in the aqueous phase, with interfacial processes providing no detectable kinetic resistance to transfer, over the range of mass transfer rates attainable from SECM.

There should be considerable scope for further developing the SECM DPSC mode. For example, reversible interfacial processes of tip-generated species could also be measured and modelled using the DPSC mode. In addition to generating reactants from solution precursor species, as in the studies described in this chapter, it should be possible to locally inject several types of metal ions, e.g. Cu^{2+}, Ag^+, Zn^{2+}, Pb^{2+}, Cd^{2+}, etc., into the gap between the probe and the interface through the anodic dissolution of metal or mercury-amalgam UMEs. This approach may be used as a means of studying the adsorption and absorption of metal ions at solid/liquid and immiscible liquid/liquid interfaces.

CHAPTER 6

MICROELECTROCHEMICAL MEASUREMENTS AT EXPANDING DROPLETS (MEMED): A NEW TECHNIQUE FOR PROBING REACTION KINETICS AT LIQUID/LIQUID INTERFACES

This chapter describes the development and characterisation of a new technique, based on UMEs, for studying reactions that occur at the interface between two immiscible liquids. The particular importance of the technique is in its application to the study of reactions that occur spontaneously on contact between the two liquids. As discussed in Chapter 1, this class of reactions is difficult to study with conventional approaches. In the proposed technique, the two liquids are brought into contact by flowing one (the feeder phase) through a capillary submerged in the second (the receptor phase), resulting in the growth of drops at the capillary tip. The reaction that occurs at the interface generates a concentration profile at the drop surface, due to the depletion of a reactant or the generation of a product in the receptor phase. This concentration profile is probed directly, at short times following the contact, using a UME positioned opposite the capillary in the solution. The UME, which may be operated in either a potentiometric or an amperometric mode, functions as a local concentration probe that intercepts the interfacial concentration profile as the drop grows, and measures it directly. A numerical model for mass transport in this configuration – termed microelectrochemical measurements at expanding droplets (MEMED) – is developed. The technique and model are analysed using the following processes: bromine transfer from aqueous sulfuric acid solutions to drops of DCE and bimolecular electron transfer between iridium (IV) chloride in the aqueous

solution and ferrocene in the organic phase, which exhibit transport-controlled transfer rates under the conditions employed.

A second contacting mode, based on making UME measurements at a free jet of one liquid in a second immiscible liquid is discussed briefly.

6.1 Introduction

The techniques described in Chapters 3 to 5 rely on the use of a probe UME to induce and monitor the reaction of interest. There are, however, a wide range of reactions that cannot be induced electrochemically, but which occur spontaneously when two immiscible liquid phases contact. Existing approaches for studying this class of reaction were described in detail in Chapter 1, and the drawbacks of each approach were highlighted.

The criteria required for an experimental investigation of reactions which occur at liquid/liquid interfaces are as follows: known interfacial area and well-defined interfacial contact are essential; controlled, variable and calculable mass transport rates are required to allow the mass transfer and interfacial kinetic contributions to the overall rate to be quantified; direct interfacial contact, rather than the support of the interface in a porous membrane is preferred; a renewable interface is useful in the study of this type of reaction as the accumulation of products at the interface is possible; ideally measurements must be made at the shortest times following contact; it is also clear from the success of the SECM studies discussed in Chapters 3 to 5 that direct measurements at the interface of interest are desirable. The new approach described here for studying this important range of reactions, MEMED, operates with all of the criteria described above.

143

The development of the MEMED technique also includes the introduction of a different type of amperometric UME probe to those used in Chapters 3 to 5. The electrode is of nanometre characteristic dimensions and has thus been termed a "nanode".[185] These electrodes are typically constructed from wires, which have been etched to form a sharp tip, and then coated with an insulating material, except at the apex of the tip, to provide a very tiny exposed electrode area. This kind of approach has been employed in development of tips for scanning tunnelling microscopy in solution,[186,187] for which the area of exposed metal must be minimised in order to reduce the Faradaic current, which is considerably larger than the tunnelling current if a bare tip is used. Other construction techniques have been successfully employed in the fabrication of nanodes, such as the use of a pipette puller to produce glass-coated nanometre sized electrodes.[188]

The advantages of using UMEs, in terms of enhanced mass transport, reduced iR_s drop and reduced double layer charging effects were described in Chapter 1. The small dimensions offered by nanodes result in a further extension of these advantages. In particular, these probes have been employed to study rapid electron transfer kinetics,[185] for high resolution SECM imaging,[189] and in small scale etching.[185] The reduced electrode dimensions have also allowed measurements to be made in microenvironments such as single cells.[185,190,191,192] These probes have not thus far been employed as amperometric detector electrodes in hydrodynamic systems, as in this current study, but they have received limited attention for making chemical measurements within diffusion layers.[128] The results of different methods of manufacture and the response of these electrodes is investigated later in this chapter.

6.2 The MEMED Approach

In the proposed technique, liquid/liquid contact is established by forming drops of one liquid from a capillary submerged in a second immiscible liquid. The feeder solution, typically comprising an organic solvent, flows into the aqueous receptor solution at a constant rate, such that drops form, grow and detach periodically in a well-defined manner. This approach is similar to the dropping mercury electrode[50] and electrolyte dropping electrode[39,49,51,52,53,54] and conveys the same advantage in terms of providing a constantly renewable, clean interface.

With MEMED the interfacial reaction is monitored with a stationary UME, positioned directly beneath or above (depending on the relative densities of the two liquids) the drop. The electrode operates in either an amperometric or potentiometric mode, to probe local changes in concentration in the receptor phase at the probe tip, as the drop approaches the electrode. The probe penetrates, and measures directly the developing concentration profile adjacent to the drop surface in the receptor phase due to the two-phase reaction. By solving the convective-diffusion problem specific to this particular configuration, with appropriate boundary conditions, theoretical concentration profiles can be generated for comparison with experiment. In this way, the nature of mass transport and the interfacial reaction can be investigated.

A schematic diagram of the set-up for measurements at an expanding drop comprising a liquid which was more dense than the receptor phase was given in Figure 2.4. The tip of the capillary is positioned directly above the electrochemical probe at the required distance using the three-axis positioners, with the aid of video microscopy. The diameter of the drop at the contact point may be controlled by initially setting the desired distance between electrode and capillary.

The drop time, from the beginning of growth to the contact time is dictated by this distance and the flow rate, which is controlled using either gravity feed from a reservoir, or via a syringe pump which drives the feeder solution flow. Typical values for the drop time and drop diameter at contact are 1 - 20 s and 1 mm respectively. The video camera enables the measurement of the electrode-capillary separation as well as observation of the motion and shape of the droplet. Continued reaction in the base of the cell due to the collection of drops was not a problem as the measurements are made directly at the drop surface. Any background build up or depletion could be accounted for in the simulation, and if it became too great it was simple and quick to replace the receptor phase.

The key strength of the technique is that the electrode measures directly the concentration profile of a target species involved in the reaction, i.e. the distribution of a product or reactant, on the receptor phase side. The shape of this concentration profile will be extremely sensitive to the mass transport characteristics of the growing drop, and to the mechanism and kinetics of the interfacial chemical reaction.

This chapter also briefly describes experiments conducted to find the effect of changing the position of the probe relative to the position of the drop. In particular, using the MEMED technique it is possible to measure, and simulate, the concentration profile at the side of a drop during growth.

6.3 Theory

As described in Chapter 1, in order to extract useful interfacial kinetic and mechanistic information, the mass transfer and interfacial reaction steps must be separated. A complete theoretical treatment of the proposed technique requires

comparison of the experimental data with simulated concentration profiles that take into account the transport and chemical reaction steps. Therefore, calculation of the mass transfer step must be possible for this hydrodynamic technique.

Mass transfer in this arrangement has been considered previously for the dropping mercury electrode[193,194,195] arrangement and other growing liquid drop techniques.[32,196] Convective-diffusion to a growing drop may be described by the following equation:

$$\frac{\partial c_i}{\partial t} = D_i \left(\frac{\partial^2 c_i}{\partial r^2} + \frac{2}{r} \frac{\partial c_i}{\partial r} \right) - v_r \frac{\partial c_i}{\partial r} \quad (6.1)$$

In equation 6.1, D_i and c_i are the diffusion coefficient and concentration of the species, i, of interest in the receptor phase, respectively and r is the spherical co-ordinate starting at the centre of the drop. The variable v_r represents the convective velocity in the receptor solution due to the moving surface of the expanding drop, and is given at each point, r, by:

$$v_r = \frac{q}{4\pi} \left(\frac{1}{r^2} - \frac{1}{r_0^2} \right) \quad (6.2)$$

where q is the volume flow rate, and r_0 is the (time-dependent) drop radius.

Equation 6.2 assumes that the drop behaves as a symmetrically expanding sphere, i.e. the drop expands from a fixed centre. Whilst this is not the case for a droplet growing from a capillary, since the centre of the drop moves, it will be shown to be a reasonable approximation to the real system at the slow volume

147

flow rates employed. The presence of the capillary is ignored in the simulation since it has a much smaller diameter than that of the drop for most of its lifetime. Moreover, the capillary is not expected to influence measurements that are made at the opposite side of the drop given the timescale (several seconds) of the measurements.

Depletion or accumulation inside the drop was not treated for two reasons. First, the probe was generally positioned close to the portion of the drop where the surface was constantly renewed. Internal streamlines in a drop expanding from a capillary have been investigated,[197,198] and tend to conform to the schematic indicated in Figure 6.1. It is suggested that fresh material may be carried from the capillary to the front face of the drop, directly opposite the capillary. Second, for the systems chosen for study, depletion and accumulation inside the droplet were not important for the measured rates and concentrations.
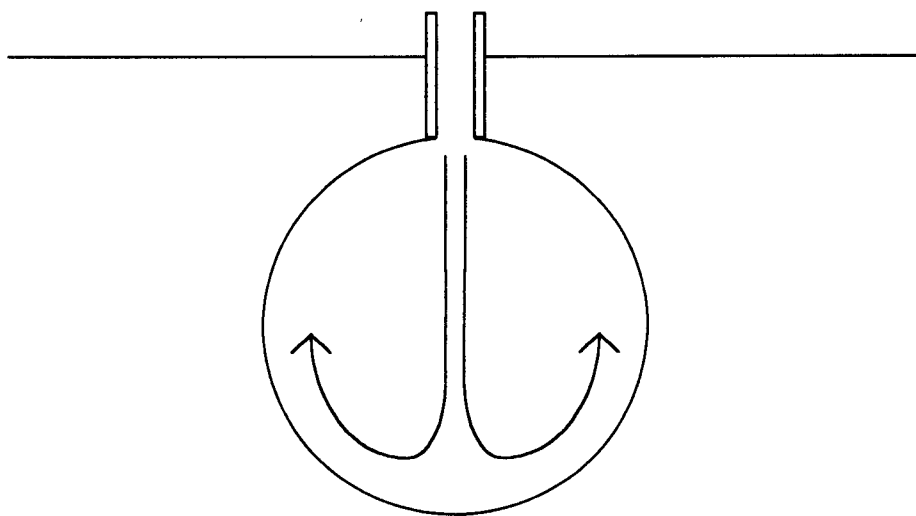
Figure 6.1   Internal streamlines in a drop expanding from a capillary tip into a second immiscible fluid phase.

The mass-transport equations were normalised using the following terms:[194]

$$R = \frac{r}{\sqrt{D_i t_d}} \quad (6.3)$$

$$\tau = \frac{t}{t_d} \quad (6.4)$$

$$C_i = \frac{c_i}{c_i^*} \quad (6.5)$$

$$V_r = v_r \sqrt{\frac{t_d}{D_i}} \quad (6.6)$$

where c_i^*, which is used to calculate the normalised concentration for the species i, is normally the initial or bulk concentration of that species in the receptor phase, but may be the concentration at the surface of the drop (for processes involving transport-limited transfer from the drop to the receptor phase). The variable, t_d, is the total drop time from the beginning of growth to the point at which the surface of the droplet makes contact with the electrode. The resulting normalised mass transport equation:

$$\frac{\partial C_i}{\partial \tau} = \frac{\partial^2 C_i}{\partial R^2} + \frac{2}{R}\frac{\partial C_i}{\partial R} - V_r \frac{\partial C_i}{\partial R} \quad (6.7)$$

was solved numerically, using the simple explicit method,[194] in normalised time with suitable boundary conditions at the drop surface, $r = r_0$, and at a semi-infinite distance from the drop, appropriate to the problem of interest. Figure 6.2 shows

the co-ordinates of the model schematically. A uniform grid was employed, with one boundary of the simulation fixed at the drop surface, while the other was situated at a distance, in the radial direction, sufficiently far from the moving drop surface such that concentrations were not influenced by the concentration gradient at the interface. A value equal to the magnitude of the final drop radius, r_f, was found to be adequate in all cases. Within the simulation, the number of points in the r direction, nr, was 1000, resulting in a step size, Δr, of $r_f / 1000$. This corresponds to a value for Δr of 0.5 μm, for a typical drop radius of 0.5 mm. If normalised values are used then for typical values of $D_i = 5 \times 10^{-6}$ cm^2 s^{-1} and $t_d = 5$ s, $\Delta R = 0.01$, and R is in the range, $0 \le R \le 10$.

The above-defined parameters were found to be adequate to obtain converged concentration distributions, confirmed by the fact that employing either half the number of points, or a domain twice as large gave identical solutions for the cases considered. The time step, $\Delta \tau$, employed was chosen such that the requirement for a stable simulation, $\Delta \tau / \Delta R^2 \le 0.5$,[194] was obeyed. The time step was calculated from, $\Delta \tau = \Delta R^2 \times 0.3$, and was of the order of 3×10^{-5}, which corresponds typically to a time step size of 0.15 ms. This model enabled the simulation of the concentration vs. radial distance profile as it developed with time, from which the time-dependent concentration vs. distance profile, observed at the probe, could be extracted. A typical program that enabled the solution of this problem (dropk.f) can be found in Appendix 3.
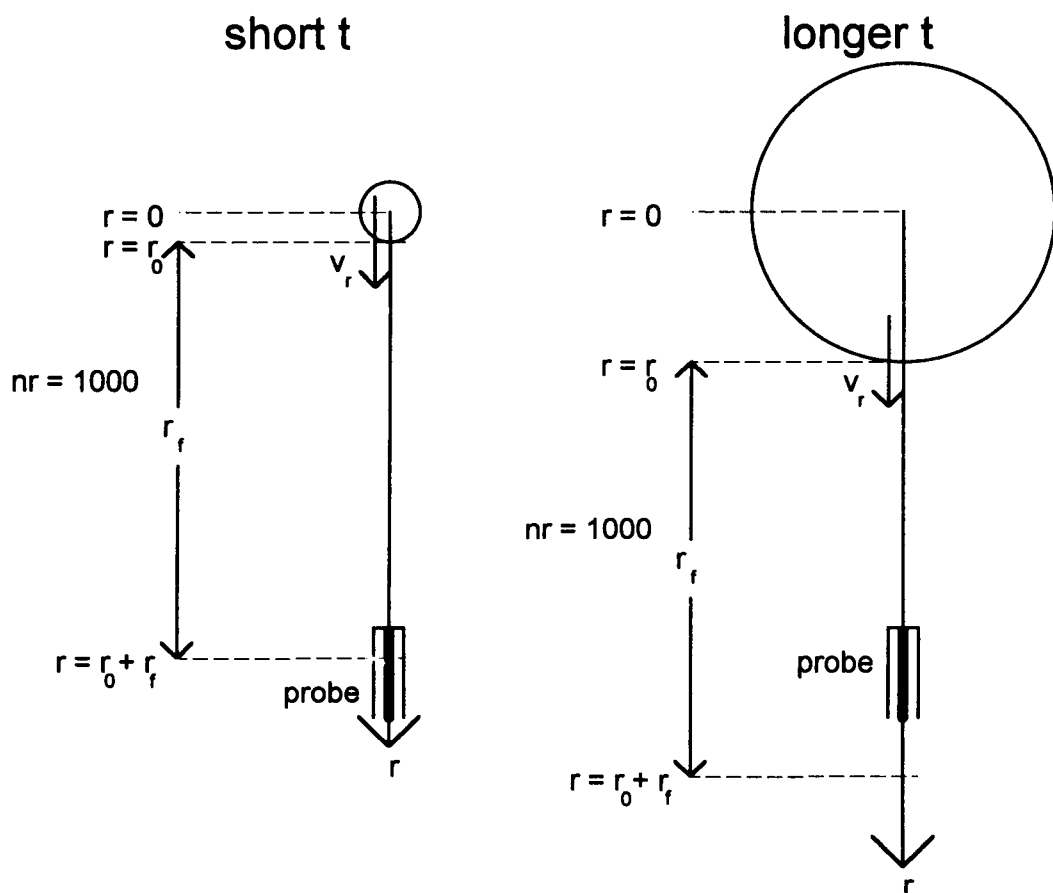
Figure 6.2   Schematic diagram illustrating the co-ordinates of the MEMED simulation.

6.4 Characterisation of the Probe UME Responses

There are two possible modes of operation for the detector electrode; amperometric or potentiometric. The potentiometric response of the electrode in this arrangement is essentially dependent on the concentrations of the potential determining species in solution, as indicated by the Nernst equation (equation 6.9), shown here for a general redox process:

$$\sum x_i O_i + ne^- \rightarrow \sum y_i R_i \qquad (6.8)$$
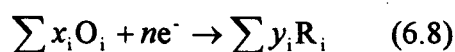
$$E = E^0 + \frac{R_g T}{nF} \ln \frac{\prod a_{O_i}^{x_i}}{\prod a_{R_i}^{y_i}} \qquad (6.9)$$

where x_i and y_i values represent the stoichiometric values for the oxidised, O_i, and reduced, R_i, forms of the redox species, i, involved in the reaction, E^0 is the standard electrode potential, R_g is the molar gas constant and T is the temperature.

The amperometric response of an electrode, in contrast, depends on the flux of the target species at the electrode as indicated by equation 6.10.

$$i = n_e F A_e j_i \qquad (6.10)$$

where A_e is the electrode area and j_i is the flux of species i at the electrode surface. Equation 1.10, which related the current at a UME to the diffusion coefficient and concentration of the mediator, assumed the flux of material was by hemispherical diffusion only, and was under steady-state conditions. Additional possible transport modes for the species of interest, specifically convection and migration, were negligible in all of the systems described thus far. In the MEMED configuration, however, the moving droplet may perturb the flux of the mediator to the electrode in two ways. First, the moving surface of the drop may prevent diffusion to the UME from achieving steady-state. The time taken for a diffusion layer to achieve steady-state may be given by:[21]

$$t_{ss} = \frac{\delta_D^2}{D} \qquad (6.11)$$

where δ_D is the size of the diffusion layer. It is important to note that the mean diffusion layer thickness for a disc-shaped UME, δ_{UME}, is of similar dimensions to the electrode radius, as indicated by equation 6.12.

$$\delta_{UME} = \pi a/4 \quad (6.12)$$

Second, the moving drop surface may generate convective currents in the solution adjacent to the electrode, which may add to the flux of material by diffusion, thus increasing the observed current. Furthermore, amperometric measurements may cause depletion of the measured species, due to electrolysis at the electrode. The effect would be to distort the concentration boundary layer adjacent to the droplet, and indeed alter the course of the interfacial reaction itself. Care must therefore be taken over the conditions employed. As potentiometry is a passive measuring method it is not subject to these problems.

For the case of an amperometric probe, it was first necessary to investigate the effect on the current response of the moving drop surface adjacent to the electrode. The simplest scenario is that perturbations to the diffusion field, and convective effects due to the drop motion are negligible, so that local mass transport to the UME is by steady-state diffusion only, in which case equation 1.10 would provide a route to local concentrations. In order to achieve this desired response, a small electrode, for which the diffusional relaxation time is fast compared to the rate of approach of the drop surface, and for which diffusion is rapid compared to convection, is mandatory.

To test this premise, the transport-limited current for the oxidation of aqueous ferrocyanide was measured as a function of drop-electrode separation for growing drops of DCE in aqueous solutions of ferrocyanide, with the UME positioned beneath the drop. The aqueous solution contained 1×10^{-2} mol dm^{-3} potassium ferrocyanide, with 0.5 mol dm^{-3} potassium chloride as the supporting electrolyte. The probe electrode was biased at a potential of 0.7 V vs. AgQRE to effect the transport-limited oxidation of ferrocyanide to ferricyanide. This type of experiment is similar to the SECM approach curve measurements, with an inert interface, described previously in Chapters 3 and 4, however in this case, instead of scanning the electrode towards the interface, the interface is mobile while the electrode remains stationary.

Figure 6.3 illustrates the two expected limiting regimes, namely hemispherical and hindered diffusion, which the electrode should display under steady-state conditions.[105] The transport-limited current responses of a 25 μm diameter Pt disc UME and a 2 μm diameter Pt disc UME are shown in Figure 6.4. The current data have been normalised with respect to the steady-state limiting current in bulk quiescent solution, while the electrode-interface separation, d, may be calculated as a function of time for a symmetrically expanding droplet from:

$$d = d_f \left(1 - \left(\frac{t}{t_d} \right)^{1/3} \right) \quad (6.13)$$
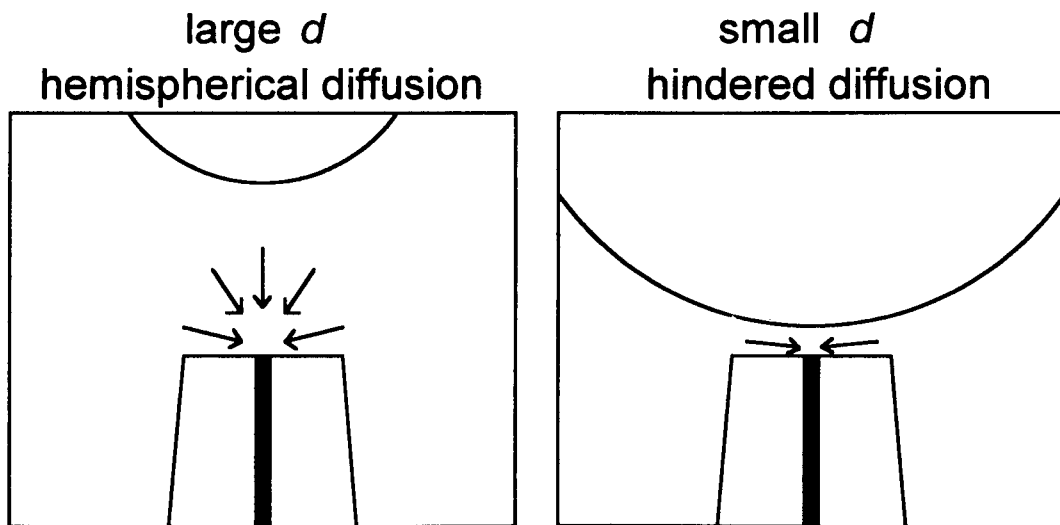
Figure 6.3 Hemispherical and hindered diffusion regimes expected for different drop-electrode separations, d, under conditions where the amperometric electrode responds under steady-state conditions.
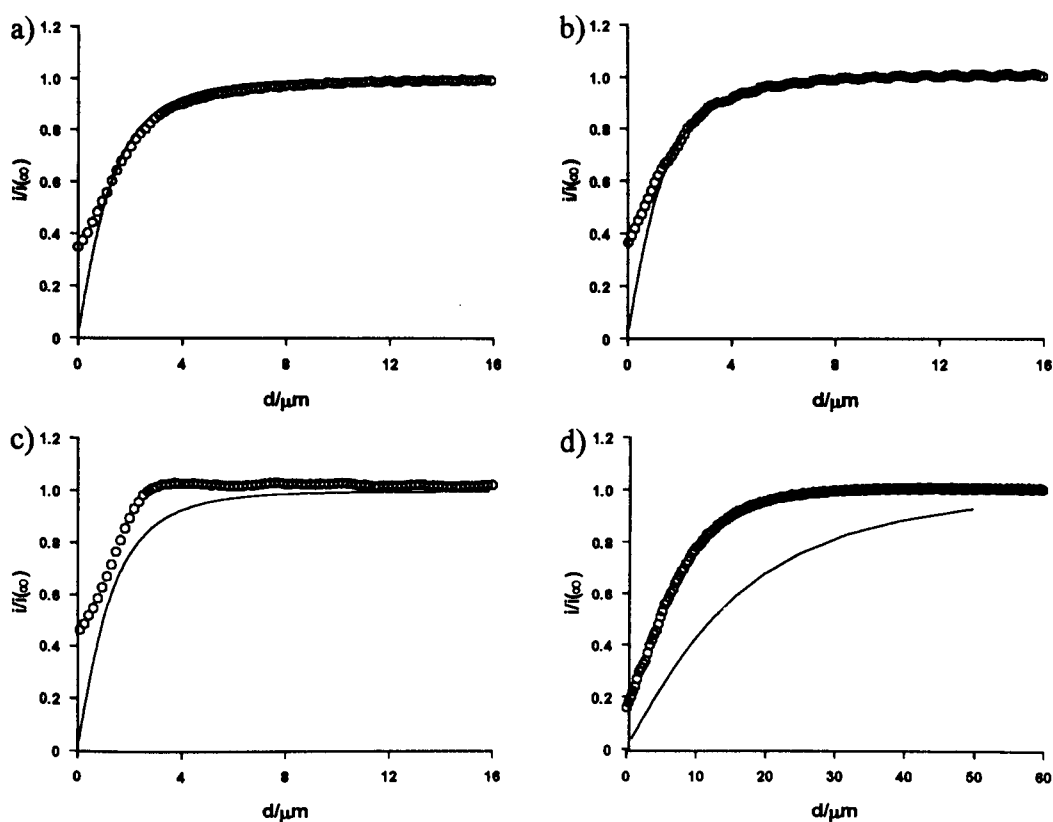
Figure 6.4 Normalised current vs. electrode-drop distance plots for ferrocyanide oxidation at a) – c) a 2 μm, and d) a 25 μm diameter UME mounted beneath a growing droplet of DCE. The drop times were a) 14.0 s, b) 10.5 s, c) 3.8 s and d) 14 s. The solid lines indicate the predicted distance dependence for steady-state diffusion-only conditions outlined in section 1.4.2.

where d_f is the final droplet diameter at the contact point, $t = t_d$. The validity of this equation was verified by examining video recordings of drop position vs. time for a range of expanding droplets.

In this experiment, the current depends only on the transport of ferrocyanide to the probe electrode, there is no chemical reaction at the drop surface, so that any deviation in the current-distance response from that expected for approach to an inert interface, under steady-state diffusion conditions, may be ascribed to perturbations to mass-transport, caused by the approaching drop. The treatment of the steady-state diffusion case was described previously in Chapter 3, for a planar interface, which is expected to be a reasonable approximation for the present situation, given that the final diameter of the drop is millimetres, while the probe UMEs employed exhibit micrometre dimensions.

For a 2 μm diameter disc electrode at long drop times (Figure 6.4(a) and (b)), the experimentally determined curve closely matches the steady-state diffusion only response for a UME approaching an inert (planar) interface, indicating that convection is negligible, and a steady-state diffusion layer is maintained, even at close separations between the surface of the drop and the electrode. Even when higher flow rates and more rapidly moving drops are employed (Figure 6.4(c)), deviations are small, and it is concluded that under most conditions, for $d > 5$ μm, the current is close to $i(\infty)$ and may be used to determine the concentration using equation 1.10. At closer distances, hindered diffusion plays a greater role. It is noted that only in Figure 6.4(c) is a small increase above the bulk current observed, which must be attributed to an effect of convection which becomes more important at short drop times. In contrast to the behaviour observed with a 2 μm diameter UME, with a 25 μm diameter electrode,

the response is modified even at slow flow rates. This is likely to be due to a time-response effect due to the relatively long diffusional relaxation times observed as the electrode size increases (equations 6.11 and 6.12), and may also contain a convective contribution. For distances up to 50 μm from the drop the response of the UME is clearly higher than predicted for steady-state diffusion. It is clear then that only very small, $a \le 1$ μm, electrodes may be used for amperometric measurements.

Part of the difference in response of the two electrodes can be understood when the rates of mass transport by diffusion and the effect of convection are evaluated. The velocity of the approaching surface can be calculated from the volume flow rate and drop diameter and gives some indication of the expected magnitude of the effects of diffusional relaxation and convection. The velocity, v, of the moving base of the drop, based on a simple expanding sphere, is given, for the time at which the drop contacts the electrode, by the following equation:

$$v = \frac{r_f}{3t_d} \qquad (6.14)$$

For a typical drop time, t_d of 5 s and a final drop radius, r_f, of 0.5 mm, the approaching velocity of the drop surface at contact approaches 34 μm s^{-1}. The rate of mass transport by steady-state diffusion can be calculated using equation 6.15, which is derived from equations 1.10 and 6.10, where in equation 6.10, the flux, $j_i = k_t c^*$.

$$k_t = \frac{4D}{\pi a} \qquad (6.15)$$

For a typical diffusion coefficient of 1×10^{-5} cm^2 s^{-1}, a 25 μm diameter UME

displays a k_t value of 100 μm s^{-1}, while at a 2 μm UME, k_t = 1270 μm s^{-1}. In

addition, the diffusional relaxation times may be evaluated from equations 6.11

and 6.12, resulting in t_{ss} = 9.6 $\times$ 10^{-2} s for a 25 μm diameter UME, and t_{ss} = 6.2 $\times$

10^{-4} s for a 2 μm diameter UME. These values clearly indicate why significant

deviation from steady-state diffusional behaviour, and also convective effects, due

to a solution velocity in the region of 30 μm s^{-1} are observed at the larger

electrode and not at the smaller one. In addition, where SECM hindered diffusion

dominates at close distances, the diffusion lengths and relaxation times increase,

leading to greater deviation from steady-state behaviour. The diffusion layer at the

smaller electrode can respond rapidly (on the MEMED timescale) to the changes

imposed upon it, and since small electrodes display such high steady-state

diffusion rates in quiescent solution, the introduction of convection due to the

moving drop surface, at the drop times of interest, contributes little significant

extra flux of material to the electrode surface.

A further advantage of using particularly small electrodes is that depletion

effects are much smaller, there is expected to be very little perturbation to the

concentration profile adjacent to the droplet, which will be demonstrated to be

approximately two orders of magnitude greater than the steady-state diffusion

layer thickness at the probe, calculated from equation 6.12. This assumption will

be tested experimentally in the next section. Furthermore, the effective volume of

solution sampled is small for a small electrode, which results in an enhanced

distance resolution for the probe. As predicted by the above equations, and evidenced by the experiments, response times at small amperometric electrodes are also considerably better than at larger electrodes.

These measurements demonstrate the ability to use both amperometric and passive potentiometric detection modes with MEMED, allowing a wide range of species to be measured, and making the possible areas for application of the technique widespread.

6.5 Characterisation of Mass Transport to the Expanding Drop

In order to determine the nature of convective-diffusion in the MEMED experimental arrangement, interfacial transfer reactions were chosen that would proceed at a transport-controlled rate in this geometry. With no interfacial kinetic resistance, the response depends only on the transport step in the receptor phase (and feeder phase), and the mass transfer model proposed in section 6.3 can therefore be tested.

6.5.1 Transfer of Bromine at the Aqueous/DCE Interface

The transfer of bromine from aqueous sulfuric acid solutions to organic solvents, which was previously shown through the SECM measurements in Chapter 5 to be a rapid process, was investigated. This reaction was described previously in Chapter 5, and is illustrated schematically in the MEMED arrangement in Figure 6.5. A further advantage of this system was that the two detection methods, namely amperometric and potentiometric detection, could be tested.

159
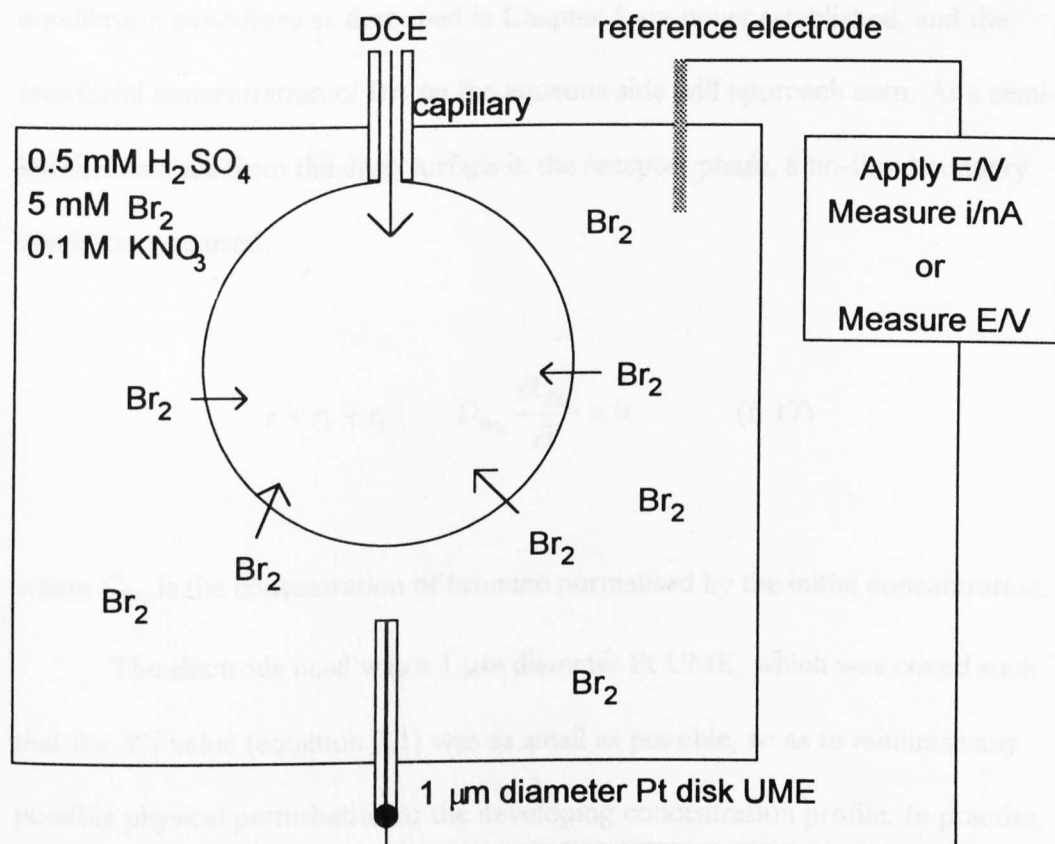
Figure 6.5   Schematic diagram illustrating the measurement of the transfer of bromine from water to a DCE drop using amperometric or potentiometric measurement of the concentration profile for bromine. In the case of potentiometric detection, the solution also contained 1×10^{-3} mol dm^{-3} KBr.

For the bromine transfer studies, the boundary condition reflecting mass transport-controlled depletion of bromine at the drop surface is as follows:

$$r = r_0: \qquad c_{Br_2} = 0 \qquad (6.16)$$

The partition coefficient for bromine in the aqueous/DCE system was calculated

in section 5.4.2.3.1, however, since the solution adjacent to the interface inside

the drop is constantly replenished by convection within the drop, then the

equilibrium conditions as described in Chapter 5 are never established, and the interfacial concentration of Br_2 on the aqueous side will approach zero. At a semi-infinite distance from the drop surface in the receptor phase, a no-flux boundary condition was used:

$$r = r_0 + r_f : \quad D_{Br_2} \frac{\partial c_{Br_2}}{\partial r} = 0 \qquad (6.17)$$

where C_{Br_2} is the concentration of bromine normalised by the initial concentration.

The electrode used was a 1 μm diameter Pt UME, which was coned such that the RG value (equation 2.1) was as small as possible, so as to minimise any possible physical perturbation to the developing concentration profile. In practise, with this sized electrode, $RG \approx 5$ was possible. For amperometric detection, the aqueous solution contained 5×10^{-3} mol dm^{-3} Br_2, 5×10^{-4} mol dm^{-3} H_2SO_4 and 0.1 mol dm^{-3} KNO_3. The electrode was biased to reduce bromine to bromide at a diffusion-controlled rate at the UME (0.7 V vs. AgQRE). The current in the bulk of solution gave $c_{Br_2}^*$ (via equation 1.10), and changes in the current when the probe was in the diffusion layer were related to corresponding changes in concentration.

In the case of potentiometric detection, the bromine concentration was determined by measuring the potential at the indicator electrode, E_{ind}/V, vs. SCE. The potentiometric UME was first calibrated to ensure the response was Nernstian, given the individual half-cell reactions:

$$\frac{1}{2}Br_2 + e^- \underset{\leftarrow}{\rightarrow} Br^- \qquad (6.18)$$

$$\frac{1}{2}Hg_2Cl_2 + e^- \underset{\leftarrow}{\rightarrow} Hg + Cl^- \qquad (6.19)$$
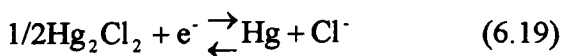
The measured potential, E_{ind}, for the one-electron process should vary according to:

$$E_{ind} = E_c + \frac{R_g T}{F} \ln \left(\frac{c_{Br_2}^{1/2}}{c_{Br^-}} \right) \qquad (6.20)$$

where E_c is a constant which can be determined from the electrode calibration plot. Figure 6.6 demonstrates that the response was Nernstian for Br_2 concentrations in the investigated range of 1×10^{-5} to 6×10^{-3} mol dm^{-3}, with Br^- at a concentration of 1×10^{-3} mol dm^{-3}. In addition to the concentrations of species outlined for amperometry, KBr was added at a concentration of 1×10^{-3} mol dm^{-3} when potentiometry was employed, in order to achieve a stable response of the redox electrode. During potentiometric MEMED experiments, the bromine concentrations in equation 6.20 were those determined locally at the UME, calculated from the electrode response using equation 6.21.

$$\Delta E / mV = E_{ind} - E_c = 59.1 \times \log \left(\frac{c_{Br_2}^{1/2}}{c_{Br^-}} \right) \qquad (6.21)$$
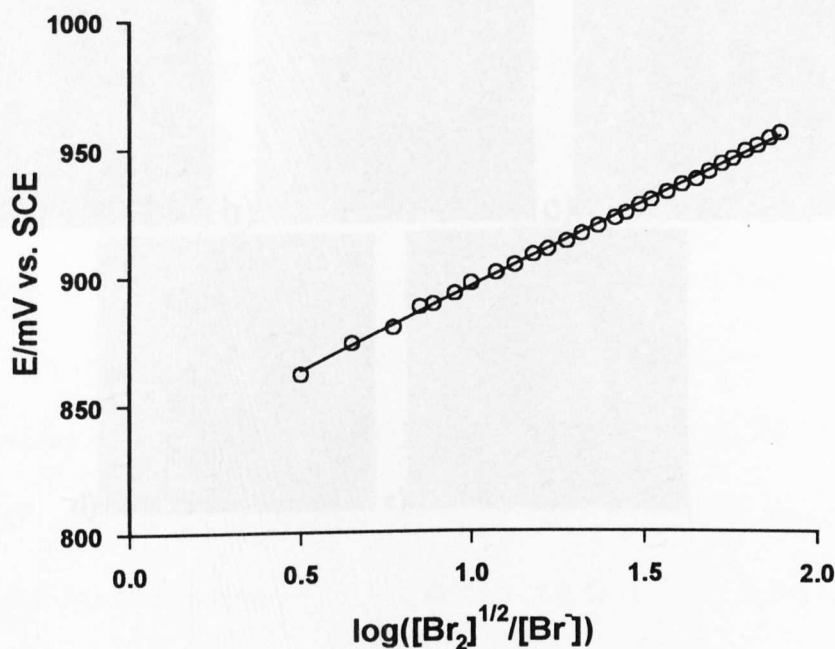
Figure 6.6 Calibration plot of the potentiometric response of a 1 μm diameter Pt UME to concentrations of Br_2. The measurement vessel initially contained 1×10^{-3} mol dm^{-3} Br$^-$, 5×10^{-4} mol dm^{-3} H_2SO_4 and 0.1 mol dm^{-3} KNO$_3$, to this was added a solution of bromine, resulting in the range of Br_2 concentrations 1×10^{-5} to 6×10^{-3} mol dm^{-3}.

6.5.1.1 Amperometric Measurements

Experimental results (raw data) for bromine transfer studied by amperometry are shown in Figure 6.7 for one particular example case. Also shown are video images recorded at particular times during the transient showing the positions of the capillary, drop and electrode. The key stages in the transient are: (a) detachment of the previous drop; (a-b) relaxation of the bulk concentration to the level of background (initial) concentrations as reflected by the magnitude of the diffusion-limited current; (b-c) background concentrations observed as the drop-electrode distance is too great for the electrode to detect the

163

Figure 6.7 Current vs. time behaviour for bromine transfer to a DCE drop measured at a 1 μm diameter Pt UME positioned beneath the drop. The images a - e indicate the relative positions of the capillary, drop and UME, and correspond to the points indicated on the transient.

interfacial concentration gradient adjacent to the drop; (c) interception of the concentration boundary layer at the drop by the UME; (c-d) decreasing current as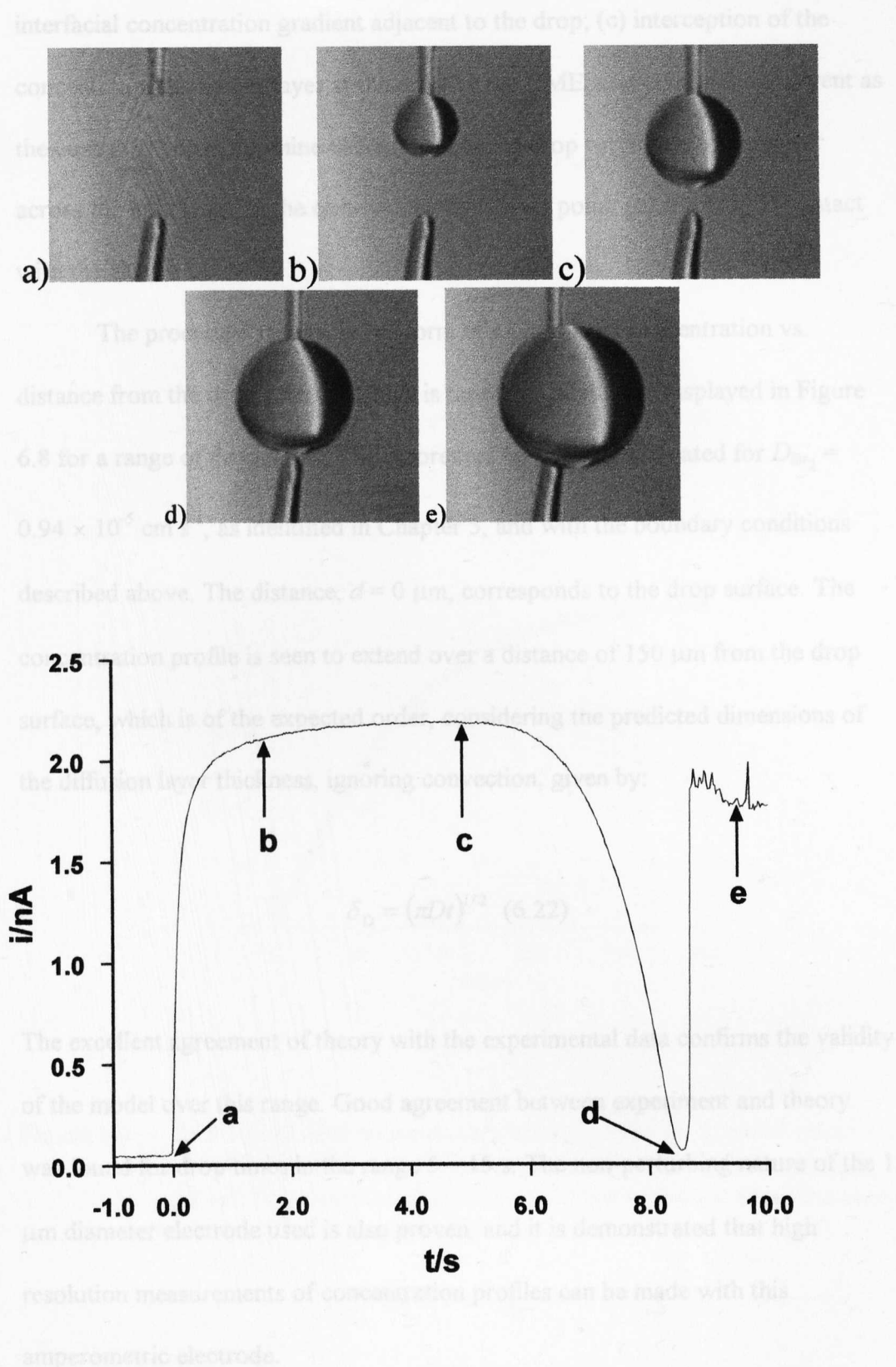 the concentration of bromine decreases near the drop surface due to transfer across the interface; (d) the clearly defined contact point; (e) the drop in contact with the electrode.

The processed results, in the form of a plot of the concentration vs. distance from the drop surface, which is time-dependent, are displayed in Figure 6.8 for a range of drop times. The theoretical response is simulated for D_{Br_2} = 0.94×10^{-5} cm s^{-1}, as identified in Chapter 5, and with the boundary conditions described above. The distance, $d = 0$ μm, corresponds to the drop surface. The concentration profile is seen to extend over a distance of 150 μm from the drop surface, which is of the expected order, considering the predicted dimensions of the diffusion layer thickness, ignoring convection, given by:

$$\delta_D = (\pi D t)^{1/2} \quad (6.22)$$

The excellent agreement of theory with the experimental data confirms the validity of the model over this range. Good agreement between experiment and theory was found for drop times in the range 5 – 15 s. The non-perturbing nature of the 1 μm diameter electrode used is also proven, and it is demonstrated that high resolution measurements of concentration profiles can be made with this amperometric electrode.

Figure 6.8   Normalised concentration vs. distance profile for bromine transfer
to a DCE drop measured amperometrically at a 1 μm diameter Pt
UME (O). Drop times were a) 4.07 s and b) 7.46 s. The solid line
indicates the theoretical response.

6.5.1.2 Potentiometric Measurements

The experiments carried out using potentiometric detection yielded similar results. The relative concentrations of Br_2 and Br^- employed ensured that the formation of Br_3^- could be neglected.[182,183] A typical potentiometric transient is displayed in Figure 6.9, where the key stages indicated are as defined before in Figure 6.7.
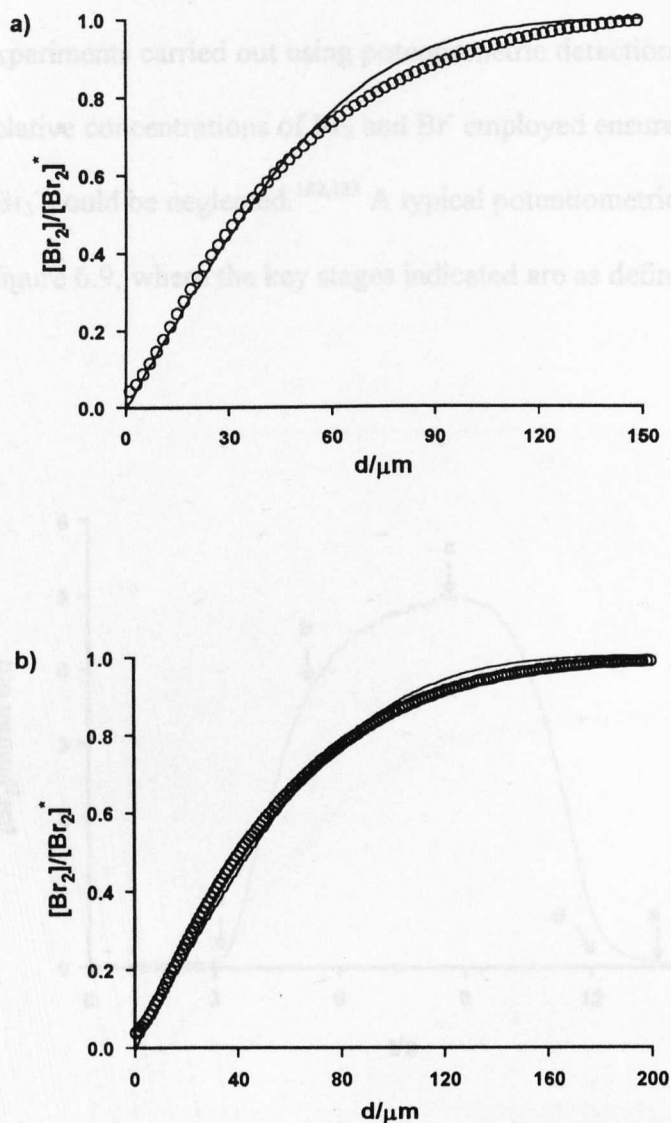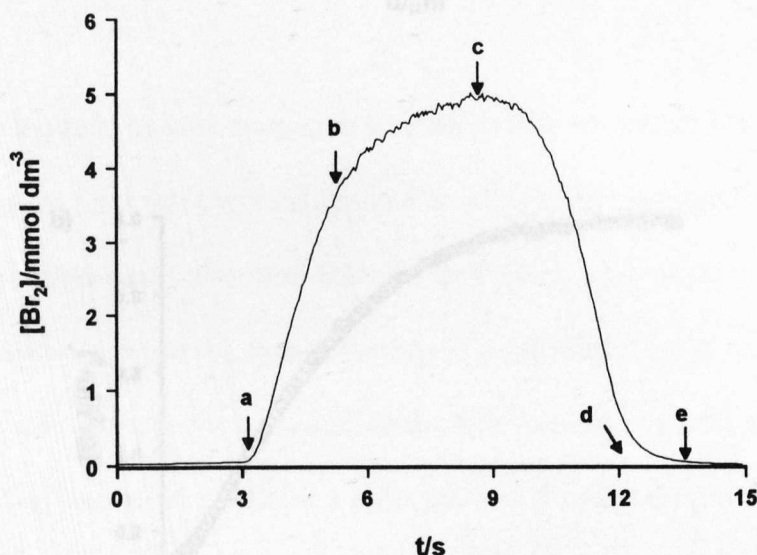
Figure 6.9   Concentration-time behaviour for bromine transfer measured potentiometrically. The images a - e correspond to the positions described previously in Figure 6.7.

When converted to concentration profiles, Figure 6.10, the results match the theory well for the greater part of the concentration profile confirming that the 1 μm diameter Pt potentiometric electrodes also respond well, with a sufficient resolution. Some deviation from the expected behaviour close to the interface is observed at all drop times. This deviation may be a problem associated with the electrode response time in the region ($[Br_2] \rightarrow 0$) where the concentration ratio

Figure 6.10   Normalised concentration vs. distance profile for bromine transfer to a DCE drop measured potentiometrically at a 1 μm Pt UME vs. SCE reference (O). Drop times were a) 7.06 s, and b) 8.30 s. The solid line indicates the theoretical response for a transport-controlled process.

168

changes most significantly. Nonetheless, the potentiometric technique works well in reflecting the concentration profile up to *ca.* 10 μm from the interface. This model example system actually represents the most difficult case for potentiometric detection since the $\log([Br_2]/[Br^-])$ expression changes most rapidly under these conditions. For finite kinetics, to which the technique will be most applicable, the concentration changes will be more gradual.

6.5.1.3 Measurement of the Concentration Profile at the Side of a Growing Drop

The bromine transfer system, as a model system was also employed in investigating the form of concentration profiles at different positions around the drop. The simplest case (other than at the base of a drop), to enable calculation of the electrode-drop separation, was at the side of a growing drop. It was possible, through the use of a cell which incorporated a hole through one side, with a flexible seal, to position the UME at a point where a growing drop would expand up to and contact the tip of the UME with the side of the drop. This arrangement is illustrated schematically in Figure 6.11, which also demonstrates how the interface-UME separation may be determined. The drop-UME separation may be calculated from:

$$d = \sqrt{h^2 + (g - r_t)^2} - r_t \qquad (6.23)$$

where g and h are the dimensions outlined in the diagram, r_t is the drop radius at any time, which is half the drop diameter, determined by equation 6.13.
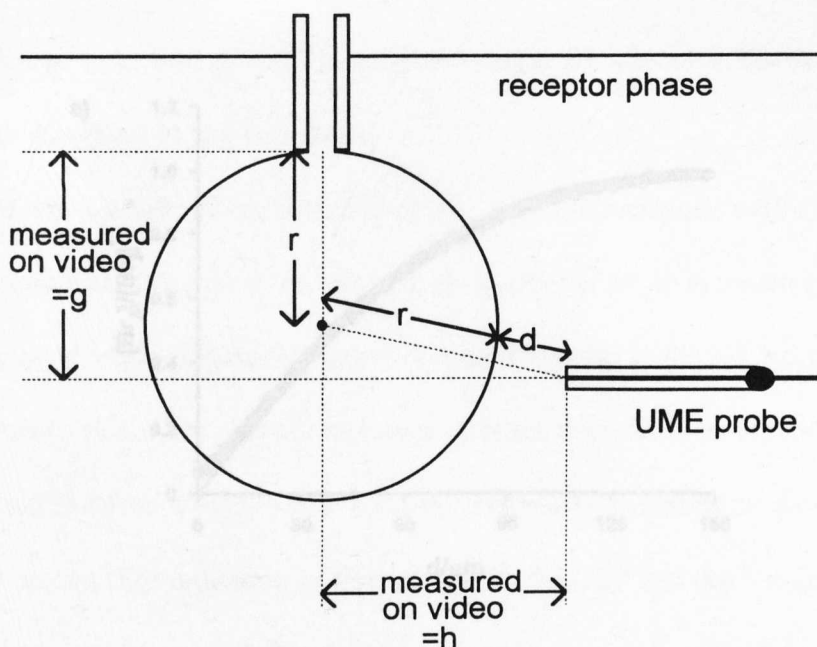
Figure 6.11 Schematic of the arrangement for measuring concentration profiles at the side of expanding droplets.

The concentration profiles in Figure 6.12 correspond to measurements of bromine transfer made in this arrangement using the amperometric approach. The solution conditions were identical to those outlined in section 6.5.1. The theoretical profiles may be calculated in a similar manner to those at the base of the drop, however, the model must be modified to allow the UME-drop distance to be evaluated from the relation described in equation 6.21. The agreement between experiment and theory confirms the validity of these measurements, which may subsequently be further developed to identify the nature of mass transport at different positions around drops and to investigate the ageing of the drop surface. These measurements may therefore be valuable in evaluating the effect of surfactants at growing drops, however, as yet, no further studies in this arrangement have been made.
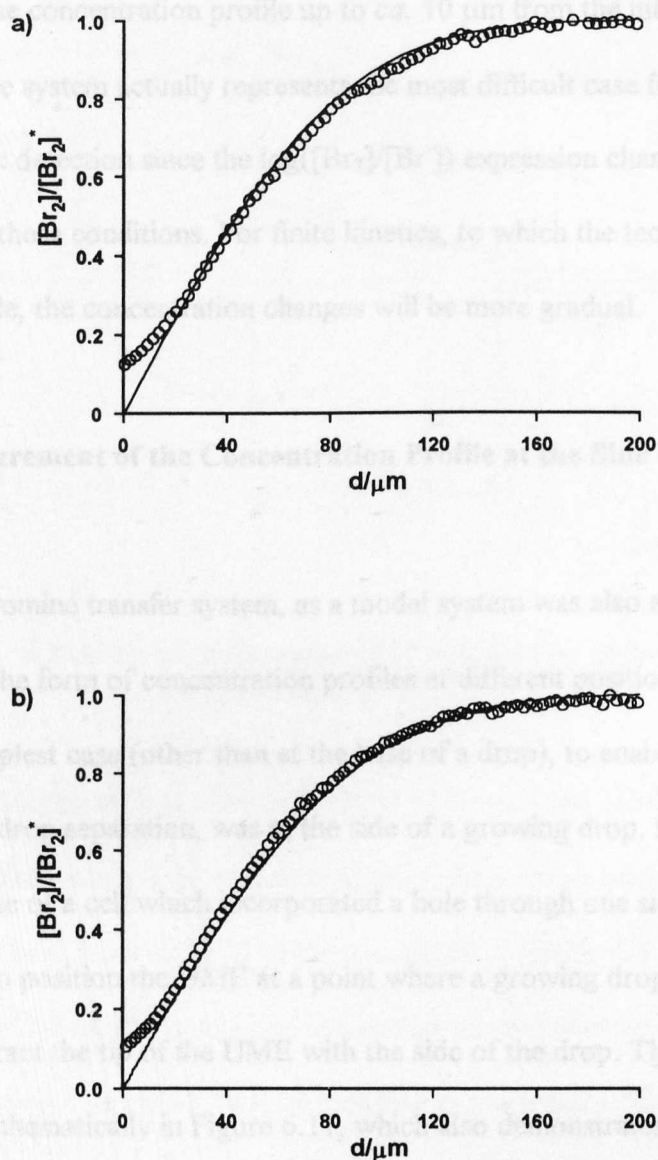
Figure 6.12 Normalised concentration vs. distance profile for bromine transfer to a DCE drop measured amperometrically at a 1 μm diameter Pt UME positioned at the side of the drop (O). Drop times were a) 6.38 s, and b) 16.44 s. The solid lines show the theoretical response for a transport-controlled process.

6.5.2 Characterisation of the Technique Using a Bimolecular Electron Transfer Reaction at the Interface

It was considered important to characterise the technique with a range of types of interfacial reactions. To this end, an interfacial electron transfer reaction was employed to investigate the nature of mass transport in the MEMED arrangement. This was a more complicated process than the bromine transfer system as it involved a bimolecular reaction between two species confined in separate phases. The oxidation of ferrocene (Fc), 5×10^{-2} mol dm^{-3} in DCE, by iridium (IV) chloride ($Ir(Cl)_6^{2-}$), 4×10^{-3} mol dm^{-3} in aqueous solution was the electron transfer reaction employed in this study, in which charge neutrality was (partly) maintained by the addition of perchlorate ion (ClO_4^-) to the two phases. The effect of introducing potential determining common ions on electron transfer processes at liquid/liquid interfaces was described in more detail in Chapter 1, section 1.4.4. The ferrocinium cation produced in this reaction could also partition between the two phases, acting as another charge transfer (and potential determining) agent.

The MEMED arrangement for this system is shown schematically in Figure 6.13, which also describes the composition of the two solutions. In this figure, THAClO$_4$ is tetra-n-hexylammonium perchlorate. This reaction has previously been studied using SECM.[120] The interest of the MEMED technique in this application was not to study the kinetics, but rather to characterise the methodology with a process which was expected to be effectively transport-controlled under the experimental conditions employed. The interfacial redox reaction of interest may be expressed by equation 6.24:

172

1,2-dichloroethane
50 mM ferrocene
0.02 M THAClO$_4$

AgQRE

4.0 mM IrCl$_6^{2-}$
1.0 M NaClO$_4$

IrCl$_6^{2-}$

Fc
Fc
Fc
Fc
Fc
Fc
Fc
Fc$^+$
Fc

IrCl$_6^{2-}$

IrCl$_6^{2-}$

IrCl$_6^{3-}$

IrCl$_6^{2-}$

IrCl$_6^{2-}$

IrCl$_6^{2-}$

IrCl$_6^{2-}$

Apply 0.4 V
Measure i$_{IrCl_6^{2-}}$ /nA
or
Apply 0.9 V
Measure i$_{IrCl_6^{3-}}$ /nA

nanode
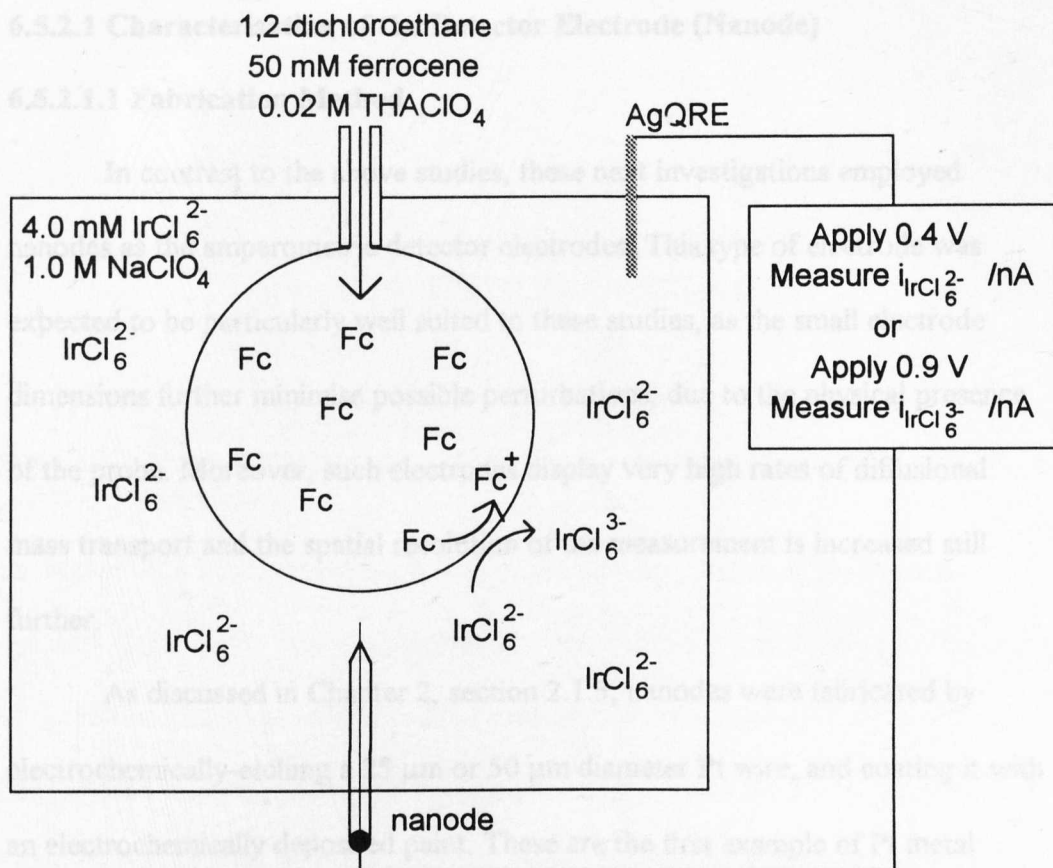
Figure 6.13 Schematic illustration of the arrangement for measuring the bimolecular interfacial reaction between IrCl$_6^{2-}$ in the aqueous receptor phase and Fc in the organic drop phase by measurement of the concentration profiles for IrCl$_6^{2-}$ and IrCl$_6^{3-}$ using a nanode detector.

$$Ir(Cl)_{6,(aq)}^{2-} + Fc_{(org)} \xrightarrow{k_{12}} Ir(Cl)_{6,(aq)}^{3-} + Fc_{(org)}^{+} \quad (6.24)$$
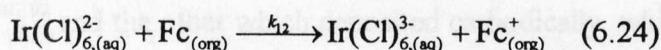
where k_{12} is the bimolecular interfacial electron transfer rate constant. As

previously mentioned, the ferrocenium cation produced partitions between both

phases.[67,199] To ensure the interfacial reaction was driven, the potentials of the two

redox couples, under identical conditions to those employed in the MEMED

arrangement, were measured. The results of this study will be described below.

6.5.2.1 Characterisation of the Detector Electrode (Nanode)

6.5.2.1.1 Fabrication Method

In contrast to the above studies, these next investigations employed nanodes as the amperometric detector electrodes. This type of electrode was expected to be particularly well suited to these studies, as the small electrode dimensions further minimise possible perturbations, due to the physical presence of the probe. Moreover, such electrodes display very high rates of diffusional mass transport and the spatial resolution of the measurement is increased still further.

As discussed in Chapter 2, section 2.1.3, nanodes were fabricated by electrochemically-etching a 25 μm or 50 μm diameter Pt wire, and coating it with an electrochemically deposited paint. These are the first example of Pt metal nanodes of this type; etched metal nanodes have typically been constructed from Pt-Ir or other wires. This is an important point, since the electrode material is crucial in defining the response. Two different coatings were used, one of which has been employed previously in the construction of nanodes, which deposited anodically,[129,130,192] and the other which deposited cathodically, which has not been used previously for this application.[131,132] As described herein, both approaches were successful in producing tips of the required small size.

6.5.2.1.2 Assessment of Tips by Optical Microscopy and Scanning Electron Microscopy

The photomicrograph in Figure 6.14 shows the tip of one of the electrodes prepared by coating with the anodic paint. The electron micrographs in Figure 6.15 show etched tips before coating and after coating with the two insulating
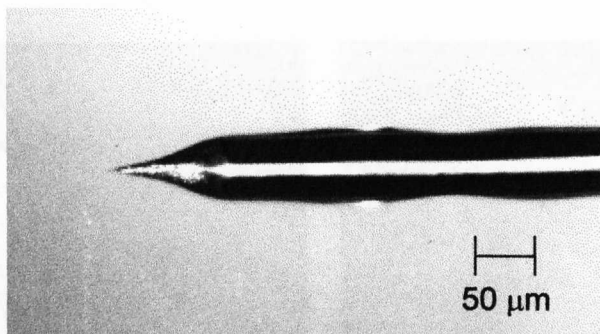
Figure 6.14   Photomicrograph showing the tip of one of the anodic paint coated electrodes.

paints. Figures 6.15(a-d) reveal the nature of the etching process at the Pt surface. The general shape of the etched tip is that of a cone, while the extreme end of the tip shows structure on a scale of hundreds of nanometres. In the case of the cathodically deposited paint, Figure 6.15(e-f), the coating has clearly covered the Pt surface, indicated by the masking of the surface structure. The extent of the coating is not clear, however, from the electron micrographs, and the tip dimensions cannot be evaluated.

The electron micrographs of the tips coated with anodically-deposited paint, Figures 6.15(g-k), show the smooth covering of the insulator, and in (g) and (h) the transition from the smoothness of the insulator to the underlying roughness of the etched Pt metal surface at the very tip is visible. Figure 6.15(i) reveals the structure of a tip which has been subjected to multiple coatings, i.e. the coating procedure was repeated several times, indicating that subsequent coatings result in further coverage at the tip end, as may be seen by optical microscopy. The end-on images Figures 6.15(j-k) reveal the exposed tip of the nanode.

Figure 6.16 contains the results of energy dispersive X-ray analysis of both the tip area of a nanode, and an area tens of microns away from the tip to one side. The peaks that correspond to Pt metal are highlighted in these plots. These
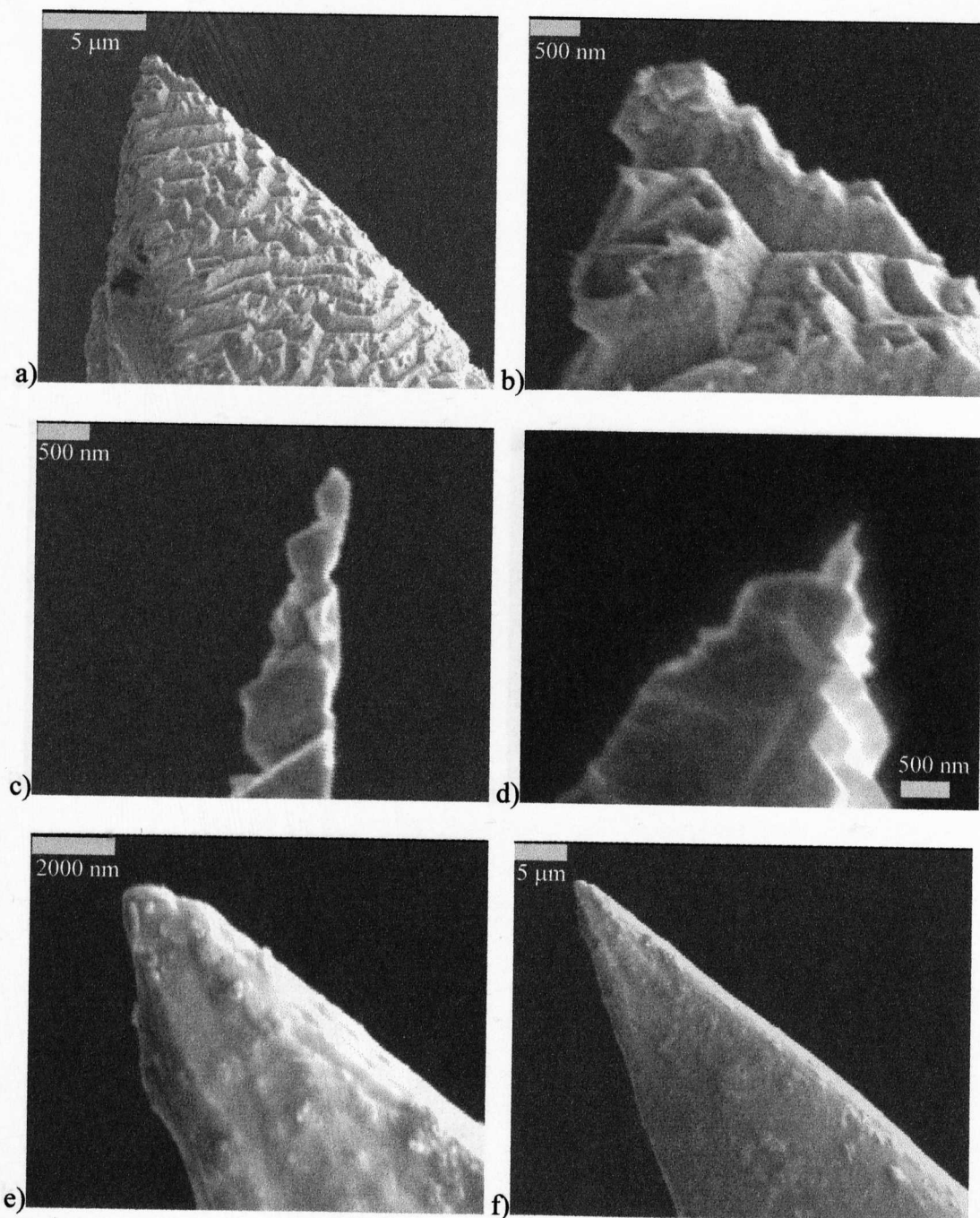
Figure 6.15 Scanning electron micrographs of a-d etched tips; a and b are the same tip at different magnifications, while c and d show further examples of tips at high magnification. Images e and f show etched tips which were coated with cathodically deposited paint.
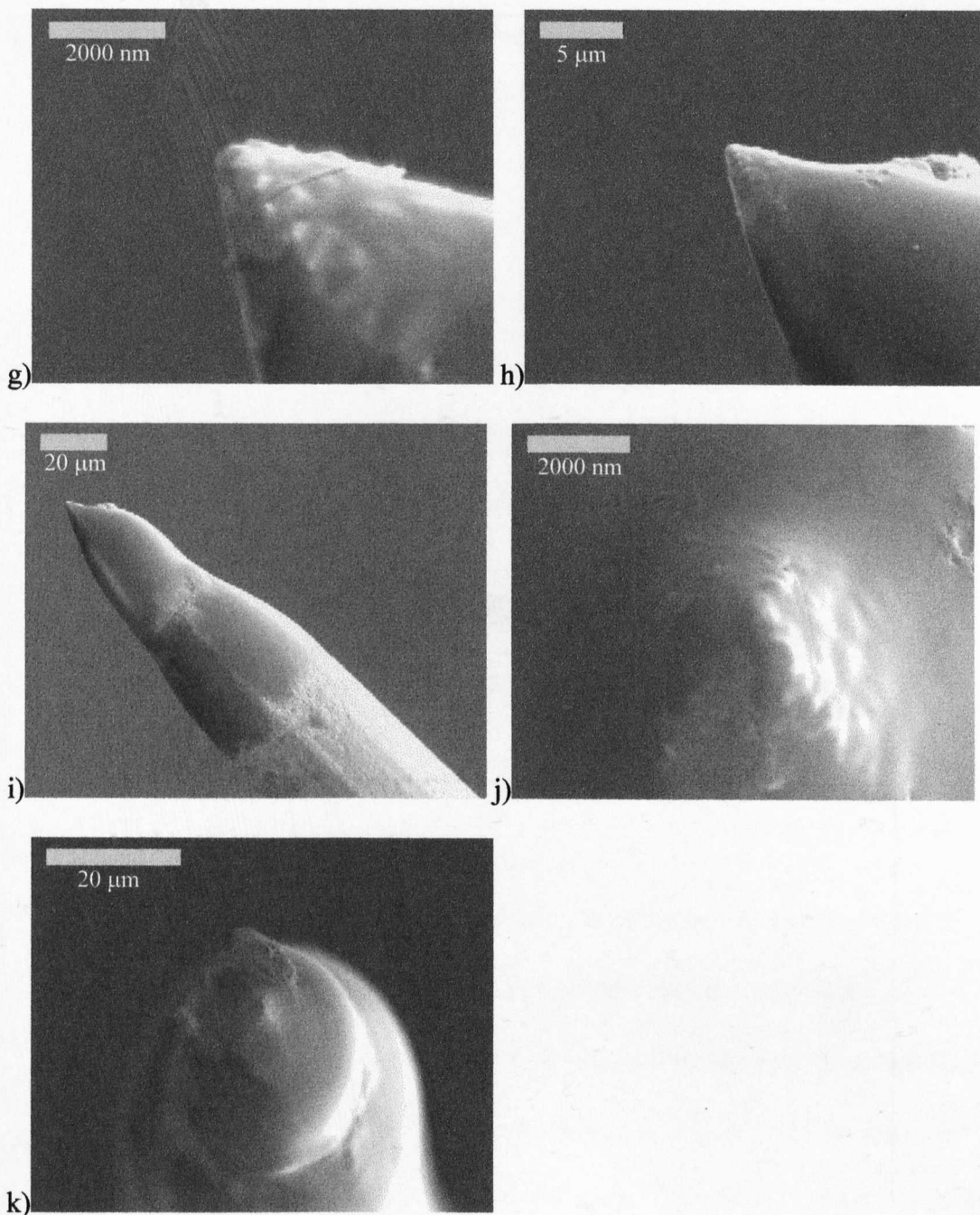
Figure 6.15 Scanning electron micrographs of one etched tip that was coated with two coatings of anodically deposited paint. Images g-i are side-on at a range of magnifications, while j and k show end on images.

Figure 6.16   Energy dispersive X-ray analysis from a) the very end of a coated tip and b) an area at the side of the nanode. The peaks which correspond to Pt are highlighted.

qualitative results confirmed that the exposed tip was Pt metal, as well as confirming the presence of coating further down the length of the coated wire, evidenced by the reduction in Pt content of the analysed area.

6.5.2.1.3 Voltammetric Response of Nanodes

In order to further characterise electrodes prepared as described above, the voltammetric responses were recorded for the oxidation of 2.0×10^{-2} mol dm^{-3} aqueous ferrocyanide with 2.0 mol dm^{-3} KCl as the supporting electrolyte. The effective electrode radius may be calculated if the diffusion coefficient and concentration are known, according to the following equation for an electrode with a hemispherical-shaped tip:[185,200]

$$i_{\text{hemi}} = 2\pi n_e F D r_{\text{hemi}} c \quad (6.25)$$

In equation 6.25, r_{hemi} is the radius of the base of the hemispherical shaped tip, which is exposed. In the case of a conical shaped tip, 2π in equation 6.25 is replaced with a constant in the range $1.9\pi - 2.2\pi$ depending on the actual tip geometry.[200] The hemispherical or conical shape is the proposed geometry for electrodes constructed from coated etched wires,[200] and is appropriate when the microscopic images of the tips are considered.

Voltammetric responses, recorded at a scan rate of 20 mV s^{-1} with AgQRE as the reference, for a range of electrodes coated using the anodic procedure are shown in Figure 6.17. For each of these electrodes three repeat coatings were applied. The size of the electrode produced is variable, and may be
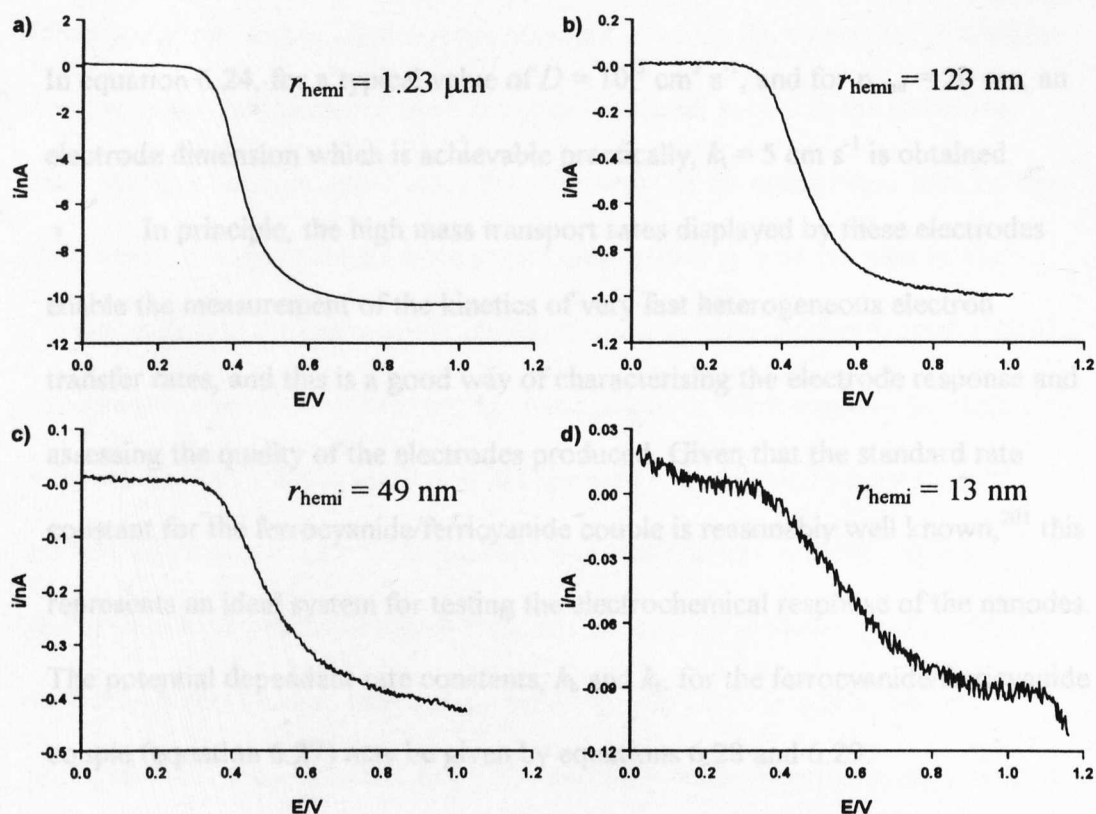
Figure 6.17 Steady-state voltammograms recorded for the oxidation of ferrocyanide with a range of electrode radii. The effective electrode radii were calculated using equation 6.25. The reference electrode was AgQRE, and the scan speed used was 20 mV s^{-1}.

dependent on factors such as the exact deposition and curing times as well as the initial shape of the etched tip. Nonetheless, in all cases the effective radius is on the micrometre or submicrometre scale.

The rates of mass transfer associated with these small electrodes, assuming a hemispherical geometry, may be calculated from equation 6.26 (*cf.* equation 6.15 for a disc shaped UME).

$$k_t = \frac{D}{r_{hemi}} \quad (6.26)$$

In equation 6.24, for a typical value of $D = 10^{-5}$ cm^2 s^{-1}, and for $r_{hemi} = 20$ nm, an electrode dimension which is achievable practically, $k_t = 5$ cm s^{-1} is obtained.

In principle, the high mass transport rates displayed by these electrodes enable the measurement of the kinetics of very fast heterogeneous electron transfer rates, and this is a good way of characterising the electrode response and assessing the quality of the electrodes produced. Given that the standard rate constant for the ferrocyanide/ferricyanide couple is reasonably well known,[201] this represents an ideal system for testing the electrochemical response of the nanodes. The potential dependant rate constants, k_b and k_f, for the ferrocyanide/ferricyanide couple (equation 6.27) may be given by equations 6.28 and 6.29:

$$Fe(CN)_6^{3-} + e^- \; \underset{k_b, \beta}{\overset{k_f, \alpha}{\rightleftharpoons}} \; Fe(CN)_6^{4-} \qquad (6.27)$$
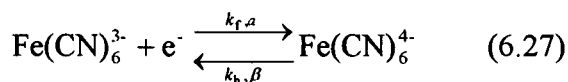
$$k_b = k_0 \exp\left[\beta\left(n_e F / R_g T\right)\left(E - E^{0'}\right)\right] \qquad (6.28)$$

$$k_f = k_0 \exp\left[-\alpha\left(n_e F / R_g T\right)\left(E - E^{0'}\right)\right] \qquad (6.29)$$

where α and β are the transfer coefficient for the reduction and oxidation reactions respectively, and $E^{0'}$ is the formal potential for the redox couple.

The standard rate constant for the electron transfer process occurring at the electrode surface, k_0, may be calculated from the voltammetric response. At low mass transfer rates, relative to k_0, for an uncomplicated, reversible electron transfer reaction, the steady-state voltammetric wave at any UME displays reversible behaviour, characterised by a sigmoidally shaped wave, where the difference between the upper and lower quartile potentials, $E_{3/4} - E_{1/4}$ is 56.5 mV

181

at 298 K.[18] Here, $E_{3/4}$ is the potential at which the measured current is 75 % of the limiting current, and $E_{1/4}$ denotes the potential at which the current is 25 % of the limiting value. As the size of the electrode is reduced, such that the increasing mass transport rate, k_t, approaches the same order or becomes larger than k_0, the voltammetric wave becomes more irreversible, resulting in an increase in $E_{3/4}$ – $E_{1/4}$ and a shift in the half wave potential, $E_{1/2}$, away from the formal potential, $E^{0'}$, to more positive values in the case of an oxidation, or more negative potentials for a reduction. This trend is illustrated in Figure 6.18, and it can be seen that the voltammograms in Figure 6.17, qualitatively, conform to this trend. As the electrode size decreases, the mass transfer rate increases (equation 6.26) and the voltammograms become increasingly irreversible in form. Evaluation of the potential shifts, $E_{3/4}$ – $E_{1/4}$ and $E_{1/2}$ – $E^{0'}$, enables k_0 to be determined as described below.
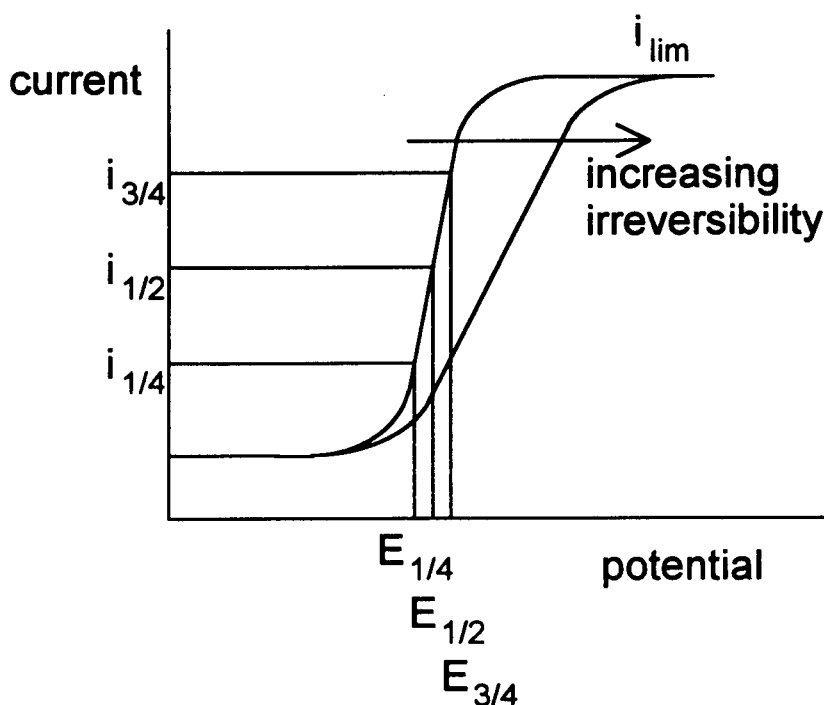
Figure 6.18 Schematic illustrating the potentials measured for the analysis of a steady-state voltammogram and the behaviour expected with increasing irreversibility of the redox couple.

The voltammograms recorded here were analysed through the construction of kinetic indicator plots,[202,201] which use the half-wave and quartile potentials obtained from the voltammogram to calculate k_0 as well as β, the transfer coefficient.

The current observed at a hemispherical UME at any applied potential may be related to the limiting current measured under diffusion-controlled conditions, i_{lim}, by:[203]

$$i = \frac{i_{lim}}{1 + \left(\dfrac{D_O}{D_R}\right)\exp\varphi + \left(\dfrac{\pi^2}{8K_v}\right)} \quad (6.30)$$

where D_O and D_R are the diffusion coefficients of the oxidised and reduced forms of the redox species, and φ and K_v are defined as follows:

$$\varphi = \left(\frac{n_e F}{R_g T}\left(E - E^{0'}\right)\right) \quad (6.31)$$

$$K_v = \frac{\pi^2 k_0 r_{hemi}}{8D_O}\exp\left(-\beta\varphi\right) \quad (6.32)$$

Equation 6.30 may be written as:

$$i = \frac{i_{lim}}{1 + \dfrac{D_O}{D_R}\exp\varphi + \dfrac{D_O}{k_0 r_{hemi}\exp\left(-\beta\varphi\right)}} \quad (6.33)$$

Substituting equation 6.26, and applying $\lambda = k_0 / k_t$ results in:

$$i = \frac{i_{\text{lim}}}{1 + \dfrac{D_O}{D_R} \exp\varphi + \left[\lambda \exp(-\beta\varphi)\right]^{-1}} \qquad (6.34)$$

Equation 6.34 may be used to generate the kinetic indicator plots, $(E_{1/2} - E^{0'})$ vs. $(E_{3/4} - E_{1/4})$ for a range of β and λ values, which may then be used to evaluate these parameters from experimentally measured voltammograms.

Figure 6.19 displays the kinetic indicator plot, and the experimental results, for the characterisation of the nanodes whose voltammetric responses were displayed in Figure 6.17. The value for $E^{0'}$ for this case was taken as the half wave potential recorded in the same solution with a 25 µm diameter Pt UME, which displayed a reversible wave. Following correction of this value to account for different diffusion coefficients of the two species using equation 6.35, a value of $E^{0'} = 364$ mV vs. AgQRE was obtained.

$$E_{1/2} = E^{0'} - \left(\frac{R_g T}{F}\right) \ln\left(\frac{D_{Fe(CN)_6^{4-}}}{D_{Fe(CN)_6^{3-}}}\right) \qquad (6.35)$$

Table 6.1 combines the results obtained for the range of electrodes tested, and reveals the rate constant for the ferrocyanide/ferricyanide redox couple is approximately 0.5 ± 0.4 cm s^{-1} with a value for β of ca. 0.4. The k_0 values obtained for the three larger electrodes are consistent with the range of values previously measured.[201] The value for β is also of the correct order, approximately
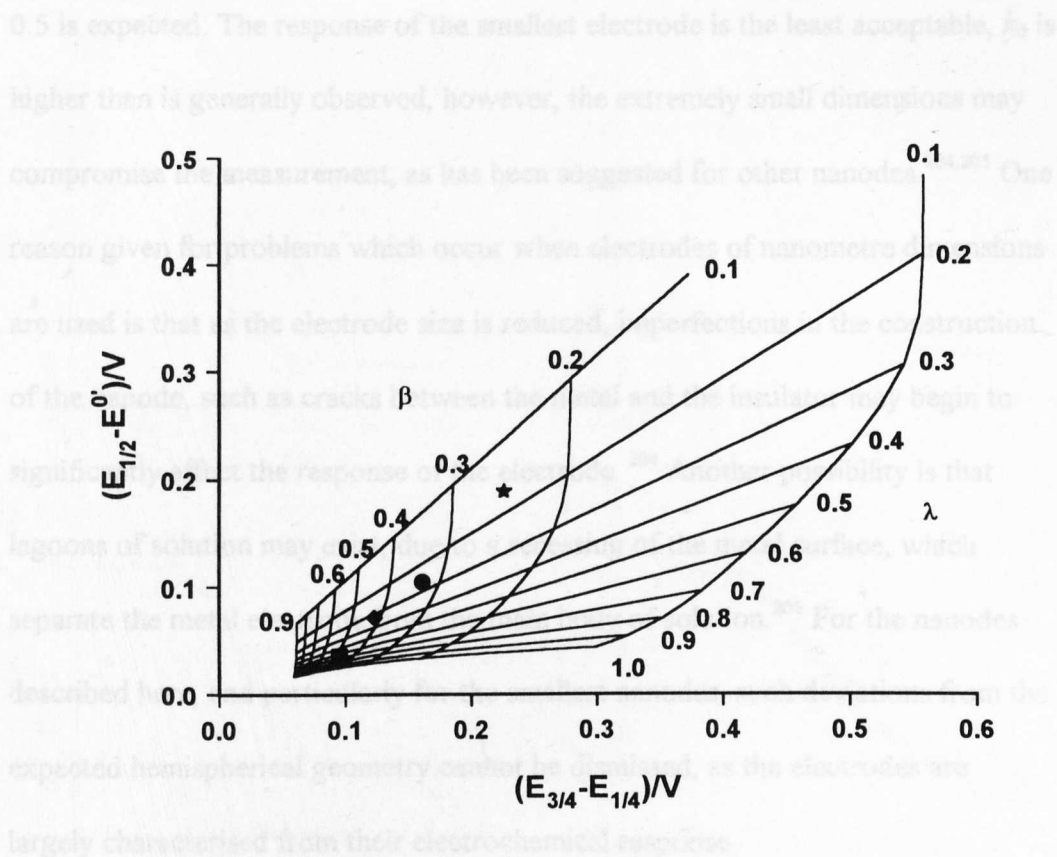
Figure 6.19 Kinetic indicator plot for the characterisation of the ferrocyanide/ferricyanide system ($D_{Fe(CN)_6^{4-}} = 6.7 \times 10^{-6}$ cm^2 s^{-1}, $D_{Fe(CN)_6^{3-}} = 7.6 \times 10^{-6}$ cm^2 s^{-1}), over the ranges $\beta = 0.1$ to 0.9, $\lambda = 0.1$ to 1.0. The data points correspond to voltammograms (Figure 6.17) recorded for the oxidation of ferrocyanide at nanodes of radius $r =$ ■1.23 μm, ◆123 nm, ●49 nm, ★13 nm.

Table 6.1 Values determined for the calculation of the electron transfer rate constant for ferrocyanide oxidation at a range of nanodes.

r_{hemi}/nm	k_t/cm s^{-1}	$E_{3/4}-E_{1/4}$/ V	$E_{1/2}-E^{0'}$/ V	β	λ	k_0/cm s^{-1}
1230	0.0545	0.095	0.056	0.48	0.65	0.035
123	0.545	0.123	0.092	0.42	0.32	0.174
49	1.37	0.161	0.125	0.34	0.27	0.370
13	5.28	0.226	0.209	0.25	0.17	0.898

185

0.5 is expected. The response of the smallest electrode is the least acceptable, k_0 is higher than is generally observed, however, the extremely small dimensions may compromise the measurement, as has been suggested for other nanodes.[204,205] One reason given for problems which occur when electrodes of nanometre dimensions are used is that as the electrode size is reduced, imperfections in the construction of the nanode, such as cracks between the metal and the insulator may begin to significantly affect the response of the electrode.[204] Another possibility is that lagoons of solution may exist, due to a recessing of the metal surface, which separate the metal electrode from the main body of solution.[205] For the nanodes described here, and particularly for the smallest nanodes, such deviations from the expected hemispherical geometry cannot be dismissed, as the electrodes are largely characterised from their electrochemical response.

Once the parameters, k_0 and β have been determined, it is possible to use equation 6.34 to generate simulated voltammetric responses. Figure 6.20 illustrates this with simulations of the experimentally recorded voltammograms for the oxidation of ferrocyanide at a range of nanodes (Figure 6.17). For the purposes of the MEMED experiments, where only the limiting current is required, then the responses of all electrodes are satisfactory.

6.5.2.2 MEMED Investigation of Bimolecular Electron Transfer

For this system, it was possible to measure both the reactant, $Ir(Cl)_6^{2-}$, and the product, $Ir(Cl)_6^{3-}$, amperometrically in the aqueous phase simply by changing the bias of the electrode. The two species were measured on subsequent drops. The linear sweep voltammograms for the oxidation of $Ir(Cl)_6^{3-}$ and the reduction of $Ir(Cl)_6^{2-}$ at nanodes are shown in Figure 6.21. The magnitude of the difference

186
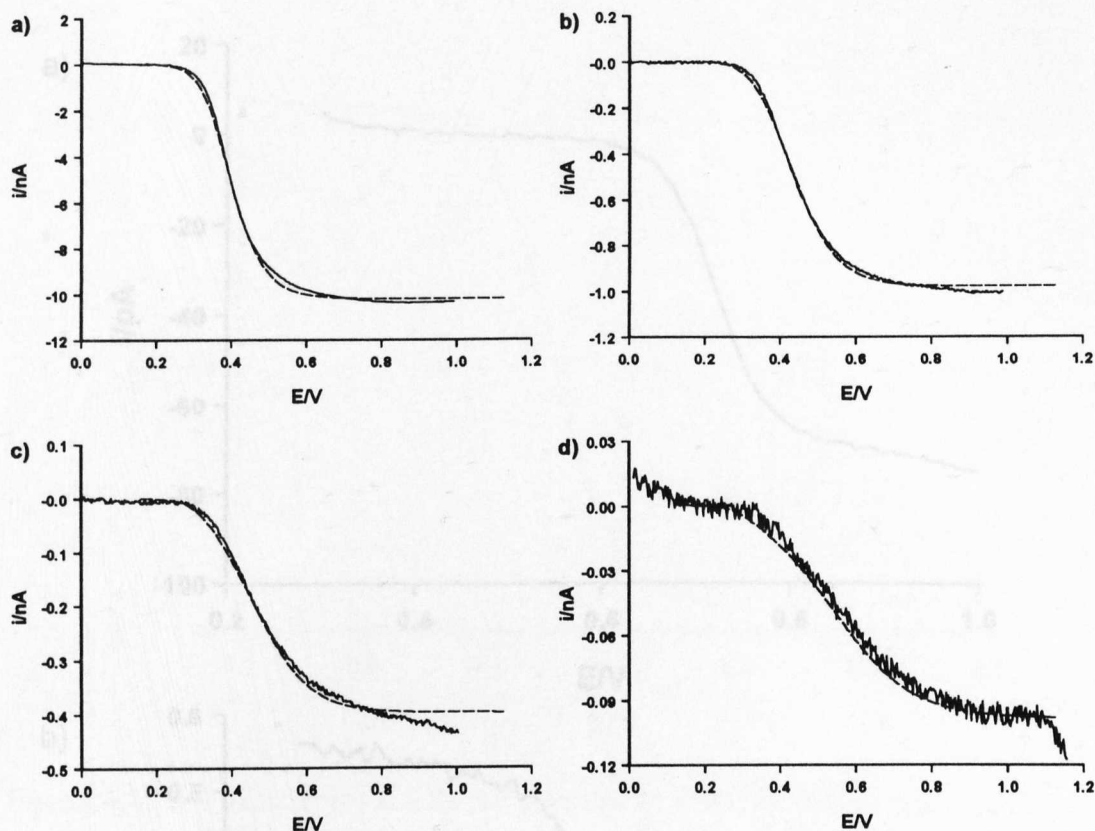
Figure 6.20 Steady-state voltammograms recorded for the oxidation of ferrocyanide at a range of nanodes, from Figure 6.17. The reference electrode was AgQRE, and the scan speed used was 20 mV s^{-1}. The dashed lines represent the modelled response based on the parameters in Table 6.1, calculated from Figure 6.19.

between the upper and lower quartile potentials, $E_{3/4} - E_{1/4}$, for the two voltammograms are a) 65.5 mV and b) 60.0 mV, indicating a shift from reversibility for the electron transfer process at these electrodes. It must be noted that the two nanodes employed were of different sizes.

Figure 6.22 shows the voltammetric response for the oxidation of Fc in DCE at a 25 μm diameter Pt UME with identical concentrations of the potential determining ion as is outlined in Figure 6.13. The solution contained 2.0×10^{-2} mol dm^{-3}, and the reference electrode was a Ag wire in an aqueous solution
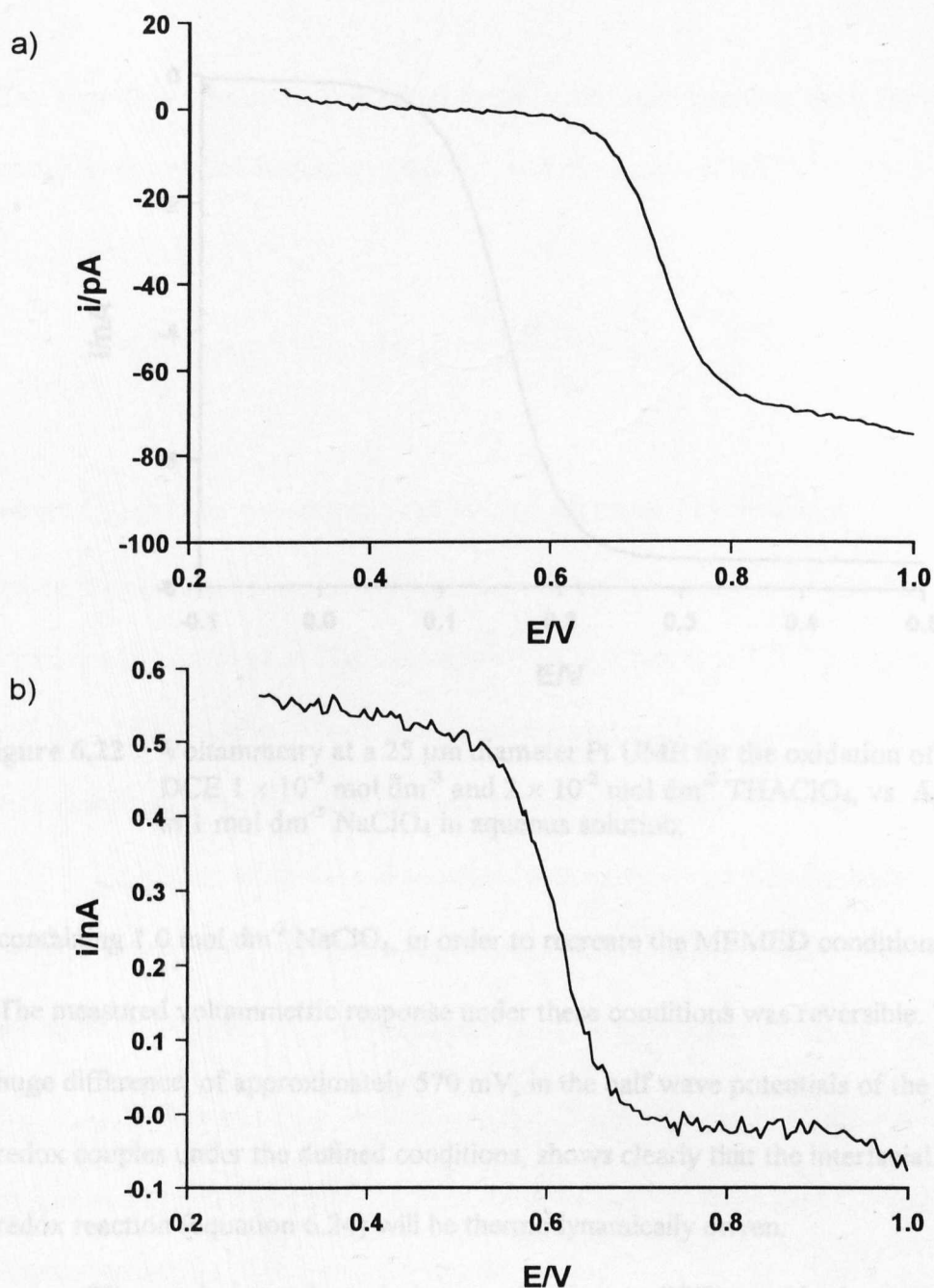
Figure 6.21 Linear sweep voltammetry for a) the oxidation of $Ir(Cl)_6^{3-}$ and b) the reduction of $Ir(Cl)_6^{2-}$ at cathodically deposited paint coated nanodes. The mediator concentration and calculated sizes of the two electrodes were a) $[IrCl_6^{3-}] = 4 \times 10^{-3}$ mol dm^{-3}, $r_{hemi} = 27$ nm, and b) $[IrCl_6^{2-}] = 1 \times 10^{-2}$ mol dm^{-3}, $r_{hemi} = 121$ nm. The supporting electrolyte was 1 mol dm^{-3} $NaClO_4$ in each case.
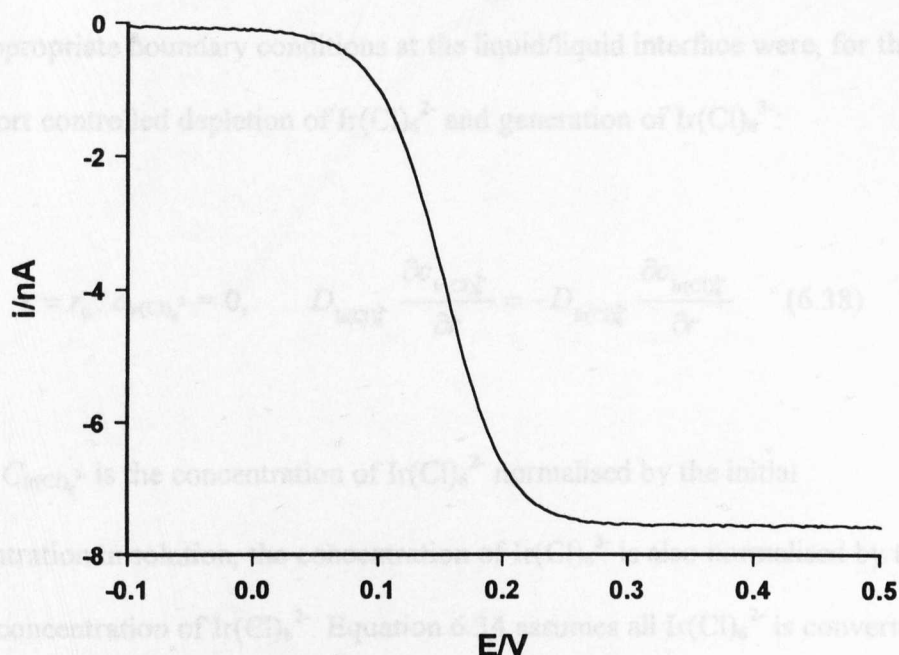
Figure 6.22 Voltammetry at a 25 μm diameter Pt UME for the oxidation of Fc in DCE 1×10^{-3} mol dm^{-3} and 2×10^{-2} mol dm^{-3} THAClO$_4$, vs. Ag wire in 1 mol dm^{-3} NaClO$_4$ in aqueous solution.

containing 1.0 mol dm^{-3} NaClO$_4$, in order to recreate the MEMED conditions.

The measured voltammetric response under these conditions was reversible. The

huge difference, of approximately 570 mV, in the half wave potentials of the two

redox couples under the defined conditions, shows clearly that the interfacial

redox reaction (equation 6.24) will be thermodynamically driven.

The steady-state electrolysis potentials (vs. AgQRE) used in the

amperometric measurement of $Ir(Cl)_6^{3-}$ and $Ir(Cl)_6^{2-}$, and the respective electrode

reactions, are shown in equations 6.36 and 6.37.

$$\text{at 0.4 V, } Ir(Cl)_6^{2-} + e^- \longrightarrow Ir(Cl)_6^{3-} \quad (6.36)$$

$$\text{at } 0.9 \text{ V, } Ir(Cl)_6^{3-} \longrightarrow Ir(Cl)_6^{2-} + e^- \quad (6.37)$$
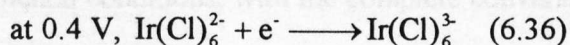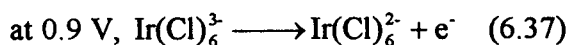
The appropriate boundary conditions at the liquid/liquid interface were, for the transport controlled depletion of $Ir(Cl)_6^{2-}$ and generation of $Ir(Cl)_6^{3-}$:

$$r = r_0 : c_{Ir(Cl)_6^{2-}} = 0, \qquad D_{Ir(Cl)_6^{2-}} \frac{\partial c_{Ir(Cl)_6^{2-}}}{\partial r} = -D_{Ir(Cl)_6^{3-}} \frac{\partial c_{Ir(Cl)_6^{3-}}}{\partial r} \quad (6.38)$$

where $C_{Ir(Cl)_6^{2-}}$ is the concentration of $Ir(Cl)_6^{2-}$ normalised by the initial concentration in solution, the concentration of $Ir(Cl)_6^{3-}$ is also normalised by the initial concentration of $Ir(Cl)_6^{2-}$. Equation 6.34 assumes all $Ir(Cl)_6^{2-}$ is converted to $Ir(Cl)_6^{3-}$ at the interface. The no-flux (semi-infinite) boundary condition, at $r = r_0 + r_f$, described for the bromine case also applies here for each species.

Typical experimental and simulated concentration profiles for both $Ir(Cl)_6^{2-}$ and $Ir(Cl)_6^{3-}$, recorded using a nanode, characterised by $r_{hemi} = 300$ nm, are shown in Figure 6.23. The simulation used the diffusion coefficients, $D_{Ir(Cl)_6^{2-}}$ and $D_{Ir(Cl)_6^{3-}}$, determined by voltammetry at a 25 μm diameter Pt UME in solutions of known concentration, 6.8×10^{-6} and 7.7×10^{-6} cm^2 s^{-1} respectively, which were in good agreement with previously quoted values.[206]

Once again, excellent agreement between experiment and theory confirms the applicability of the model in this bimolecular interfacial electron transfer reaction. The interfacial reaction is confirmed to be transport-controlled, under the defined experimental conditions, with the complete conversion of $Ir(Cl)_6^{2-}$ to $Ir(Cl)_6^{3-}$ at the interface. The versatility of the technique in measuring both

190

a)

b)
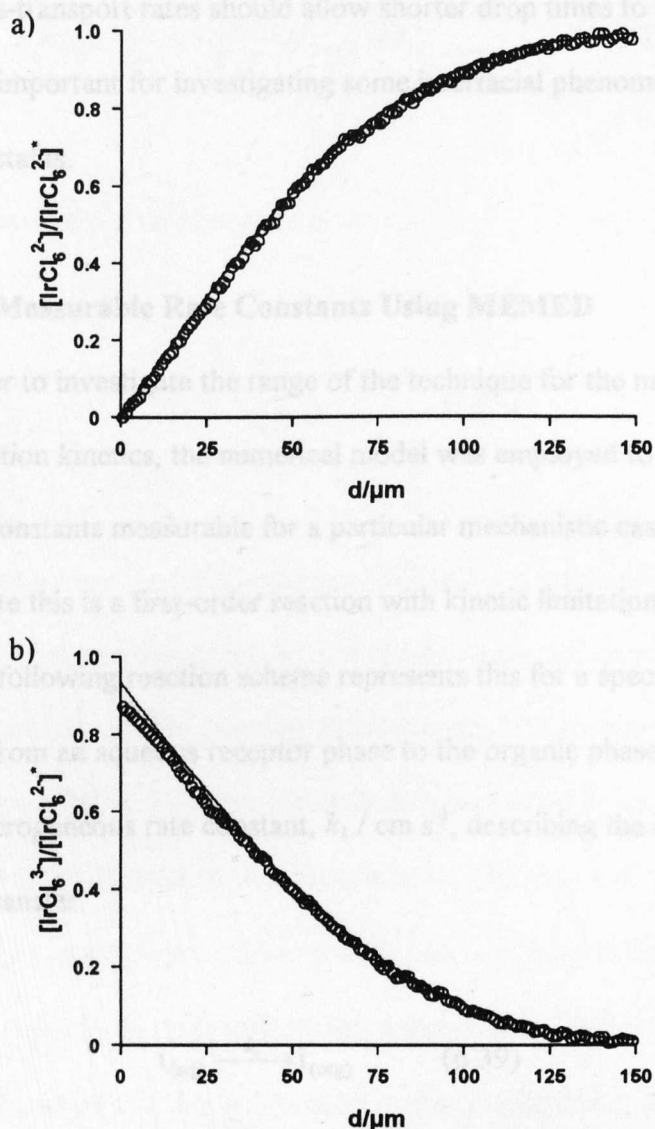
Figure 6.23 Normalised concentration-distance profiles for a) $IrCl_6^{2-}$ and b) $IrCl_6^{3-}$, recorded during the reaction of $IrCl_6^{2-}$ in aqueous solution with Fc in a DCE drop (O). The drop time was 8.46 s. The solid lines indicates the theoretical response based on the diffusion coefficients outlined in the text.

reactants and products on subsequent drops is also proven. The nanodes are

shown to function successfully, giving an excellent response and offering the

possibility of making very high-resolution measurements of concentration profiles.

An additional advantage of using nanodes is that their rapid diffusional relaxation

times and mass-transport rates should allow shorter drop times to be employed, which may be important for investigating some interfacial phenomena, such as the effect of surfactants.

6.6 Range of Measurable Rate Constants Using MEMED

In order to investigate the range of the technique for the measurement of interfacial reaction kinetics, the numerical model was employed to determine the range of rate constants measurable for a particular mechanistic case. The simplest case to illustrate this is a first-order reaction with kinetic limitations at the interface. The following reaction scheme represents this for a species i, crossing the interface, from an aqueous receptor phase to the organic phase droplet, with a first-order heterogeneous rate constant, k_1 / cm s^{-1}, describing the interfacial resistance to transfer.

$$i_{(aq)} \xrightarrow{\ k_1\ } i_{(org)} \qquad (6.39)$$
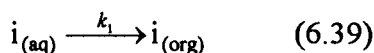
The interfacial boundary condition required for this case is derived from the interfacial flux expression:

$$r = r_0: \quad -D_i \frac{\partial c_i}{\partial r} = k_1 c_i \qquad (6.40)$$

In equation 6.40, c_i is the concentration of the reacting species (at the interface). In normalised terms, this boundary condition becomes:

$$r = r_0: \quad \frac{\partial C_i}{\partial R} = -\sqrt{\frac{t_d}{D_i}} k_1 C_{i,r=r_0} = K_1 C_{i,r=r_0} \qquad (6.41)$$

where K_1 is a normalised rate constant given by:

$$K_1 = -\sqrt{\frac{t_d}{D_i}} k_1 \qquad (6.42)$$

Figure 6.24 shows simulated concentration profiles for a range of typical drop times, with different rate constants, k_1. The results clearly indicate that for a simple heterogeneous transfer reaction, the maximum rate constant resolvable by this approach is ca. 10^{-2} cm s^{-1}. The lower limit is controlled by the ability of the probe to detect small changes in concentrations and the nature of the particular reaction, however, rate constants over several orders of magnitude (below 10^{-4} cm s^{-1}) should typically be resolvable by this approach. The effect of changing the drop time on the shape of the concentration profile is significant, and some effect on the ability to ascertain a particular rate constant is seen. In particular, and as expected, shorter drop times are more suitable for determining rate constants at the higher end of the scale, whereas when detection limits are a problem due to a slow reaction, longer drop times will improve the performance of the method.

Figure 6.24 Simulated normalised concentration vs. distance profiles for typical $D = 10^{-5}$ cm^2 s^{-1}, a drop time of a) 1 s, b) 5 s, c) 15 s, and a range of rate constants, k_1, from top to bottom of 10^{-5}, 10^{-4}, 10^{-3}, 10^{-2}, 10^{-1} and 1 cm s^{-1}.

6.7 Measurements at a Free Liquid Jet Using UME Probes

6.7.1 Description of the Proposed Approach

An alternative approach to the measurement of spontaneous reactions at immiscible liquid/liquid interfaces is to jet one liquid into the second phase. The basic set-up is similar to the MEMED arrangement with a few modifications, and is illustrated in Figure 6.25. If the feeder solution is flowed through the capillary at much higher rates than those used in the dropping technique, then stable jets of the feeder liquid are established in the receptor phase. Figure 6.26 shows a video microscope image of a jet of DCE flowing though water (capillary diameter = 200 μm, electrode diameter 25 μm, RG = 20, 180 cm s^{-1} mean jet velocity). No ripples are seen on the portion of the jet surface under study, and the column of liquid remains stable. The jet may be caught by a second capillary in the cell, thus eliminating any problems of build up of reaction products due to the collection of reactant in the cell. This has been demonstrated by other workers,[29,30] as described in Chapter 1, who analysed the interfacial reaction by measuring changes in the bulk solution phase concentrations following contact. They relied on the short contact times and defined hydrodynamics for their analysis.

It is also possible to introduce a UME into the cell in the receptor phase close to the flowing jet in order to probe local concentration gradients due to reaction at the jet surface. Reactant or product concentration profiles near to the interface should be very informative in terms of reaction mechanisms and kinetics. The advantage of this approach is that, once again the interface is constantly refreshed, however, now it is possible to achieve extremely short contact times between the two liquids. For example, with a detector at micrometre distances downstream of a jet flowing at 1 m s^{-1}, the contact time is microseconds. This
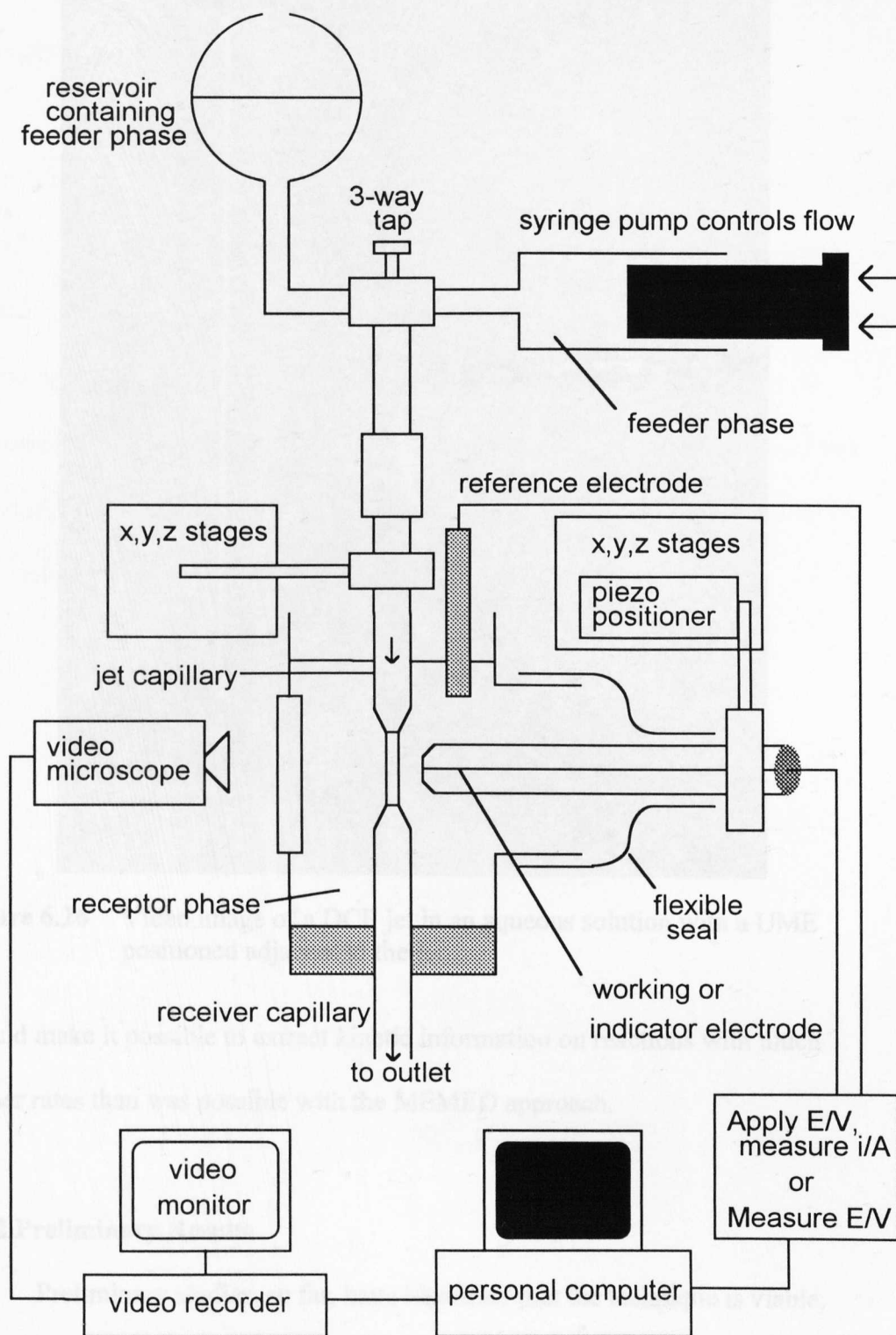
Figure 6.25   Schematic diagram of the set-up for microelectrochemical measurements at liquid jets (not to scale).
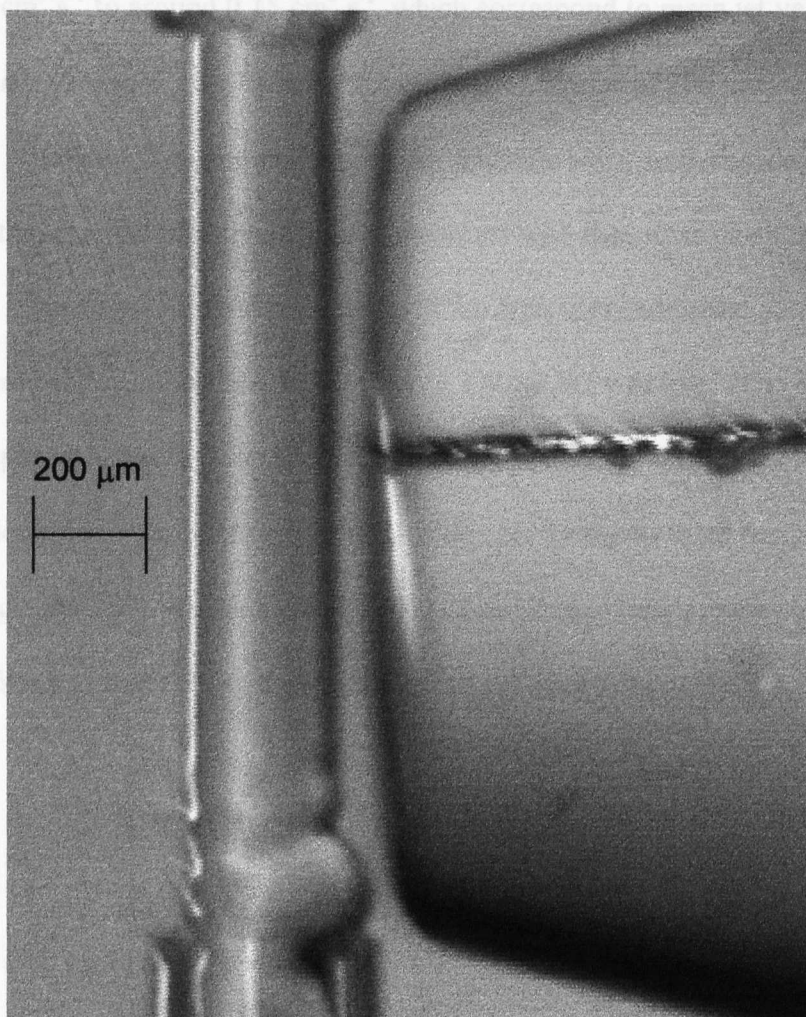
Figure 6.26 Video image of a DCE jet in an aqueous solution with a UME positioned adjacent to the jet.

should make it possible to extract kinetic information on reactions with much higher rates than was possible with the MEMED approach.

6.7.2 Preliminary Results

Preliminary studies, so far, have identified that the technique is viable, and are intended to reveal the optimum operating conditions, i.e. the types of electrodes to be used, and the general set-up parameters have been evaluated.

Using the syringe pump, a range of flow rates were investigated, it was found that stable jets of at least 1 mm length were achieved for flow rates from

0.02 cm^3 s^{-1} to around 0.15 cm^3 s^{-1}, which correspond to mean jet velocities in the region of 60 cm s^{-1} to 470 cm s^{-1} for a nozzle diameter of 200 μm.

Initially, conventional glass coated UMEs were used, the idea being to set up a thin channel of receptor phase in contact with the jet, as illustrated in Figure 6.27. Figure 6.27 also indicates some of the typical experimental parameters. For this case a 25 μm diameter Pt UME with a large *RG* was used. The difficulty with this approach was that the presence of the glass coated UME disturbed the solution flow at distances closer than a few μm. This prevented the use of this arrangement as it is essential that the electrode is able to approach close to the interface and that the separation is well defined and measurable.
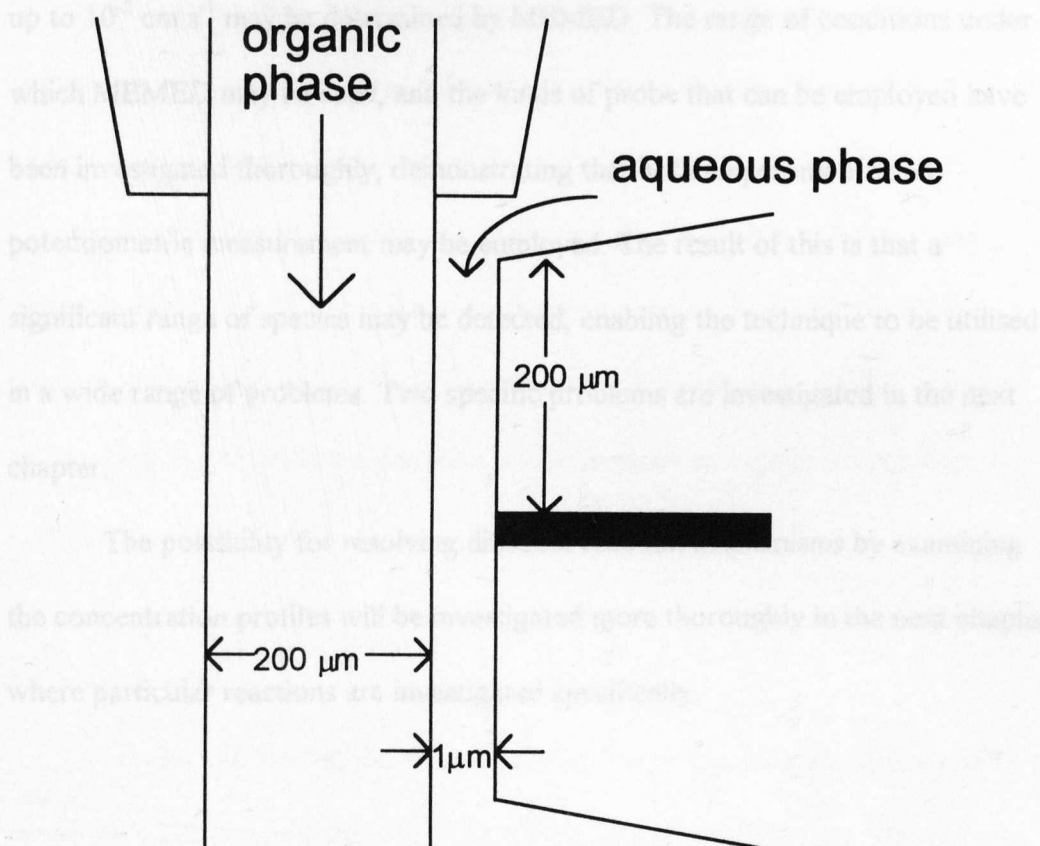
Figure 6.27   Schematic diagram of the proposed jet geometry.

More success is, however, expected through the use of nanodes, which, due to their small size should not disturb the flow. This has now been confirmed,[207] but as yet, further work has not been carried out. This preliminary study was intended to demonstrate the possibilities for this approach.

6.8 Conclusions

The MEMED approach has been developed as a new technique for probing reactions which occur spontaneously on contact between two immiscible liquids. The technique has been shown to operate under well-defined hydrodynamic conditions, which have been evaluated theoretically using a simple model. It has been shown that first-order interfacial processes with rate constants up to 10^{-2} cm s^{-1} may be determined by MEMED. The range of conditions under which MEMED may be used, and the kinds of probe that can be employed have been investigated thoroughly, demonstrating that both amperometric and potentiometric measurement may be employed. The result of this is that a significant range of species may be detected, enabling the technique to be utilised in a wide range of problems. Two specific problems are investigated in the next chapter.

The possibility for resolving different reaction mechanisms by examining the concentration profiles will be investigated more thoroughly in the next chapter where particular reactions are investigated specifically.

CHAPTER 7

APPLICATION OF MEMED TO THE STUDY OF REACTION

MECHANISMS AND KINETICS IN TWO-PHASE REACTIONS

This chapter describes the application of the MEMED technique described in the previous chapter to the measurement of the kinetics of some two-phase reactions. The hydrolysis of triphenylmethyl chloride (TPMCl), at the DCE/water interface is first studied. The reaction rate is determined by measuring the concentration profile for chloride ions potentiometrically at a Ag/AgCl electrode in the aqueous phase adjacent to the interface. By applying the model described in Chapter 6, it is shown unambiguously that the reaction is first-order in TPMCl and occurs interfacially with a rate constant of 6.5×10^{-5} cm s^{-1}. The second system studied is the oxidation of methylanisole (MA) by solutions of cerium (IV) (Ce(IV)), where MA forms the organic phase and Ce(IV) is in the aqueous phase. Under the conditions of this study, the reaction at the interface is shown to be dominant, with a negligible contribution from the reaction between MA dissolved in the aqueous phase and Ce(IV). The competition between the two possible reaction routes, heterogeneous at the interface vs. homogeneous in aqueous solution, is investigated in detail.

7.1 Introduction

Having determined the mass-transport characteristics and the range of measurable kinetics accessible to MEMED, in the previous chapter, this new approach was applied to some kinetically-limited two-phase reactions. The aim ⸱⸱⸱s to elucidate the nature and rates of the reactions from the concentration

profiles, through measurement and simulation. A key question in many studies of reactions at liquid/liquid interfaces is whether the reaction is truly interfacial, or whether it occurs in one of the two phases following transfer. The MEMED method described here, in which concentration profiles at the interface are measured directly, is ideally suited to resolve this important question.

There are a wide range of important reactions that occur spontaneously on contact between two immiscible liquids, such as phase transfer catalysis[3] and metal extraction processes,[1,2] as mentioned in earlier chapters. The two reactions chosen for study were the hydrolysis of TPMCl at the organic solvent/water interface, a simple two-phase reaction,[208] and the oxidation of MA by aqueous acidic solutions of Ce(IV), an important reaction in organic synthesis.[209,210,211]

7.1.1 Hydrolysis of Triphenylmethyl Chloride

The hydrolysis of TPMCl in a two-phase arrangement is illustrated in equation 7.1.

$$TPMCl_{(org)} + H_2O \longrightarrow TPMOH_{(org)} + H^+_{(aq)} + Cl^-_{(aq)} \qquad (7.1)$$
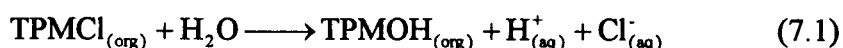
The kinetics of the reaction have been investigated previously using a stirred toluene/water contactor.[208] The reaction was proposed to take place in a laminar layer on the aqueous side, adjacent to the interface, but it has also been noted that the reaction could be truly interfacial,[3] although with the experimental methodology adopted it was impossible to establish this. Furthermore, it has recently been shown that the hydrolysis of solid TPMCl occurs at the solid/aqueous solution interface.[212] With the methodology described herein, the

aim was to investigate this reaction, in order to accurately measure the hydrolysis

rate constant and determine whether the reaction was truly heterogeneous or

occurred in the aqueous phase following dissolution.

7.1.2 Oxidation of Methylanisole by Aqueous Sulfuric Acid Solutions of Cerium (IV)

The second system to be investigated by the MEMED technique was the

oxidation of MA by aqueous sulfuric acid solutions of Ce(IV). This is one of a

class of reactions in which solutions of strong oxidising agents are used to

synthesise higher oxidation state organic species. There are many examples of this

process, for example the oxidation of alkylaromatics by 12-

tungstocobalt(III)ate,[213,214] nitrate radical,[215] tris(phenanthroline)iron(III),[216]

tris(bipyridine)ruthenium(III)[217] and Ce(IV) in a single phase[218,219,220,221,222] or by

Ce(IV) in a two phase arrangement.[209,210,211,223] Direct oxidation of the organic

substrate at an anode has also been employed,[224,225,226,227,228] however, the use of a

chemical oxidation is often preferred, to achieve specific control over the product

distribution.[213,221,222] Moreover, the electrochemical route can lead to deactivation

of the anode due to blocking of the electrode by products.[211] The-two phase

liquid/liquid system offers some advantages over the single phase method, in that

the aqueous phase containing the spent redox mediator may be easily separated

and passed over an electrode to regenerate the active redox species, and product

separation is also simplified.[209,210,211]

Ce(IV) is a commonly used oxidant, given that the standard electrode

potential, vs. the standard hydrogen electrode (SHE), for the Ce(IV)/Ce(III)

couple is 1.72 V.[18] The oxidation of MA by Ce(IV) has been investigated in detail
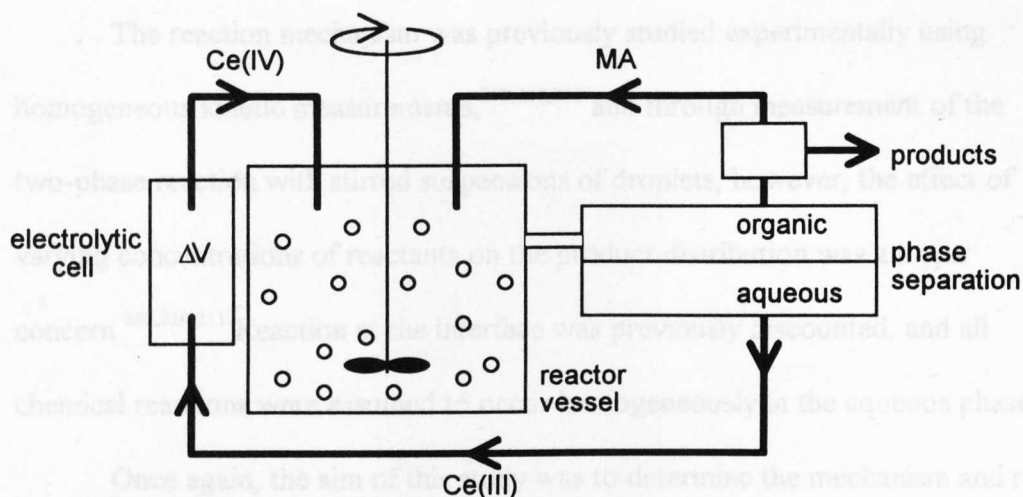
Figure 7.1 Indirect oxidation of MA by Ce(IV) solutions, incorporating recycling of the oxidant by ex-cell electrolysis.
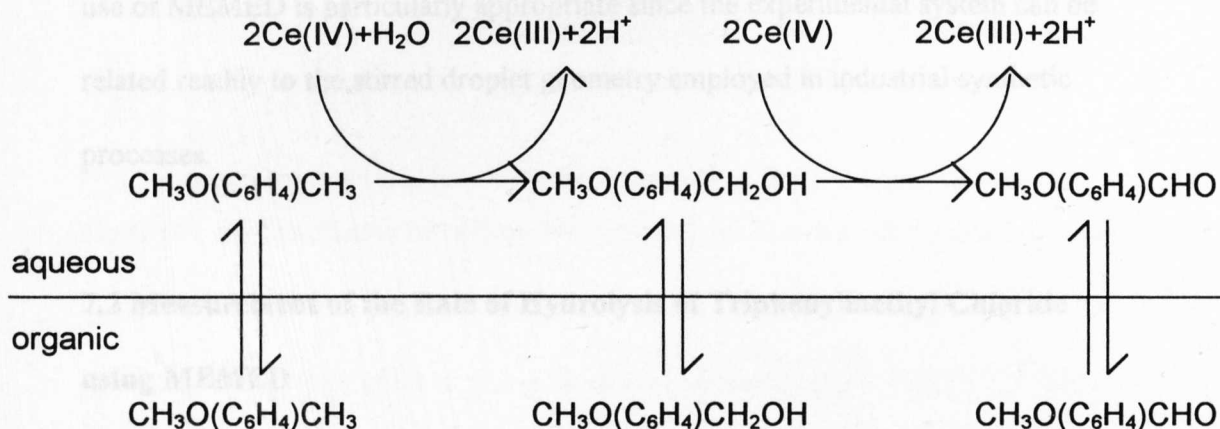
Figure 7.2 Schematic representation of the two-phase reaction between methylanisole (organic reactant and solvent) and Ce (IV) in sulfuric acid.

in a two-phase arrangement which incorporates recycling of the oxidant.[209,210,211]

The process is illustrated schematically in Figure 7.1. A simplified scheme for the reaction occurring in the reactor vessel is shown in Figure 7.2.[209] The redox reaction is proposed to occur in the aqueous phase following dissolution of the MA from neat MA drops. Subsequently, extraction of the products back into the organic phase occurs. MA thereby acts as reactant and organic solvent, and further oxidation is possible by dissolution and reaction (Figure 7.2).

The reaction mechanism was previously studied experimentally using homogeneous kinetic measurements,[209,210,211] and through measurement of the two-phase reaction with stirred suspensions of droplets, however, the effect of varying concentrations of reactants on the product distribution was a major concern.[209,210,211] Reaction at the interface was previously discounted, and all chemical reactions were assumed to occur homogeneously in the aqueous phase.

Once again, the aim of this study was to determine the mechanism and rate of the reaction by direct measurement of concentration profiles to resolve whether the reaction was truly homogeneous, heterogeneous or in a mixed regime. The use of MEMED is particularly appropriate since the experimental system can be related readily to the stirred droplet geometry employed in industrial synthetic processes.

7.2 Measurement of the Rate of Hydrolysis of Triphenylmethyl Chloride using MEMED

The interfacial reaction (equation 7.1) was investigated by employing a potentiometric Ag/AgCl ultramicroelectrode probe to measure local changes in the chloride ion concentration in the aqueous receptor phase near to an expanding DCE drop in which TPMCl was dissolved.

7.2.1 The Probe Electrode

The construction of the indicator electrode was different to those used thus far, a 50 μm diameter wire, insulated with a thin layer of polyester insulation, and coated with an AgCl film was used. Despite the relatively large size of the
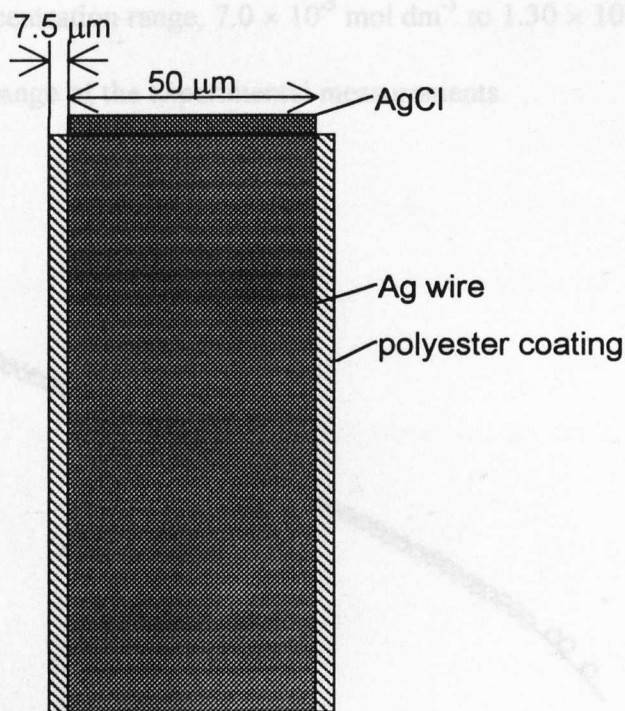
Figure 7.3   Diagram of the AgCl coated microwire chloride probe.

electrode, the insulation dimensions were minimised to ensure that mass transport

at the expanding drop was not significantly perturbed during measurements. The

geometry of this type of electrode is illustrated schematically in Figure 7.3. The

relatively large diameter of the electrode should not compromise the resolution in

the direction normal to the electrode. All Potentials were measured vs. SCE. As

outlined in the previous chapter, potentiometric detection ensured that there was

no electrolytic perturbation of the concentration profile of the analyte. Potential

changes were measured as a function of time for a complete drop period and were

converted to concentrations by first calibrating the electrode over the full range of

chloride ion concentrations observed experimentally. A typical calibration curve is

shown in Figure 7.4. A fourth order regression line was fitted to the data, from

which the [Cl⁻] was calculated, from the measured potential, E/mV. The

calibration curve is linear, with a slope of 58.4 mV per decade change in ([Cl⁻] /

mol dm^{-3}), over the concentration range, 7.0×10^{-5} mol dm^{-3} to 1.30×10^{-2} mol

dm^{-3}, which covers the range of the experimental measurements.
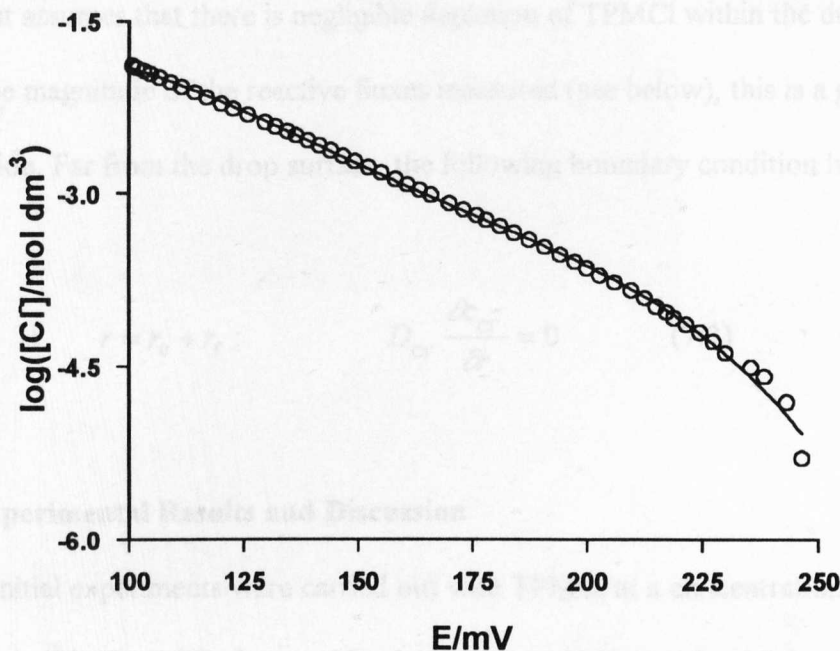
Figure 7.4   Calibration curve for a typical Ag/AgCl electrode, the solution
contained 0.1 mol dm^{-3} KNO$_3$, and phosphate buffer set at pH 6.9.
The solid line indicates a fourth order regression line of equation: y
= ((((-1.246 $\times$ 10^{-8} $\times$ x + 7.814 $\times$ 10^{-6}) $\times$ x $-$1.812 $\times$ 10^{-3}) $\times$ x +
0.16620) $\times$ x $-$ 6.9635. The linear portion has a slope of 58.4 mV
per decade change in ([Cl$^-$] / mol dm^{-3}), over the concentration
range, 7.0×10^{-5} mol dm^{-3} to 1.30×10^{-2} mol dm^{-3}.

7.2.2 Theoretical Treatment

The experimental results were analysed theoretically assuming a

heterogeneous (interfacial) hydrolysis process. The flux of chloride at the surface

of the drop was given by:

$$r = r_0 : \qquad D_{Cl^-} \frac{\partial c_{Cl^-}}{\partial r} = k_z \qquad (7.2)$$

where k_z is a pseudo zero-order rate constant for the interfacial reaction. This treatment assumes that there is negligible depletion of TPMCl within the droplet. Given the magnitude of the reactive fluxes measured (see below), this is a good assumption. Far from the drop surface, the following boundary condition holds:

$$r = r_0 + r_f : \qquad D_{Cl^-} \frac{\partial c_{Cl^-}}{\partial r} = 0 \qquad (7.3)$$

7.2.3 Experimental Results and Discussion

Initial experiments were carried out with TPMCl at a concentration of 5×10^{-2} mol dm^{-3} in the DCE phase, while the aqueous phase contained 0.1 mol dm^{-3} KNO$_3$ to maintain a constant ionic strength in the aqueous phase during the hydrolysis process and pH 7 buffer (made with 6.32×10^{-2} mol dm^{-3} potassium dihydrogen phosphate and 3.68×10^{-2} mol dm^{-3} sodium hydroxide; the measured pH was 6.9) to prevent local changes in pH due to the release of protons during the interfacial reaction. A typical potentiometric transient, with $t_d = 2.97$ s and $d_f = 0.967$ mm, is shown in Figure 7.5, which illustrates the changing potential (or chloride ion concentration) with time. The transient has a characteristic shape, which reflects the key stages during the period of growth of one drop as already outlined in the previous chapter, section 6.5.1.1 (Figure 6.7). In this case, a drop in the potential is observed as the drop approaches the electrode, reflecting the increasing concentration of chloride ions due to the hydrolysis process. The video
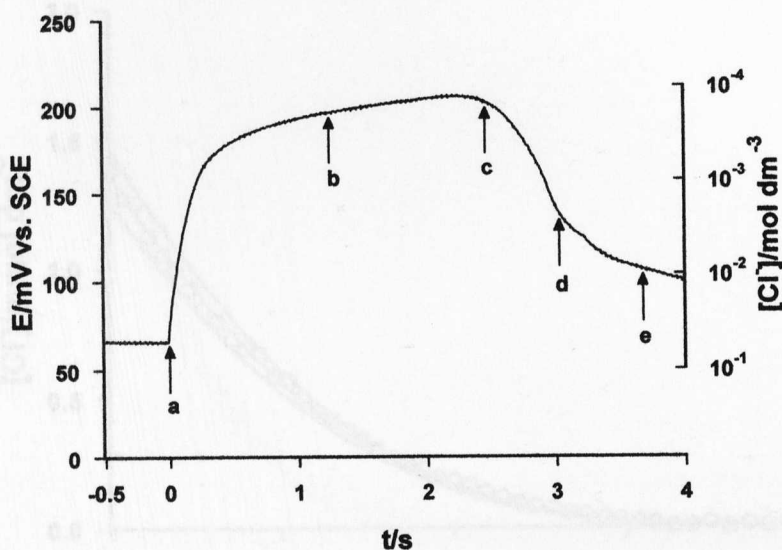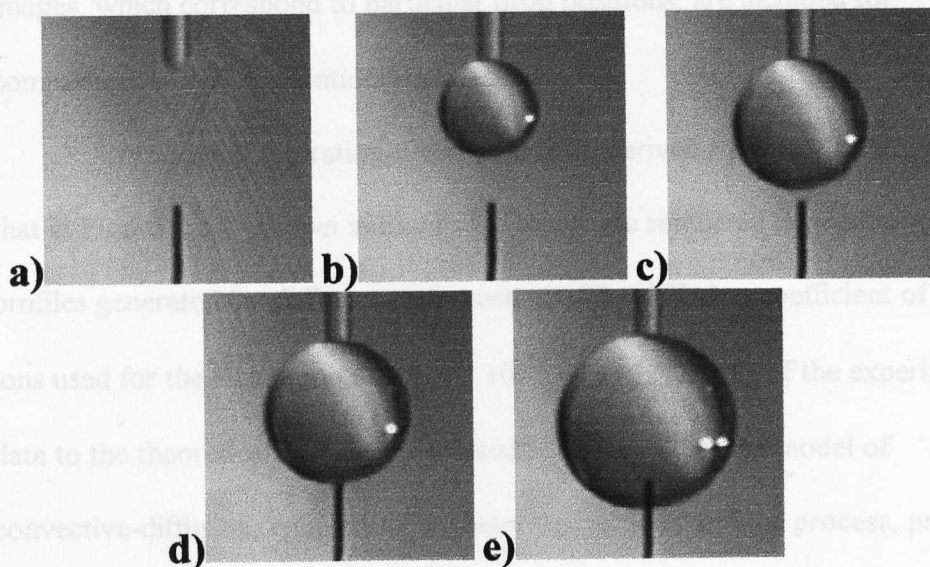
Figure 7.5 Potential (and concentration) vs. time behaviour for chloride ions measured at a 50 μm diameter chloride-sensitive UME positioned beneath an expanding DCE drop containing 5×10^{-2} mol dm^{-3} triphenylmethyl chloride. The images (a) – (e) indicate the relative positions of the capillary, drop and UME, and correspond to the points indicated on the transient. Note that in (e), the electrode is not inside the drop; rather the droplet rolls to one side after contacting the electrode, before finally detaching from the capillary.

images, which correspond to particular drop positions, are included for comparison with the potentiometric data.

A typical concentration-distance profile, derived from raw data such as that in Figure 7.5, is shown in Figure 7.6 alongside simulated concentration profiles generated for different rate constants. The diffusion coefficient of chloride ions used for the simulation was 1.8×10^{-5} cm^2 s^{-1}.[229] The fit of the experimental data to the theoretical concentration profile indicates that the model of convective-diffusion, coupled with a heterogeneous hydrolysis process, provides
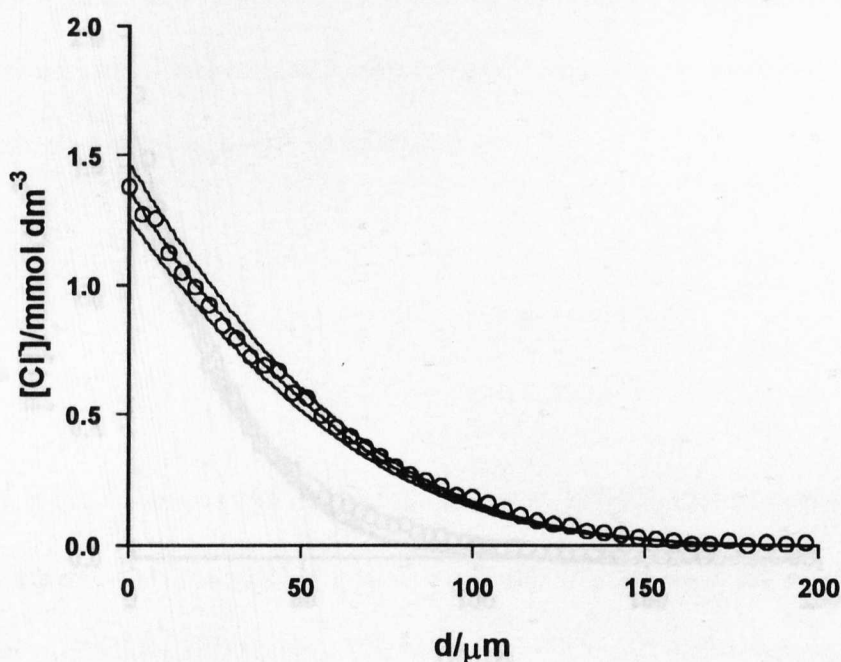
Figure 7.6   Chloride concentration profile recorded by a microelectrode probe during the hydrolysis of TPMCl at a DCE drop/aqueous phase interface (O). The concentration of TPMCl in the organic phase was 5×10^{-2} mol dm^{-3}, the drop time from formation to contact with the probe was 4.80 s and the final drop radius was 0.55 mm. The solid lines represent theoretical time-dependent concentration profiles, from top to bottom, generated for $k_2 = 3.50 \times 10^{-9}$ mol cm^{-2} s^{-1}, 3.25×10^{-9} mol cm^{-2} s^{-1} and 3.00×10^{-9} mol cm^{-2} s^{-1}. A value of 1.8×10^{-5} cm^2 s^{-1} was employed for the diffusion coefficient of chloride ions.

an excellent description of the transport processes and interfacial reaction. The concentration profile also indicates that low concentrations of chloride are produced in the aqueous phase, compared to the bulk concentration of TPMCl in the organic phase, even very close to the interface, validating the assumption that depletion of TPMCl in the drop need not be considered. The interfacial flux of chloride ions measured under these conditions was characterised by a zero order rate constant, $k_z = 3.25 \, (\pm 0.25) \times 10^{-9}$ mol cm^{-2} s^{-1}.
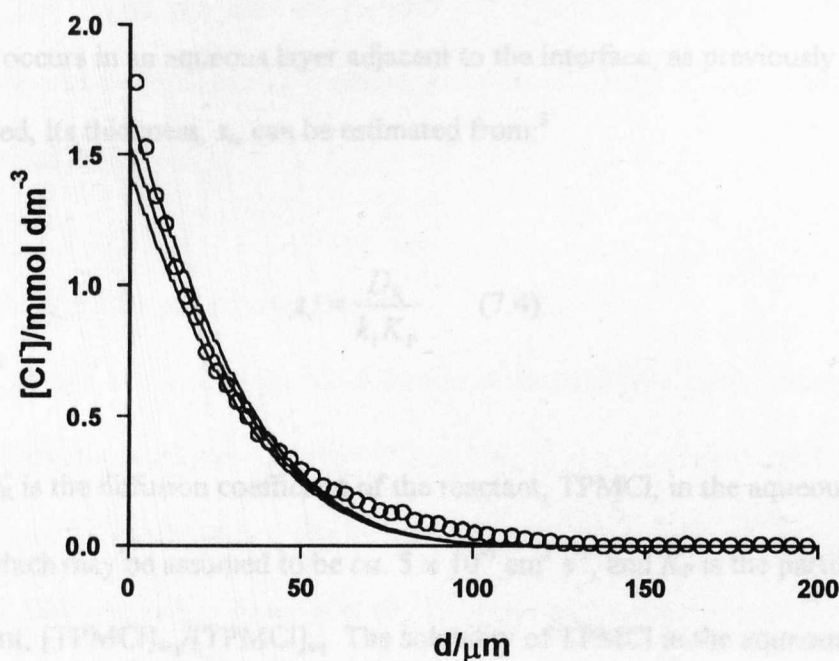
Figure 7.7   Chloride concentration profile recorded by a microelectrode probe during the hydrolysis of TPMCl at a DCE drop/aqueous phase interface (O). The concentration of TPMCl in the organic phase was 0.1 mol dm^{-3}, the drop time from formation to contact with the probe was 1.39 s and the final drop radius was 0.48 mm. The solid lines represent theoretical time-dependent concentration profiles, from top to bottom, generated for $k_z = 7.00 \times 10^{-9}$ mol cm^{-2} s^{-1}, 6.50×10^{-9} mol cm^{-2} s^{-1} and 6.00×10^{-9} mol cm^{-2} s^{-1}. A value of 1.8×10^{-5} cm^2 s^{-1} was employed for the diffusion coefficient of chloride ions.

210

A typical chloride ion concentration profile for the case where the concentration of TPMCl in the organic phase was doubled to 0.1 mol dm^{-3} (all other concentrations were unchanged) is shown in Figure 7.7. The best fit of theory to the experimental data for this case was obtained by considering an interfacial flux of chloride ions of 6.5 ($\pm$ 0.5) $\times$ 10^{-9} mol cm^{-2} s^{-1}. Coupled with the previous data, these results indicate that the interfacial hydrolysis reaction is first-order in [TPMCl] in the organic phase with an effective rate constant, k_1, of 6.5 $\times$ 10^{-5} cm s^{-1}.

As well as giving an accurate value for the rate constant, this approach offers an effective route to directly investigating the location of the reaction. If the reaction occurs in an aqueous layer adjacent to the interface, as previously considered, its thickness, z_r, can be estimated from:[3]

$$z_r = \frac{D_R}{k_1 K_P} \qquad (7.4)$$

where D_R is the diffusion coefficient of the reactant, TPMCl, in the aqueous phase, which may be assumed to be *ca.* 5 $\times$ 10^{-6} cm^2 s^{-1}, and K_P is the partition coefficient, [TPMCl]$_{org}$/[TPMCl]$_{aq}$. The solubility of TPMCl in the aqueous phase is estimated as 10^{-8} mol dm^{-3},[212] and in DCE is in excess of 10^{-1} mol dm^{-3}, so that K_P > 10^7. Thus, the reaction layer thickness, z_r < 1 Å indicating that the reaction is interfacial, as found recently for the hydrolysis process at the solid TPMCl/liquid interface.[212]

7.3 Investigation of the Oxidation of Methylanisole by Cerium (IV) Solutions

The oxidation of MA by aqueous sulfuric acid solutions of Ce(IV) has been considered to occur via the initial dissolution of MA into aqueous solution, followed by a homogeneous oxidation reaction.[209,210,211] In order investigate whether this is indeed the case, the dissolution of MA from drops of the neat reactant was first measured by the MEMED method. Subsequently, in order to probe the two-phase reaction, the form of the MA and Ce(IV) concentration profiles were probed directly, after introducing Ce(IV) into the bulk of the aqueous (receptor) phase. The homogeneous reaction kinetics for the reaction between Ce(IV) and MA were measured separately using UV/visible spectrophotometry, so that all possible steps in the oxidation process could be characterised individually.

7.3.1 Voltammetry of MA and Ce(IV)

The two-phase reaction was followed in the MEMED configuration by amperometric measurement of both MA and Ce(IV) at a 1 μm diameter Pt UME in the aqueous receptor phase. The voltammetric responses for Ce(IV) reduction at a 1 μm diameter and a 25 μm diameter Pt UME are shown in Figure 7.8. This redox couple shows significant irreversibility at both electrodes, with $E_{3/4} - E_{1/4}$ of 107 mV and 229 mV at the 1 μm diameter and 25 μm diameter Pt UMEs, respectively. It has previously been pointed out that the mechanism of the electron transfer reaction for the Ce(IV) / Ce(III) couple at a Pt electrode surface is not simple, and involves complex intermediate species.[230] The oxidation of Ce(III) occurs beyond the solvent window and cannot therefore be observed. The Ce(IV) concentration may be measured by amperometry, and the diffusion coefficient of

212

Ce(IV) under these solution conditions calculated from the steady-state reduction

current at a 25 μm diameter Pt UME (Figure 7.8(b)), $D_{Ce(IV)} = 4.6 \times 10^{-6}$ cm^2 s^{-1}

agrees reasonably with the value measured previously using a rotating disc

electrode.[230]
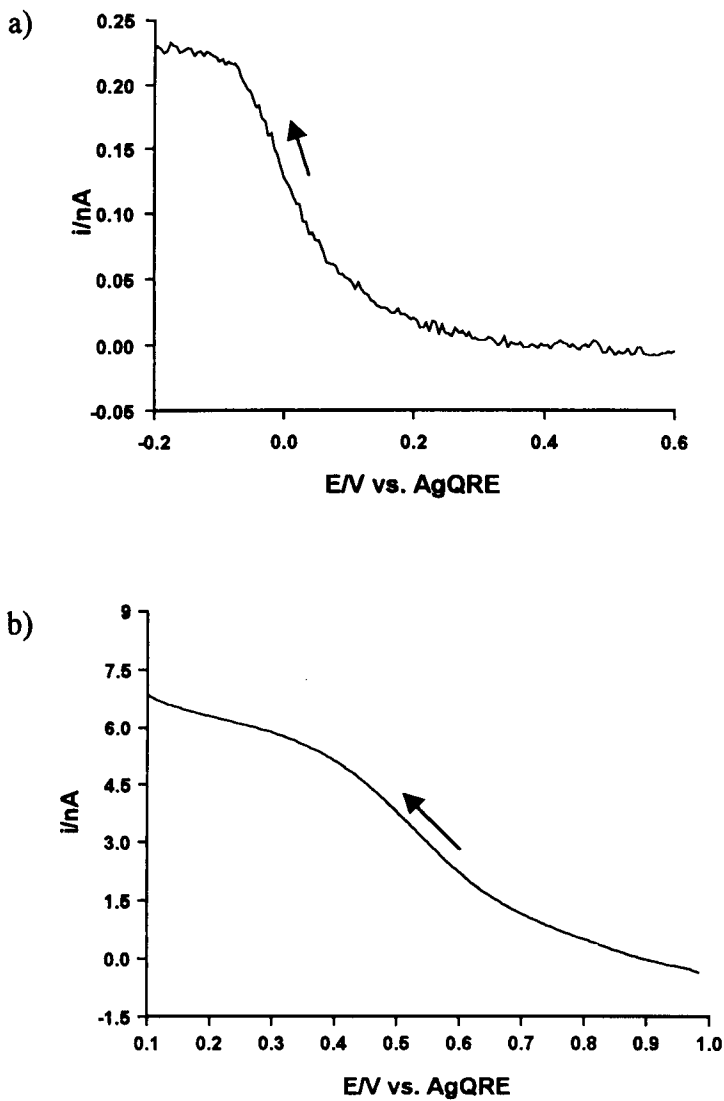
Figure 7.8   Voltammograms recorded for the reduction of Ce (IV) at a) a 1 μm diameter Pt UME and b) a 25 μm diameter Pt UME. The aqueous solution contained 3×10^{-3} mol dm^{-3} Ce(SO$_4$)$_2$ in 1 mol dm^{-3} H$_2$SO$_4$ and the scan rate used was 10 mV s^{-1}.
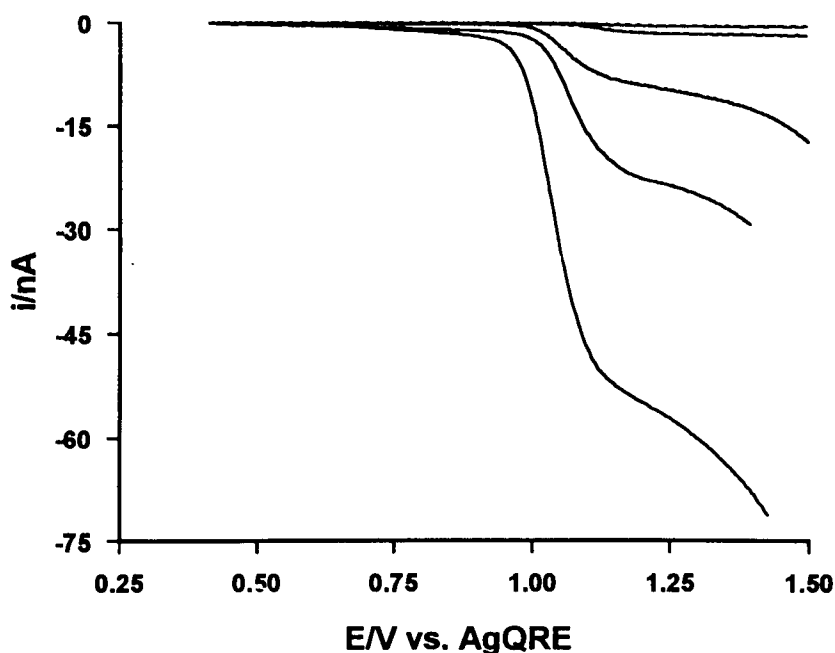
Figure 7.9 Voltammograms recorded for the oxidation of MA at a range of Pt UMEs of diameter, top to bottom, 1, 2, 10, 25 and 50 μm. The aqueous solution was saturated with MA in 1 mol dm^{-3} H$_2$SO$_4$. Scan speeds varied; 200 mV s^{-1} for the 1 and 2 μm diameter UMEs, 100 mV s^{-1} for the 10 μm diameter UME and 20 mV s^{-1} for the 25 and 50 μm diameter UMEs.

The voltammetry of MA is less straightforward. A series of voltammograms, recorded at a range of UME sizes are shown in Figure 7.9. It was necessary to use fast scan speeds to record the voltammograms in order to prevent blocking of the electrode by products, as found in previous rotating disc electrode studies.[209] The ratio i_{lim} / a, which should be invariable for an uncomplicated electron transfer reaction (see equation 1.10) shifts from larger to smaller values as the electrode size is decreased, due to an increase in the rate of mass transfer to the electrode (see equation 6.15).

Rotating disc electrode studies of MA oxidation at Pt electrodes found a two-electron process, invariant with rotation speed (up to 50 Hz), from which a diffusion coefficient of 4.5×10^{-6} cm^2 s^{-1} was deduced for MA.[209] The mass transfer rate for a rotating disc electrode with a rotation frequency of 50 Hz (equation 1.5) is double the mean mass transfer coefficient at a 50 μm diameter UME, so that a 50 μm diameter UME may also be expected to show a two-electron process for MA oxidation. The effective number of electrons transferred, n_{eff}, for the other electrode sizes may then be calculated from the limiting currents, resulting in the values shown in Table 7.1. The apparent trend of decreasing n_{eff}, between two and one electrons, with increasing k_t is indicative of a more complicated electron transfer reaction, in which the interfacial electron transfer steps are coupled to an interposed homogeneous solution reaction. This observation is consistent with previous studies of the oxidation of MA in a range of solvents, including acetic acid/water,[214,218] methanol,[222] sulfuric acid/acetone[228] and acetonitrile,[227] which has been considered to occur via the ECE process illustrated in Figure 7.10. This mechanism has been suggested for the reaction of MA with oxidising species in solution[214,218,219,222] as well as for direct anodic oxidation of MA.[226,227,228]

Table 7.1   The number of electrons transferred in the oxidation of MA, calculated from the limiting current, for a range of UME sizes.

Electrode radius/μm	n_{eff}
0.5	1.130
1.0	1.253
5.0	1.787
12.5	1.898
25.0	2.000
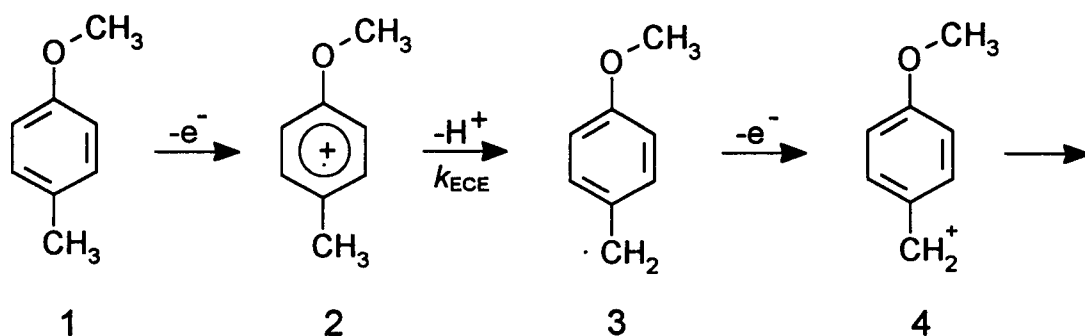
Figure 7.10 Proposed ECE mechanism for the electrochemical oxidation of methylanisole.

In the ECE mechanism the first electron transferred, the E step, forming the cation radical species, occurs at the electrode. In the second (C) step, this species undergoes a chemical reaction in solution, in this case deprotonation, before the second electron is transferred at the electrode (E step). The experimental results are consistent with this, i.e. as the transport rate is increased, with the use of smaller electrodes, then the C step becomes too slow compared to mass transport, and the second E step occurs to a lesser extent due to the rapid diffusion of the initially-formed cation radical away from the electrode surface.

If the results are interpreted in terms of this mechanism, the rate constant, k_{ECE}, for the chemical step can be determined according to equation 7.5.[231]

$$\frac{1}{\Delta n} = \frac{4}{\pi a}\left(\frac{D}{n_2{}^2 k_{ECE}}\right)^{1/2} + \frac{1}{n_2} \quad (7.5)$$

In equation 7.5, $\Delta n = n_{eff} - n_1$, where n_{eff} is the effective total number of electrons transferred, $n_1 = 1$ is the number of electrons transferred in the first step, $n_2 = 1$ is the number of electrons transferred in the second step and D is the diffusion

coefficient of MA. The plot of Δn^{-1} vs. a^{-1} in Figure 7.11, indicates that this analysis provides a good description of the limiting-current data for the oxidation of MA. The rate constant for the deprotonation reaction was found to be, $k_{ECE} = 77 \text{ s}^{-1}$ from the slope of the line.
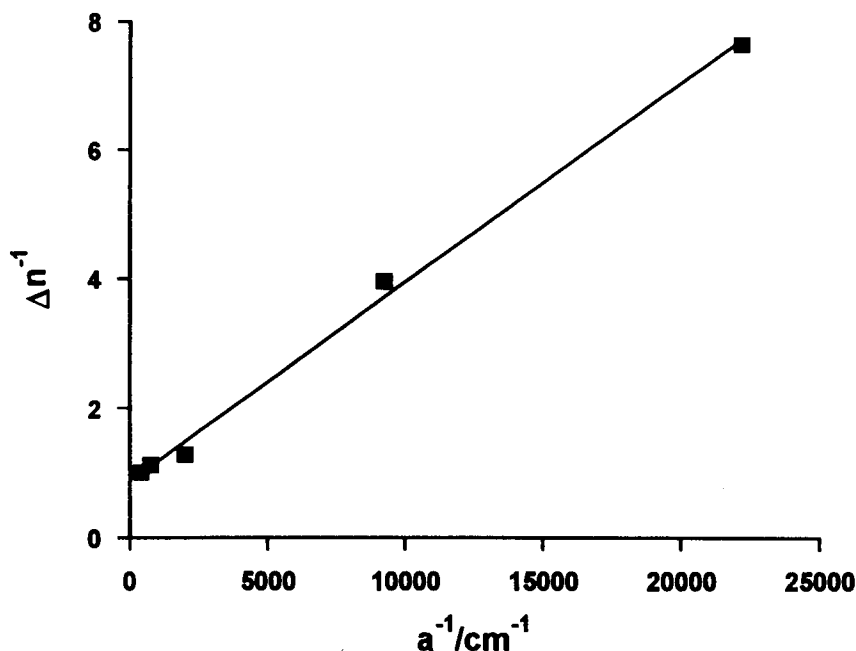
Figure 7.11   Analysis of the limiting current data in Figure 7.9 in terms of equation 7.5, to determine the rate constant for the homogeneous chemical step (deprotonation of the methylanisole radical cation), assuming an ECE process describes the oxidation of MA at the electrode.

Alternatively, a DISP1 mechanism may also account for the observed behaviour, in which species 2 and 3 from Figure 7.10 react together to form species 1 and 4. The rate constant may be calculated, in this case, from equation 7.6.[231]

$$\frac{1}{\Delta n} = \frac{4}{\pi a}\left(\frac{2D}{n_1^2 k_{DISP1}}\right)^{1/2} + \frac{1}{n_1} \quad (7.6)$$

The value of k_{DISP1}, 154 s^{-1}, is simply twice that for the ECE process for this case. This reaction gives the same stoichiometry for the overall reaction, and whichever mechanism holds, the MA radical cation is relatively short-lived with a lifetime $\approx$ 10 ms.

Despite the complicated voltammetry displayed by MA, its concentration measurement in the MEMED arrangement is still possible by amperometry at a 1 μm diameter Pt UME. The only concern is that oxidation products should not block the electrode, but it will be shown below that conditions can readily be chosen such that the electrode response remains stable during a MEMED measurement.

7.3.2 Dissolution of MA in Aqueous Solution from an Expanding Droplet in the Absence of Ce(IV)

As discussed above, since the reaction has been proposed to proceed via the initial dissolution of MA into aqueous solution, and since amperometric detection of MA in aqueous sulfuric acid medium has been proven, the dissolution process was first investigated in the MEMED arrangement.

MA has a slightly lower density than water, $\rho_{MA} = 0.969$ g cm^{-3}, and so the capillary carrying the MA feeder phase was mounted in the base of the cell, while the probe electrode, a 1 μm diameter glass-coated Pt disc UME was positioned directly above it. The syringe pump contained only neat MA, while the cell contained 1.0 mol dm^{-3} sulfuric acid. The UME was biased at 1.2 V vs. AgQRE to oxidise MA at a diffusion-controlled rate. Only the characteristic

approach region of the transient was recorded as it was found that use of the electrode for long periods resulted in a diminution in the current flow, attributed to the deposition of products at the electrode surface. The electrode was also polished before each MEMED approach for this reason. The normalised MA concentration-distance profiles resulting from several experimental runs at different dropping rates are shown in Figure 7.12. The accompanying simulated profiles were obtained from simulations run with the following boundary condition at the surface:

$$r = r_0 : \qquad c_{MA} = c_{MA}{}^* \qquad (7.7)$$

where $c_{MA}{}^*$ is the saturated concentration of MA in the aqueous phase. The value quoted in the literature, $c_{MA}{}^* = 4.26 \times 10^{-3}$ mol dm^{-3},[209] agrees with that observed here. The normalised MA concentration, C_{MA}, corresponds to $c_{MA}/c_{MA}{}^*$. The usual no-flux boundary condition applies at the outer boundary. The MA diffusion coefficient, $D_{MA} = 4.50 \times 10^{-6}$ cm s^{-1} was used in the simulation.

The observation of saturated levels of MA at the interface suggests that the dissolution step is rapid on the MEMED timescale. The excellent agreement between theoretically simulated and experimentally measured concentration profiles confirms that the dissolution of MA into aqueous solutions of sulfuric acid is a transport-controlled process under these conditions.
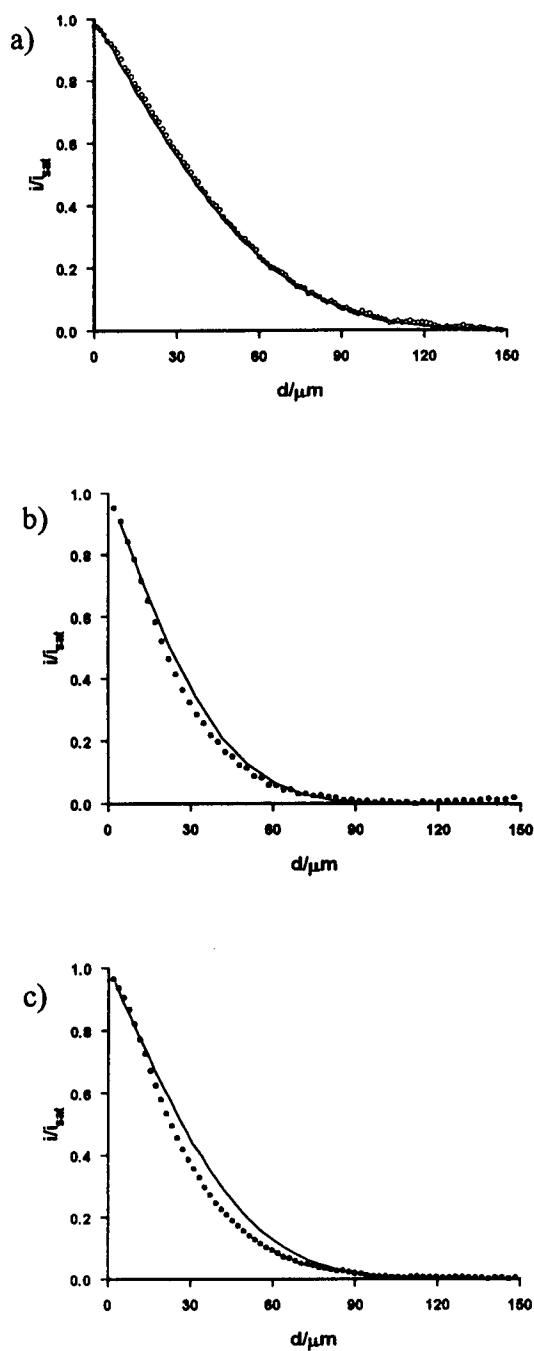
Figure 7.12 Normalised concentration vs. distance from the drop surface behaviour for MA dissolution from a growing droplet of neat MA in 1 mol dm^{-3} H$_2$SO$_4$ (O). Drop times were a) 7.18 s, b) 3.59 s, c) 4.28 s, the solid line indicates the simulated response for mass-transport controlled dissolution.

220

7.3.3 Rate of the Homogeneous Reaction of MA with Ce(IV)

Having identified that the dissolution of MA is transport-controlled, it was necessary to determine the rate equation for the reaction between MA and Ce(IV) in the sulfuric acid solution. Based on earlier studies of the oxidation of substituted methylbenzenes, the reaction is proposed to occur via the following steps:[214,218,219,222]

$$MA + Ce\,(IV) \underset{k_{h-1}}{\overset{k_{h1}}{\rightleftarrows}} MA_{\bullet}^{+} + Ce\,(III) \qquad (7.8)$$

$$MA_{\bullet}^{+} \xrightarrow{\;k_{h2}\;} MA^{\bullet} + H^{+} \qquad (7.9)$$

$$MA^{\bullet} + Ce\,(IV) \xrightarrow{\;k_{h3}\;} products \qquad (7.10)$$
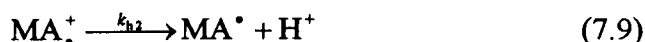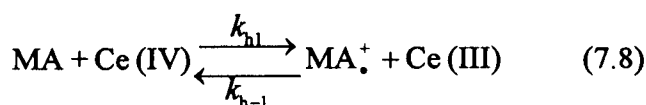
where $MA_{\bullet}^{+}$ is the cation radical, the lifetime of which has already been identified in the anodic oxidation of MA (see section 7.3.1), with a rate constant, k_{h2} in equation 7.9, of 77 s^{-1}. It is assumed that the ECE process, not the DISP1 mechanism, occurs, as will be shown to be the most likely mechanism. MA· is the radical product of the deprotonation reaction which should undergo oxidation, by Ce(IV) or $MA_{\bullet}^{+}$ on a rapid timescale (again based on the electrochemical observation, in section 7.3.1, that MA· is more readily oxidised than MA).

The products formed in this process can also be further oxidised (see scheme in Figure 7.2), but this was not important on the timescale of the homogeneous kinetic studies or the MEMED studies which follow.

The overall kinetics of the solution reaction were followed simply by measuring the initial rate of reaction immediately following mixing of aqueous sulfuric acid solutions of MA and Ce(IV) of known initial concentration. The reaction was probed by measuring the concentration of Ce(IV) spectrophotometrically. UV/visible spectra for MA, Ce(III) and Ce(IV) solutions, as well as a mixed solution of MA and Ce(IV) are shown in Figure 7.13. These spectra illustrate that the absorbance at 320 nm corresponds only to Ce(IV). The molar absorptivity was determined over a range of [Ce(IV)], $\varepsilon = 4.95 \times 10^6$ cm^2 mol^{-1}, enabling the Ce(IV) concentration to be calculated from the Beer-Lambert law, equation 3.2.

A typical Ce(IV) concentration-time curve, for initial concentrations of Ce(IV) and MA of 5.0×10^{-5} mol dm^{-3} and 1.5×10^{-3} mol dm^{-3} respectively, is displayed in Figure 7.14. The rate constant for the reaction may be determined from the slope of a plot of $\log c_{Ce(IV)}$ vs. t, as in the example Figure 7.14(b), using equation 7.11 or, through rearrangement, equation 7.12.

$$\log(c_{Ce(IV),0}/c_{Ce(IV)}) = kt \qquad (7.11)$$

$$\log c_{Ce(IV)} = -kt + \log c_{Ce(IV),0} \qquad (7.12)$$

where $c_{Ce(IV),0}$ is the initial concentration of Ce(IV) at $t = 0$. All measurements of this type were made under isolation conditions, where MA was always in considerable excess. The application of equations 7.11 and 7.12 assumes that the reaction is first order in Ce(IV). The excellent fit of the experimental data to equation 7.12 in Figure 7.14(b) confirms that this is the case and further
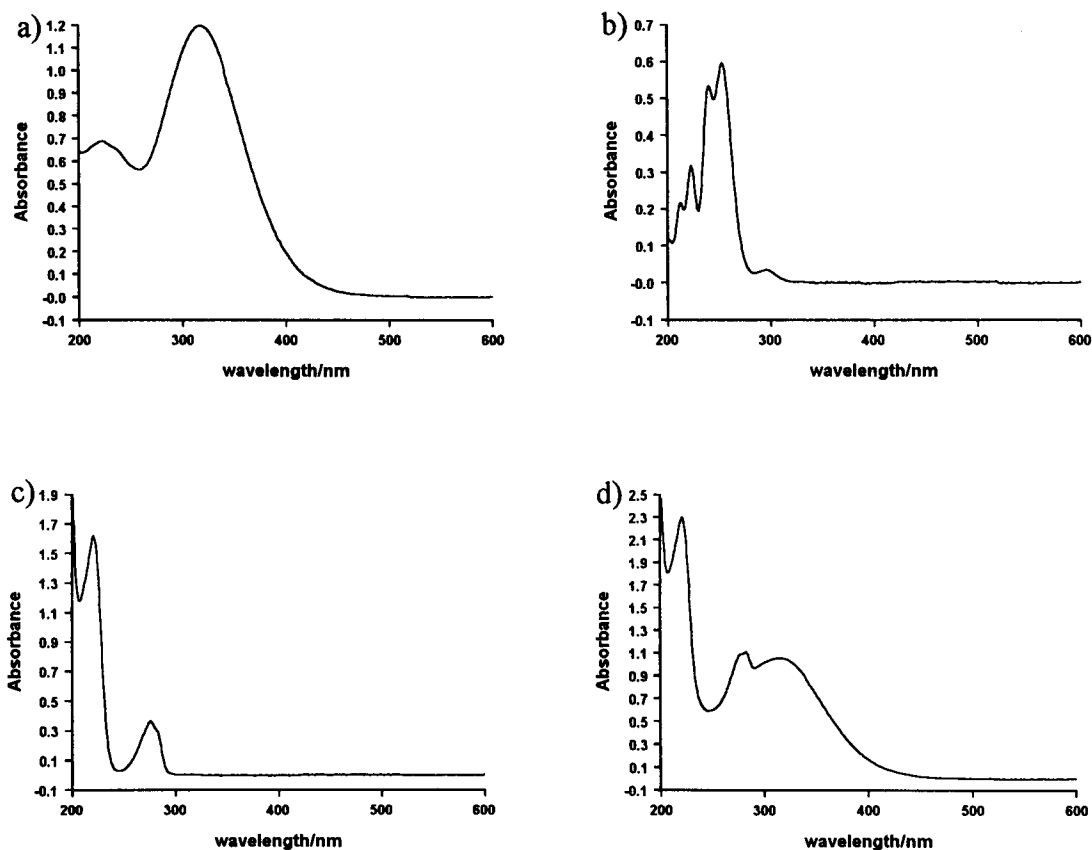
Figure 7.13 UV/visible absorption spectra for the following solutions: a) 2.5×10^{-4} mol dm^{-3} Ce(IV), b) 5×10^{-4} mol dm^{-3} Ce(III), c) 2.5×10^{-4} mol dm^{-3} MA, and d) a 50:50 mix of solutions, one containing 5×10^{-4} mol dm^{-3} Ce(IV) and one with 5×10^{-4} mol dm^{-3} MA, 100 s after mixing. All spectra were obtained in aqueous solutions containing 1 mol dm^{-3} H$_2$SO$_4$.
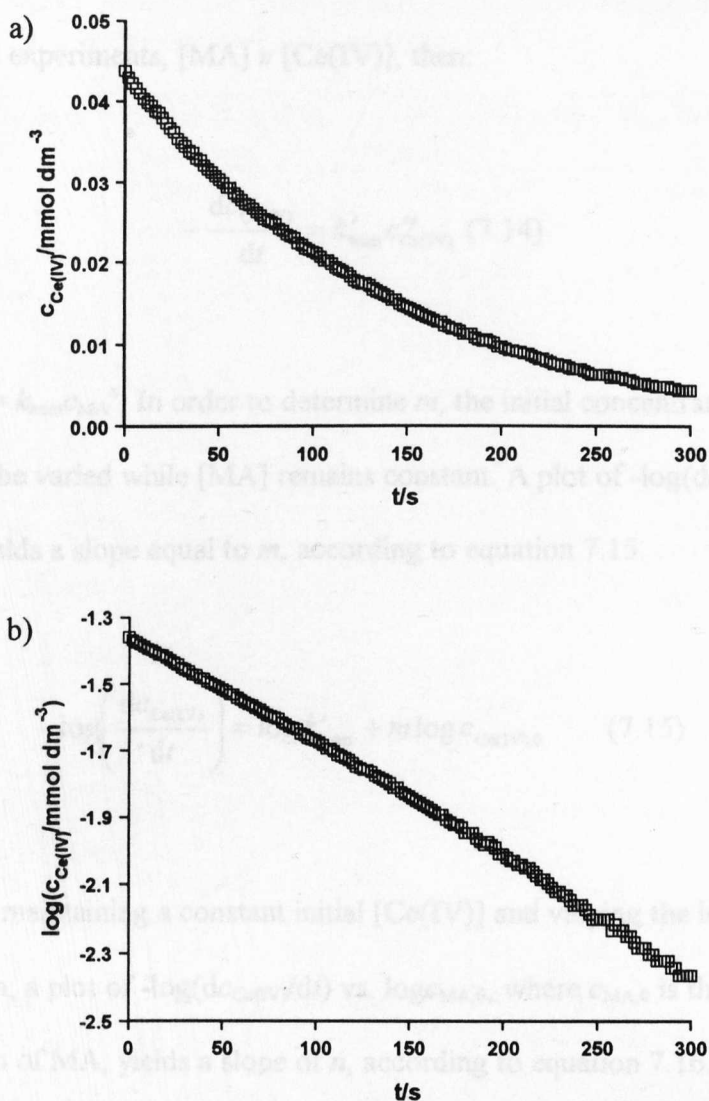
Figure 7.14   a) Plot of the Ce(IV) concentration, measured
spectrophotometrically, as it changes with time for a typical
homogeneous reaction with dissolved MA (initially $c_{Ce(IV)} = 5 \times 10^{-5}$ mol dm^{-3} and $c_{MA} = 1.5 \times 10^{-3}$ mol dm^{-3}). b) Plot of the same
data as log$c$ vs. t.

experiments below will also demonstrate this fact. The rate expression for the

overall reaction may be considered as follows:

$$-\frac{dc_{Ce(IV)}}{dt} = -2\frac{dc_{MA}}{dt} = k_{hom}\,c_{Ce\,(IV)}{}^{m}\,c_{MA}{}^{n} \qquad (7.13)$$

where m and n are the orders of the reaction in Ce(IV) and MA, respectively.

Since, for all experiments, [MA] » [Ce(IV)], then:

$$-\frac{dc_{Ce(IV)}}{dt} = k'_{hom} c^{m}_{Ce(IV)} \quad (7.14)$$

where $k'_{hom} = k_{hom} c_{MA}{}^{n}$. In order to determine m, the initial concentration of Ce(IV) may be varied while [MA] remains constant. A plot of $-\log(dc_{Ce(IV)}/dt)$ vs. $\log c_{Ce(IV),0}$ yields a slope equal to m, according to equation 7.15.

$$-\log\left(\frac{dc_{Ce(IV)}}{dt}\right) = \log k'_{hom} + m\log c_{Ce(IV),0} \quad (7.15)$$

Similarly, by maintaining a constant initial [Ce(IV)] and varying the initial MA concentration, a plot of $-\log(dc_{Ce(IV)}/dt)$ vs. $\log c_{MA,0}$, where $c_{MA,0}$ is the initial concentration of MA, yields a slope of n, according to equation 7.16.

$$-\log\left(\frac{dc_{Ce(IV)}}{dt}\right) = n\log c_{MA,0} + m\log c_{Ce(IV),0} \quad (7.16)$$

The results for a range of experiments are summarised in Table 7.2 and illustrated graphically in Figure 7.15. From the results of these experiments, it can be concluded that the reaction is first order in both $c_{Ce(IV)}$ and c_{MA}, described by the rate equation:

Table 7.2   Rate constant for the homogeneous reaction between MA and Ce (IV), determined from the initial rate of the reaction in solution. k_{hom} was calculated from equation 7.17.

Initial [MA]/mmol dm^{-3}	Initial [Ce(IV)] /mmol dm^{-3}	(-d[Ce(IV)]/dt) /mol m^{-3} s^{-1}	k_{hom}/mol^{-1} m^3 s^{-1}
0.93	0.150	1.646×10^{-4}	1.18×10^{-3}
0.93	0.050	5.164×10^{-5}	1.12×10^{-3}
0.93	0.015	1.234×10^{-5}	8.8×10^{-4}
1.50	0.050	7.410×10^{-3}	9.9×10^{-4}
1.00	0.050	3.988×10^{-3}	7.9×10^{-4}
0.50	0.050	2.493×10^{-3}	1.00×10^{-3}
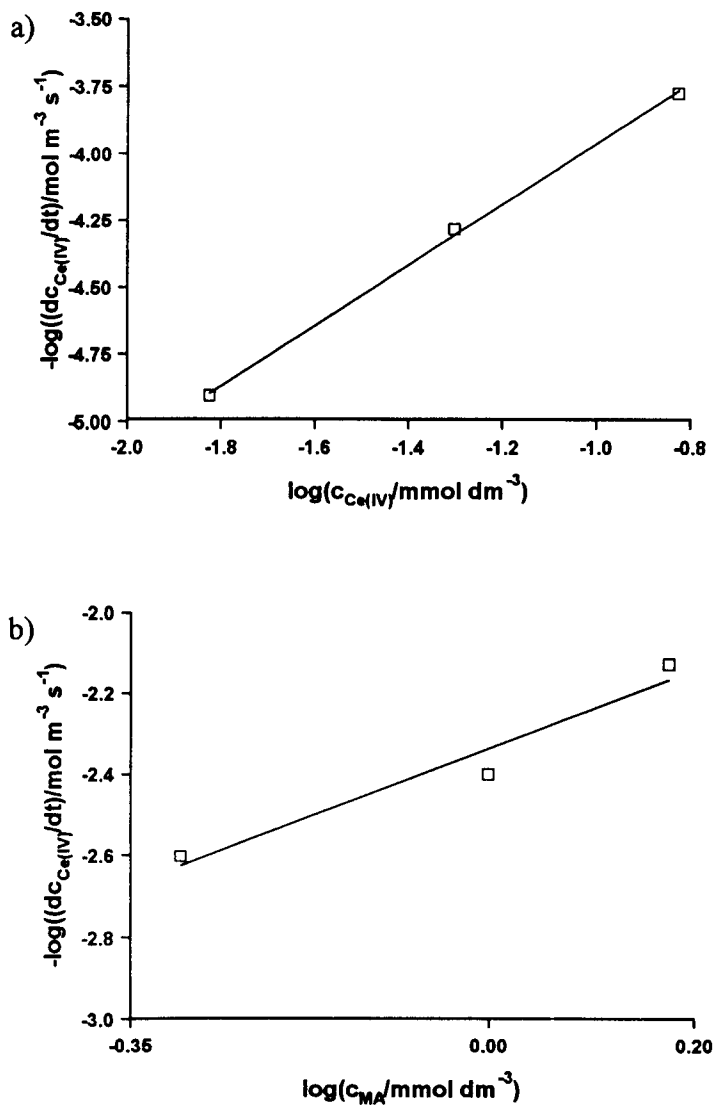
Figure 7.15 $-\log(dc_{Ce(IV)}/dt)$ vs. log initial concentration plots for determining the order of the reaction in MA and Ce(IV). The slopes of the lines are a) 1.13 and b) 0.96.

$$-\frac{dc_{Ce(IV)}}{dt} = -2\frac{dc_{MA}}{dt} = k_{hom}c_{Ce(IV)}c_{MA} \quad (7.17)$$

where the rate constant, calculated as a mean of the measured values, $k_{hom} = 1.0 \times 10^{-3}$ mol^{-1} m^{3} s^{-1}. The order of the reaction with respect to sulfuric acid is not measured, as this concentration remains constant throughout this st idy.

These studies demonstrate that, under the present conditions, the rate determining step for the homogeneous reaction defined in equations 7.8 –7.10 is likely to be the initial electron transfer step (equation 7.8), and that subsequent steps are rapid. This observation contrasts with the results of other oxidation reactions of methylbenzenes by metal ions in solution, where the second step (equation 7.9 in this case) was identified as the slow step.[214,215,216,217,218] However, the conditions used here differ considerably from those previous studies, which employed quite different solvents and oxidants.

7.3.4 Concentration Profiles for MA and Ce(IV) Under MEMED Conditions

The measurement of the MA and Ce(IV) concentration profiles for the system with expanding droplets of MA, and Ce(IV) in aqueous sulfuric acid (receptor phase) is illustrated schematically in Figure 7.16. The Ce(IV) profile was measured by biasing the 1 μm diameter Pt UME at 0.0 V vs. AgQRE during the period of one drop and recording the current for Ce(IV) reduction. The potential was then switched to 1.2 V vs. AgQRE in order to record the MA dissolution profile on a subsequent drop. The electrode was then removed and polished before subsequent runs, avoiding problems from the contamination of the electrode which might arise from prolonged electrolysis of MA, in particular.
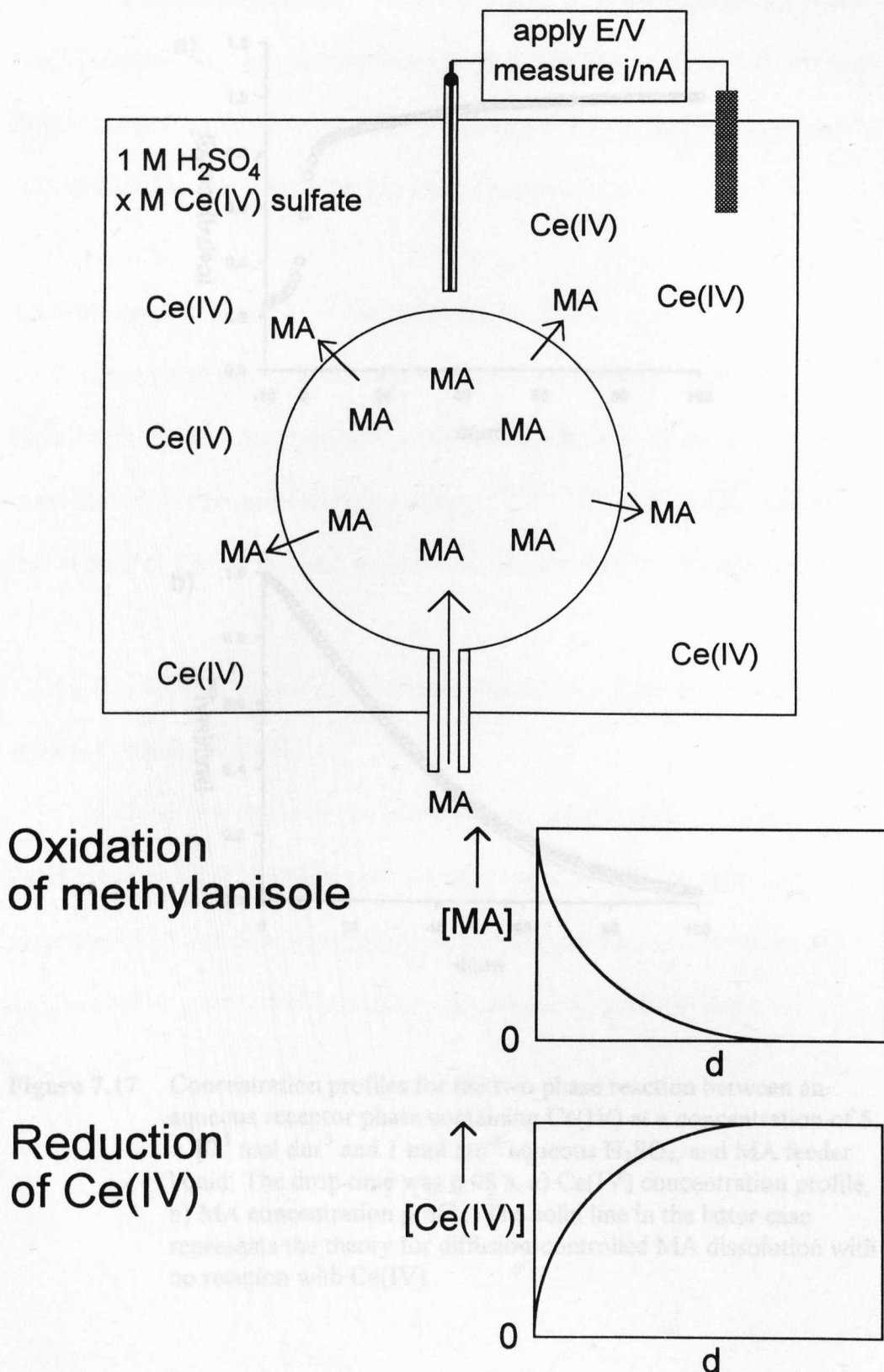
Figure 7.16 Schematic illustration of the method for measuring the two-phase reaction between MA and Ce(IV) by amperometric determination of the concentration profiles of the two reactants.
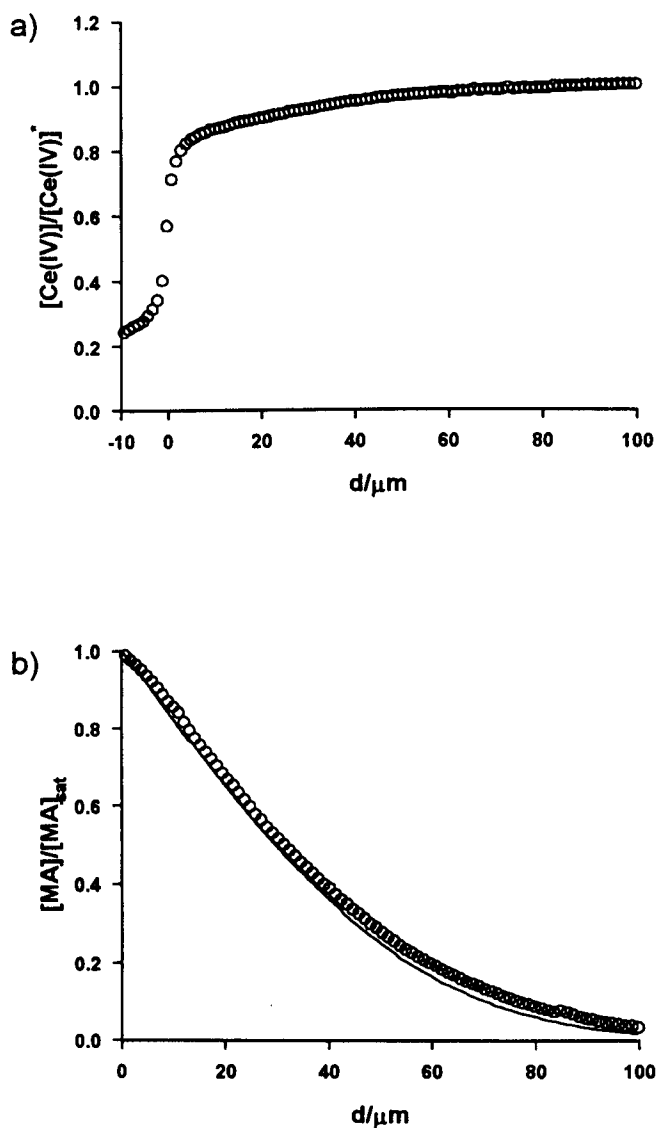
Figure 7.17 Concentration profiles for the two phase reaction between an aqueous receptor phase containing Ce(IV) at a concentration of 5 $\times$ 10^{-3} mol dm^{-3} and 1 mol dm^{-3} aqueous H_2SO_4, and MA feeder liquid. The drop time was 6.08 s. a) Ce(IV) concentration profile, b) MA concentration profile. The solid line in the latter case represents the theory for diffusion-controlled MA dissolution with no reaction with Ce(IV).

The typical concentration profiles in Figure 7.17, correspond to MA and Ce(IV) concentrations for a drop time of 6.08 s. The MA profile is little changed from the dissolution only case (solid line theory), while the Ce (IV) profile can be seen to decrease significantly near to the drop surface.

7.3.5 Theoretical Analysis of MEMED Data

In order to extract kinetic and mechanistic information from the experimental results, concentration profiles were simulated for various kinetic cases. Based on the results of earlier studies,[209,210,211] the first case to consider was the reaction of Ce(IV) and MA in solution only, preceded by MA dissolution.

7.3.5.1 Simulated Concentration Profiles Based on a Homogeneous Reaction Between MA and Ce(IV)

A model that describes the purely homogeneous reaction of MA with Ce(IV) in the MEMED arrangement was developed, to compare with the experimental results. The model, which required consideration of both the MA and the Ce(IV) species, was formulated by considering the following two reactions:

$$MA_{drop} \xrightarrow{\text{rapid}} MA_{aq} \qquad (7.18)$$

$$MA_{aq} + 2Ce\,(IV)_{aq} \xrightarrow{k_{hom}} products \qquad (7.19)$$
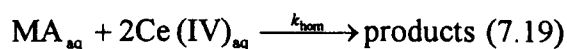
These two processes have been fully characterised above, and so the theoretical concentration profile can be generated for this case with no unknown parameters.

Under these conditions the boundary conditions at the interface for the MA and Ce(IV) are, respectively:

$$r = r_0: \qquad c_{MA} = c_{MA}^* \qquad (7.20)$$

$$r = r_0: \qquad D_{Ce(IV)} \frac{\partial c_{Ce(IV)}}{\partial r} = 0 \qquad (7.21)$$

The initial condition is that for all $r > r_0$, the normalised MA and Ce(IV) concentrations are, $C_{MA} = 0$ and $C_{Ce(IV)} = 1$. MA and Ce(IV) concentrations are normalised by the saturated MA concentration, c_{MA}^*, and the bulk solution Ce(IV) concentration, c_{Ce}^*, respectively.

The homogeneous reaction is represented by equation 7.17. This reaction modifies the convective-diffusion equations, resulting in new expressions for Ce(IV) and MA:

$$\frac{\partial c_{Ce(IV)}}{\partial t} = D_{Ce(IV)} \left(\frac{\partial^2 c_{Ce(IV)}}{\partial r^2} + \frac{2}{r} \frac{\partial c_{Ce(IV)}}{\partial r} \right) - v_r \frac{\partial c_{Ce(IV)}}{\partial r} - k_{hom} c_{Ce(IV)} c_{MA} \qquad (7.22)$$

$$\frac{\partial c_{MA}}{\partial t} = D_{MA} \left(\frac{\partial^2 c_{MA}}{\partial r^2} + \frac{2}{r} \frac{\partial c_{MA}}{\partial r} \right) - v_r \frac{\partial c_{MA}}{\partial r} - \frac{1}{2} k_{hom} c_{Ce(IV)} c_{MA} \qquad (7.23)$$

These expressions may be solved consecutively at each time step within the model, applying the boundary conditions, equations 7.20 and 7.21, to generate simulated concentration profiles for both Ce(IV) and MA.

The simulation is first demonstrated for a range of homogeneous reaction rates with typical drop parameters, $t_d = 5$ s, $r_f = 0.5$ mm, with $c_{Ce}^* = 5 \times 10^{-3}$ mol

231

dm^{-3} and c_{MA}^{*} = 5 × 10^{-3} mol dm^{-3}, and the same diffusion coefficient for each

species, D = 5 × 10^{-6} cm^2 s^{-1}. Figure 7.18 illustrates the results of these

simulations. It can be seen that as the homogeneous rate constant increases,

Ce(IV) becomes increasingly depleted close to the interface and the MA profile

becomes steeper, although only noticeably so at k_{hom} > 0.1 mol^{-1} m^3 s^{-1}. Based on

the experimental results obtained, the range of rates was such that the Ce(IV)

profile was the most sensitive kinetic indicator, while the MA profile was less

affected. For this reason, the Ce(IV) profile was mainly used to quantify

experimental rate data.
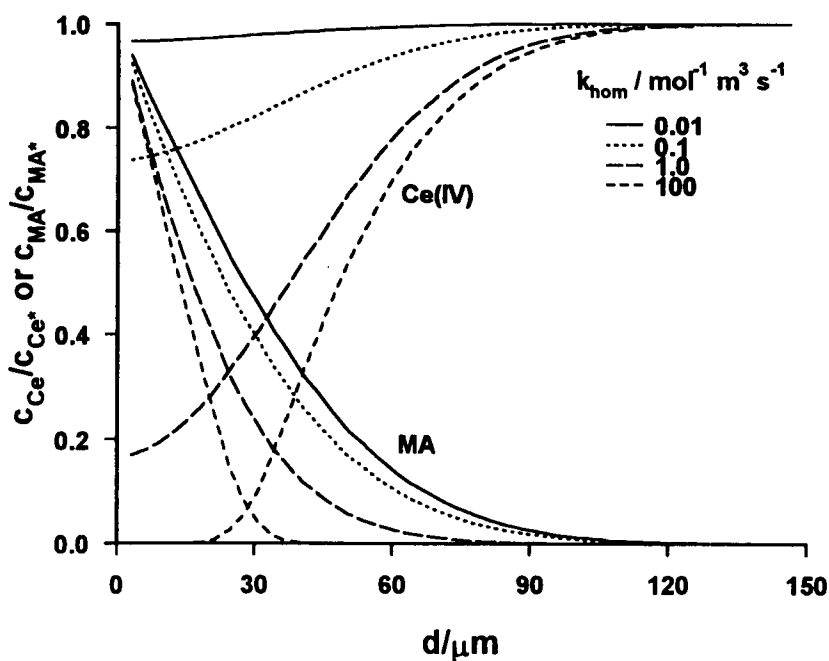
Figure 7.18 Simulated concentration profiles for the two reactants, Ce(IV) and
MA, under homogeneous-only reaction conditions with the rate
constants indicated. The drop time and final drop radius used in
this case were 5 s and 0.5 mm respectively. Ce(IV) concentrations
decrease near the interface while MA concentrations increase.

Typical MA and Ce(IV) concentration profiles measured experimentally are displayed in Figure 7.19 alongside the simulated response based on equations 7.18 and 7.19, with the homogeneous rate constant deduced in section 7.3.3. The model predicts a relatively small change in the Ce(IV) concentration, indicating that under these experimental conditions, the homogeneous mechanism does not adequately describe the experimental observations. The experimentally-observed depletion of Ce(IV) must therefore be attributed to a heterogeneous, interfacial reaction.

7.3.5.2 Simulated Concentration Profiles Based on an Interfacial Reaction Between MA and Ce(IV)

Based on the above observations, the homogeneous reaction between dissolved MA and Ce(IV) may be neglected, and the reaction between MA and Ce(IV) be considered to instead occur interfacially as follows:

At the interface: $\qquad MA_{drop} + Ce(IV)_{aq} \xrightarrow{k_{het}} MA^{+}_{\bullet aq} + Ce(III)_{aq}$ (7.24)
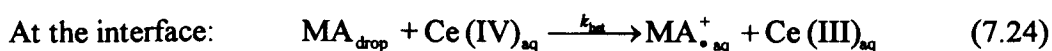
where k_{het} is the heterogeneous rate constant. The solution reactions, equations 7.9 and 7.10 also apply, however, considering the lifetime of the radical cation ($\approx$ 10 ms), its diffusion length, d_D, into the aqueous phase is limited:

$$d_D = \sqrt{\frac{D}{k_{ECE}}} \quad (7.25)$$
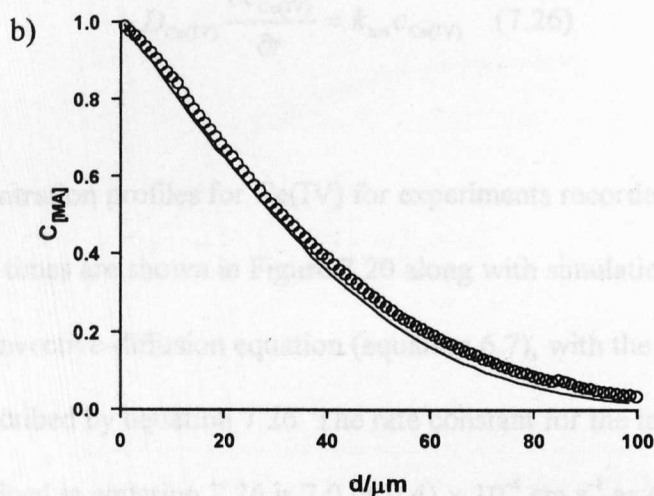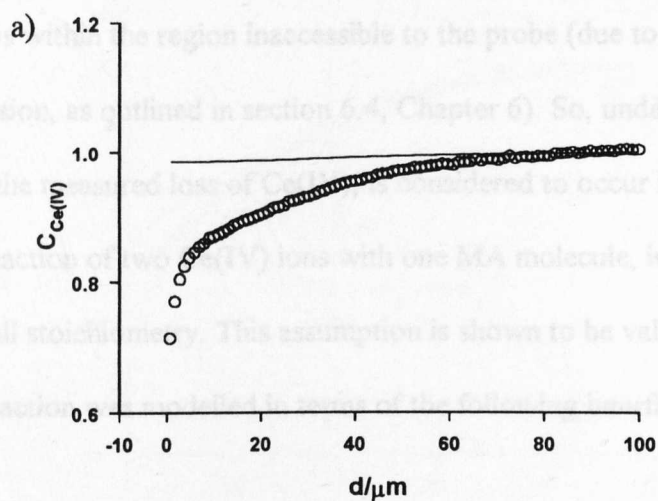
Figure 7.19 Concentration profiles for the two-phase reaction between a Ce(IV) receptor phase, and MA feeder liquid. The drop time was 6.08 s. a) Ce(IV) concentration profile, b) MA concentration profile. The solid lines represent the theoretical profiles for the homogeneous reaction of MA with Ce(IV) following diffusion-controlled MA dissolution, with $k_{hom} = 1 \times 10^{-3}$ mol^{-1} m^3 s^{-1}.

where for a value of $D = 5 \times 10^{-6}$ cm^2 s^{-1} and the measured k_{ECE}, $d_D = 2.5$ μm. This distance is within the region inaccessible to the probe (due to the onset of hindered diffusion, as outlined in section 6.4, Chapter 6). So, under the conditions of this study, the measured loss of Ce(IV), is considered to occur interfacially through the reaction of two Ce(IV) ions with one MA molecule, in accordance with the overall stoichiometry. This assumption is shown to be valid below.

The reaction was modelled in terms of the following interfacial boundary condition.

$$-D_{Ce(IV)} \frac{\partial c_{Ce(IV)}}{\partial r} = k_{het} c_{Ce(IV)} \quad (7.26)$$

Concentration profiles for Ce(IV) for experiments recorded at two different drop times are shown in Figure 7.20 along with simulations based on solving the convective-diffusion equation (equation 6.7), with the boundary condition, described by equation 7.26. The rate constant for the interfacial reaction described in equation 7.26 is 2.0 ($\pm$ 0.4) $\times$ 10^{-4} cm s^{-1} as determined by this method. Note that this model assumes that MA continues to dissolve at a diffusion controlled rate, unaffected by the heterogeneous reaction (which proceeds at a rather slow rate). This is found to be the case experimentally (see Figure 7.17).

Reaction profiles, which included the effect of the homogeneous reactions involving MA$^+$, were simulated for completeness. In this case, the concentration profiles for both Ce(IV) and MA$^+$ were calculated. In accordance with equation 7.24, the boundary conditions for Ce(IV) and MA$^+$ were:

235

$$-D\frac{\partial c_{Ce(IV)}}{\partial t} = D\frac{\partial c_{MA}}{\partial t} = k'_{het}c_{Ce(IV)} \quad (7.27)$$

This assumes that the MA radical cation produced diffuses into the aqueous phase, which is likely to be the case in order to maintain electroneutrality of both phases. The MA$^+$ radical cation decays in the bulk according to equation 7.9,

the loss of Ce(IV) homogeneously (*via* equation 7.10) which may be expressed

$$\frac{\partial c_{MA}}{\partial t} = k_{hom}c_{MA} \quad (7.28)$$

Assuming that MA$^+$ is short lived, which is valid based on the relatively high concentration of Ce(IV) in solution, and the fact that the reaction will be driven, the steady-state approximation may be applied to MA$^+$:

$$\frac{\partial c_{MA}}{\partial t} = k_{het}c_{MA} - k_{het}c_{MA}c_{Ce(IV)} = 0 \quad (7.29)$$

from which an expression for the concentration of MA$^+$ is obtained:

Figure 7.20 Ce(IV) concentration profiles recorded during reaction of Ce(IV) with MA in the MEMED arrangement, with drop times of a) 6.08 s and b) 3.80 s. The solid lines represent the theoretically predicted behaviour based on a heterogeneous reaction at the interface with the rate constants indicated.

The loss of Ce(IV) homogeneously (*via* equation 7.10) can be expressed as

$$\frac{\partial c_{Ce(IV)}}{\partial t} = k_{het}c_{MA}c_{Ce(IV)} \quad (7.31)$$

$$-D\frac{\partial c_{Ce(IV)}}{\partial r} = D\frac{\partial c_{MA^{+}_{\bullet}}}{\partial r} = k'_{het}\, c_{Ce(IV)} \quad (7.27)$$

This assumes that the MA radical cation produced diffuses into the aqueous phase, which is likely to be the case, in order to maintain electroneutrality of both phases. The $MA^{+}_{\bullet}$ radical cation decays in solution according to equation 7.9,

$$-\frac{\partial c_{MA^{+}_{\bullet}}}{\partial t} = k_{h2}c_{MA^{+}_{\bullet}} \quad (7.28)$$

Assuming that $MA\cdot$ is short lived, which is valid based on the relatively high concentration of Ce(IV) in solution, and the fact that the reaction will be driven, the steady-state approximation may be applied to $MA\cdot$:

$$\frac{\partial c_{MA\bullet}}{\partial t} = k_{h2}c_{MA^{+}_{\bullet}} - k_{h3}c_{MA\bullet}c_{Ce(IV)} = 0 \quad (7.29)$$

from which an expression for the concentration of $MA\cdot$ is obtained:

$$c_{MA\bullet} = \frac{k_{h2}c_{MA^{+}_{\bullet}}}{k_{h3}c_{Ce(IV)}} \quad (7.30)$$

The loss of Ce(IV) homogeneously (via equation 7.10) can be expressed as:

$$-\frac{\partial c_{Ce(IV)}}{\partial t} = k_{h3}c_{MA\bullet}c_{Ce(IV)} \quad (7.31)$$

which, after substitution of equation 7.30, can be written as:

$$-\frac{\partial c_{Ce(IV)}}{\partial t} = k_{h2} c_{MA_.^+} \quad (7.32)$$

The convective-diffusion equations for Ce(IV) and $MA_.^+$ when the interfacial process, described by equation 7.24, is followed by a solution process, defined in equations 7.9 and 7.10, are therefore:

$$\frac{\partial c_{Ce(IV)}}{\partial t} = D_{Ce(IV)}\left(\frac{\partial^2 c_{Ce(IV)}}{\partial r^2} + \frac{2}{r}\frac{\partial c_{Ce(IV)}}{\partial r}\right) - v_r \frac{\partial c_{Ce(IV)}}{\partial r} - k_{h2} c_{MA_.^+} \quad (7.33)$$

$$\frac{\partial c_{MA_.^+}}{\partial t} = D_{MA_.^+}\left(\frac{\partial^2 c_{MA_.^+}}{\partial r^2} + \frac{2}{r}\frac{\partial c_{MA_.^+}}{\partial r}\right) - v_r \frac{\partial c_{MA_.^+}}{\partial r} - k_{h2} c_{MA_.^+} \quad (7.34)$$

This simulation has only one fitting parameter, the heterogeneous rate constant, as the deprotonation rate constant has been measured by voltammetry at UMEs (section 7.3.1). In the simulation, the concentration of $MA_.^+$ was normalised with respect to $c_{Ce(IV)}{}^*$, and the diffusion coefficient, $D = 4.6 \times 10^{-6}$ cm^2 s^{-1}, which was previously determined for Ce(IV), was also used for $MA_.^+$ for simplicity.

The theoretical concentration profile for Ce(IV), simulated by this method, is very close to the profile for a pure interfacial process at an equivalent rate, as illustrated in Figure 7.21(a). Note that for the profiles in Figure 7.21(a), the value
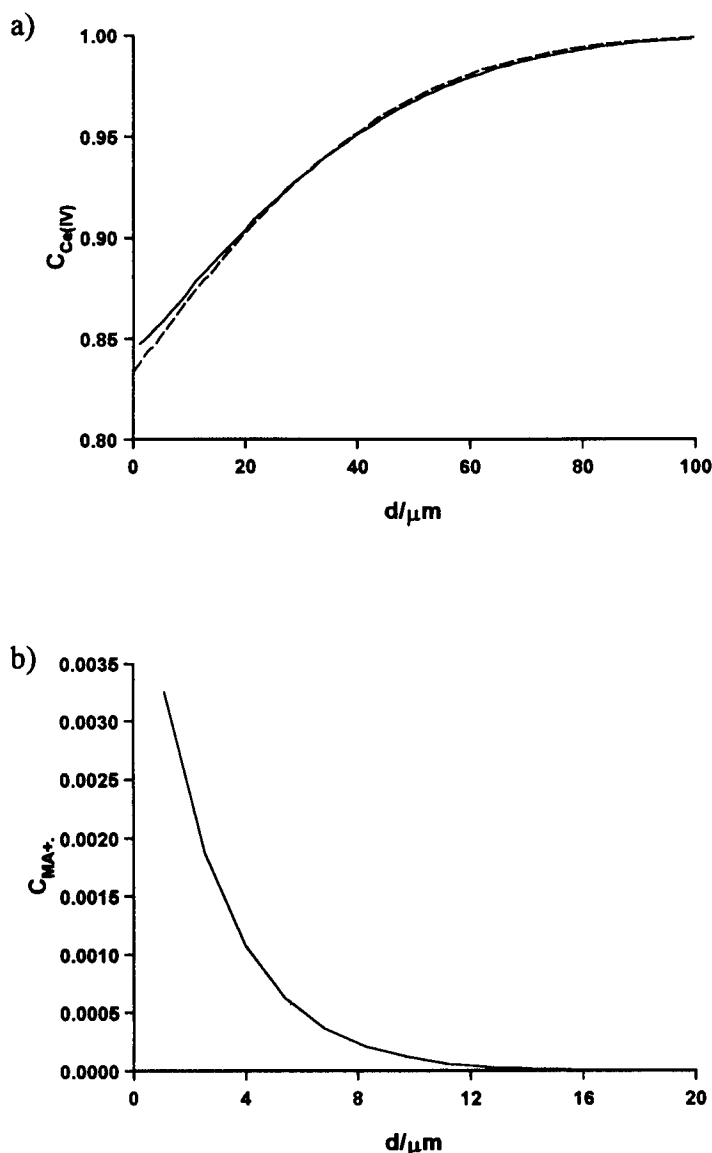
Figure 7.21 Theoretical concentration profiles for a) Ce(IV) and b) MA$^+$., based on the reaction of Ce(IV) with MA in the MEMED arrangement, for the drop time 6.08 s. The solid lines represent the theoretically predicted behaviour based on a combination of heterogeneous and homogeneous reactions as defined by equations 7.33, 7.34 and 7.27, with $k_{het}` = 1.0 \times 10^{-4}$ cm s^{-1}. The dashed line represents the Ce(IV) concentration profile based only on a heterogeneous reaction involving Ce(IV) with a rate constant, k_{het} $= 2.0 \times 10^{-4}$ cm s^{-1}.

of k'_{het} is exactly half that for k_{het}, which indicates that, as expected, the follow-up solution reaction described by equation 7.10 (in which one further Ce(IV) ion is consumed by reaction with MA· after each interfacial reaction event) is rapid on the timescale of these measurements. The MA⁺· profile, Figure 7.21(b), (c.f. the dimensions predicted in equation 7.25) demonstrates that the reaction is essentially confined to the vicinity of the interface, inaccessible to the probe UME. Note that MA· could be lost via a reaction in solution with MA⁺· (disproportionation) rather than with Ce(IV), but this has correctly not been considered due to the much lower concentration of MA⁺· compared to Ce(IV).

7.3.6 Further Discussions

These experiments demonstrate that under the conditions employed, the predominant reaction between Ce(IV) and MA is interfacial, rather than homogeneous, i.e. dissolution of MA followed by reaction in aqueous solution. In fact, the measurements described here enable the heterogeneous reaction to be probed away from the influence of the solution reaction, conditions which are inaccessible to previous approaches used to investigate this process. Being able to determine both the heterogeneous reaction rate and the homogeneous reaction rate separately makes it possible to identify how these two reaction routes would compete under a range of experimental conditions.

Consider the example of an industrial reactor consisting of a suspension of stirred droplets. Figure 7.22 is a kinetic indicator plot for the two-phase reaction, which indicates the relative importance of the heterogeneous and homogeneous reaction routes in terms of certain specific experimental parameters. The rate coefficient, k_t, represents transport of Ce(IV) to the interface, and AV^{-1} is the ratio
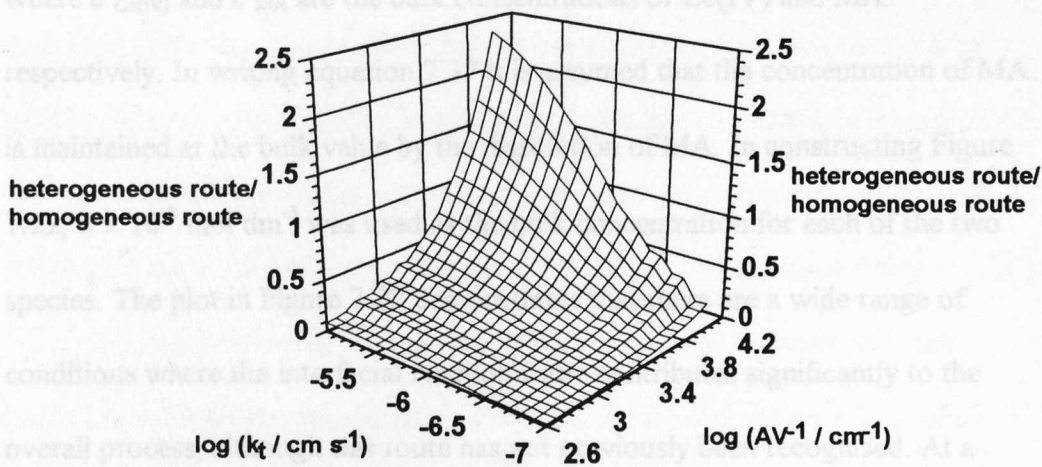
Figure 7.22 Kinetic indicator plot for the two-phase reaction between Ce(IV) and MA, which indicates the relative importance of the heterogeneous and homogeneous reaction routes in terms of the transport rate constant, k_t, and the area to volume ratio, AV^{-1}.

of interfacial area to the volume of the aqueous solution, both of which are crucial parameters to consider in the construction of an industrial reactor. The upright axis represents the relative contributions of the homogeneous and heterogeneous reactions, calculated from equation 7.35.

$$\frac{\text{heterogeneous route}}{\text{homogeneous route}} = \frac{\text{heterogeneous rate} \times AV^{-1}}{\text{homogeneous rate}} \quad (7.35)$$

where the homogeneous and heterogeneous rates are given by:

$$\text{heterogeneous rate} = \frac{k_{\text{het}} k_t c^*_{\text{Ce(IV)}}}{k_{\text{het}} + k_t} \quad (7.36)$$

$$\text{homogeneous rate} = k_{\text{hom}} c^*_{\text{Ce(IV)}} c^*_{\text{MA}} \quad (7.37)$$

241

where $c^{*}_{Ce(IV)}$ and c^{*}_{MA} are the bulk concentrations of Ce(IV) and MA respectively. In writing equation 7.37 it is assumed that the concentration of MA is maintained at the bulk value by the dissolution of MA. In constructing Figure 7.22, 5×10^{-3} mol dm^{-3} was used as the bulk concentration for each of the two species. The plot in Figure 7.22 demonstrates that there are a wide range of conditions where the interfacial reaction route contributes significantly to the overall process, although this route has not previously been recognised. At a general level, the ability to identify new reaction routes by MEMED, to which other techniques are blind, may have important implications in other processes, where competing processes are involved, and where the distribution of products may be effected by the competition between interfacial and homogeneous routes.

Differences between heterogeneous and homogeneous rate constants for bimolecular reactions have been analysed in terms of geometric effects resulting from the reduced dimensionality of interfacial processes.[232] An implication of this work is that the reduction in the dimensionality of the reaction, by transforming a homogeneous to a heterogeneous process, with no change in the activation energy (energetics) of the reaction, is to reduce the rate due to geometric factors alone. This was quantified, and may be described by equation 7.38, which considers the effect in terms of collision theory between a reactant in one phase, A, with a second reactant, B, confined to a supporting surface.

$$\frac{k_{het^{*}}}{k_{hom^{*}}} = \frac{1}{\pi}\left(\frac{m_{B}}{m_{A} + m_{B}}\right)^{1/2}\left(\frac{r_{B}}{r_{A} + r_{B}}\right)^{2}\exp\left(\frac{-\Delta E_{A}}{k_{B}T}\right) \quad (7.38)$$

In equation 7.38, m_A and m_B are the masses of the reactants, and r_A and r_B are their radii. This equation predicts that the heterogeneous reaction rate will be smaller than the corresponding homogeneous rate due to geometric factors alone, disregarding the exponential activation energy term. For typical reactants and conditions, the difference may be of the order of tens to a hundred times.

Having determined rate constants for the reaction between MA and Ce(IV) in solution and interfacially, analysis in terms of equation 7.38 enables important information about the nature of the reaction to be inferred. The first step is to obtain the two rate constants in identical dimensions. For this purpose, the heterogeneous rate constant is converted to the units of the homogeneous reaction as follows. The density of the MA, ρ, is 0.969 g cm^{-3}, and the relative molecular mass, RMM, is 122 g mol^{-1}. The surface density of MA, $\rho^{\backprime}$, in units of molecules cm^{-2}, is therefore:

$$\rho' = \left(\frac{\rho N_A}{RMM} \right)^{2/3} \qquad (7.39)$$

The surface concentration of MA in contact with the aqueous phase is then given by $\rho^{\backprime} / N_A = 5.0 \times 10^{-10}$ mol cm^{-2}. By dividing the heterogeneous rate constant by this value a second order rate constant is obtained, $k_{het2} = 0.4$ mol^{-1} m^3 s^{-1}, which is 400 times larger than the measured homogeneous rate constant.

Evaluating the geometric factors, making the assumption that the masses and radii of the two species are similar, results in an expected reduction in the rate, on going from homogeneous to heterogeneous conditions, of approximately 18 times. So, since the heterogeneous rate is expected to be 18 times smaller than

243

the homogeneous rate from geometric factors alone, it appears to be approximately 7200 times larger due to other factors. On one level, this result may be interpreted as indicating that the interfacial reaction has a smaller activation energy associated with it, which may be calculated from:

$$\frac{1}{7200} = \exp\left(\frac{-\Delta E_A}{R_g T}\right) \quad (7.40)$$

ΔE_A is in the region of 22.0 kJ mol^{-1} smaller for the interfacial process. It has been calculated that for a two phase liquid/liquid reaction, a stabilization of the interfacial transition state of approximately 20 kJ mol^{-1} would lead to the heterogeneous route being favoured.[233]

Several possible reasons exist for this difference between the expected and observed behaviour. In particular, the environment at the interface is quite different to that in bulk solution. In fact, the effect and presence of a mixed solvent region in the vicinity of the interface has been the subject of much consideration in the interpretation of electrochemical measurements[8] and has been treated through molecular dynamics simulations.[83,84,92] If the reaction is treated as occurring in a mixed layer close to the interface, which consists of a high concentration of MA, then the thickness of that layer, z_r, may be determined from equation 7.41.

$$k_{het} = k_{hom} c_{MA} z_r \quad (7.41)$$

If the concentration of MA in this layer is on average 50 % of its bulk phase concentration, i.e. $c_{MA} = \rho_{MA} / (2 \times RMM_{MA}) = 4.0$ mol dm^{-3}, then from the rate constants measured, $z_r = 500$ nm. This is considerably larger than expected, and so it is unlikely that a mixed solvent layer alone can account for the observed rate constants. A further factor may be interfacial potential effects, which may strongly affect this redox reaction. Further studies examining the the effect of potential on the overall kinetics of the of the reaction would be beneficial.

7.4 Conclusions

The MEMED approach has been employed to investigate the kinetics and mechanism of two different two-phase reactions. In the case of the hydrolysis of TPMCl, the reaction was shown to occur at the interface and was first-order in [TPMCl] with a rate constant of 6.5×10^{-5} cm s^{-1}. The reaction between MA and Ce(IV) in a two phase arrangement was shown, under MEMED conditions, to be dominated by the direct interfacial reaction of Ce(IV) with MA at the drop surface, while the homogeneous reaction between Ce(IV) and dissolved MA was slow. The MEMED method allowed this interfacial process to be probed, without the influence of the solution reaction, thereby enabling the accurate determination of the heterogeneous rate constant. This value was then employed to determine important information about the controlling process in industrial reactors, as well as giving information on the fundamental nature of the reaction.

Having demonstrated the strengths of the MEMED technique, it is envisaged that many previously inaccessible processes may be studied quantitatively under the well-defined conditions offered by this methodology.

ABBREVIATIONS

A	species A
ADIFDM	alternating direction implicit finite difference method
AgQRE	silver quasi-reference electrode
B	species B
DCE	1,2-dichloroethane
DISP1	disproportionation reaction
DPSC	double potential step chronoamperometry
ECE	electrochemical – chemical – electrochemical reaction
EP	equilibrium perturbation
HL	oxime ligand (Acorga P50)
ITIES	interface between two immiscible electrolyte solutions
LJRR	liquid jet recycle reactor
MA	methylanisole
MEMED	microelectrochemical measurements at expanding droplets
o	oil phase
Ox or O	oxidised form of redox couple
RDC	rotating diffusion cell
Red or R	reduced form of redox couple
SCE	saturated calomel electrode
SECM	scanning electrochemical microscope/microscopy
SHE	standard hydrogen electrode

TPMCl	triphenylmethyl chloride
UME	ultramicroelectrode
w	water phase
(aq)	aqueous phase
(org)	organic phase

SYMBOLS

a	electrode radius
a_i	activity of species i
A	absorbance
A_e	electrode area
A_{int}	interfacial area
A_s	area per molecule of surface
AV^{-1}	ratio of area to volume
A_0	area per molecule at collapse point
c_a	air phase concentration
c_i	concentration of species i
c_i^*	bulk concentration of species i
c_w	water phase concentration
$c_{w,i}$	water phase concentration at the interface
C	normalised concentration
$C_{w,i}$	normalised water phase concentration at the interface
d	UME-interface separation
d_f	final droplet diameter
d_D	diffusion length
D_i	diffusion coefficient of species i
E	electrode potential
E_A	energy of activation

E_c potential constant

E_{ind} indicator electrode potential

$E_{1/2}$ half-wave potential

$E_{1/4}$ lower quartile potential

$E_{3/4}$ upper quartile potential

E^0 standard electrode potential

$E^{0'}$ formal potential

F Faraday constant

g length dimension

h length dimension

i current

i_{hemi} current measured at a hemispherical-shaped UME

i_{lim} limiting current

i_{L1} current in liquid 1

i_{L2} current in liquid 2

i_t tip current

$i(\infty)$ steady-state diffusion-limited current at a UME in bulk solution

j flux

j_i interfacial reaction flux

j_r overall reaction flux

j_t mass-transport flux

k rate constant

k_b potential dependent electron transfer rate constant

k_e	extraction reaction rate constant
k_f	potential dependent electron transfer rate constant
k_{het}	heterogeneous rate constant
k_{het}'	alternative heterogeneous rate constant
k_{hom}	homogeneous rate constant
k_{hom}'	alternative homogeneous rate constant
k_i	interfacial reaction rate constant
k_{aw}	first-order interfacial transfer rate constant (air – water)
k_{wa}	first-order interfacial transfer rate constant (water – air)
k_{hn}	n = 1, 2, 3: homogeneous reaction rate constant for step n
k_s	stripping reaction rate constant
k_t	mass-transport rate constant
k_z	zero order rate constant
k_B	Boltzmann constant
k_D	diffusional resistance rate constant
k_{DISP1}	rate constant in DISP1 process
k_{ECE}	rate constant in ECE process
k_1	first order heterogeneous rate constant
k_{-1}	first order heterogeneous rate constant
k_{12}	bimolecular electron transfer rate constant
k_0	standard rate constant for electron transfer
k'	zero-order transfer rate constant
K	normalised rate constant

K_1 normalised first order heterogeneous rate constant

K_{ex} equilibrium constant for the extraction/stripping process

K_p partition coefficient

K_v coefficient of voltammetric measurement

l characteristic length

l_m membrane thickness

L normalised electrode-interface separation

m reaction order

m_i molecular mass of species i

n reaction order

n_e number of electrons

n_{eff} effective number of electrons

nr number of points in radial direction in MEMED simulation

N_A Avogadro number

pKa   acid dissociation constant

P permeability constant

P_i product species, phase i

q volume flow rate

r radial coordinate

r_f final drop radius

r_{glass} radius of electrode and glass sheath

r_{hemi} radius of hemispherical geometry UME

r_i radius of species i

r_t	radius at time t
r_0	drop radius
R	normalised radial coordinate
R_g	molar gas constant
R_s	solution resistance
Re	Reynolds number
RG	characteristic dimension of UME
RMM	relative molecular mass
R_i	reactant species, phase i
Sc	Schmidt number
t	time
t_d	drop time
t_{ss}	time to reach steady-state
t_{switch}	switching time
T	temperature
v	velocity
v_r	radial velocity
V	volume
V_r	normalised radial velocity
x	stoichiometric value
y	stoichiometric value
z	cylindrical coordinate
z_r	thickness of reaction layer

Z	normalised cylindrical coordinate
α	coefficient of electron transfer
α_m	membrane porosity
β	coefficient of electron transfer
δ_D	diffusion layer thickness
δ_H	hydrodynamic boundary layer thickness
δ_{UME}	mean diffusion layer thickness at a disc-shaped UME
ε	molar absorptivity
κ	Ilkovich constant
π	surface pressure
θ	fraction of surface free from surfactant
ρ	density
ρ'	surface density
τ	normalised time
τ_{switch}	normalised switching time
ω	rotation frequency (Hz)
φ	coefficient of voltammetric measurement
ν	kinematic viscosity
λ	ratio of reaction rate constant to transport rate constant
λ_i	diffusion coefficient ratio
$\Delta_w^o\varphi$	potential drop across the interface
$\Delta_w^o\varphi^0 i$	standard potential for transfer of species i across the interface

253

APPENDIX 1

Data Acquisition Programs

cv.bas

```
'CV PROGRAM

'SET UP BOARD

DECLARE SUB Err.Exit (procname$, err.num%)

REM $INCLUDE: 'c:\qb45\progs\nidaq1.inc'

CONST labpc.brd.code% = 9

heap.size = SETMEM(-5000)

brd% = 1

err.num% = Init.DA.Brds(brd%, brd.code%)

choice% = 1

err.num% = AI.Clear(brd%)
chan0% = 0
chan1% = 1
num.chan% = 2

'INPUT VALUES

CLS
SCREEN 12
COLOR 12
LOCATE 2, 10: PRINT "---VOLTAMMOGRAM RECORDER---"
COLOR 15
LOCATE 4, 8: PRINT "(1) Set the gain (1,2,5,10)"
LOCATE 5, 8: INPUT "    (note: 5 V / gain = +/- Vmax )"; gain%
LOCATE 7, 8: INPUT "(2) CURRENT FOLLOWER SETTING (nA/V) "; cfol#
LOCATE 9, 8: INPUT "(3) REDUCTION (1), OXIDATION (2) OR CV (3)"; sign%
LOCATE 11, 8: INPUT "(4) ENTER LOWEST POTENTIAL "; start#
LOCATE 13, 8: INPUT "(5) ENTER HIGHEST POTENTIAL "; final#
LOCATE 15, 8: INPUT "(6) ENTER NUMBER OF mV per POINT "; mvpp#
vpp# = mvpp# / 1000
xgain% = 1!

rerun:

DIM xvolt#(1000), yvolt#(1000)
j% = 0

'PRIME PC

CLS
```

```
LOCATE 9, 15: PRINT "Press any key to prime PC"

LOCATE 11, 18: PRINT "Then start the scan"
DO
LOOP WHILE INKEY$ = ""

'SET UP SCREEN

CLS
COLOR 12
SELECT CASE sign%

CASE 1
LOCATE 30, 7: PRINT ; start#; "V"
LOCATE 30, 71: PRINT ; final#; "V"

LOCATE 29, 2: PRINT ; "0 nA"
LOCATE 4, 1: PRINT ; 5 * cfol# / gain%; "nA"

xstart# = 1000!
ystart# = 1000!
yscale# = 1

CASE 2
LOCATE 30, 7: PRINT ; start#; "V"
LOCATE 30, 73: PRINT ; final#; "V"

LOCATE 29, 1: PRINT ; 5 * cfol# / gain%; "nA"
LOCATE 4, 2: PRINT ; "0 nA"

xstart# = 1000!
ystart# = 11000!
yscale# = 1

CASE 3
LOCATE 30, 7: PRINT ; start#; "V"
LOCATE 30, 73: PRINT ; final#; "V"

LOCATE 29, 1: PRINT ; 5 * cfol# / gain%; "nA"
LOCATE 4, 2: PRINT ; -5 * cfol# / gain%; "nA"

xstart# = 1000!
ystart# = 6000!
yscale# = .5

END SELECT

SCREEN 12
COLOR 9
WINDOW (0, 0)-(12000, 12000)
LINE (1000, 1000)-(11000, 1000)
LINE (1000, 1000)-(1000, 11000)
LINE (1000, 11000)-(11000, 11000)
LINE (11000, 11000)-(11000, 1000)
IF sign% = 3 THEN LINE (1000, 6000)-(11000, 6000)
```

```
COLOR 15

'DATA ACQUISITION

err.num% = AI.Read(brd%, chan0%, xgain%, value%)
err.num% = AI.Scale(brd%, xgain%, value%, xvolt#)

i# = xvolt#

DO

DO
sum# = 0
FOR s% = 1 TO 10
err.num% = AI.Read(brd%, chan0%, xgain%, sigav%)
sum# = sum# + sigav%
NEXT s%
value% = sum# / 10

err.num% = AI.Scale(brd%, xgain%, value%, xvolt#)

IF xvolt# > i# + vpp# THEN i# = i# + vpp#: EXIT DO
IF xvolt# < i# - vpp# THEN i# = i# - vpp#: EXIT DO

LOOP

'SIGNAL AVERAGE

sum# = 0
FOR s% = 1 TO 1000
err.num% = AI.Read(brd%, chan1%, gain%, sigav%)
sum# = sum# + sigav%
NEXT s%
value% = sum# / 1000
err.num% = AI.Scale(brd%, gain%, value%, yvolt#)

'PLOT VOLTAGES

COLOR 15
xscale# = final# - start#
xoffset# = start# / xscale# * 10000!
xpos# = xstart# - xoffset# + 10000! * xvolt# / xscale#
ypos# = ystart# + 10000! * gain% * yscale# * yvolt# / 5!
PSET (xpos#, ypos#)

j% = j% + 1
xvolt#(j%) = xvolt#
yvolt#(j%) = yvolt#

LOOP UNTIL INKEY$ = " "

'DATA CURSOR

l% = j%

DO
```

```
xpos# = xstart# - xoffset# + 10000! * xvolt#(I%) / xscale#
ypos# = ystart# + 10000! * gain% * yscale# * yvolt#(I%) / 5!
COLOR 15
LINE (xpos#, ypos# + 50)-(xpos#, ypos# + 200)

LOCATE 2, 20: PRINT , USING "####.#### "; xvolt#(I%); yvolt#(I%) * cfol#

SELECT CASE INPUT$(1)
CASE "1"
IF sign% = 1 THEN I% = I% + 10 ELSE I% = I% - 10
CASE "3"
IF sign% = 1 THEN I% = I% - 10 ELSE I% = I% + 10
CASE "4"
IF sign% = 1 THEN I% = I% + 1 ELSE I% = I% - 1
CASE "6"
IF sign% = 1 THEN I% = I% - 1 ELSE I% = I% + 1
CASE " "
GOTO save

END SELECT

COLOR 0
LINE (xpos#, ypos# + 50)-(xpos#, ypos# + 200)

IF I% < 1 THEN I% = j%
IF I% > j% THEN I% = 1

LOOP

'SAVE

save:

CLS

LOCATE 14, 8: INPUT "do you wish to save the wave (y/n)"; save$
IF save$ = "n" THEN GOTO bye


CLS

LOCATE 14, 8: INPUT "ENTER FILENAME "; filnam$
OPEN filnam$ FOR OUTPUT AS #1

PRINT #1, gain%; cfol#; sign%; start#; final#

FOR m% = 1 TO j%
PRINT #1, USING "####.##### "; xvolt#(m%); yvolt#(m%) * cfol#
NEXT m%

CLOSE

bye:

err.num% = Init.DA.Brds(brd%, brd.code%)
```

```
err.num% = Al.Clear(brd%)

CLS
LOCATE 14, 8: INPUT "Do you want to run again with the same values "; again$
IF again$ = "y" THEN GOTO rerun

CLEAR

END
```

trans.bas

```
'TRANSIENT RECORDER -single potential step-

'SET UP BOARD

DECLARE SUB Err.Exit (procname$, err.num%)
REM $INCLUDE: 'c:\qb45\progs\nidaq1.inc'
CONST labpc.brd.code% = 9
heap.size = SETMEM(-5000)
brd% = 1
err.num% = Init.DA.Brds(brd%, brd.code%)
choice% = 1
err.num% = Al.Clear(brd%)
chan% = 1
num.chan% = 1

'INPUT VALUES

'GENERATOR (TRIGGER) TRANSIENT
CLS
SCREEN 12
COLOR 12
LOCATE 2, 6: PRINT "---transient collector single potential step---"
COLOR 15
'LOCATE 3, 8: PRINT "GENERATOR (Trigger) TRANSIENT"
LOCATE 5, 8: PRINT "(1) Set the gain (1,2,5,10)"
LOCATE 6, 8: INPUT "   (note: 5 V / gain = +/- Vmax )"; gain%
LOCATE 8, 8: INPUT "(2) Enter the current follower setting"; cfol%
LOCATE 10, 8: INPUT "(3) Reduction (1) or Oxidation (2) transient "; sign%
LOCATE 12, 8: INPUT "(4) Set the TRIGGER level (Volts/sign)"; vtrig#
vtr% = 2048 * gain% * vtrig# / 5!
LOCATE 14, 8: INPUT "(5) sample rate (samples/s)"; acq.rate#
LOCATE 16, 8: INPUT "(6) transient length (s)"; tlen#
num.samp% = acq.rate# * tlen#
samp.int% = 1000000 / acq.rate#
DIM SHARED data.buf%(2500), volt#(2500)

'LOCATE 18, 8: PRINT "(7) TIMEBASE            "
'LOCATE 19, 10: PRINT "    (1)    1-microsec resolution"
'LOCATE 20, 10: PRINT "    (2)   10-microsec resolution"
'LOCATE 21, 10: PRINT "    (3) 100-microsec resolution"
'LOCATE 22, 10: PRINT "    (4)    1-millisec resolution"
```

```
'LOCATE 23, 10: PRINT "    (5)   10-millisec resolution"
'LOCATE 24, 12: INPUT "enter resolution of timer"; timebase%
timebase% = 1


rerun:

'PRIME PC

CLS
LOCATE 9, 15: PRINT "Press any key to prime PC"
LOCATE 11, 15: PRINT "Then TRIGGER transient"


DO
LOOP WHILE INKEY$ = ""
COLOR 12
LOCATE 13, 15: PRINT "WAITING FOR TRIGGER"

'DATA ACQUISITION

SELECT CASE sign%
CASE 1
trigger1:
err.num% = AI.Read(brd%, chan%, gain%, value%)
IF value% < vtr% GOTO trigger1
FOR i% = 1 TO num.samp% - 1
err.num% = DAQ.Start(brd%, chan%, gain%, data.buf%(), num.samp%, timebase%,
samp.int%)
NEXT i%


CASE 2
trigger2:
err.num% = AI.Read(brd%, chan%, gain%, value%)
IF value% > vtr% GOTO trigger2
FOR j% = 1 TO num.samp% - 1
err.num% = DAQ.Start(brd%, chan%, gain%, data.buf%(), num.samp%, timebase%,
samp.int%)
NEXT j%
END SELECT


IF tlen# > .9999 THEN

LET timon# = INT(TIMER)
CLS
COLOR 15
LOCATE 9, 15: PRINT "Transient is being collected"
DO
a# = tlen# + timon#
LET b# = a# - INT(TIMER)
LOCATE 10, 20: PRINT INT(b#); " seconds to go   "
LOOP UNTIL b# = 0

ELSE
CLS
LOCATE 9, 15: PRINT "Transient is being collected"
DO
```

```
LOOP WHILE INKEY$ = ""

END IF

'SET UP SCREEN

CLS
SCREEN 12
COLOR 15
WINDOW (0, 0)-(12000, 12000)
LINE (1000, 1000)-(11000, 1000)
LINE (1000, 1000)-(1000, 11000)
LINE (1000, 11000)-(11000, 11000)
LINE (11000, 11000)-(11000, 1000)
COLOR 15


FOR i% = 1 TO num.samp% - 1
err.num% = DAQ.Scale(brd%, gain%, num.samp%, data.buf%(), volt#())

offset! = 0!
div! = 5!

SELECT CASE sign%
CASE 1
offset1! = 0!
CASE 2
offset1! = 10000!
CASE 3
offset1! = 0!
END SELECT


COLOR 15
xpos# = 1000! + 10000! * i% / num.samp%
ypos# = 1000! + offset! + offset1! + 10000! * gain% * volt#(i%) / div!
PSET (xpos#, ypos#)
NEXT i%

'CALCULATE AN AVERAGE CURRENT

yav# = 0
FOR j% = i% TO i% - 50 STEP -1
yav# = yav# + volt#(j%)
NEXT j%
yvoltav# = yav# / 50

LOCATE 15, 15: PRINT yvoltav# * cfol%


COLOR 12
LOCATE 29, 7: PRINT ; "0 s"
LOCATE 28, 73: PRINT ; tlen#; "s"
LOCATE 28, 38: PRINT ; tlen# / 2

SELECT CASE sign%
```

```
CASE 1
LOCATE 27, 2: PRINT ; "0 nA"
LOCATE 2, 2: PRINT ; 5 * cfol% / gain%; "nA"

CASE 2
LOCATE 27, 2: PRINT ; -5 * cfol% / gain%; "nA"
LOCATE 2, 2: PRINT ; "0 nA"

END SELECT

DO
LOOP WHILE INKEY$ = ""

'SAVING DATA

CLS
COLOR 15
LOCATE 9, 15: INPUT "do you want to save the transient"; save$
IF save$ = "n" THEN GOTO bye
CLS
LOCATE 9, 15: INPUT "ENTER filename for data"; filnam$
OPEN filnam$ FOR OUTPUT AS #1

FOR i% = 1 TO num.samp% - 1

PRINT #1, USING "####.##### "; i% / acq.rate#; volt#(i%) * cfol%
NEXT i%

bye:

ERASE data.buf%
CLOSE
'err.num% = Init.DA.Brds(brd%, brd.code%)
err.num% = DAQ.Clear(brd%)
err.num% = AI.Clear(brd%)

CLS
COLOR 15
LOCATE 9, 15: INPUT "Do you want to run again with the same values"; again$
IF again$ = "y" THEN GOTO rerun

CLEAR

END




scan.bas

'SCANNING PROGRAM

'SET UP BOARD

DECLARE SUB Err.Exit (procname$, err.num%)
```

```
REM $INCLUDE: 'c:\qb45\progs\nidaq1.inc'
CONST labpc.brd.code% = 9
heap.size = SETMEM(-5000)
brd% = 1
err.num% = Init.DA.Brds(brd%, brd.code%)
err.num% = AO.Config(brd%, 0, 1, 0, 0)
choice% = 1
err.num% = AI.Clear(brd%)
chan0% = 0
chan1% = 1
num.chan% = 2

DIM curr#(1600), dist#(1600)

err.num% = AO.VWrite(brd%, 0, 0!)
vrest# = 0#

CHDIR "c:\chris"

settings:
CLS
SCREEN 12
'INPUT PARAMETERS

LOCATE 8, 10: INPUT "enter gain"; gain%
LOCATE 10, 10: INPUT "enter current follower setting"; cfol%
LOCATE 12, 10: INPUT "oxidation(1) or reduction(2)"; sign%
LOCATE 14, 10: INPUT "enter initial expansion"; dstart#
LOCATE 16, 10: INPUT "enter final expansion"; dend#

vstart# = dstart# / 4#
vend# = dend# / 4#
IF dend# > dstart# THEN direct% = 1 ELSE direct% = -1

restart:

IF vrest# = vstart# THEN GOTO vok:

FOR vout# = vrest# TO vstart# STEP .0001 * SGN(vstart# - vrest#)
err.num% = AO.VWrite(brd%, 0, vout#)
NEXT vout#

vok:

CLS
LOCATE 9, 15: PRINT "Press any key to prime PC"
LOCATE 11, 18: PRINT "Then start the scan"
DO
LOOP WHILE INKEY$ = ""

'SET UP SCREEN

CLS
COLOR 12

LOCATE 30, 7: PRINT ; dstart#
```

```basic
LOCATE 30, 73: PRINT ; dend#
LOCATE 29, 2: PRINT ; "0 nA"
LOCATE 4, 1: PRINT ; 5 * cfol% / gain%; "nA"

SCREEN 12
COLOR 9
WINDOW (0, 0)-(12000, 12000)
LINE (1000, 1000)-(11000, 1000)
LINE (1000, 1000)-(1000, 11000)
LINE (1000, 11000)-(11000, 11000)
LINE (11000, 11000)-(11000, 1000)
COLOR 15

j% = 0

'START SCAN

FOR vout# = vstart# TO vend# STEP .0125 * direct%

err.num% = AO.VWrite(brd%, 0, vout#)

'READ AVERAGE CURRENT

sum# = 0

FOR i% = 1 TO 2000

err.num% = AI.Read(brd%, chan1%, gain%, value%)
err.num% = AI.Scale(brd%, gain%, value%, vin#)

sum# = sum# + vin#

NEXT i%

av# = sum# / 2000
curr# = av# * cfol%
IF sign% = 1 THEN curr# = curr# * -1
dist# = vout# * 4

'OUTPUT

LOCATE 10, 10: PRINT , USING "####.####"; dist#
LOCATE 12, 10: PRINT , USING "####.####"; curr#

j% = j% + 1
dist#(j%) = dist#
curr#(j%) = curr#

'PLOT VOLTAGES

COLOR 15
xscale# = dend# - dstart#
xstart# = 1000!
ystart# = 1000!
xoffset# = dstart# / xscale# * 10000!
xpos# = xstart# - xoffset# + 10000! * dist# / xscale#
```

```
ypos# = ystart# + 10000! * gain% * curr# / (5! * cfol%)
PSET (xpos#, ypos#)

IF INKEY$ <> "" THEN GOTO save

NEXT vout#

DO
LOOP UNTIL INKEY$ <> ""

save:

vrest# = vout#

CLS

LOCATE 14, 8: INPUT "do you wish to save the data (y/n)"; save$
IF save$ = "n" THEN GOTO bye

CLS

LOCATE 14, 8: INPUT "ENTER FILENAME "; filnam$
OPEN filnam$ FOR OUTPUT AS #1

'SAVE
FOR m% = 1 TO j%
PRINT #1, USING "####.##### "; dist#(m%); curr#(m%)
NEXT m%

CLOSE

bye:
CLS

LOCATE 14, 8: PRINT "do you wish to:"
LOCATE 15, 10: PRINT "1) run again with the same values"
LOCATE 16, 10: PRINT "2) change the settings"
LOCATE 17, 10: PRINT "3) exit"
LOCATE 18, 10: INPUT " "; again$
IF again$ = "1" THEN GOTO restart
IF again$ = "2" THEN GOTO settings

CLS
LOCATE 14, 8: PRINT "piezo going to 0.0"
FOR vout# = vrest# TO 0# STEP -.0001
err.num% = AO.VVrite(brd%, 0, vout#)
NEXT vout#

LOCATE 16, 8: PRINT "switch off piezo"
DO
LOOP WHILE INKEY$ = ""
err.num% = Init.DA.Brds(brd%, brd.code%)
err.num% = AI.Clear(brd%)
CLEAR

END
```

SECM Simulation

secm-br.f

```
C SECM-BR.F
C DOUBLE POTENTIAL STEP BR-/BR2
C EQUIL BETWEEN Br- AND Br2 IGNORED


C    A=Br- B=Br2


    IMPLICIT DOUBLE PRECISION(A-H,O-Z)
    DOUBLE PRECISION LL,LLOG,LAMP(500),LAMQ(500),LAMZ
   >,DIFFA,DIFFB,CBS,CIB(500),clb(500)
   >,GAM,LAMZB,LAMPB(500),LAMQB(500)
    INTEGER NP,NZ,NQ,NUM
    CHARACTER*20 FILENAME

    DIMENSION COA(0:500,0:500),FA(500),ALRA(500),BERA(500)
   >,ALZA(500),BEZA(500),ALZGA(500),BEZGA(500),DA(500)
   >,HA(500),CNA(0:500,0:500),RRS(500),CCOMPA(0:500)

    DIMENSION COB(0:500,0:500),FB(500),ALRB(500),BERB(500)
   >,ALZB(500),BEZB(500),ALZGB(500),BEZGB(500),DB(500)
   >,HB(500),CNB(0:500,0:500),RRT(500),ccompb(0:500)

C.....SORTING OUT FILENAMES
C    LNAM=1
C    PRINT*, 'ENTER NUMBER OF CYCLES: '
C    READ*, NUM
C    DO 902 M=1,NUM
    PRINT*, 'ENTER FILENAME: '
    READ*, Filename
C 902  CONTINUE

C.....DIFFERENT DIFFUSION COEFFICIENTS
C    PRINT*,'ENTER DIFFUSION COEFFICIENT FOR SPECIES A ()/CM2 S-1:'
C    READ*, DIFFA
    DIFFA=1.8E-5
C    PRINT*,'ENTER DIFFUSION COEFFICIENT FOR SPECIES B (): '
C    READ*, DIFFB
    DIFFB=0.94E-5
    GAMB=DIFFB/DIFFA

C ELECTRODE RADIUS
    A=12.5E-4


C set time for reverse step
    PRINT*,'ENTER tswitch/s'
    READ*,TSWITCH
    tswitch=tswitch*diffa/(a*a)


C SET HETEROGENEOUS RATE CONSTANTS
```

```
C HET RATE CONST/ FIRST IN CM S-1 AND THEN DIMENSIONLESSc
c     HETK=0.4
      print*,'rate constant/cm/s'
      read*,hetk

      HETK=HETK*A/DIFFB


C.....CREATION OF THE INITIAL GRID

C.....VALUE OF THE HALF TIMESTEP
      DELTIN=2.E-6
      DELT=DELTIN
C.....NUMBER OF POINTS OVER ELECTRODE IN J SPACE (NQ)
      NQ=60
C.....NUMBER OF POINTS OVER GLASS IN J SPACE (NP)
      NP=60
C.....NUMBER OF POINTS IN K SPACE (NZ)
      NZ=100
C.....VALUE OF ELECTRODE RG
      RG=10.
C.....VALUE FOR (d/a) IN REAL SPACE (LL)
c     PRINT*, 'ENTER TIP/SUBSTRATE DISTANCE: '
c     READ*, TSD
C     TSD=0.3
C.....ELECTRODE RADIUS ASSUMED TO BE 12.5 MICRONS
C 501 LLOG=LOG10(TSD/12.5)
c     LLOG=-0.6
      print*,'enter log(d/a)'
      read*,llog

 501  LL=10.**LLOG
C     TSD=12.5*LL
C     PRINT*, 'TIP-SUBSTRATE SEPARATION: ', TSD
C     PRINT*, 'LOG(d/a) = ', LLOG
C     PRINT*, 'GAM = ', GAM
C.....SET VALUE FOR CONSTANT (F)
      FF=10.
      QT=LOG(1.+FF)
C.....DELQ IS (RHO) OVER THE ELECTRODE
      DELQ=QT/NQ
C.....SET VALUE FOR [1-R] OVER THE ELECTRODE (REXT)
      REXT=(1.-EXP(-DELQ))/FF
C.....SET VALUE FOR 'G' OVER THE GLASS TO MATCH GRIDS
      GG=0.1
      DIFF=0.1
 138  RES=NP*LOG(1.+(REXT*GG))-LOG(1.+((RG-1.)*GG))
      IF(RES.GT.0.0000001)THEN
      GG=GG-DIFF
      DIFF=DIFF/10.
      GOTO 138
      ENDIF
      IF(RES.LT.-0.0000001)THEN
      GG=GG+DIFF
      GOTO 138
      ENDIF
      PT=LOG(1.+(GG*(RG-1.)))
C.....DELP IS (RHO) OVER THE GLASS
      DELP=PT/NP
C.....SET GRID CONSTANTS OVER K SPACE
```

```
         DELZ=LL/NZ
         CURROLD=(DELZ**-1.)*3.142
C.....OPEN DATA FILE
         OPEN (67, FILE=FILENAME, STATUS='new')
c        OPEN (67, FILE=FNAM(LNAM), STATUS='unknown')
C.....SETTING INITIAL BULK CONCENTRATION VALUES
         DO 201 J=0,NQ+NP
         DO 202 K=0,NZ
         COA(J,K)=1.
         COB(J,K)=0.

         CNA(J,K)=1.
         CNB(J,K)=0.

 202  CONTINUE
 201  CONTINUE
C.....SETTING INITIAL SURFACE CONCENTRATIONS (OVER ELECTRODE)
         DO 30 J=0,NQ
         COA(J,0)=0.
         CNA(J,0)=0.
c        COB(J,0)=1./GAM
         CCOMPA(J)=1.
 30   CONTINUE

C.....CALCULATING LAMQ, LAMP, LAMZ CONSTANTS
C.....LAMZ (K SPACE)
 500  DO 150 K=1,NZ-1
         LAMZ=0.5*DELT/(DELZ*DELZ)
         LAMZB=LAMZ*GAMB

 150  CONTINUE
C.....LAMP (GLASS AREA) (J SPACE)
         DO 151 J=1,NP-1
         LAMP(J)=(0.5*GG*GG*DELT*(EXP(-2.*DELP*J)))/(DELP**2.)
         LAMPB(J)=LAMP(J)*GAMB

 151  CONTINUE
C.....LAMQ (ELECTRODE AREA) (J SPACE)
         DO 190 J=1,NQ
         LAMQ(J)=0.5*FF*FF*DELT*(EXP(2.*(-QT+(J*DELQ))))/
        >(DELQ*DELQ)
         LAMQB(J)=LAMQ(J)*GAMB

 190  CONTINUE

C.....CONSTANTS FOR THE THOMAS ALGORITHM
C.....CONSTANTS WHEN VECTORS ARE RADIAL
C.....BOUNDARY (J=1) VALUES
         ALRA(1)=1.+LAMQ(1)*(1.+(DELQ/2.)+(0.5*DELQ*
        >(EXP(QT-DELQ))/
        >(FF+1.-(EXP(QT-DELQ)))))
         BERA(1)=-LAMQ(1)*(1.+(DELQ/2.)+(0.5*DELQ*
        >(EXP(QT-DELQ))/
        >(FF+1.-(EXP(QT-DELQ)))))/ALRA(1)

         ALRB(1)=1.+LAMQB(1)*(1.+(DELQ/2.)+(0.5*DELQ*
        >(EXP(QT-DELQ))/
        >(FF+1.-(EXP(QT-DELQ)))))
         BERB(1)=-LAMQB(1)*(1.+(DELQ/2.)+(0.5*DELQ*
        >(EXP(QT-DELQ))/
```

267

```
    >(FF+1.-(EXP(QT-DELQ)))))/ALRB(1)


C.....J SPACE OVER THE ELECTRODE
      DO 100 J=2,NQ
      ALRA(J)=1.+(2.*LAMQ(J))+
     >(LAMQ(J)*(1.-(0.5*DELQ)-
     >(0.5*DELQ*(EXP(QT-(DELQ*J)))/(FF+1.-EXP(QT-
     >(J*DELQ)))))*BERA(J-1))
      BERA(J)=-LAMQ(J)*(1.+(0.5*DELQ)+(0.5*DELQ*
     >(EXP(QT-(J*DELQ)))/
     >(FF+1.-(EXP(QT-(J*DELQ))))))/ALRA(J)

      ALRB(J)=1.+(2.*LAMQB(J))+
     >(LAMQB(J)*(1.-(0.5*DELQ)-
     >(0.5*DELQ*(EXP(QT-(DELQ*J)))/(FF+1.-EXP(QT-
     >(J*DELQ)))))*BERB(J-1))
      BERB(J)=-LAMQB(J)*(1.+(0.5*DELQ)+(0.5*DELQ*
     >(EXP(QT-(J*DELQ)))/
     >(FF+1.-(EXP(QT-(J*DELQ))))))/ALRB(J)


100  CONTINUE

C.....J SPACE OVER THE INSULATOR
      DO 160 J=NQ+1,NQ+NP-2
      ALRA(J)=1.+(2.*LAMP(J-NQ))+(LAMP(J-NQ)*BERA(J-1)*
     >(1.+(DELP/2.)-(DELP*0.5*EXP((J-NQ)*DELP))*
     >((((EXP((J-NQ)
     >*DELP))-1.+GG)**-1.)))
      BERA(J)=LAMP(J-NQ)*(-1.+(DELP/2.)-(0.5*DELP*
     >(EXP((J-NQ)*DELP))
     >*(((EXP((J-NQ)*DELP))-1.+GG)**-1.)))/ALRA(J)

      ALRB(J)=1.+(2.*LAMPB(J-NQ))+(LAMPB(J-NQ)*BERB(J-1)*
     >(1.+(DELP/2.)-(DELP*0.5*EXP((J-NQ)*DELP))*
     >((((EXP((J-NQ)
     >*DELP))-1.+GG)**-1.)))
      BERB(J)=LAMPB(J-NQ)*(-1.+(DELP/2.)-(0.5*DELP*
     >(EXP((J-NQ)*DELP))
     >*(((EXP((J-NQ)*DELP))-1.+GG)**-1.)))/ALRB(J)


160  CONTINUE

C.....J SPACE AT ELECTRODE EDGE
      ALRA(NQ+NP-1)=1.+(LAMP(NP-1)*(2.+(BERA(NQ+NP-2)*
     >(1.+(DELP/2.)-
     >(DELP*0.5*(EXP((NP-1)*DELP)))*(((EXP((NP-1)*DELP))-
     >1.+GG)**-1.)))))

      ALRB(NQ+NP-1)=1.+(LAMPB(NP-1)*(2.+(BERB(NQ+NP-2)*
     >(1.+(DELP/2.)-
     >(DELP*0.5*(EXP((NP-1)*DELP)))*(((EXP((NP-1)*DELP))-
     >1.+GG)**-1.)))))

C.....CONSTANTS WHEN VECTORS ARE DOWN (K)
C.....BOUNDARY (K=1) OVER THE ELECTRODE
      ALZA(1)=(2.*LAMZ)+1.
      BEZA(1)=-LAMZ/ALZA(1)
```

```
      ALZB(1)=LAMZB+1.
      BEZB(1)=-(LAMZB)/ALZB(1)


C.....K SPACE OVER THE ELECTRODE
      DO 300 K=2,NZ-2
      ALZA(K)=((2.*LAMZ)+1.)+(LAMZ*BEZA(K-1))
      BEZA(K)=-LAMZ/ALZA(K)

      ALZB(K)=((2.*LAMZB)+1.)+(LAMZB*BEZB(K-1))
      BEZB(K)=-LAMZB/ALZB(K)


 300  CONTINUE

C.....K SPACE AT SUBSTRATE BOUNDARY (ELECTRODE)
      ALZA(NZ-1)=1.+LAMZ+(LAMZ*BEZA(NZ-2))
      ALZB(NZ-1)=1.+LAMZB*2.-LAMZB/(1.+HETK*DELZ)+(LAMZB*BEZB(NZ-2))

C.....BOUNDARY (K=1) OVER THE GLASS
      ALZGA(1)=LAMZ+1.
      BEZGA(1)=-LAMZ/ALZGA(1)
      ALZGB(1)=LAMZB+1.
      BEZGB(1)=-LAMZB/ALZGB(1)



C.....K SPACE OVER GLASS
      DO 301 K=2,NZ-2
      ALZGA(K)=((2.*LAMZ)+1.)+(LAMZ*BEZGA(K-1))
      BEZGA(K)=-LAMZ/ALZGA(K)
      ALZGB(K)=((2.*LAMZB)+1.)+(LAMZB*BEZGB(K-1))
      BEZGB(K)=-LAMZB/ALZGB(K)


 301  CONTINUE

C.....K SPACE AT SUBSTRATE BOUNDARY (GLASS)
      ALZGA(NZ-1)=1.+LAMZ+(LAMZ*BEZGA(NZ-2))
      ALZGB(NZ-1)=1.+LAMZB*2.-LAMZB/(1.+HETK*DELZ)+LAMZB*BEZGB(NZ-2)


C.....FIRST HALF TIMESTEP CALCULATION
C.....(K=OLD) AND (J=NEW)
C.....
      DO 1 K=1,NZ-1
      DO 2 J=1,NQ+NP-1

      DA(J)=(LAMZ*COA(J,K-1))-(((2.*LAMZ)-1.)
     >*COA(J,K))+(LAMZ*COA(J,K+1))

 2   CONTINUE
C.....
      DA(NQ+NP-1)=DA(NQ+NP-1)+(LAMP(NP-1)*(1.-(DELP/2.)+
     >(0.5*DELP*(EXP((NP-1)*DELP))*(((EXP((NP-1)*DELP))
     >-1.+GG)**-1.))))
C.....
      FA(1)=DA(1)/ALRA(1)
```

```fortran
      DO 3 J=2,NQ
      FA(J)=(DA(J)+(LAMQ(J)*(1.-(DELQ/2.)-(0.5*DELQ*
     >(EXP(QT-(J*DELQ)))
     >/(FF+1.-(EXP(QT-(J*DELQ))))))*FA(J-1)))/ALRA(J)
 3    CONTINUE
C.....
      DO 41 J=NQ+1,NQ+NP-1
      FA(J)=(DA(J)+((LAMP(J-NQ)*(1.+(0.5*DELP)-
     >((0. *DELP*(EXP((J-NQ)*DELP)))
     >*(((EXP((J-NQ)*DELP))-1.+GG)**-1.))))*FA(J-1)))
     >/ALRA(J)
 41   CONTINUE
C.....
      CNA(NQ+NP-1,K)=FA(NQ+NP-1)

      DO 4 J=NQ+NP-2,1,-1
      CNA(J,K)=FA(J)-(BERA(J)*CNA(J+1,K))
 4    CONTINUE
 1    CONTINUE


C CALCULATION FOR B

      DO 601 K=1,NZ-1
 606  DO 602 J=1,NQ+NP-1
      DB(J)=(LAMZB*COB(J,K-1))-(((2.*LAMZB)-1.)
     >*COB(J,K))+(LAMZB*COB(J,K+1))
 602  CONTINUE

      FB(1)=DB(1)/ALRB(1)

      DO 603 J=2,NQ

      FB(J)=(DB(J)+(LAMQB(J)*(1.-(DELQ/2.)-(0.5*DELQ*
     >(EXP(QT-(J*DELQ)))
     >/(FF+1.-(EXP(QT-(J*DELQ))))))*FB(J-1)))/ALRB(J)
 603  CONTINUE
C.....
      DO 641 J=NQ+1,NQ+NP-1

      FB(J)=(DB(J)+((LAMPB(J-NQ)*(1.+(0.5*DELP)-
     >((0.5*DELP*(EXP((J-NQ)*DELP)))
     >*(((EXP((J-NQ)*DELP))-1.+GG)**-1.))))*FB(J-1)))
     >/ALRB(J)
 641  CONTINUE
C.....
      CNB(NQ+NP-1,K)=FB(NQ+NP-1)
      DO 604 J=NQ+NP-2,1,-1
      CNB(J,K)=FB(J)-(BERB(J)*CNB(J+1,K))
 604  CONTINUE
 601  CONTINUE



C.....UPDATING BOUNDARY CONDITIONS

      DO 555 J=0,NQ
      COA(J,0)=0.
      COB(J,0)=CNB(J,1)+(CNA(J,1)/GAMB)
 555  CONTINUE
```

```fortran
      DO 101 J=NQ+1,NP+NQ-1
      COA(J,0)=CNA(J,1)
      COB(J,0)=CNB(J,1)
101   CONTINUE

      DO 777 K=1,NZ-1
      COA(0,K)=CNA(1,K)
      COB(0,K)=CNB(1,K)
777   CONTINUE

      DO 778 J=0,NP+NQ-1
      COA(J,NZ)=CNA(J,NZ-1)
      COB(J,NZ)=CNB(J,NZ-1)/(1.+HETK*DELZ)
778   CONTINUE

C.....UPDATING REST OF CONCENTRATION VALUES
      DO 103 J=1,NP+NQ-1
      DO 104 K=1,NZ-1
      COA(J,K)=CNA(J,K)
      COB(J,K)=CNB(J,K)
104   CONTINUE
103   CONTINUE


c output selected concs for b and c


C.....CALCULATIONS IN OTHER DIRECTION
C.....(J=NEW OLD) AND (K=NEW NEW)

C.....DO A CALCULATION FIRST
      DO 50 J=1,NQ
      DO 51 K=1,NZ-1
      HA(K)=(LAMQ(J)*(1.-(0.5*DELQ)-(0.5*DELQ*
     >(EXP(QT-(DELQ*J)))/
     >(FF+1.-(EXP(QT-(DELQ*J)))))))*COA(J-1,K)+(COA(J,K)*
     >(1.-(2.*LAMQ(J))))
     >+(LAMQ(J)*(1.+(0.5*DELQ)+(0.5*DELQ*
     >(EXP(QT-(J*DELQ)))/
     >(FF+1.-EXP(QT-(J*DELQ)))))*COA(J+1,K))

51    CONTINUE

      FA(1)=HA(1)/ALZA(1)

      DO 53 K=2,NZ-1
      FA(K)=(HA(K)+(LAMZ*FA(K-1)))/ALZA(K)
53    CONTINUE
      CNA(J,NZ-1)=FA(NZ-1)
      DO 54 K=NZ-2,1,-1
      CNA(J,K)=FA(K)-(BEZA(K)*CNA(J,K+1))
54    CONTINUE

50    CONTINUE

      DO 70 J=NQ+1,NQ+NP-1
      DO 71 K=1,NZ-1
      HA(K)=(LAMP(J-NQ)*(1.+(DELP*0.5)-(DELP*0.5*
     >(EXP((J-NQ)*DELP))*((EXP((J-NQ)*DELP))-1.
```

271

```
      >+GG)**-1.))
      >*COA(J-1,K))+(COA(J,K)*(1.-(2.*LAMP(J-NQ))))
      >+(LAMP(J-NQ)*(1.-(0.5*DELP)+
      >(0.5*DELP*EXP((J-NQ)*DELP)*((EXP((J-NQ)
      >*DELP))-1.+GG)**-1.))*COA(J+1,K))
   71 CONTINUE

      FA(1)=HA(1)/ALZGA(1)
      DO 73 K=2,NZ-1
      FA(K)=(HA(K)+(LAMZ*FA(K-1)))/ALZGA(K)
   73 CONTINUE
      CNA(J,NZ-1)=FA(NZ-1)
      DO 74 K=NZ-2,1,-1
      CNA(J,K)=FA(K)-(BEZGA(K)*CNA(J,K+1))
   74 CONTINUE
   70 CONTINUE




C CONTINUE CALCULATION FOR B

      DO 550 J=1,NQ
      DO 551 K=1,NZ-1


      HB(K)=(LAMQB(J)*(1.-(0.5*DELQ)-(0.5*DELQ*
      >(EXP(QT-(DELQ*J)))/
      >(FF+1.-(EXP(QT-(DELQ*J))))))*COB(J-1,K))+(COB(J,K)*
      >(1.-(2.*LAMQB(J))))
      >+(LAMQB(J)*(1.+(0.5*DELQ)+(0.5*DELQ*
      >(EXP(QT-(J*DELQ)))/
      >(FF+1.-EXP(QT-(J*DELQ)))))*COB(J+1,K))

  551 CONTINUE

      HB(1)=HB(1)+(LAMZB*CNA(J,1)/GAMB)

      FB(1)=HB(1)/ALZB(1)
      DO 553 K=2,NZ-1
      FB(K)=(HB(K)+(LAMZB*FB(K-1)))/ALZB(K)
  553 CONTINUE
      CNB(J,NZ-1)=FB(NZ-1)

      DO 554 K=NZ-2,1,-1
      CNB(J,K)=FB(K)-(BEZB(K)*CNB(J,K+1))
  554 CONTINUE
  550 continue

C.....
      DO 60 J=NQ+1,NQ+NP-1
      DO 61 K=1,NZ-1

      HB(K)=(LAMPB(J-NQ)*(1.+(DELP*0.5)-(DELP*0.5*
      >(EXP((J-NQ)*DELP))*((EXP((J-NQ)*DELP))-1.
      >+GG)**-1.))
      >*COB(J-1,K))+(COB(J,K)*(1.-(2.*LAMPB(J-NQ))))
      >+(LAMPB(J-NQ)*(1.-(0.5*DELP)+
      >(0.5*DELP*EXP((J-NQ)*DELP)*((EXP((J-NQ)
```

```fortran
     >*DELP))-1.+GG)**-1.))*COB(J+1,K)
 61  CONTINUE

C.... B CALCULATION

     FB(1)=HB(1)/ALZGB(1)
     DO 63 K=2,NZ-1
     FB(K)=(HB(K)+(LAMZB*FB(K-1)))/ALZGB(K)
 63  CONTINUE
     CNB(J,NZ-1)=FB(NZ-1)


     DO 64 K=NZ-2,1,-1
     CNB(J,K)=FB(K)-(BEZGB(K)*CNB(J,K+1))



 64  CONTINUE

 60  CONTINUE

C.....
     DO 360 J=1,NQ
     IF(CURRT.GT.2.)THEN
     COMA=0.95*CCOMPA(J)
     ELSE IF(CURRT.GT.1.)THEN
     COMA=0.98*CCOMPA(J)
     ELSE IF(CURRT.GT.0.5)THEN
     COMA=0.995*CCOMPA(J)
     ELSE
     COMA=0.999*CCOMPA(J)
     ENDIF
     IF(CNA(J,1).GT.COMA)THEN
     KLMA=KLMA+1
     ENDIF
 360 CONTINUE

C.....
C.....UPDATING BOUNDARY CONDITIONS

     DO 5555 J=0,NQ
     COA(J,0)=0.
     COB(J,0)=CNB(J,1)+(CNA(J,1)/GAMB)
 5555 CONTINUE

     DO 1015 J=NQ+1,NP+NQ-1
     COA(J,0)=CNA(J,1)
     COB(J,0)=CNB(J,1)
 1015 CONTINUE

     DO 7777 K=1,NZ-1
     COA(0,K)=CNA(1,K)
     COB(0,K)=CNB(1,K)
 7777 CONTINUE

     DO 7778 J=0,NP+NQ-1
     COA(J,NZ)=CNA(J,NZ-1)
     COB(J,NZ)=CNB(J,NZ-1)/(1.+HETK*DELZ)
 7778 CONTINUE
```

```
C.....UPDATING REST OF CONCENTRATION VALUES
      DO 1030 J=1,NP+NQ-1
      DO 1040 K=1,NZ-1
      COA(J,K)=CNA(J,K)
      COB(J,K)=CNB(J,K)
 1040 CONTINUE
 1030 CONTINUE



C.....
      DO 900 J=1,NQ
      CCOMPA(J)=CNA(J,1)
      IF(COA(J,1).LT.0.0.AND.IIIA.EQ.0)THEN
      IIIA=1
      ENDIF
 900  CONTINUE

C.....CALCULATING TIP(RRT) CURRENT

      DO 880 J=1,NQ-1
      RRT(J)=1.-((EXP(QT-(J*DELQ)))-1.)/FF
C     RRS(J)=1.-((EXP(QT-(J*DELQ)))-1.)/FF
 880  CONTINUE

      RRT(NQ)=1.
      RRS(NQ)=1.

C     DO 944 J=NQ+1,NQ+NP-1
C     RRS(J)=1.+(((EXP(((J-NQ)*DELP)))-1.)/GG)
C 944  CONTINUE

C     RRS(NQ+NP)=RG

      FLUXT=CNA(1,1)*(RRT(1)**2.)/DELZ
C     FLUXS=CNB(1,NZ-1)*(RRS(1)**2.)/DELZ

      DO 689 J=2,NQ
      FLUXT=FLUXT+((RRT(J)**2.)-(RRT(J-1)**2.))*
     >(CNA(J,1))/DELZ
C     FLUXS=FLUXS+((RRS(J)**2.)-(RRS(J-1)**2.))*
C    >(CNB(J,NZ-1))/DELZ
 689  CONTINUE

C     DO 693 J=NQ+1,NQ+NP-1
C     FLUXS=FLUXS+((RRS(J)**2.)-(RRS(J-1)**2.))*
C    >(CNB(J,NZ-1))/DELZ
C 693  CONTINUE

C.....NORMALISED CURRENT - CALCULATION
      CURRT=FLUXT*(3.1419/4.)
C     CURRS=GAM*FLUXS*(3.1419/4.)
      T=T+DELT
      PRINT*, CURRT,t
      print*,'surface conc:A,B'
      print*,coa(1,nz),cob(1,nz)

      IF(KLMA.EQ.NQ.AND.IIIA.EQ.0)THEN
      DELT=DELT*1.3
      ELSE IF(KLMB.EQ.NQ.AND.IIIB.EQ.0) THEN
```

```
      DELT=DELT*1.3
      ENDIF
      IF(IIIA.EQ.1.)THEN
      DELT=DELT/2.
      ENDIF
      CURROLD=CURRT
      IIIA=0
      KLMA=0
      FLUXT=0.



      if((t+delt).gt.tswitch)then
      delt=tswitch-t
      endif


C.....SAVING THE DATA
      WRITE (67,11) currt,t

C.....CONTINUING THE CYCLE

c 999  continue

      IF (T.LT.(tswitch-5.e-7)) GOTO 500
C     CLOSE (67)


c REVERSE STEP

      DELTin=2.e-7
      delt=deltin


C.....CALCULATING LAMQ, LAMP, LAMZ CONSTANTS
C.....LAMZ (K SPACE)
 5000 DO 1500 K=1,NZ-1
      LAMZ=0.5*DELT/(DELZ*DELZ)
      LAMZB=LAMZ*GAMB

 1500 CONTINUE
C.....LAMP (GLASS AREA) (J SPACE)
      DO 1510 J=1,NP-1
      LAMP(J)=(0.5*GG*GG*DELT*(EXP(-2.*DELP*J)))/(DELP**2.)
      LAMPB(J)=LAMP(J)*GAMB
 1510 CONTINUE
C.....LAMQ (ELECTRODE AREA) (J SPACE)
      DO 1900 J=1,NQ
      LAMQ(J)=0.5*FF*FF*DELT*(EXP(2.*(-QT+(J*DELQ))))/
     >(DELQ*DELQ)
      LAMQB(J)=LAMQ(J)*GAMB
 1900 CONTINUE

C.....CONSTANTS FOR THE THOMAS ALGORITHM
C.....CONSTANTS WHEN VECTORS ARE RADIAL
C.....BOUNDARY (J=1) VALUES

      ALRB(1)=1.+LAMQB(1)*(1.+(DELQ/2.)+(0.5*DELQ*
     >(EXP(QT-DELQ))/
     >(FF+1.-(EXP(QT-DELQ)))))
```

```
      BERB(1)=-LAMQB(1)*(1.+(DELQ/2.)+(0.5*DELQ*
     >(EXP(QT-DELQ))/
     >(FF+1.-(EXP(QT-DELQ)))))/ALRB(1)

C.....J SPACE OVER THE ELECTRODE
      DO 1000 J=2,NQ

      ALRB(J)=1.+(2.*LAMQB(J))+
     >(LAMQB(J)*(1.-(0.5*DELQ)-
     >(0.5*DELQ*(EXP(QT-(DELQ*J)))/(FF+1.-EXP(QT-
     >(J*DELQ)))))*BERB(J-1))
      BERB(J)=-LAMQB(J)*(1.+(0.5*DELQ)+(0.5*DELQ*
     >(EXP(QT-(J*DELQ)))/
     >(FF+1.-(EXP(QT-(J*DELQ))))))/ALRB(J)

1000  CONTINUE

C.....J SPACE OVER THE INSULATOR
      DO 1600 J=NQ+1,NQ+NP-2

      ALRB(J)=1.+(2.*LAMPB(J-NQ))+(LAMPB(J-NQ)*BERB(J-1)*
     >(1.+(DELP/2.)-(DELP*0.5*EXP((J-NQ)*DELP))*
     >(((EXP((J-NQ)
     >*DELP))-1.+GG)**-1.)))
      BERB(J)=LAMPB(J-NQ)*(-1.+(DELP/2.)-(0.5*DELP*
     >(EXP((J-NQ)*DELP))
     >*(((EXP((J-NQ)*DELP))-1.+GG)**-1.)))/ALRB(J)


1600  CONTINUE

C.....J SPACE AT ELECTRODE EDGE

      ALRB(NQ+NP-1)=1.+(LAMPB(NP-1)*(2.+(BERB(NQ+NP-2)*
     >(1.+(DELP/2.)-
     >(DELP*0.5*(EXP((NP-1)*DELP)))*(((EXP((NP-1)*DELP))-
     >1.+GG)**-1.)))))

C.....CONSTANTS WHEN VECTORS ARE DOWN (K)
C.....BOUNDARY (K=1) OVER THE ELECTRODE

      ALZB(1)=2.*LAMZB+1.
      BEZB(1)=-(LAMZB)/ALZB(1)

C.....K SPACE OVER THE ELECTRODE
      DO 3000 K=2,NZ-2
      ALZB(K)=((2.*LAMZB)+1.)+(LAMZB*BEZB(K-1))
      BEZB(K)=-LAMZB/ALZB(K)
3000  CONTINUE

C.....K SPACE AT SUBSTRATE BOUNDARY (ELECTRODE)

      ALZB(NZ-1)=1.+LAMZB*2.-LAMZB/(1.+HETK*DELZ)+(LAMZB*BEZB(NZ-2))
C.....BOUNDARY (K=1) OVER THE GLASS
      ALZGB(1)=LAMZB+1.
      BEZGB(1)=-LAMZB/ALZGB(1)


C.....K SPACE OVER GLASS
      DO 3010 K=2,NZ-2
```

```
      ALZGB(K)=((2.*LAMZB)+1.)+(LAMZB*BEZGB(K-1))
      BEZGB(K)=-LAMZB/ALZGB(K)

3010 CONTINUE

C.....K SPACE AT SUBSTRATE BOUNDARY (GLASS)

      ALZGB(NZ-1)=1.+LAMZB*2.-LAMZB/(1.+HETK*DELZ)+LAMZB*BEZGB(NZ-2)

      DO 1601 K=1,NZ-1
      DO 1602 J=1,NQ+NP-1

      DB(J)=(LAMZB*COB(J,K-1))-(((2.*LAMZB)-1.)
     >*COB(J,K))+(LAMZB*COB(J,K+1))

1602 CONTINUE

      FB(1)=DB(1)/ALRB(1)
      DO 1603 J=2,NQ

      FB(J)=(DB(J)+(LAMQB(J)*(1.-(DELQ/2.)-(0.5*DELQ*
     >(EXP(QT-(J*DELQ)))
     >/(FF+1.-(EXP(QT-(J*DELQ)))))))*FB(J-1)))/ALRB(J)

1603 CONTINUE
C.....
      DO 1641 J=NQ+1,NQ+NP-1

      FB(J)=(DB(J)+((LAMPB(J-NQ)*(1.+(0.5*DELP)-
     >((0.5*DELP*(EXP((J-NQ)*DELP)))
     >*(((EXP((J-NQ)*DELP))-1.+GG)**-1.))))*FB(J-1)))
     >/ALRB(J)

1641 CONTINUE
C.....
      CNB(NQ+NP-1,K)=FB(NQ+NP-1)

      DO 1604 J=NQ+NP-2,1,-1
      CNB(J,K)=FB(J)-(BERB(J)*CNB(J+1,K))

1604 CONTINUE
1601 CONTINUE

C.....UPDATING BOUNDARY CONDITIONS

      DO 1555 J=0,NQ
      COB(J,0)=0.

1555 CONTINUE

      DO 1101 J=NQ+1,NP+NQ-1
      COB(J,0)=CNB(J,1)

1101  CONTINUE

      DO 1777 K=1,NZ-1
      COB(0,K)=CNB(1,K)

1777 CONTINUE
```

```
      DO 1778 J=0,NP+NQ-1
      COB(J,NZ)=CNB(J,NZ-1)/(1.+HETK*DELZ)

1778 CONTINUE

C.....UPDATING REST OF CONCENTRATION VALUES
      DO 1103 J=1,NP+NQ-1
      DO 1104 K=1,NZ-1
      COB(J,K)=CNB(J,K)
1104 CONTINUE
1103 CONTINUE




C..... OTHER DIRECTION



      DO 1550 J=1,NQ
      DO 1551 K=1,NZ-1

      HB(K)=(LAMQB(J)*(1.-(0.5*DELQ)-(0.5*DELQ*
     >(EXP(QT-(DELQ*J)))/
     >(FF+1.-(EXP(QT-(DELQ*J))))))*COB(J-1,K))+(COB(J,K)*
     >(1.-(2.*LAMQB(J))))
     >+(LAMQB(J)*(1.+(0.5*DELQ)+0.5*DELQ*
     >(EXP(QT-(J*DELQ)))/
     >(FF+1.-EXP(QT-(J*DELQ)))))*COB(J+1,K))

1551 CONTINUE

C.... B CALCULATION

      FB(1)=HB(1)/ALZB(1)
      DO 1553 K=2,NZ-1
      FB(K)=(HB(K)+(LAMZB*FB(K-1)))/ALZB(K)
1553 CONTINUE
      CNB(J,NZ-1)=FB(NZ-1)

      DO 1554 K=NZ-2,1,-1
      CNB(J,K)=FB(K)-(BEZB(K)*CNB(J,K+1))
1554 CONTINUE

1550 CONTINUE

C.....
      DO 6000 J=NQ+1,NQ+NP-1
      DO 6100 K=1,NZ-1

      HB(K)=(LAMPB(J-NQ)*(1.+(DELP*0.5)-(DELP*0.5*
     >(EXP((J-NQ)*DELP))*((EXP((J-NQ)*DELP))-1.
     >+GG)**-1.))
     >*COB(J-1,K))+(COB(J,K)*(1.-(2.*LAMPB(J-NQ))))
     >+(LAMPB(J-NQ)*(1.-(0.5*DELP)+
     >(0.5*DELP*EXP((J-NQ)*DELP)*((EXP((J-NQ)
     >*DELP))-1.+GG)**-1.))*COB(J+1,K))

6100 CONTINUE
```

```
C.... B CALCULATION

      FB(1)=HB(1)/ALZGB(1)
      DO 6300 K=2,NZ-1
      FB(K)=(HB(K)+(LAMZB*FB(K-1)))/ALZGB(K)
6300 CONTINUE
      CNB(J,NZ-1)=FB(NZ-1)


      DO 6400 K=NZ-2,1,-1
      CNB(J,K)=FB(K)-(BEZGB(K)*CNB(J,K+1))
6400 CONTINUE


6000 CONTINUE

      DO 2555 J=0,NQ
      COB(J,0)=0.

2555 CONTINUE

      DO 2101 J=NQ+1,NP+NQ-1
      COB(J,0)=CNB(J,1)

2101 CONTINUE

      DO 2777 K=1,NZ-1
      COB(0,K)=CNB(1,K)
2777 CONTINUE

      DO 2778 J=0,NP+NQ-1
      COB(J,NZ)=CNB(J,NZ-1)/(1.+HETK*DELZ)

2778 CONTINUE

C.....UPDATING REST OF CONCENTRATION VALUES
      DO 2103 J=1,NP+NQ-1
      DO 2104 K=1,NZ-1
      COB(J,K)=CNB(J,K)
2104 CONTINUE
2103 CONTINUE

C WORKING OUT CURRENT

      FLUXT=CNB(1,1)*(RRT(1)**2.)/DELZ
      DO 1689 J=2,NQ
      FLUXT=FLUXT+((RRT(J)**2.)-(RRT(J-1)**2.))*
     >(CNB(J,1))/DELZ
1689 CONTINUE

C.....NORMALISED CURRENT - CALCULATION
      CURRT=-FLUXT*GAMB*3.1419/4.
      T=T+DELT
      PRINT*, CURRT,t
      print*,'surface conc:B'
      print*,cob(1,nz)


C.....SAVING THE DATA
```

```
      WRITE (67,11) CURRT, t

C.....CONTINUING THE CYCLE

c 999  continue

C UPDATE TIMESTEP

      DO 3600 J=1,NQ
      IF(-CURRT.GT.2.)THEN
      COMB=0.98*CCOMPB(J)
      ELSE IF(-CURRT.GT.1.)THEN
      COMB=0.99*CCOMPB(J)
      ELSE IF(-CURRT.GT.0.5)THEN
      COMB=0.995*CCOMPB(J)
      ELSE
      COMB=0.999*CCOMPB(J)
      ENDIF
      IF(CNB(J,1).GT.COMB)THEN
      KLMB=KLMB+1
      ENDIF
3600  CONTINUE


      DO 9000 J=1,NQ
      CCOMPB(J)=CNB(J,1)
      IF(COB(J,1).LT.0.0.AND.IIIB.EQ.0)THEN
      IIIB=1
      ENDIF
9000 CONTINUE

      IF(KLMB.EQ.NQ.AND.IIIB.EQ.0)THEN
      DELT=DELT*1.3
      ENDIF
      IF(IIIB.EQ.1.)THEN
      DELT=DELT/2.
      ENDIF
      CURROLD=CURRT
      IIIB=0
      KLMB=0
      FLUXT=0.




      IF (T.LT.TSWITCH*2) GOTO 5000
```

```
C.....INCREASING GRID POINTS OVER K SPACE
C     NZ=NZ+5

C.....LOOPING BACK TO CALCULATE CURRENT AT NEXT (d/a)
C     DELT=DELTIN
C     T=0.
C     LNAM=LNAM+1
C     GAM=GAM+0.1
C     IF (GAM.LT.0.81) GOTO 501

C     TSD=TSD+0.05

C     LLOG=LLOG+0.1
C     LNAM=LNAM+1
C     IF (LLOG.LT.-0.41) GOTO 501

C.....FORMAT STATEMENTS
 11   FORMAT(2X,E16.10,2X,E16.10)
      STOP
      END
```

MEMED Simulation

dropk.f

```
      program dropk.f
c
      double precision lambda,delt,delr,nr,numt,tout
     >,ratenorm,rate,diff,dropt,s,mts,orgconc,sep
      dimension cold(0:1000),cnew(0:1000)
      character*20 filename

c.....file details
      print*, 'enter filename '
      read*,filename
      open (99,file = filename,status = 'new')

c.....input parameters
      print*, 'enter drop time/s '
      read*, dropt
      print*, 'enter final drop radius/cm '
      read*, radfin
      print*, 'enter rate constant/cms-1 '
      read*, rate

      diff = 1.0e-5.

c.....set some values
      nr = 1000
      s=(diff*dropt)**0.5/radfin
      ratenorm = (rate*((diff*dropt)**0.5))/(diff)
      delr = (s**(-1.))/nr
      delt = 0.3*delr**2.
      print*, delr
      lambda = delt / delr ** 2.
      numt = 1. / delt
      tout=numt/3

c.....set initial conditions
      do 1 j = 1,nr
      cold(j) = 1.
1     continue

c.....calculation
      do 2 m = 1,numt
      mts=(m*delt)**(1./3.)*(s**-1.)
c
c.....interfacial boundary
      cold(0)=cold(1)/(1.+ratenorm*delr)
c
      do 3 k = 1,nr - 1
      cnew(k)=1./(((k*delr)+mts)**2.)
      cnew(k)=cnew(k)-(1./(mts**2.))
      cnew(k)=cnew(k)*(1./(3.*s**3.))
      cnew(k)=2./((k*delr)+mts)-cnew(k)
      cnew(k)=cnew(k)*(delt/(2.*delr))*(cold(k+1)-cold(k-1))
      cnew(k)=lambda*cold(k+1)+(1.-(2.*lambda))*cold(k)
     >+lambda*cold(k-1)+cnew(k)
```

```
c
3     continue
      do 5 i = 1,nr-1
      cold(i)=cnew(i)
5     continue

c.....output to screen and file
      if (m.gt.(tout)) then
      tout=tout+5000000*delt
      sep=(s**(-1.)-mts)
      print*, 2*sep*(diff*dropt)**(0.5),cold((2*sep)/delr)
      write(99,100) 2*sep*(diff*dropt)**(0.5),cold(2*sep/delr)
      endif
c
2     continue

100   format (2x,e16.10,2x,e16.10)
      close(99)
      end
```

REFERENCES

1. Freiser, H. *Chem. Rev.* **1980**, *88*, 611.

2. Danesi, P. R.; R. Chiarizia, R. *CRC Crit. Rev. Anal. Chem.* **1980**, *10*, 1.

3. Atherton, J. H. *Res. Chem. Kinet.* **1994**, *2*, 193.

4. Gennis, R. B. *Biomembranes: Molecular Structure and Function*, Springer-Verlag, New York, 1989.

5. Volkov, A. G.; Deamer, D. W.; Tanelian, D. L.; Markin, V. S. *Liquid Interfaces in Chemistry and Biology*, Wiley, New York, 1998.

6. Koryta, J. *Electrochim. Acta* **1979**, *24*, 293.

7. Arai, K.; Kusu, F.; Takamura, K. *Electrochemical behavior of drugs at the oil/water interface* in *Liquid-Liquid Interfaces: Theory and Methods*, Volkov, A. G.; Deamer, D. W. (eds.), CRC Press, Boca Raton, 1996, p 375.

8. Girault, H. H. J.; Schiffrin, D. J. *Electrochemistry of liquid-liquid interfaces* in *Electroanalytical Chemistry* vol. 15, Bard, A. J. (ed.), Marcel Dekker, New York, 1989, p 1.

9. Vanýsek, P. *Electrochim. Acta* **1995**, *40*, 2841.

10. Senda, M.; Yamamoto, Y. *Amperometric ion-selective electrode sensors* in *Liquid-Liquid Interfaces: Theory and Methods*, Volkov, A. G.; Deamer, D. W. (eds.), CRC Press, Boca Raton, 1996, p 277.

11. Volkov, A. G.; Deamer, D. W. (eds.), *Liquid-Liquid Interfaces: Theory and Methods* CRC Press, Boca Raton, 1996.

12. Lewis, J. B. *Chem. Eng. Sci.* **1954**, *3*, 218.

13. Lewis, J. B. *Chem. Eng. Sci.* **1954**, *3*, 260.

14. Nitsch, W.; Hillekamp, K. *Chem. Ztg.* **1972**, *96*, 254.

15. Danesi, P. R.; Cianetti, C.; Horowitz, E. P.; Diamond, H. *Sep. Sci. Tech.* **1982**, *17*, 961.

16. Bhaduri, M.; Hanson, C.; Hughes, M. A.; Whewell, R. J. *Int. Solv. Extr. Conf. (Proc.)* **1983**, 293.

17. Albery, W. J.; Burke, J. F.; Leffler, E. B.; Hadgraft, J. *J. Chem. Soc., Faraday Trans. I* **1976**, *72*, 1618.

18. Brett, C. M. A.; Brett, A. M. O. *Electrochemistry: Principles, Methods and Applications*, Oxford University Press Inc., New York, 1993.

19. Macpherson, J. V.; Unwin, P. R. *Progress in Reaction Kinetics* **1995**, *20*, 185.

20. Leahy, D. E.; Wait, A. R. *J. Pharm. Sci.*, **1986**, *75*, 1157.

21. Bard, A. J.; Faulkner, L. R. *Electrochemical Methods*, John Wiley, New York, 1980.

22. Albery, W. J.; Hitchman, M. L. *Ring-Disc Electrodes*, Oxford University Press, 1971.

23. Albery, W. J.; Choudhery, R. A.; Fisk, P. R. *Faraday Discuss. Chem. Soc.* **1984**, *77*, 53.

24. Albery, W. J.; Choudhery, R. A. *J. Phys. Chem.* **1988**, *92*, 1142.

25. Albery, W. J.; Hadgraft, J. *J. Pharm. Pharmacol.* **1979**, *31*, 65.

26. Guy, R. H.; Aquino, T. R.; Honda, D. H. *J. Phys. Chem.* **1982**, *86*, 280.

27. Guy, R. H.; Aquino, T. R.; Honda, D. H. *J. Phys. Chem.* **1982**, *86*, 2861.

28. Albery, W. J.; Choudhery, R. A.; Atay, N. Z.; Robinson, B. H. *J. Chem. Soc.,*

Faraday Trans. I **1987**, *83*, 2407.

29. Freeman, R. W.; Tavlarides, L. L. *Chem. Eng. Sci.* **1980**, *35*, 559.

30. Freeman, R. W.; Tavlarides, L. L. *Chem. Eng. Sci.* **1982**, *37*, 1547.

31. Sawistowski, H.; Goltz, G. E. *Trans. Inst. Chem. Engrs* **1963**, *41*, 174.

32. Bauer, G. L. *Solvent Extraction of Copper: Kinetic and Equilibrium Studies*, Ph. D. Thesis, University of Wisconsin, 1975.

33. Zheng, Z.; Lu, J.; Li, D.; Ma, G. *Chem. Eng. Sci.* **1998**, *53*, 2327.

34. Bakker, C. A. P.; Fentener van Vlissingen, F. H.; Beek, W. J. *Chem. Eng. Sci.* **1967**, *22*, 1349.

35. Maroudas, N. G.; Sawistowski, H. *Chem. Eng. Sci.* **1964**, *19*, 919.

36. Guy, R. H.; Hinz, R. S.; Amantea, M. *Faraday Discuss. Chem. Soc.* **1984**, *77*, 127.

37. Samec, Z.; Marecek, V.; Koryta, J.; Khalil, M. W. *J. Electroanal. Chem.* **1977**, *83*, 393.

38. Samec, Z.; Marecek, V.; Weber, J. *J. Electroanal. Chem.* **1979**, *100*, 841.

39. Koryta, J.; Vanýsek, P.; Brezina, M. *J. Electroanal. Chem.* **1976**, *67*, 263.

40. Kakutani, T.; Osakai, T.; Senda, M. *Bull. Chem. Soc. Jpn.* **1983**, *56*, 991.

41. Samec, Z.; Marecek, V.; Homolka, D. *J. Electroanal. Chem.* **1981**, *126*, 121.

42. Samec, Z. *Chem. Rev.* **1988**, *88*, 617.

43. Homolka, D.; Wendt, H. *Ber. Bunsenges. Phys. Chem.* **1985**, *89*, 1075.

44. Koryta, J. *Electrochim. Acta* **1979**, *24*, 293.

45. Reymond, F.; Steyaert, G.; Carrupt, P.-A.; Testa, B.; Girault, H. H. *Helv. Chim. Acta* **1996**, *79*, 101.

46. Guainazzi, M.; Silvestri, G.; Serravalle, G. *J. Chem. Soc., Chem. Comm.* **1975**, 200.

47. Samec, Z.; Marecek, V. Weber, J. *J. Electroanal. Chem.* **1977**, *96*, 245.

48. Cheng, Y.; Schiffrin, D. J. *J. Chem. Soc., Faraday Trans.* **1994**, *90*, 2517.

49. Samec, Z.; Marecek, V. Weber, J.; Homolka, D. *J. Electroanal. Chem.* **1979**, *99*, 385.

50. Heyrovsky, J. *Chem. Listy* **1922**, *16*, 256.

51. Wang, E.; Sun, Z. *Trends in Anal. Chem.* **1988**, *7*, 99.

52. Kihara, S.; Suzuki, M.; Maeda, K.; Ogura, K.; Umetani, S.; Matsui, M.; Yoshida, Z. *Anal. Chem.* **1986**, *58*, 2954.

53. Marecek, V.; Samec, Z. *Anal. Chim. Acta* **1983**, *151*, 265.

54. Kihara, S.; Suzuki, M.; Maeda, K.; Ogura, K.; Matsui, M.; Yoshida, Z. *J. Electroanal. Chem.* **1989**, *271*, 107

55. Taylor, G.; Girault, H. H. J. *J. Electroanal. Chem.* **1986**, *208*, 179.

56. Stewart, A. A.; Taylor, G.; Girault, H. H.; McAleer, J. *J. Electroanal. Chem.* **1990**, *296*, 491.

57. Shao, Y.; Mirkin, M. *J. Am. Chem. Soc.* **1997**, *119*, 8103

58. Stewart, A. A.; Shao, Y.; Pereira, C. M.; Girault, H. H. *J. Electroanal. Chem.* **1991**, *305*, 135.

59. Shao, Y.; Osborne, M. D.; Girault, H. H. *J. Electroanal. Chem.* **1991**, *318*, 101.

60. Beattie, P. D.; Delay, A.; Girault, H. H. *J. Electroanal. Chem.* **1995**, *380*, 167.

61. Beattie, P. D.; Delay, A.; Girault, H. H. *Electrochimica Acta.* **1995**, *40*, 2961.

62. Murtomäki, L.; Kontturi, K. *J. Electroanal. Chem.* **1998**, *449*, 225.

63. Osborne, M. C.; Shao, Y.; Pereira, C. M.; Girault, H. H. *J. Electroanal. Chem.* **1994**, *364*, 155.

64. Cunnane, V. J.; Schiffrin, D. J.; Williams, D. E. *Electrochim. Acta.* **1995**, *40*, 2943.

65. Wilke, S.; Osborne, M. D.; Girault, H. H. *J. Electroanal. Chem.* **1997**, *436*, 53.

66. Beriet, C.; Girault, H. H. *J. Electroanal. Chem.* **1998**, *444*, 219.

67. Nakatani, K.; Uchida, T.; Misawa, H.; Kitamura, N.; Masuhara, H. *J. Phys. Chem.* **1993**, *97*, 5197.

68. Nakatani, K.; Uchida, T.; Misawa, H.; Kitamura, N.; Masuhara, H. *J. Electroanal. Chem.* **1994**, *367*, 109.

69. Nakatani, K.; Uchida, T.; Kitamura, N.; Masuhara, H. *J. Electroanal. Chem.* **1994**, *375*, 383.

70. Nakatani, K.; Wakabayashi, M.; Chikama, K.; Kitamura, N. *J. Phys. Chem.* **1996**, 100, 6749.

71. Nakatani, K.; Sudo, M.; Kitamura, N. *J. Phys. Chem. B* **1998**, 102, 2908.

72. Nakatani, K.; Uchida, T.; Funakura, S.; Sekiguchi, A.; Misawa, H.; Kitamura, N.; Masuhara, H. *Chem. Lett.* **1993**, 717.

73. Nakatani, K.; Suto, T.; Wakabayashi, M.; Kim, H. -B.; Kitamura, N. *J. Phys. Chem.* **1995**, *99*, 4745.

74. Nakatani, K.; Chikama, K.; Kim, H. -B.; Kitamura, N. *Chem. Phys. Lett.* **1995**, *237*, 133.

75. Chikama, K.; Nakatani, K.; Kitamura, N. *Chem. Lett.* **1996**, 665.

76. Kakiuchi, T.; Takasu, Y.; Senda, M. *Anal. Chem.* **1992**, *64*, 3096.

77. Kakiuchi, T.; Takasu, Y. *Anal. Chem.* **1994**, *66*, 1853.

78. Kakiuchi, T.; Takasu, Y. *J. Phys. Chem. B* **1997**, *101*, 5963.

79. Ding, Z.; Wellington, R. G.; Brevet, P.-F.; Girault, H. H. *J. Phys. Chem.* **1996**, *100*, 10658.

80. Fermin, D. J.; Ding, Z.; Brevet, P.-F.; Girault, H. H. *J. Electroanal. Chem.* **1998**, *447*, 125.

81. Eisenthal, K. B. *Chem. Rev.* **1996**, *96*, 1343.

82. Brevet, P. F.; Girault, H. H. in *Second harmonic generation at liquid/liquid interfaces* in *Liquid-Liquid Interfaces: Theory and Methods*, Volkov, A. G.; Deamer, D. W. (eds.), CRC Press, Boca Raton, 1996, p 103.

83. Benjamin, I. *J. Chem. Phys.* **1992**, *97*, 1432.

84. Benjamin, I.; Michael, D. *J. Electroanal. Chem.* **1998**, *450*, 335.

85. Benjamin, I. *Science* **1993**, *261*, 1558.

86. Hayoun, M.; Meyer, M.; Turq, P. *J. Phys. Chem.* **1994**, *98*, 6626.

87. Schweighofer, K. J.; Benjamin, I. *J. Phys. Chem.* **1995**, *99*, 9974.

88. Lauterbach, M.; Engler, E.; Muzet, N.; Troxler, L.; Wipff, G. *J. Phys. Chem. B* **1998**, *102*, 245.

89. Osakai, T.; Ebina, K. *J. Electroanal. Chem.* **1996**, *412*, 1.

90. Schmickler, W. *J. Electroanal. Chem.* **1997**, *426*, 5.

91. Sánchez, C. G.; Leiva, E. P. M.; Dassie, S. A.; Baruzzi, A. M. *J. Electroanal. Chem.* **1998**, *451*, 111.

92. Benjamin, I. *Chem. Rev.* **1996**, *96*, 1449.

93. Bard, A. J.; Fan, F-R. F.; Kwak, J.; Lev, O. *Anal. Chem.* **1989**, *61*, 132.

94. Wightman, R. M. *Science* **1988**, *240*, 415.

95. Heinze, J. *Angew. Chem. Int. Ed. Engl.* **1993**, *32*, 1268.

96. Forster, R. J. *Chem. Soc. Rev.* **1994**, 289.

97. Bard, A. J.; Fan, F.-R. F.; Mirkin, M. V. in *Electroanalytical Chemistry*, Vol. 18, Bard, A. J. (ed.), Marcel Dekker, New York, 1989.

98. Bard, A. J.; Fan, F.-R. F.; Pierce, D. T.; Unwin, P. R.; Wipf, D. O.; Zhou, F. *Science* **1991**, *254*, 68.

99. Arca, M.; Bard, A. J.; Horrocks, B. R.; Richards, T. C.; Triechel, D. A. *Analyst* **1994**, *119*, 719.

100. Unwin, P. R.; Macpherson, J. V. *Chem. Ind.* **1995**, *21*, 874.

101. Mirkin, M. V. *Anal. Chem.* **1996**, *68*, 177A.

102. Barker, A. L.; Gonsalves, M.; Macpherson, M. V.; Slevin, C. J.; Unwin, P. R. *Anal. Chim. Acta.* in press.

103. Wei, C.; Bard, A. J.; Mirkin, M. V. *J. Phys. Chem.* **1995**, *99*, 16033.

104. Saito, Y. *Rev. Polarogr. Jpn.* **1968**, *15*, 177.

105. Kwak, J.; Bard, A. J. *Anal. Chem.* **1989**, *61*, 1221.

106. Wipf, D. O.; Bard, A. J.; Tallman, D. E. *Anal. Chem.* **1993**, *65*, 1373.

107. Wipf, D. O.; Bard, A. J. *Anal. Chem.* **1992**, *64*, 1362.

108. Wipf, D. O.; Bard, A. J. *J. Electrochem. Soc.* **1991**, *138*, 5, L4.

109. Wipf, D. O.; Bard, A. J. *J. Electrochem. Soc.* **1991**, *138*, 469.

110. Mirkin, M. V.; Bard, A. J. *J. Electrochem. Soc.* **1992**, *139*, 3535.

111. Mirkin, M. V.; Richards, T. C.; Bard, A. J. *J. Phys. Chem.* **1993**, *97*, 7672.

112. Unwin, P. R.; Bard, A. J. *J. Phys. Chem.* **1992**, *96*, 5035.

113. Macpherson, J. V.; Unwin, P. R. *J. Chem. Soc., Faraday Trans.* **1993**, *89*, 1883.

114. Macpherson, J. V.; Unwin, P. R. *J. Phys. Chem.* **1994**, *98*, 1704.

115. Macpherson, J. V.; Unwin, P. R. *J. Phys. Chem.* **1994**, *98*, 11764.

116. Macpherson, J. V.; Unwin, P. R. *J. Phys. Chem.* **1995**, *99*, 3338.

117. Macpherson, J. V.; Unwin, P. R. *J. Phys. Chem.* **1995**, *99*, 14842.

118. Macpherson, J. V.; Unwin, P. R. *J. Phys. Chem.* **1996**, *100*, 19475.

119. Macpherson, J. V.; Unwin, P. R.; Hillier, A. C.; Bard, A. J. *J. Am. Chem. Soc.* **1996**, *112*, 6445.

120. Solomon, T.; Bard, A. J. *J. Phys. Chem.* **1995**, *99*, 17487.

121. Tsionsky, M.; Bard, A. J.; Mirkin, M. V. *J. Phys. Chem.* **1996**, *100*, 17881.

122. Selzer, Y.; Mandler, D. *J. Electroanal. Chem.* **1996**, *409*, 15.

123. Tsionsky, M.; Bard, A. J.; Mirkin, M. V. *J. Am. Chem. Soc.* **1997**, *119*, 10785

124. Delville, M. H.; Tsionsky, M.; Bard, A. J. *Langmuir* **1998**, *14*, 2774.

125. Shao, Y. H.; Mirkin, M. V.; Rusling, J. F. *J. Phys. Chem. B* **1997**, *101*, 3202.

126. Yamada, H.; Akiyama, S.; Inoue, T.; Koike, T.; Matsue, T.; Uchida, I. *Chem. Lett.* **1998**, 147.

127. Solomon, T.; Bard, A. J. *Anal. Chem.* **1995**, *67*, 2787.

128. Solomon, T.; Bard, A. J. *Bull. Chem. Soc. Ethiopia* **1997**, *11*, 55.

129. Shao, Y. H.; Mirkin, M. V. *J. Electroanal. Chem.* **1997**, *439*, 137.

130. Lee, Y. H.; Tsao, G. T.; Wankat, P. C. *Ind. Eng. Chem. Fundam.* **1978**, *17*, 59.

131. Bach, C. E.; Nichols, R. J.; Meyer, H.; Besenhard, J. O. *Surf. Coatings Technol.* **1994**, *67*, 139.

132. Bach, C. E.; Nichols, R. J.; Beckman, W.; Meyer, H.; Schulte, A.; Besenhard, J.

O.; Jannakoudakis, P. D. *J. Electrochem. Soc.* **1993**, *140*, 1281.

133. Pierce, P. *J. Coatings Technol.* **1981**, *53*, 52.

134. Boyd, D.; Zwack, R. *Progress Org. Coatings* **1996**, *27*, 25.

135. Dalton, R. F. *International Solvent Extraction Conference 1977*, Canadian Institute of Mining and Metallurgy, 1979, p. 40.

136. Quickenden, T. I.; Xu, Q. Z. *J. Electrochem. Soc.* **1996**, *143*, 1248.

137. Winlove, C. P.; Parker, K. H.; Oxenham, R. K. C. *J. Electroanal. Chem.* **1984**, *170*, 293.

138. O'Hare, D.; Winlove, C. P.; Parker, K. H. *J. Biomed. Eng.* **1991**, *13*, 304.

139. Denuault, G.; Mirkin, M. V.; Bard, A. J. *J. Electroanal. Chem.* **1991**, *86*, 27.

140. Shoup, D.; Szabo, A. *J. Electroanal. Chem. Interfacial Electrochem.* **1982**, *140*, 237.

141. Komasawa, I.; Otake, T. *J. Chem. Eng. Jpn.* **1983**, *16*, 377.

142. Bard, A. J.; Denuault, G.; Friesner, R. A.; Dornblaser, B. C.; Tuckerman, L. S. *Anal. Chem.* **1991**, *63*, 1282.

143. Bard, A. J.; Unwin, P. R.; Wipf, D. O.; Zhou, F. *Am. Inst. Phys., Conf. Proc.,* **1992**, *241*, 235.

144. Martin, R. D.; Unwin, P. R. *J. Electroanal. Chem. Interfacial Electrochem.* **1997**, *439*, 123.

145. Bard, A. J.; Mirkin, M. V.; Unwin, P. R.; Wipf, D. O. *J. Phys. Chem.* **1992**, *96*, 1861.

146. Unwin, P. R.; Bard, A. J. *J. Phys. Chem.* **1991**, *95*, 7814.

147. Zhou, F.; Unwin, P. R.; Bard, A. J. *J. Phys. Chem.* **1992**, *96*, 4917.

148. Demaille, C.; Unwin, P. R.; Bard, A. J. *J. Phys. Chem.* **1996**, *100*, 14137.

149. Barker, A. L.; Macpherson, J. V.; Slevin, C. J.; Unwin, P. R. *J. Phys. Chem. B* **1998**, *102*, 1586.

150. Volkov, A. G.; Deamer, D. W.; Tanelian, D. L.; Markin, V. S. *Liquid Interfaces in Chemistry and Biology*, Wiley, New York, 1998.

151. *Oxygen Transport in Biological Systems*, Egginton, S.; Ross, H. F., Eds., Cambridge University Press, New York, 1993.

152. Thibodeaux, L. J. *Environmental Chemodynamics: Movement of Chemicals in Air, Water and Soil, 2nd Ed.*, Wiley, New York, 1996.

153. Schwarzenbach, R. P.; Gschwend, P. M.; Imboden, D. M. *Environmental Organic Chemistry*, Wiley, New York, 1993.

154. Barnes, G. T.; Hunter, D. S. *J. Colloid Interface Sci.* **1990**, *136*, 198.

155. Seaver, M.; Peele, J. R.; Manuccia, T. J.; Rubel, G. O.; Ritchie, G. *J. Phys. Chem.* **1992**, *96*, 6389.

156. Drummond, C. J.; Elliot, P.; Furlong, D. N.; Barnes, G. T. *J. Colloid Interface Sci.* **1992**, *151*, 189.

157. *Retardation of Evaporation by Monolayers*, LaMer, V. K., Ed., Academic Press, New York, 1962.

158. Rideal, E. K. *J. Phys. Chem.* **1925**, *29*, 1585.

159. Linton, M.; Sutherland, K. L. *Australian J. Appl. Sci.* **1958**, *9*, 18.

160. Blank, M.; Roughton, F. J. W. *Trans. Faraday Soc.* **1960**, *56*, 1832.

161. Blank, M. In *Retardation of Evaporation by Monolayers*, LaMer, V. K., Ed., Academic Press, New York, 1962; p 75.

162. Hawke, J. G.; Alexander, A. E. In *Retardation of Evaporation by Monolayers,* LaMer, V. K., Ed., Academic Press, New York, 1962; p 67.

163. Davies, J. T.; Rideal, E. K. *Interfacial Phenomena,* Academic Press, New York, 1961.

164. Charych, D. H.; Landau, E. M.; Majda, M. *J. Am. Chem. Soc.* **1991,** *113,* 3340.

165. Charych, D. H.; Anvar, D. J.; Majda, M. *Thin Solid Films* **1994,** *242,* 1, and refs. therein.

166. Caruso, F.; Grieser, F.; Murphy, A.; Thistlethwaite, P.; Urquhart, R.; Almgren, M.; Wistus, E. *J. Am. Chem. Soc.* **1991,** *113,* 4838.

167. Prats, M.; Gabriel, B.; Tessié, J. *J. Am. Chem. Soc.* **1993,** *115,* 10153.

168. Adamson, A. W. *Physical Chemistry of Surfaces,* Wiley, New York, 1997.

169. See for example: Ulman, A. *An Introduction to Ultrathin Organic Films,* Academic Press, New York, 1991.

170. Pletcher, D.; Sotiropoulos, S. *J. Electroanal. Chem.* **1993,** *356,* 109.

171. Pletcher, D.; Sotiropoulos, S. *J. Chem. Soc., Faraday Trans.* **1995,** *91,* 457.

172. Han, P.; Bartels, D. M. *J. Phys. Chem.* **1996,** *100,* 5597.

173. Zaitsev, S. Y.; Kalmer, U.; Möbius, D. *Colloids Surf., A* **1995,** *94,* 137.

174. Lundquist, M. *Chem. Scr.* **1971,** *1,* 5.

175. Blank, M. *J. Phys. Chem.* **1964,** *68,* 2793.

176. Hubbard, A. T.; Anson, F. C. in *Electroanalytical Chemistry,* Vol 18., Bard, A. J. (ed.), Marcel Dekker, New York, 1970, p156.

177. Macpherson, J. V.; Unwin, P. R. *Anal. Chem.* **1997,** *69,* 2063.

178. Andrieux, C. P.; Hapiot, P.; Savéant, J. M. *J. Phys. Chem.* **1988,** *92,* 5992.

179. Andrieux, C. P.; Savéant, J. M. In *Investigations of Rates and Mechanisms of Reactions*, Bernasconi, C., Ed., Wiley, New York, 1986; Vol. 6, 4/E, Part 2, p 305.

180. Bard, A. J.; Denuault, G.; Friesner, R. A.; Dornblaser, B. C.; Tuckerman, L. S. *Anal. Chem.* **1991**, *63*, 1282.

181. Unwin, P. R.; Bard, A. J. *J. Phys. Chem.* **1991**, *95*, 7814.

182. Compton, R. G.; Stearn, G. M.; Unwin, P. R.; Barwise, A. J. *J. Appl. Electrochem.* **1988**, *18*, 657, and references therein.

183. Griffith, R. O.; McKeown, A; Winn, A. G. *Trans. Faraday Soc.* **1932**, *28*, 101.

184. Seidell, A.; Linke, W. F. *Solubilities: Inorganic and Metal-Organic Compounds*, 4th ed., American Chemical Society, Washington, DC, 1958; Vol. 1.

185. Penner, R. M.; Heben, M. J.; Longin, T. L., Lewis, N. S. *Science* **1990**, *250*, 1118.

186. Gewirth, A. A.; Craston, D. H.; Bard, A. J. *J. Electroanal. Chem.* **1989**, *261*, 477.

187. Nagahara, L. A.; Thundat, T.; Lindsay, S. M. *Rev. Sci. Instrum.* **1989**, *60*, 3128.

188. Shao, Y.; Mirkin, M. V.; Fish, G.; Kokotov, S.; Palanker, D.; Lewis, A. *Anal. Chem.* **1997**, *69*, 1627.

189. Lee, C.; Miller, C. J.; Bard, A. J. *Anal. Chem.* **1991**, *63*, 78.

190. Wang, D. K. Y; Xu, L. Y. F. *Anal. Chem.* **1995**, *67*, 4086.

191. Pendley, B. D.; Abruna, H. D. *Anal. Chem.* **1990**, *62*, 782.

192. Schulte, A.; Chow, R. H. *Anal. Chem.* **1996**, *68*, 3054.

193. Levich, V. G. *Physicochemical Hydrodynamics*; Prentice-Hall: N.J., 1962.

194. Britz, D. *Digital Simulation in Electrochemistry*, 2nd ed.; Springer-Verlag:

New York, 1988.

195. Pons, S.; Speiser, B.; McAleer, J. F.; Schmidt, P. P. *Electrochim. Acta* **1982**, *27*, 1711.

196. Popovich, A. T.; Jervis, R. E.; Trass, O. *Chem. Eng. Sci.* **1964**, *19, 357.*

197. Clift, R.; Grace, J. R.; Webber, M. E. *Bubbles, Drops and Particles*; Academic Press; New York, 1978.

198. Guha, D. K.; Vyarawalla, F.; De, F. *Can. J. Chem. Eng.* **1987**, *65*, 448.

199. Barker, A. L.; Unwin, P. R. manuscript in preparation.

200. Penner, R. M.; Heben, M. J.; Lewis, N. J. *Anal. Chem.* **1989**, *61*, 1630.

201. Macpherson, J. V.; Jones, C. E.; Unwin, P. R. *J. Phys. Chem. B* **1998**, *102*, 9891.

202. Oldham, K.; Myland, J.; Zoski, C.; Bond, A. *J. Electroanal. Chem.* **1989**, *270*, 79.

203. Oldham, K.; Zoski, C. *J. Electroanal. Chem.* **1988**, *256*, 11.

204. Baranski, A. S. *J. Electroanal. Chem.* **1991**, *307*, 287.

205. Oldham, K. B. *Anal. Chem.* **1992**, *64*, 646.

206. Birkin, P.; Silva-Martinez, S. *Anal. Chem.* **1997**, *69*, 2055.

207. Webb, M. A. *Construction and Application of Nanometre-Sized Ultramicroelectrodes for Dynamic Electrochemistry Studies*, M. Sc. Thesis, University of Warwick, 1998.

208. Silhanek, J.; Konradova, L.; Simeckova, O.; Horak, J. *Collect. Czechoslovak Chem. Commun.* **1982**, *47*, 2904.

209. Tzedakis, T.; Savall, A. *Chem. Eng. Sci.* **1991**, *46*, 2269.

210. Tzedakis, T; Savall, A. J. *Ind. Eng. Chem. Res.* **1992**, *31*, 2475.

211. Tzedakis, T; Savall, A. J. *J. Appl. Electrochem.* **1997**, *27*, 589.

212. Tam, K. Y.; Compton, R. G.; Atherton, J. H.; Brennan, C. M.; Docherty, R. *J. Am. Chem. Soc.* **1996**, *118*, 4419.

213. Eberson, L. *J. Am. Chem. Soc.* **1983**, *105*, 3192.

214. Baciocchi, E.; Bietti, M.; Mattioli, M. *J. Org. Chem.* **1993**, *58*, 7106

215. Ito, O.; Akiho, S.; Iino, M. *J. Org. Chem.* **1989**, *54*, 2436.

216. Schlesener, C. J.; Kochi, J. K. *J. Org. Chem.* **1984**, *49*, 3142.

217. Reed, R. A.; Murray, R. W. *J. Electroanal. Chem.* **1990**, *285*, 149.

218. Baciocchi, E.; Rol, C.; Mandolini, L. *J. Am. Chem. Soc.* **1980**, *102*, 7597.

219. Kreh, R. P.; Spotnitz, R. M.; Lundquist, J. T. *Tetrahedron Lett.* **1987**, *28*, 1068.

220. Ho, T-L. *Synthesis* **1973**, 347.

221. Trahanovsky, W. S.; Young, L. B. *J. Org. Chem.* **1966**, 2033.

222. Torii, S.; Tanaka, H.; Inokuchi, T.; Nakane, S.; Akada, M.; Saito, N.; Sirakawa, T. *J. Org. Chem.* **1982**, *47*, 1647.

223. Pletcher, D.; Valdes, E. M. *J. Chem. Res. (S)* **1987**, 386.

224. Nilsson, A.; Palmquist, U.; Pettersson, T.; Ronlán, A. *J. Chem. Soc., Perkin I* **1978**, 708.

225. Yoshida, K.; Shigi, M.; Fueno, T. *J. Org. Chem.* **1975**, *40*, 63.

226. Marquez, J.; de Marquez, O. P. *Revue Roumaine de Chemie* **1993**, *38*, 775.

227. Parker, V. D.; Adams, R. M. *Tetrahedron Lett.* **1969**, *21*, 1721.

228. Hlavatý, J. *J. Appl. Electrochem.* **1994**, *24*, 989.

229. Turq, P.; Lantelme, F.; Chemla, M. *Electrochim. Acta* **1969**, *14*, 1081.

230. Randle, T. H.; Kuhn, A. T. *J. Chem. Soc., Faraday Trans. 1* **1983**, *79*, 1741.

231. Fleischmann, M.; Lasserre, F.; Robinson, J. *J. Electroanal. Chem.* **1984**, *177*, 115.

232. Astumian, R. D.; Schelly, Z. A. *J. Am. Chem. Soc.* **1984**, *106*, 304.

233. Albery, W. J.; Choudhery, R. A. *J. Phys. Chem.* **1988**, *92*, 1151.